FRP Strengthened RC Beams Subjected to Drop Weight Impact and Static load

Experimental study for structural response

Master's thesis in the Master's Program Structural Engineering and Building Technology

YEABKAL ZELEKE NIGANI
GABRIELLA NORDSTRÖM

FRP Strengthened RC Beams Subjected to Drop Weight Impact and Static Load

Experimental study for structural response

Master's Thesis in the Master's Programme Structural Engineering and Building Technology

YEABKAL ZELEKE NIGANI
GABRIELLA NORDSTRÖM

FRP Strengthened RC Beams Subjected to Drop Weight Impact and Static Load
Experimental study for structural response

Master's Thesis in the Master's Programme Structural Engineering and Building Techology

YEABKAL ZELEKE NIGANI

GABRIELLA NORDSTRÖM

Cover:
Illustration of drop weight impact of FRP strengthened RC beam.

FRP Strengthened RC Beams Subjected to Drop Weight Impact and Static Load

Experimental study for structural response

Master's thesis in the Master's Programme Structural Engineering and Building Technology

YEABKAL ZELEKE NIGANI

GABRIELLA NORDSTRÖM

Department of Architecture and Civil Engineering
Division of Structural Engineering
Concrete Structures
Chalmers University of Technology

ABSTRACT

Using Fibre Reinforced Polymer (FRP) to repair and strengthen concrete structures have been a widely used method recently. Therefore, the aim of this master's thesis is to increase the understanding of the structural response of FRP strengthened Reinforced Concrete (RC) beams subjected to impact loading by studying the response of deformation capacity and the energy absorption under impact loading. The remaining residual capacity is also of interest in this study which is established by static loading of impacted beams until failure by rupture of reinforcement.

Drop weight impact for different drop heights were carried out on different amount of FRP strengthened RC beams in order to give a good overview of the intensity of the impact loading and the influence of strengthening area. The response of the beams for the drop weight tests were captured by high speed cameras and the recorded footages were analysed by using Digital Image Correlation (DIC).

Literature study was done to give background information and to estimate the structural response of structures under impact and static loading. Comparison between the behaviour of different strengthening types as well as comparison between experimental results and prediction calculations are also included in this thesis work.

It is observed that FRP strengthening resulted in increased load capacity and maximum deformation for static loading. Rotation capacity slightly increased in 1 layer FRP strengthening and slightly decreased in 3 layers FRP strengthening. Internal work was also observed to be increased in FRP strengthend beams.

FRP strenghthening over all indicated positive effect for impact tests. The residual capacity of FRP strengthened beams also exihibited improvement significantly.

Key words: reinforced concrete (RC), fibre reinforced polymer (FRP), aramid fibre, strengthening, impact load, drop weight impact, digital image correlation (DIC), load capacity, plastic deformation, internal work, static loading.

FRP förstärkta armerade betongbalkar utsatta för fallvikt och statisk last

Experimentell studie för strukturresponsen

Examensarbete inom masterprogrammet Konstruktionsteknik och Byggnadsteknologi

YEABKAL ZELEKE NIGANI

GABRIELLA NORDSTRÖM

Institutionen för arkitektur och samhällsbyggnadsteknik
Avdelningen för Konstruktionsteknik
Betongbyggnad
Chalmers tekniska högskola

SAMMANFATTNING

Detta exjobb är en experimentell studie som fokuserar på att öka förståelsen för externt fiberförstärkta (FRP) stålarmerade betongbalkar som utsätts för fallviktsförsök och statisk last. Fiberarmering blir mer vanlig att använda som förstärkning av befintliga betongkonstruktioner. Det finns många studier och experimentella undersökningar inom detta område men de innebär att fiberförstärkta balkar utsätts för endast statisk last och inte fallviktsförsök som studeras i denna rapport.

Experimenten genomfördes på armerade betongbalkar som utsattes för stötlast av en fallvikt på 20 kg som föll från olika höjder. Balkar som inte var förstärkta testades som referenser till balkar som hade olika lager aramidfiberförstärkning. Kvarvarande lastkapacitet för balkarna var också av intresse att veta, därför testades de under statisk last också. Lika många balkar med och utan förstärkning testades dessutom för enbart statisk last för att ha som referenser och för att se kompositfiberns påverkan på dessa balkar. Experimenten filmades med höghastighetskameror och resultaten analyserades genom Digital Image Correlation (DIC).

Innan experimenten utfördes även en litteraturstudie för att öka förståelsen för strukturresponsen av de involverade materialen och stötlast. Litteraturstudien innefattade dessutom analytiska och numeriska uträkningar som även utfördes för att förutspå de experimentella resultaten.

Det observerades att aramidfibrets påverkan resulterade i ökad last och maximal deformation, ökad absorptionskapacitet och rotationskapaciteten var liknande för 1 lager aramidfiberförstärkning och lägre för 3 lager. Kvarvarande lastkapacitet ökade med ökat antal lager aramidfiberförstärkning.

Aramidfiberförstärkning resulterade överlag med positiv effekt för betongbalkarna både under statisk last och fallviktsförsök.

Nyckelord: armerad betong, aramidfiber, kompositmaterial, förstärkning, stötlast, fallvikt, DIC, lastkapacitet, plastisk deformationskapacitet, statisk last.

Table of Contents

Preface

In this master's thesis influence of FRP strengthening on structural response of reinforced concrete beams under impact and static loading is studied. Several drop weight impact tests and static tests were performed, and test results were compared with analytical and numerical results.

The work was carried out between January and September 2020 at Chalmers and Norconsult in Gothenburg. The project is a part of an ongoing research project executed in collaboration between Chalmers and Norconsult financed by the Swedish Civil Contingencies Agency (MSB). The project is a continuation of five MSc theses projects carried out between 2016 and 2019.

Gothenburg, September 2020

Yeabkal Zeleke Nigani and Gabriella Nordström

Notations

Abbrevations

B	Batch
DIC	Digital image correlation
DIF	Dynamic increase factor
D3	Drop height 3 m
D3.5	Drop height 3.5 m
D4	Drop height 4 m
FRP	Fibre reinforced polymer
RC	Reinforced concrete
S	Static load case
SDOF	Single degree of freedom
ULS	Ultimate limit state
WST	Wedge splitting test
2DOF	Two degree of freedom

Roman letters

A	Area
A_s	Area of reinforcement
A_{fe}	Area of FRP
A_{ADH}	Area of adhesive
E_c	Mean modulus of elasticity for concrete
E_s	Mean modulus of elasticity for reinforcing steel
E_{fe}	Mean modulus of elasticity for FRP
E_k	Kinetic energy
F	Force
F_{cr}	Cracking load
F_{imp}	Impact force
F_{max}	Maximum load from test results
F_u	Ultimate load from predictions
F_s	Static force
F_{Rmax}	Average maximum load of reference beams
G	Shear modulus
G_f	Fracture energy
I	Impulse, moment of inertia
I_K	Characteristic impulse
L_e	Length from support to plastic hinge
L	Length of span of the beam
M_{cr}	Cracking moment
M_u	Ultimate moment

M_y	Yield moment
R	Internal resisting force
R_{cr}	Internal resisting force when cracking occurs
R_{dyn}	Dynamic internal response
R_m	Dynamic internal response
R_{stat}	Static internal response
T_n	Smallest time period
W_e	External work
W_i	Internal work
W_{imp}	Internal work due to impact load
W_{tot}	Total internal work

Roman letters

a	Acceleration
b	Width of beam
b_f	Width of FRP
c	Damping coefficient, concrete cover
d	Effective height, bottom reinforcement
d'	Effective height, top reinforcement
d_f	Effective height, FRP layer
f_{cc}	Compressive cylinder strength of concrete
f_{ck}	Characteristic compressive cylinder strength of concrete
f_{cm}	Mean compressive cylinder strength of concrete
$f_{cm,cube}$	Mean compressive cube strength of concrete
f_{ct}	Tensile strength of concrete
$f_{ct,fl}$	Flexural tensile strength of concrete
f_{ctm}	Mean tensile strength of concrete
$f_{ct,sp}$	Splitting tensile strength of concrete
fu	Ultimate tensile strength of steel
fu	Yield strength of steel
$f_{0.2}$	Proof stress of steel
h	Height of beam cross-section
k	Linear elastic stiffness
k'	Stiffness after cracking has occurred
k_λ	Correction factor for slenderness
x_0	Distance from zero moment section to the point of maximum moment after redistribution
l_{pl}	Length of plastic hinge
m	Mass
p	Momentum
r	Radius, curvature radius
t	Time
t_o	Time for active portion of the beam to span the entire beam

u	Displacement
u_{cr}	Displacement when cracking occurs
u_{el}	Elastic deformation
u_{pl}	Plastic deformation
u_s	Displacement of system point
u_{SDOF}	Displacement of SDOF system
u_{tot}	Total displacement
$\dot{u}$	Velocity
$\ddot{u}$	Acceleration
v	Velocity
v_0	Velocity before impact
v_1	Velocity for particle one after impact
v_2	Velocity for particle two after impact
x	Height of compressive zone, length coordinate in x-direction

Greek letters

a_R	Stress block factor
β_R	Stress block factor
ΔT	Time step
Δ	Deformation at impact zone
ε_{cu}	Ultimate compressive strain for concrete
ε_{cc}	Compressive strain for concrete
ε_{ct}	Tensile strain for concrete
ε_s	Tensile strain for steel
ε_{su}	Ultimate strain for steel
ε_{sy}	Tensile strain at yielding for steel
ε_{fd}	Ultimate strain for FRP
ε_{fe}	Tensile strain in FRP
ϕ	Curvature, reduction factor
ϕ_{FRP}	Resistance factor for FRP
k	Transformation factor
v	Poisson's ratio
λ	Slenderness
ω	Eigenfrequency
ω_s	Mechanical reinforcement ratio
$\varnothing$	Angle
ψ	Stress block parameter
ρ	Reinforcement ratio, density
σ	Compressive stress
δ_G	Stress block parameter
θ_{pl}	Plastic rotation
$\theta_{pl,BK25}$	Plastic rotation according to Bk25

$\theta_{pl,EC}$	Plastic rotation according to Eurocode 2
$\theta_{pl,x\%}$	Plastic rotation at given load level

Index

b	Beam
c	Concrete
$crit$	Critical
el	Elastic
F	Force
I	State I
II	State II
k	Characteristic, stiffness
m	Mean value
max	Maximum
pl	Plastic
rel	Relative
s	Reinforcing steel
t	Tangent
tot	Total
u	Ultimate
y	Yielding
0	Initial
1	Drop weight
2	Beam

1 Introduction

1.1 Background

Impulse load highly affects the structural response of a structure. It is of great interest to study the behaviour of concrete under impact load since concrete is used in structures exposed to impulse loads. This could for example be due to collisions or explosions. The response of Reinforced Concrete (RC) structures subjected to impact load might be very different compared with statically loaded structures. One reason for this is that impact loaded structures often withstand load energy by using a combination of force and large deformations, while statically loaded structures withstand force only.

Retrofitting concrete structures using Fibre Reinforced Polymer (FRP) is a widely used method to strengthen RC structures nowadays. Researches show FRP strengthening results in smaller crack width, smaller deflection, and higher load capacity. However, it might not always result in higher energy absorption capacity when subjected to dynamic loading due to debonding of FRP or fibre rupture, rather the structure might encounter lower energy absorption and plastic deformation capacity which results from a brittle response of debonding of FRP.

Even though debonding of FRP to concrete interface is one of the common failures both in static and dynamic loading, the behaviour of FRP strengthening of concrete structures subjected to dynamic loading might not give the same result as in static loading. Therefore, it is important to investigate the influence of impact loading for FRP strengthened concrete structures.

This master's thesis is part of an ongoing research project, financed by the Swedish Civil Contingencies Agency, at the Division of Structural Engineering, Chalmers. It is carried out in cooperation between Norconsult and Chalmers and is a continuation of five previous theses projects carried out from 2016 to 2019. In this thesis the effect of FRP strengthening is introduced to the previously investigated studies.

1.2 Aim

The aim of this thesis is to get a better understanding of the structural response of FRP strengthened RC structures subjected to impact loading by using experimental study. The effect of strengthening RC beams with FRP was studied by focusing on residual and plastic deformation capacity, which explains how plastic deformation capacity under dynamic loading is influenced by FRP strengthening in RC structures.

A literature study of the mechanical properties of FRP material and how the use of FRP strengthening affects the structural response of RC structures subjected to static and impact loading was also believed to give a better over view of influence of FRP strengthening in impact and statically loaded structures.

Furthermore, this study includes comparison of the predicted response with dynamic and static experimental results using simplified 2DOF numerical models and analytical predictions. Which is helpful to see what degree the predicted calculations can show and to indicate desired future developments in these calculations.

This master's thesis will hopefully be of good use in future studies about FRP strengthened RC and to inspire further interest of the subject. It also provides experimental test results for future analyses using different types of methods (e.g. 2DOF and FEM).

1.3 Limitations

The number of beams that were experimentally studied were limited to 19. Which limited the number of tests in the impact testing to be one of a kind and scatter of results were not considered in these loading cases.

In this study the only failure mode that is aimed to study is bending failure. Therefore, only the bottom part of the beams which would be in tension was strengthened and the expected limitation in load capacity was due to bending failure by crushing of concrete or debonding of FRP. However, strong FRP strengthened RC beams could exhibit shear type failure.

The 2DOF prediction was limited to only estimation of the response of reference beams and the analytical prediction of static loading was done without taking into consideration of different factors such as bond strength for FRP strengthened beams. Material parameters used were only based on static testing.

1.4 Methodology

The starting point for the project was a literature study of previous MSc theses projects and other publications to get an understanding of the response of RC structures subjected to impulse loading compared with static loading. Detailed study about plastic rotation capacity and energy absorption under the influence of impulse loading was carried out.

Another main focus of the literature study was the material properties of FRP material, how it influence the structural response of RC structures under static loading, what changes are encountered for impulse loading and the pros and cons of using FRP strengthening for structures subjected to dynamic loading.

For the drop weight and the static experiments 18 + 1 beams were used. The RC beams had a geometry of 1.3 m x 0.1 m x 0.1 m and had simply supported test set up loaded at the mid span.

Manufacturing of concrete and standard tests to determine the mechanical properties of both concrete and steel was done.

Half of the beams were subjected to drop weight impact followed by static loading. Some of these beams were strengthened with different amount of FRP prior to loading. The other half of the beams were loaded in static loading only to be used as a reference, in which some of these beams were also strengthened with different amount of FRP.

A high speed camera was used to register the development of cracks and deformation of the beams for the drop weight tests. Digital Image Correlation (DIC) was used to calculate the strain field in concrete. The static tests were recorded by a normal camera. Simplified 2DOFs system was used to predict dynamic response to do comparison of the experimental results with the predicted ones.

2   Structural Response and Materials

This chapter introduces the basic behaviour and material properties for the materials that were involved in the experiments carried out in this thesis, these are concrete, reinforcing steel and fibre reinforced polymer. For this study the most important thing is how the material strength and behaviour would be affected when RC structure is strengthened with FRP, therefore this concept will also be explained. This information will give basic knowledge that will improve the understanding of the results for this study.

2.1   Structural response for materials

The structural response of materials can vary depending on the material properties or the composition of materials. The responses for linear elastic, ideal plastic, elasto-plastic, tri-linear and non-linear, are relevant for this study and will be explained in this chapter. Furthermore, ductile and brittle failures will also be addressed.

2.1.1   Linear elastic response

Linear elastic response is characterised by a linear response in a stress-strain curve, see Figure 2.1. When unloading a structure with linear elastic behaviour, the current deformation will go back to its initial state, as it was before loading. The unloading response will also be the same as the loading response, but in opposite direction (Ljung et al., 2015).
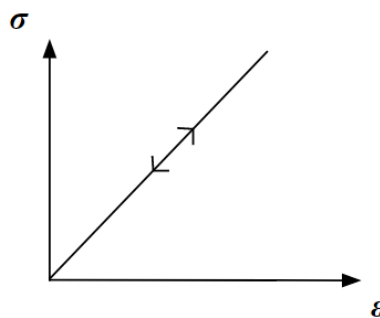
Figure 2.1   Stress–strain relation for a linear elastic response. The arrows show the response when unloading and reloading.

The stress can be calculated as

$$\sigma = E \cdot \varepsilon \tag{2.1}$$

where σ = stress [Pa]

           ε = strain [-]

           E = modulus of elasticity (young's modulus) [Pa]

When studying Hooke's law, Equation (2.1), it can be seen that stress is proportional to the strain. Stiffness is constant and therefore this results in a linear response.

2.1.2 Ideal plastic response

Ideal plastic response is characterised by irreversible strain or deformations. The material increases its strain with constant stress, shown in Figure 2.2. The structure has reached its maximum capacity and therefore cannot carry a higher load, neither does it has any strain hardening after yielding. Furthermore, the structure within the material is breaking down, which leads to a decreased stiffness, and for the ideal plastic response it ceases to exist (Dahlblom and Olsson, 2015). For a material with ideal plastic behaviour, there will be no deformation until the maximum stress capacity is reached.
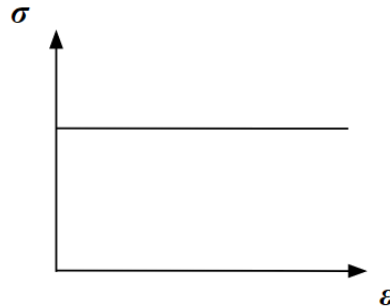
Figure 2.2   Stress–strain relation for an ideal plastic response.

2.1.3 Elasto-plastic response

Elasto-plastic response is here denoted as when a structure first shows a linear elastic response and after reaching its maximum stress capacity, the material will plasticise and continues with a plastic response until failure, see Figure 2.3. The material is denoted to yield when it reaches its stress that initiate plasticity (Dahlblom and Olsson, 2015). If the structure is unloaded the linear elastic part returns, while the plastic part of the deformation remains.

Figure 2.3   Stress–strain relation for an elasto-plastic response. The arrows show the response when unloading and reloading.

2.1.4 Tri-linear response

Tri-linear response results in a more refined response curve. This behaviour includes the possibility of more than one stiffness for the linear elastic response (Jönsson and Stenseke, 2018). The response curve for steel subjected to tensile forces can be modelled as tri-linear, see Figure 2.4. The steel behaves as linear elastic until yielding where the yielding plateau is depicted and continues with strain hardening until reaching ultimate tensile stress.
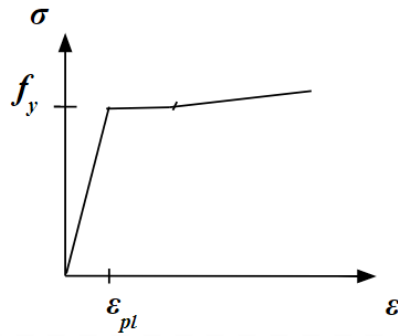
Figure 2.4   Stress–strain relation for a tri-linear response.

2.1.5   Non-linear elastic response

Non-linear elastic response depends on the stiffness of the structure (Dahlblom and Olsson, 2015). In this case the stress will not be linearly related to the strain, although deformations will still be able to go back to its initial state if the structure is unloaded, see Figure 2.5.
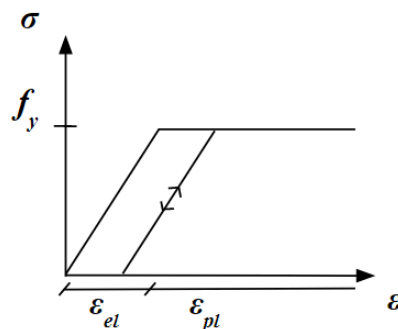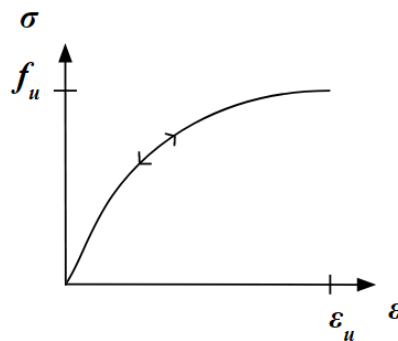

Figure 2.5   Stress–strain relation for a non-linear elastic response. The arrows show the response when unloading and reloading.

The simplified method for calculations is to use linear elastic response, based on Hooke's law. However, when size of forces and deformations becomes larger, the accuracy will become worse (Dahlblom and Olsson, 2015). For RC it can be assumed that before cracking there is a good estimation to use linear elastic response. However, after cracking the behaviour will be less accurate. Therefore, to get a more precise description of a materials behaviour, a non-linear response should be used.

2.1.6   Ductile and brittle behaviour

It is common to talk about two kinds of response failure types; ductile and brittle that are interesting when studying the stress–strain relationship for materials. A schematic illustration of the structural response for these failure types are shown in Figure 2.6. The figure also illustrates what the rupture looks like for test objects with ductile and brittle behaviours, subjected by tensile stresses. A material with ductile behaviour will have a plastic rupture, while a brittle behaviour results in a clear rupture.
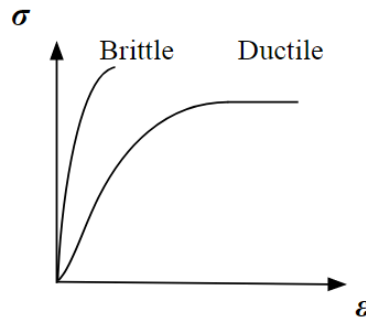
Figure 2.6   Stress–strain relation illustrating ductile and brittle behaviours.

Ductile materials have large plastic deformations before rupture (Ljung et al., 2015). This enables the material to absorb more energy before failure, see Figure 2.6, which is an important material property when studying structures subjected to impulse load. Material behaviours also depends on the temperature, high temperatures usually make materials more ductile (Ljung et al., 2015). Examples of ductile materials are many metals and some plastics (Burström, 2015).

As opposite to ductile materials, brittle materials will show very little plastic deformations before rupture (Ljung et al., 2015). This makes it difficult to know when the failure will occur by only studying the structure visually. The failure can be predicted but will occur without warning. As result, a structure of brittle material with the same maximum load capacity will not be able to absorb as much energy when compared to a ductile material, see Figure 2.6. Examples of brittle materials are plain concrete, stone and brick (Burström, 2015).

2.2   Material properties

In this chapter the mechanical and structural behaviour of materials used in this experimental study is treated. The behaviour of plain concrete, reinforcing steel, FRP material and reinforced concrete will be elaborated.

2.2.1   Concrete

Concrete is a widely used composite construction material which is weak in tension and strong in compression, see Figure 2.7. It also exhibits a brittle failure in tension when compared with its behaviour in compression (Engström, 2014).
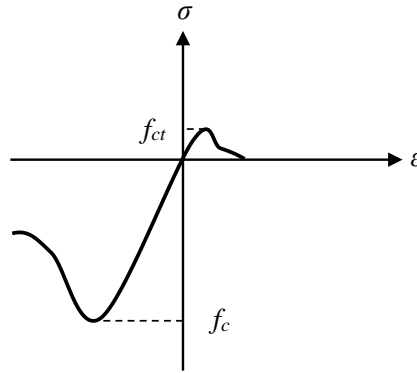
Figure 2.7   Stress-strain relation for concrete under stress-strain relation for concrete under uniaxial loading. f_c and f_{ct} correspond to the strength in compression and tension respectively. From Engström, 2014.

2.2.1.1   Compressive strength

Concrete strength class is categorized based on compressive strength that is gained from standard cylindrical test or from cube test, at the age of 28 days. The measured strength of a cylindrical test is smaller than the cube test due to the slenderness of the cylinder specimen which results in a less transverse confining stress in the mid region. This effect is adjusted in the following relation between the mean cylinder strength and mean cube strength as

$$f_{cm} = 0.8 \cdot f_{cm,cube} \tag{2.2}$$

where f_{cm} = mean cylindrical compressive strength

$f_{cm,cube}$ = mean cubic compressive strength

According to (CEN, 2004), for a standardized concrete grade the mean compressive strength is developed from characteristics value at an age of 28 days. Considering the standard deviation of 8 MPa, independent of concrete strength, it is calculated as

$$f_{cm} = f_{ck} + 8 \, MPa \tag{2.3}$$

where f_{ck} = characteristic compressive strength

2.2.1.2   Tensile strength

Tensile strength of concrete can be assessed by pure tensile test, splitting test or by bending of prismatic beam specimens. Tensile strength under pure tension can be obtained from splitting tests using

$$f_{ctm} = 0.9 \cdot f_{ct,sp} \tag{2.4}$$

where $f_{ct,sp}$ = mean tensile strength determined in splitting test

The tensile strength of concrete can also be calculated from the characteristic compressive strength as

$$f_{ctm} = 0.3 \cdot f_{ck}^{\frac{2}{3}} \text{ for concrete class } \leq C50/60 \tag{2.5}$$

The flexural tensile strength of concrete can be determined from tensile strength under pure tension as

$$f_{ct,fl} = k \cdot f_{ctm} \text{ for concrete class } \leq C50/60 \qquad (2.6)$$

$$k = 1.6 - \frac{h}{1000} \geq 1.0 \qquad (2.7)$$

where h = the sectional depth in [mm]

2.2.1.3 Modulus of elasticity

The modulus of elasticity of concrete increases with increasing compressive strength. The modulus of elasticity of concrete is described as the secant modulus between the points $\sigma_c = 0$ and $\sigma_c = 0.4 \cdot f_{cm}$ (Engström, 2014) as shown in Figure 2.8 and expressed in equation as

$$E_{cm} = 22 \left(\frac{f_{cm}}{10} \right)^{0.3} [GPa] \qquad (2.8)$$
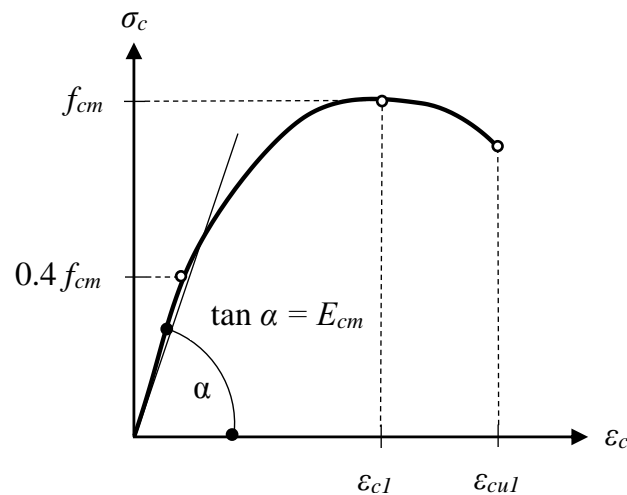
Figure 2.8   Ideal stress-strain relation for concrete in compression (Jönsson and Stenseke, 2018).

2.2.1.4 Structural response in compression

According to (Engström, 2014) the stress-strain relationship of concrete in compression is almost linear until reaching $0.5 \cdot f_{cm} - 0.6 \cdot f_{cm}$. For the peak compressive stress, the strain increases with increasing compressive strength which shows a non-linear stress-strain relation around peak compressive stress. However, the strain capacity decreases with increasing strength of concrete which means concrete has a more brittle failure mechanism as the strength class increases, see Figure 2.9 (Engström, 2014).
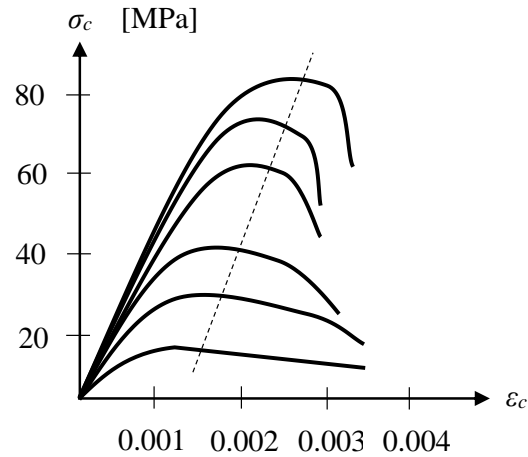
Figure 2.9   Stress-strain relation for different strength class of concrete in compression (Engström, 2014).

The Compressive strength of concrete also depends on the loading rate, which can be shown in Figure 2.10. The faster the loading rate the higher the strength, which means the compressive strength of concrete is higher for short-term loading such as impact loads (Engström, 2014). According to BBK 04 and Eurocode 2, adjustment for this loading rate effect should be considered in design calculations. In case of the presence of short-term loading such as accidental loading in load combinations, BBK 04 accounts for such effects by multiplication of the design strength value by 1.1. Eurocode 2 states that the characteristics compressive strength can be reduced by a factor of α_{cc} in case of long-term loading. This relationship is given as

$$f_{cd} = \alpha_{cc} \cdot \frac{f_{ck}}{\gamma_c} \tag{2.9}$$

where f_{cd} = design compressive strength of concrete

f_{ck} = characteristic compressive strength of cylinder according to EN-Standard at normal loading rate

α_{cc} = 0.8 – 1.0, the recommended value in design is 1.0

γ_c = 1.5, partial factor for concrete in ordinary situations
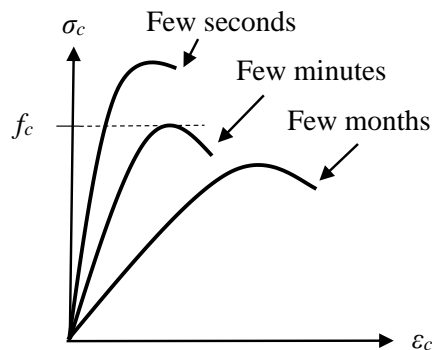
Figure 2.10   Illustration of compressive strength dependency on loading rate (Engström, 2014).

2.2.2 Reinforcing steel

The stress-strain relationship of reinforcing steel under tension is of main interest since reinforcing steel is provided to amend the need for tensile strength of concrete. Ductility of reinforcing bar after yielding, i.e. the increase in strain after yielding up to reaching ultimate strain, εsu, is an important parameter to determine the deformation property of reinforcing steel. Therefore, both the ultimate strain and the ratio between tensile strength and yield strength are used for the classification of reinforcing steel regarding ductility characteristics. The ductility behaviour of steel is an essential parameter for structures under impulse loading since a larger plastic deformation is required to withstand impact load (Johansson and Laine, 2012).

Reinforcing steel is also classified as hot rolled or cold worked based on the manufacturing process (Engström, 2015). Hot rolled steel has a prominent yield stress and large plastic deformation before reaching the ultimate stress due to higher strain hardening. On the contrary cold worked steel usually has a very small plastic deformation and strain hardening before reaching the ultimate stress, i.e. no plastic plateau is seen. Hence, proof stress, f0.2, is used instead of yield stress for cold worked steel (Ljung et al., 2015). Proof stress is the stress, when unloading a structure gives lasting deformations corresponding to 0.2 % of the total deformation, see Figure 2.11 (Ljung et al., 2015).

(a) (b)
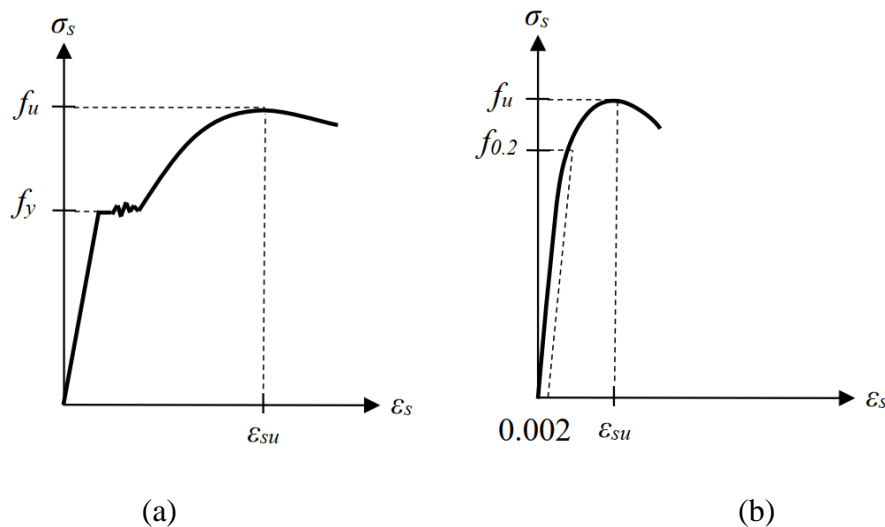
Figure 2.11   Stress–strain relation for a) hot rolled and b) cold worked reinforcing steel from (Engström, 2015).

2.2.3 Fibre reinforced polymer

Fibre Reinforced Polymer (FRP) is a composite material, which include fibres and a polymer matrix (Nordin, 2005). A composite material consists of two or more materials with different properties, whose combination results with a material that has more desired properties. For FRP, the fibres contribute with high tensile capacity while the polymer matrix transfer forces between fibres, but also bind the fibres together and protects them (Nordin, 2005).

FRP is strong in tension and weak in compression, these are qualities that makes it adequate as strengthening materials for concrete structures and should be applied on the side that is subjected to tensile forces. There are three things that control the mechanical properties of different FRP materials; constituent materials, amount of fibres and the orientation of fibres (Nordin, 2003).

The most common FRP materials to be used for civil engineering applications are Carbon Fibre Reinforced Polymer (CFRP), Aramid Fibre Reinforced Polymer (AFRP) and Glass Fibre Reinforced Polymer (GFRP) (Nordin, 2005). CFRP are known to have the highest modulus of elasticity of the fibre types and all fibre types have linear elastic response and brittle failure, see Figure 2.12, (Wu and Eamon, 2017). GFRP have relatively low modulus of elasticity and AFRP have a high modulus of elasticity, however, not as high as CFRP (Wu and Eamon, 2017). The properties of FRP is further explained in Section 5.
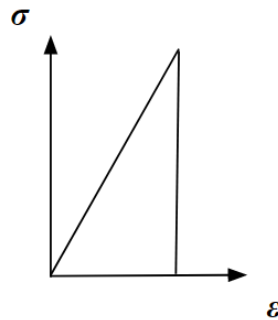
Figure 2.12   Stress–strain relation for FRP material.

2.2.4   Reinforced concrete

Reinforced concrete (RC) is a combination of concrete and reinforcement in which the reinforcement is provided with an arrangement to keep the structure in equilibrium with the external load even after cracking. The behaviour of RC can be studied using different relationships in regional or sectional response in uncracked and cracked state.

In the uncracked stage, i.e. state I, the curvature response of the beam increases linearly as the bending moment increases, thus the beam will have a linear elastic global response in state I. Even though it is common to only consider the stiffness of concrete in state I, a large reinforcement amount may still contribute about 20 % to the concrete stiffness according to (Engström, 2015).

After cracking takes place the state is considered as state II. For state II, it is assumed that stiffness of the cracked region mainly depends on the reinforcement stiffness and the configuration of the cross section. However, the tensile stress is transferred from the reinforcement bars to the surrounding concrete resulting in less average steel strain than the assumed steel strain in the fully cracked region. Hence, the uncracked concrete between the flexural cracks contribute to the stiffness of the region due to tension stiffening. Therefore, the stiffness calculated in state II model will be underestimated (Engström, 2015).

The response in state II is assumed to be a linear material response for both steel and concrete in the cracked stage. However, this holds true until yielding is reached in steel and concrete holds a non-linear stress-strain behaviour (Engström, 2015).
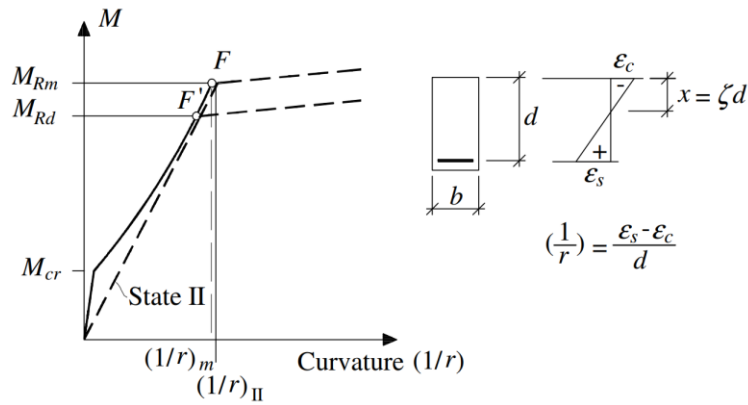
Figure 2.13   Moment-curvature relation of cracked region showing tensioning stiffening effect on state II (Engström, 2015).

If the beam is loaded until yielding of reinforcement is reached, the beam should be analyzed with a state III model. A state III model is used when either the concrete or the reinforcement has non-linear response. After the yield moment is reached a plastic flow will be started and continues as result of strain hardening of steel following the increment of external load. As the load increases further the ultimate moment will be reached at a certain load level. The plastic flow then continues as the curvature increases under a constant ultimate moment until the section becomes completely plastic and attain ultimate strain in the section (Plem, 1981) .

These responses can be simplified to a bilinear elasto-plastic response considering a cracked region in state II. This simplification assumes elastic response for the load-displacement relation of the section starting from the beginning until yield stress is reached and completely plastic response when the yield stress is reached considering the yielding moment is equal to the ultimate moment the section can withstand according to (Johansson and Laine 2012).
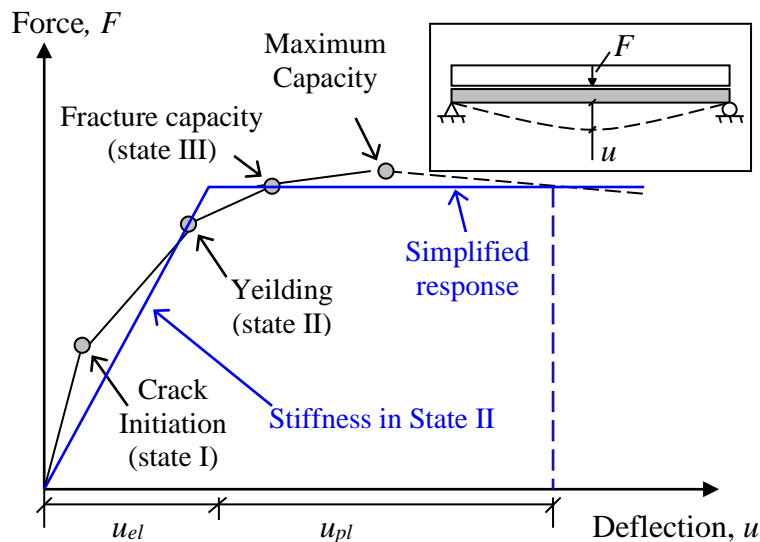
Figure 2.14   Simplified Structural response for RC beam (Johansson and Laine, 2012).

2.3 Strain rate

According to Johansson (2000) the material properties of concrete and reinforcement varies when subjected to static loading and dynamic loading. Hence, the rate of loading is considered to affect the mechanical properties of materials. This effect due to the rate of load application is referred to as strain rate effect and it is defined as the change of strain rate over time. This effect is commonly expressed in terms of the dynamic increase factor (DIF), which is determined as

$$\text{DIF} = \frac{F_{dyn}}{F_{stat}}$$

(2.10)

Where F_{dyn} is dynamic strength and F_{stat} is static strength.

Since the rate of loading differs between distinct load types, illustration of different strain rate in comparison with static loading is shown in Figure 2.15.
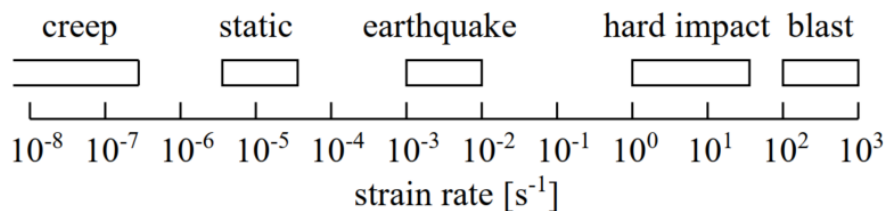
Figure 2.15 Strain rates for different loading conditions (Johansson, 2000).

Even though different test parameters such as: concrete strength, specimen dimension, moisture content, test set up, loading type and measurement type, can generate various effects on the test results, increased strain rate is observed to result in increase of material strength (Johansson and Laine, 2012).

2.3.1 Influence of strain rate on concrete strength

Johansson (2000) summarises different researches made on the influence of strain rate effects on concrete strength. It is stated that strain rate effect differs among various parameters that are considered by the proposal. Comparisons of DIF and strain rate relation presented on Johansson (2000) for concrete in compression and concrete in tension are presented in Figure 2.16 and Figure 2.17 respectively.
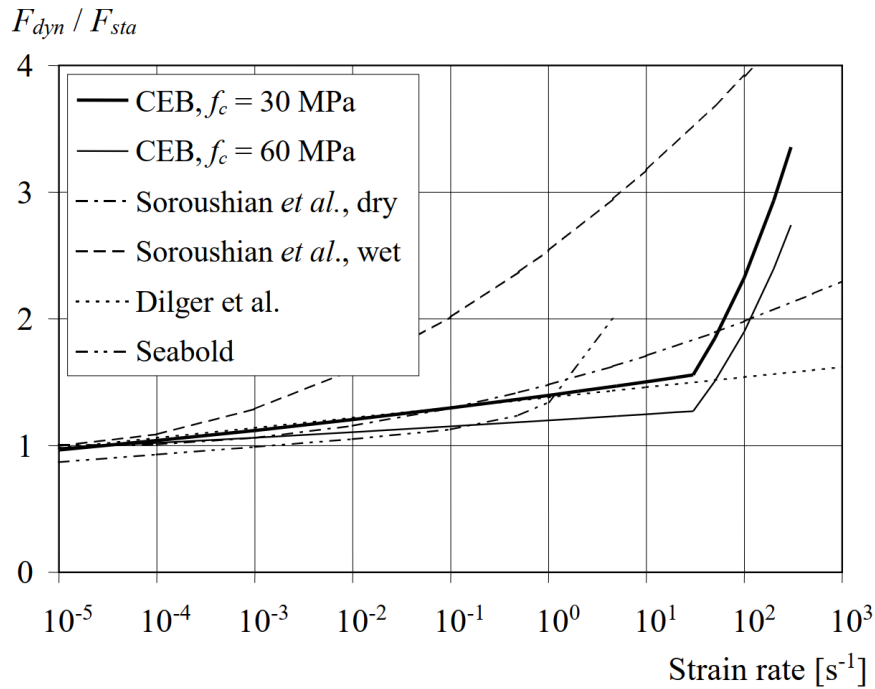
Figure 2.16   Comparison of DIF and strain rate relation for concrete in compression (Johansson, 2000).
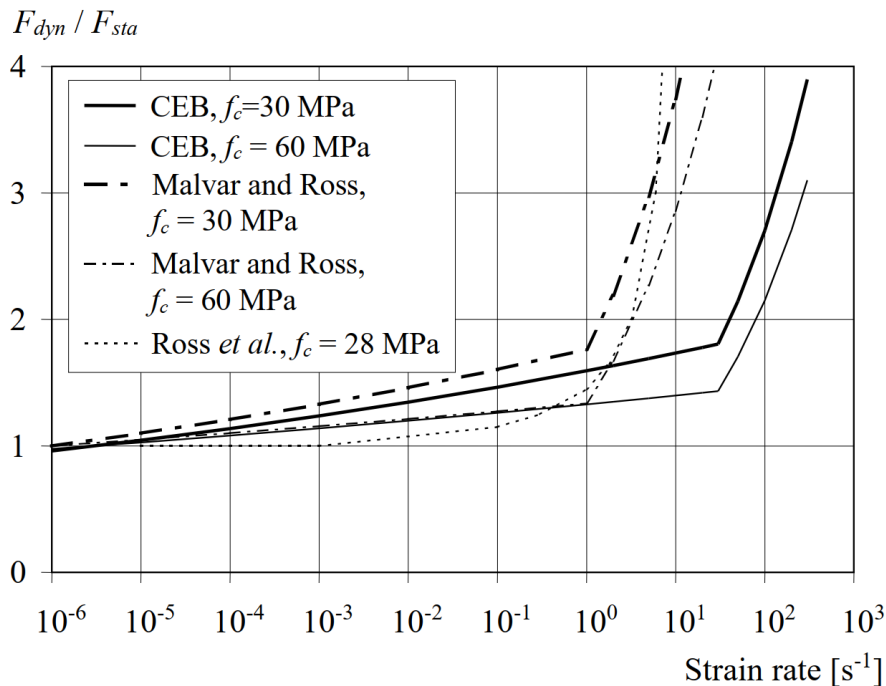
Figure 2.17   Comparison of DIF and strain rate relation for concrete in tension (Johansson, 2000).

Johansson (2000) states that strain effect on concrete strength can be compiled into viscous effect and structural effect. Viscous effect arises due to the pressure of water in micropores of concrete and is a mild increase of strength at increased strain rate until the transition zone, see Figure 2.18.

After the transition zone the increase of strength is considered as structural effect and it is drastic characterized by a drastic increase of strength at increased strain rate. This strength effect is obtained from change of inertial and confinement due to changed stressed and energy distribution around the concrete crack tips. This is further explained as in a faster loading rate, concrete will not have time to react which results in significant increase of concrete strength due to multiaxial stress state (Johansson, 2000).
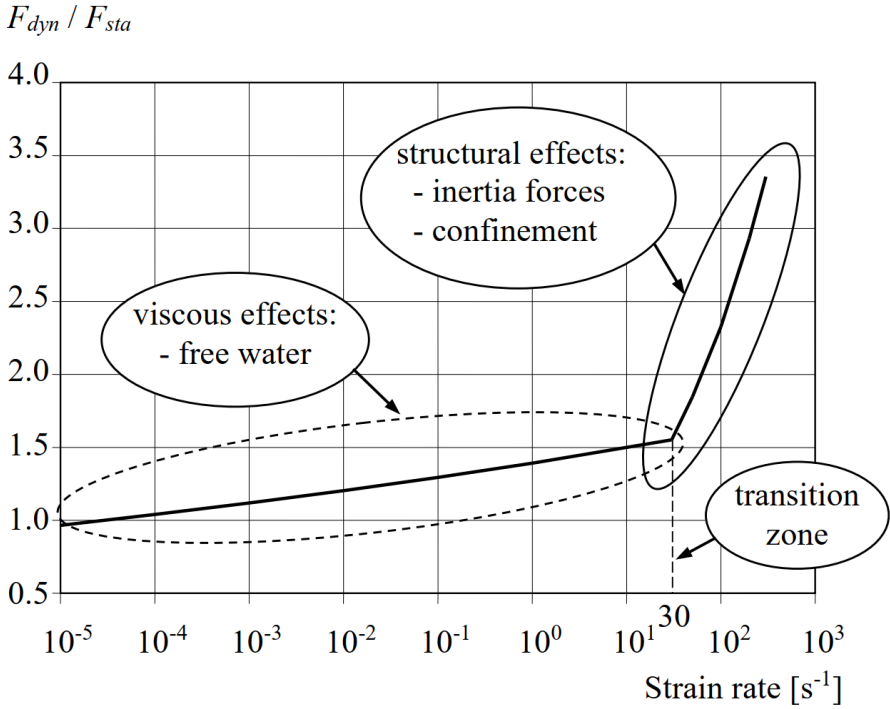
Figure 2.18   Stages of strain rate effects of concrete (Johansson, 2000).

2.3.2   Influence of strain rate on reinforcement

The strength of reinforcement steel is also impacted by strain rate effect, i.e. yield stress and ultimate stress increases at high strain rates. Hence, the observed effect from different researches on ultimate strain is not clear according to different (Johansson, 2000). Relation between DIF and strain rate for hot rolled steel is illustrated in Figure 2.19.
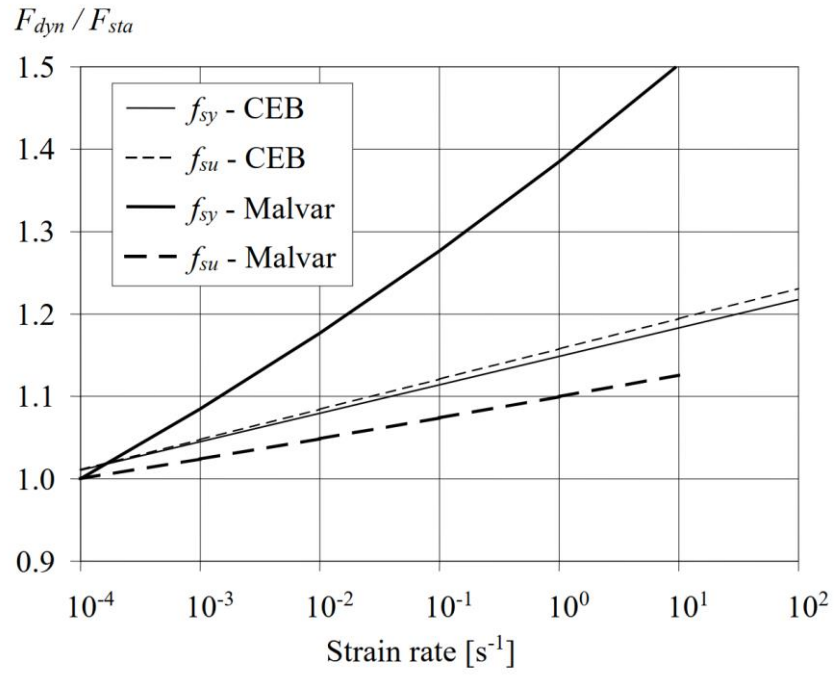
Figure 2.19   Comparison of DIF and strain rate relation for reinforcement steel in tension (Johansson, 2000).

3 Dynamic Loading

There are two types of extreme cases for dynamic loads: characteristic impulse load and characteristic pressure load, see Figure 3.1. Characteristic impulse load has infinite high load for a very short time, while characteristic pressure load is a characteristic load for infinite time. Most cases for dynamic loading is something in-between these two extreme cases (Johansson and Laine, 2012). The drop weight loading that will be studied in this thesis is considered to be an impulse load, since the load will be of high intensity with short duration.

(a)   (b)
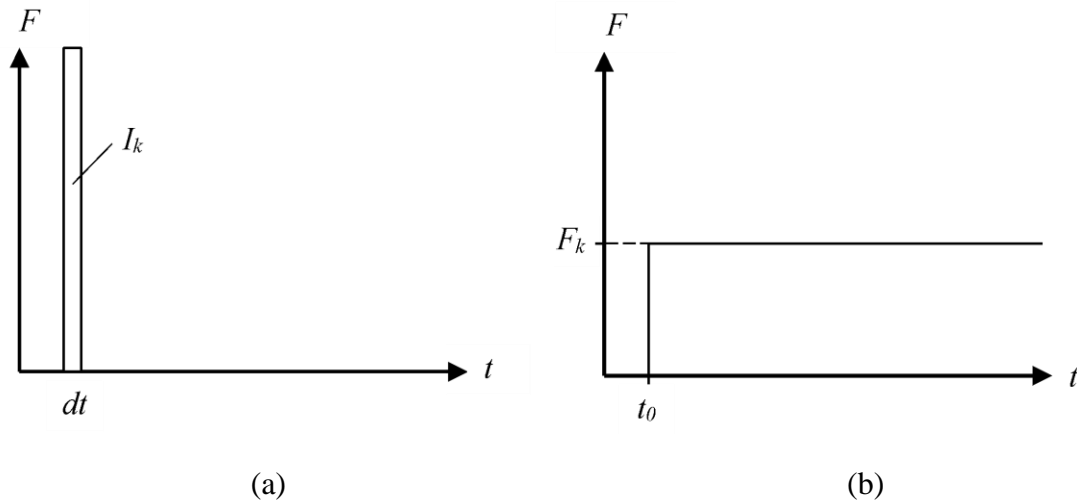
Figure 3.1   Two extreme cases of dynamic loading at initial time, t_0. a) characteristic impulse, I_k, and b) characteristic pressure load, F_k (Johansson and Laine, 2012).

The response for dynamic loaded structures can be very different when compared to being loaded statically. This is especially true if the structure is subjected to impulse load (Johansson, 2000). This phenomenon can be explained by studying the stress waves inside a structure. When subjected to a load, stress waves distribute inside the structure, how fast depends on wave speed and the shape of structure. The time this distribution takes does not cause any problem when subjected to static loading, since it goes very fast. However, for impulse loaded structures, there might not be enough time for the stress waves to be distributed along the whole beam since the duration is so short. Hence, the response might be very different in that case (Johansson, 2000). This phenomenon causes a risk that there might be a local failure, since the whole structure doesn't have time to be affected by the impulse load (Ekengren et al., 2005).

To simplify calculations, an equivalent static load can be used which results in the same maximum deflection as the dynamic load. However, there will most likely be large differences in the structures initial global response compared with the equivalent static simplification (Ekengren, et al., 2005).

3.1 Impulse

An impulse, I [Ns], is defined by the change in momentum afflicted by an external force (Johansson and Laine, 2012).

Momentum of a particle, p [Ns], is described as

$$p = m \cdot v \tag{3.1}$$

where m = mass [kg]

               v = velocity [m/s]

If the particle has an initial velocity, v_0, and is subjected to an external force, $F(t)$, during time t_0 to t_1, the velocity changes to v_1 and the momentum will change according to

$$m \cdot v_1 = m \cdot v_0 + \int_{t_0}^{t_1} F(t)\, dt \tag{3.2}$$

Hence, the impulse is described as

$$I = \int_{t_0}^{t_1} F(t)\, dt \tag{3.3}$$

An impulse can also be described as a step-change in momentum (Nyström, 2006), which is illustrated in Figure 3.2.
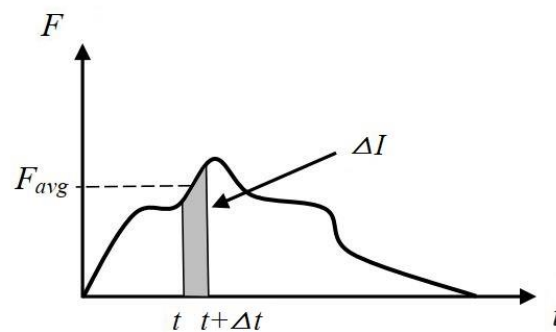
Figure 3.2   *Load–time relation where F_{avg} is the average value of the load inbetween time t and t+Δt. Modified from Jönsson and Stenseke (2018).*

Impulse can also be calculated by multiplying impulse intensity with the area, see Equations (3.4) and (3.5). Impulse intensity is the area in the diagram of pressure over time which is illustrated in Figure 3.3.
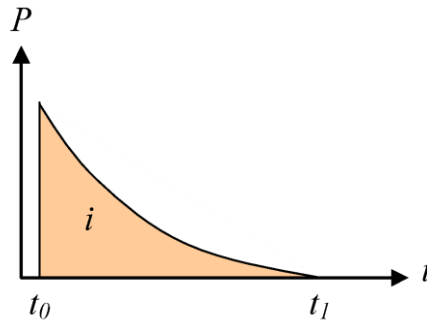
Figure 3.3   Pressure–time relation to illustrate impulse intensity. From Johansson and Laine 2012).

$$i = \int_{t_0}^{t_1} P(t)dt \tag{3.4}$$

$$I = i \cdot A = A \int_{t_0}^{t_1} P(t)dt \tag{3.5}$$

where i = impulse intensity [Pa·s]

P = pressure [Pa]

A = area [m²]

3.2   Kinetic energy

Kinetic energy, E [J], is the energy a particle contains when it is in motion, it depends on its mass and velocity (Johansson and Laine, 2012). If the speed is constant, it means that also the kinetic energy will be constant. It can be described by following equation

$$E = \frac{m \cdot v^2}{2} \tag{3.6}$$

where m = mass [kg]

v = velocity [m/s]

3.3   External work

Work, W [Nm], occur when a particle is subjected to a force which cause a displacement (Johansson and Laine, 2012), it is defined by Equations (3.7) and (3.8). An illustration which explains the forces can be seen in Figure 3.4.

$$W = F \cdot u \cdot \cos \varphi = F_x \cdot u \tag{3.7}$$

$$W = \int_0^u F_x(x)\, dx \tag{3.8}$$

where F = external force [N]

F_x = projection of the force to displacement [N]

u = displacement [m]

φ = angulation between force and displacement [degree]

(a)   (b)
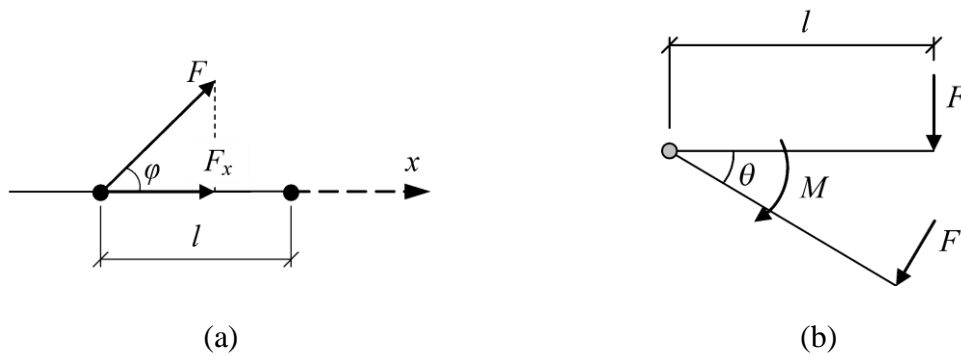
Figure 3.4   Work done by a) an external force and b) an external force that creates a moment (Johansson and Laine, 2012).

Work can also be calculated by using the moment that it is subjected to, by multiply it with its rotation, see Equations (3.9) and (3.10).

$$W = M \cdot \boldsymbol{\theta} \tag{3.9}$$

$$W = \int_{0}^{\theta} M(\alpha) \, d\alpha \tag{3.10}$$

where M = external moment [Nm]

$\boldsymbol{\theta}$ = rotation [degree]

Impulse loaded structures can be said have an external work which is equal to its kinetic energy. Moreover, by combining Equation (3.6) for kinetic energy with Equation (3.2) for impulse, we get Equation (3.11) which defines the external work (Johansson and Laine, 2012).

$$W_e = \Delta E_k = \frac{m \cdot v^2}{2} - \frac{m \cdot v_0^2}{2} = \frac{(m \cdot \Delta v)^2}{2 \cdot m} = \frac{I^2}{2 \cdot m} \tag{3.11}$$

where m = mass [kg]

v = velocity [m/s]

I = impulse [Ns]

3.4   Energy equilibrium

It is essential that there is energy equilibrium for a structure subjected to a load. It means that the internal work must be equal to the external work, see Figure 3.5. The internal work capacity must therefore be greater than the external work to fulfil this condition.
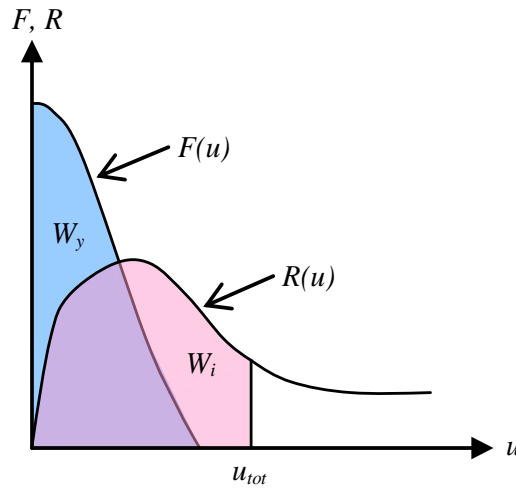
Figure 3.5   Force-deformation relation, where the external work, W_e, is the area under the external force, $F(u)$, and the internal work, W_i, is the area under the reaction force, $R(u)$. From Johansson and Laine (2012).

3.5   Internal work

The internal work for a material depends on their material behaviour and the external work. Figure 3.6 shows a force-deflection diagram for the internal work of two materials, the internal work is the area under the curve.

In Figure 3.6, the area $W_{i,1}$ represents a material with high stiffness, whereas area $W_{i,2}$ represents a material with low stiffness. High stiffness often results in a material with higher reaction forces and lower deformation capacities. Low stiffness materials have often smaller reaction forces but is able to larger plastic deformations. For structures subjected to static loading it can be more desirable to have a high stiffness to withstand the external forces. However, that is not the case for impulse loaded structures. For a structure subjected to impulse loading it need to be able to absorb the energy (Johansson and Laine, 2012). Since the area $W_{i,2}$ is more compared with the area $W_{i,1}$, then this shows that this material is able to absorb more energy and is therefore more resistant against impulse load.

A structure's stiffness, strength and deformation capacity depends on its material response. The most common and simplified responses have been presented in Section 2.1, and in the following sections it will be treated how it affects the internal work.
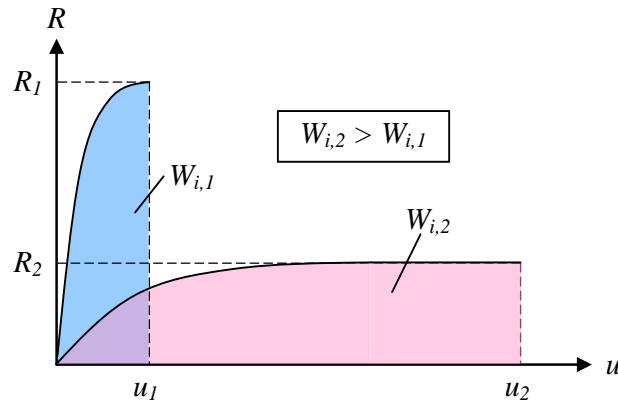
Figure 3.6   *Work absorption for two structures, one with low stiffness and high ability to deform and the other with high stiffness and low ability to deform (Johansson and Laine, 2012).*

3.5.1   Linear elastic response

The internal work for linear elastic response can be calculated by using

$$W_i = \frac{R \cdot u_{el}}{2} = \frac{k \cdot u_{el}^2}{2} \tag{3.12}$$

where R = reaction force [N]

k = stiffness [N/m]

u_{el} = elastic deformation [m]

The internal work equals the external work and therefore by combining Equation (3.11) and (3.12), the elastic deformation can be calculated by using Equation (3.13). These relations are also illustrated in Figure 3.7 (Johansson and Laine, 2012).

$$u_{el} = \frac{I}{\sqrt{m \cdot k}} \tag{3.13}$$

where I = impulse [Ns]

m = mass [kg]

k = stiffness [N/m]

Figure 3.7   Force-deformation relation for linear elastic response illustrating the internal work (Johansson and Laine, 2012).

3.5.2   Ideal plastic response

The internal work for ideal plastic response can be calculated by using Equation (3.14). The reaction force is constant, and the plastic deformation becomes large enough so the internal work equals the external work.

$$W_i = R \cdot u_{pl} \tag{3.14}$$

where R = reaction force [N]

u_{pl} = plastic deformation [m]

The internal work equals the external work and therefore by combining Equations (3.11) and (3.14), can the plastic deformation be calculated by using Equation (3.15). These relations are also illustrated in Figure 3.8 (Johansson and Laine, 2012).

$$u_{pl} = \frac{I_k^2}{2 \cdot m \cdot R} \tag{3.15}$$

where I = impulse [Ns]

m = mass [kg]

R = reaction force [N]

u_{pl} = plastic deformation [m]

Figure 3.8   Force-deformation relation for plastic response illustrating the internal work (Johansson and Laine, 2012).

3.5.3   Elasto-plastic response

For the internal work of elasto-plastic materials, it needs to be considered that there is both an elastic and plastic part of response which can be seen in Figure 3.9. This is accounted for in the calculation for internal work, see Equation (3.16).

$$W_i = \frac{1}{2} \cdot R \cdot u_{el,1} + R \cdot u_{pl,1} = \frac{R}{2}\left(u_{el,1} + 2 \cdot u_{pl,1}\right) \tag{3.16}$$

where R = reaction force [N]

$u_{el,1}$ = elastic deformation for elasto-plastic response [m]

$u_{pl,1}$ = plastic deformation for elasto-plastic response [m]

The total deformation for elasto-plastic materials is the sum of the elastic and plastic deflections (Johansson et al., 2014). Following Equations (3.17), (3.18) and (3.19) shows how the total deformation for elasto-plastic materials is calculated.

$$u_{tot} = u_{el,1} + u_{pl,1} \tag{3.17}$$

$$u_{pl,1} = u_{pl} - \frac{u_{el,1}}{2} \tag{3.18}$$

$$u_{el,1} = u_{el} \tag{3.19}$$

where u_{el} = elastic deformation for elastic response [m]

u_{pl} = plastic deformation for plastic response [m]

$u_{el,1}$ = elastic deformation for elasto-plastic response [m]

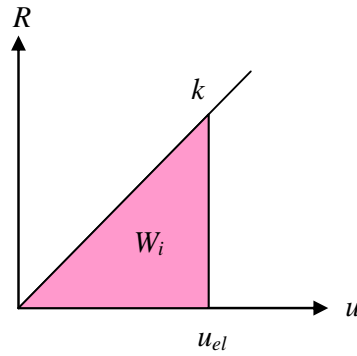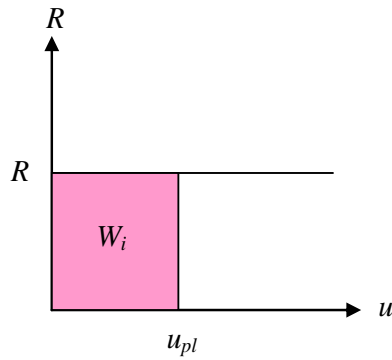$u_{pl,1}$ = plastic deformation for elasto-plastic response [m]
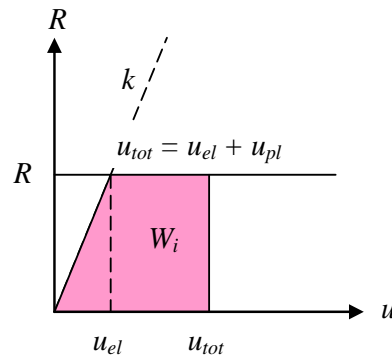
Figure 3.9   *Force-deformation relation for elasto-plastic response illustrating the internal work (Johansson and Laine, 2012).*

3.6   Classic impact theory

Classic impact theories for a collision between two particles with masses m_1 and m_2 will be treated in this chapter, see Figure 3.10. There are two extreme cases that can occur that have elastic or plastic behaviour. Mass of the respective particles are an important factor to determine what kind of behaviour will occur (Johansson and Laine, 2012). Kinetic energy, Equation (3.6), and momentum, Equation (3.1), will be analysed for the two extreme cases for collisions to determine the differences.
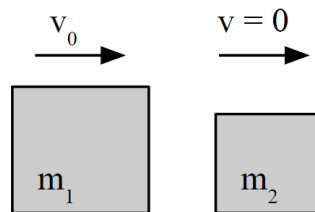
Figure 3.10   *Two particles before collision. v_0 is the initial velocity of particle one and particle two is not moving before impact.*

3.6.1   Elastic impact

The total momentum and kinetic energy for an elastic impact will remain the same after impact (Johansson, 2014). Moreover, particle one will have a loss in velocity, whereas particle two will obtain a velocity different from particle one, see Figure 3.11.
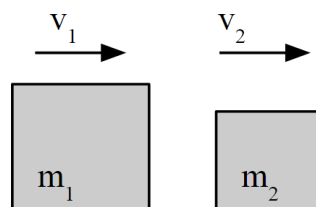
Figure 3.11   *Two particles after collision with elastic behaviour. Particles one and two get different velocities, v_1 and v_2, after impact.*

The velocities for the two particles can be calculated by using Equations (3.20) and (3.21). Furthermore, it can be observed that particle one gets a negative direction in velocity if the mass

of particle one is smaller than particle two, and particle two will obtain a positive velocity for all values of the masses (Johansson, 2014).

$$v_{el,1} = \frac{m_1 - m_2}{m_1 + m_2} \cdot v_0 \tag{3.20}$$

$$v_{el,2} = \frac{2 \cdot m_1}{m_1 + m_2} \cdot v_0 \tag{3.21}$$

where v_0 = velocity for particle one before impact [m/s]

           $v_{el,1}$ = velocity for particle one after impact [m/s]

           $v_{el,2}$ = velocity for particle two after impact [m/s]

           m_1 = mass for particle one [kg]

           m_2 = mass for particle two [kg]

Kinetic energy for the two particles after elastic collision is then calculated as

$$E_{k,el,1} = \frac{m_1 \cdot v_{el,1}^2}{2} = \cdots = \left(\frac{m_1 - m_2}{m_1 + m_2}\right)^2 \cdot E_{k,0} \tag{3.22}$$

$$E_{k,el,2} = \frac{m_2 \cdot v_{el,2}^2}{2} = \cdots = \frac{4 \cdot m_1 \cdot m_2}{(m_1 + m_2)^2} \cdot E_{k,0} \tag{3.23}$$

where $E_{k,0}$ = kinetic energy before impact [J]

$$E_{k,0} = \frac{m \cdot v_0^2}{2} \tag{3.24}$$

3.6.2   Plastic impact

The momentum remain the same after plastic impact, but the total kinetic energy will decrease. The plastic impact result with the same velocity for both particles after a plastic collision (Jönsson and Stenseke, 2018), see Figure 3.12.
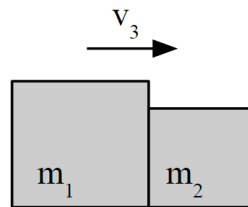
Figure 3.12   Two particles after collision with plastic behaviour. Particles one and two get the same velocity, v_3, after impact.

Velocity for the two particles can be calculated with following equation

$$v_{pl} = v_{pl,1} = v_{pl,2} = \frac{m_1}{m_1 + m_2} \cdot v_0 \tag{3.25}$$

where v_0 = velocity for particle one before impact [m/s]

$v_{pl,1}$ = velocity for particle one after impact [m/s]

$v_{pl,2}$ = velocity for particle two after impact [m/s]

m_1 = mass for particle one [kg]

m_2 = mass for particle two [kg]

Kinetic energy for the two particles after plastic collision is then calculated as

$$E_{k,pl,12} = \frac{(m_1 + m_2) \cdot v_{pl}^2}{2} = \cdots = \frac{m_1}{m_1 + m_2} \cdot E_{k,0} \tag{3.26}$$

4   Response of Plastic Regions

Ductility is one of the important factors that determines how the structure withstand the applied load, especially when it comes to structures subjected to impact loading hence a large plastic deformation is required to meet the required energy absorption capacity.

4.1   Plastic deformation of a cross section for RC

The plastic deformation is represented by a strain distribution or curvature of the section. The ultimate curvature can be expressed as the ultimate concrete strain or as ultimate steel strain in the case of less ductile steel or high steel ratio (Engström, 2015). The plastic curvature at yielding and at maximum moment including the plastic curvature in between is shown in Figure 4.1 for an under reinforced concrete section and by the following relationships according to (Engström, 2015).
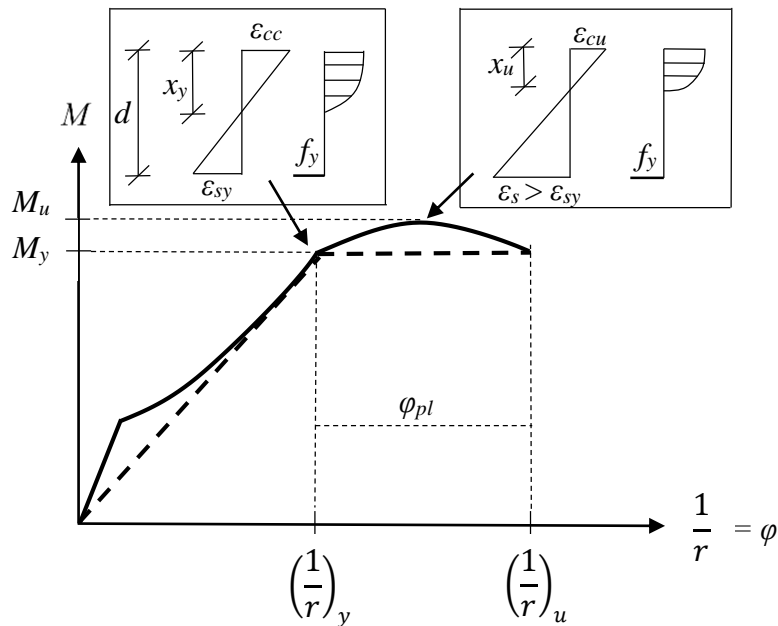
Figure 4.1   Typical moment-curvature diagram for a reinforced concrete cross-section together with a simplified bi-linear response based on (Engström, 2015).

The curvature $\left(\frac{1}{r}\right)_y$ at yielding of steel

$$\left(\frac{1}{r}\right)_y = \frac{\varepsilon_{cy}}{x_y} = \frac{\varepsilon_{sy}}{d - x_y} \tag{4.1}$$

The ultimate curvature $\left(\frac{1}{r}\right)_u$ when the concrete strain is governing

$$\left(\frac{1}{r}\right)_{cu} = \frac{\varepsilon_{cu}}{x_u} = \frac{\varepsilon_s}{d - x_u} \tag{4.2}$$

The ultimate curvature $\left(\frac{1}{r}\right)_u$ when steel strain ε_{sud} is governing

$$\left(\frac{1}{r}\right)_{su} = \frac{\varepsilon_{cc}}{x_u} = \frac{\varepsilon_{sud}}{d - x_u}$$

(4.3)

The ultimate curvature $\left(\frac{1}{r}\right)_u$ will then be

$$\left(\frac{1}{r}\right)_u = min\left(\left(\frac{1}{r}\right)_{cu}, \left(\frac{1}{r}\right)_{su}\right)$$

(4.4)

The plastic curvature $\left(\frac{1}{r}\right)_{pl}$ can be founded by the difference between ultimate curvature and curvature at yielding

$$\left(\frac{1}{r}\right)_{pl} = \left(\frac{1}{r}\right)_u - \left(\frac{1}{r}\right)_y$$

(4.5)

The plastic curvature $\left(\frac{1}{r}\right)_{pl}$ can also be expressed by the steel strain as

$$\left(\frac{1}{r}\right)_{pl} = \frac{\varepsilon_s}{d - x_u} - \frac{\varepsilon_{sy}}{d - x_y} \approx \frac{\varepsilon_s - \varepsilon_{sy}}{d - x_u}$$

(4.6)

4.2 Plastic rotation capacity in reinforced concrete

For a RC structure, an initial plastic hinge is formed when yielding of the reinforcement is reached. As the load further increases the plastic hinge enlarges along the plastic region until the final plastic hinge is formed resulting in a failure mechanism of the structure (Plem, 1981). A plastic rotation capacity can be defined as the aptitude of the former plastic hinge to rotate during the increase of load beyond yielding until attainment of ultimate load or the ultimate curvature $\left(\frac{1}{r}\right)_u$ along the length of the plastic zone (Plem, 1981). Thus, in reality a plastic hinge is not concentrated at one point rather it is distributed along the plastic zone l_{pl} (Plem, 1981).

(a)   (b)
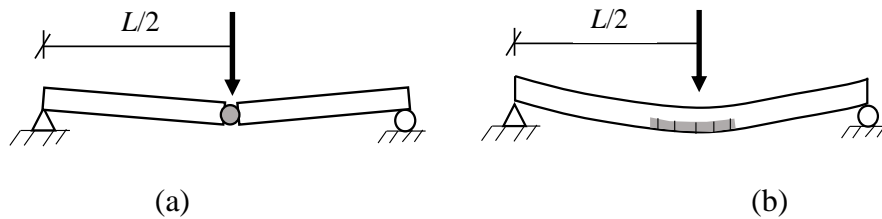
Figure 4.2   a) assumption of concentrated plastic hinge and b) real distribution of plastic hinge (Jönsson and Stenseke, 2018).

There are different approaches to express a plastic rotation depending on different parameters. According to (Engström, 2015) for sectional model in state III a plastic rotation θ_{pl} depends on the strain distribution or the curvature in the section and the extension of the plastic zone as shown in Figure 4.3.
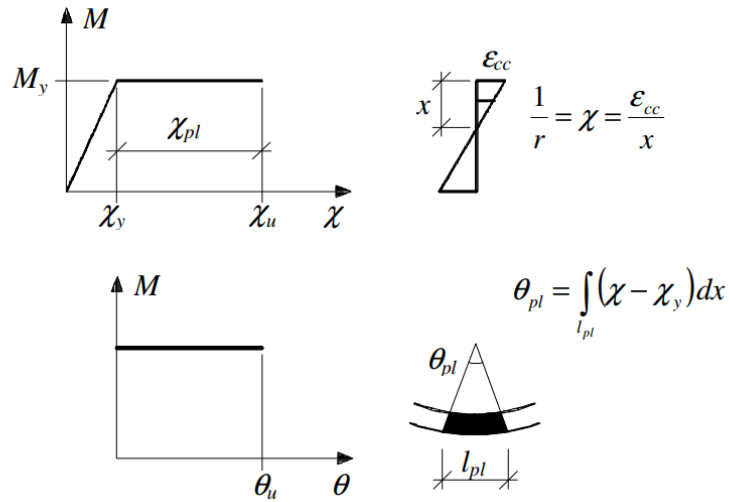
Figure 4.3   Plastic rotation dependency on the extension of the plastic region and the plastic curvature of each section in this region. (Engström, 2015).

A plastic rotation can be founded by integrating the plastic curvature over the length of the plastic extension zone l_{pl}, between any curvature in the plastic zone and the curvature at failure where the tensile steel strain exceeds the yield strain as

$$\theta_{pl} = \int_0^{l_{pl}} \left(\left(\frac{1}{r} \right)_{(x)} - \left(\frac{1}{r} \right)_y \right) dx = \int_0^{l_{pl}} \left(\frac{\varepsilon_s (x) - \varepsilon_s (y)}{d - x_u} \right) dx \qquad (4.7)$$

In Figure 4.4 two approaches to define a plastic rotation for a simply supported beam are shown. One considering a linear elastic curvature response at yielding and the other showing constant yielding curvature as in Figure 4.4 (a) and Figure 4.4 (b) respectively, where the plastic rotation is shown as the shaded area under the curve.
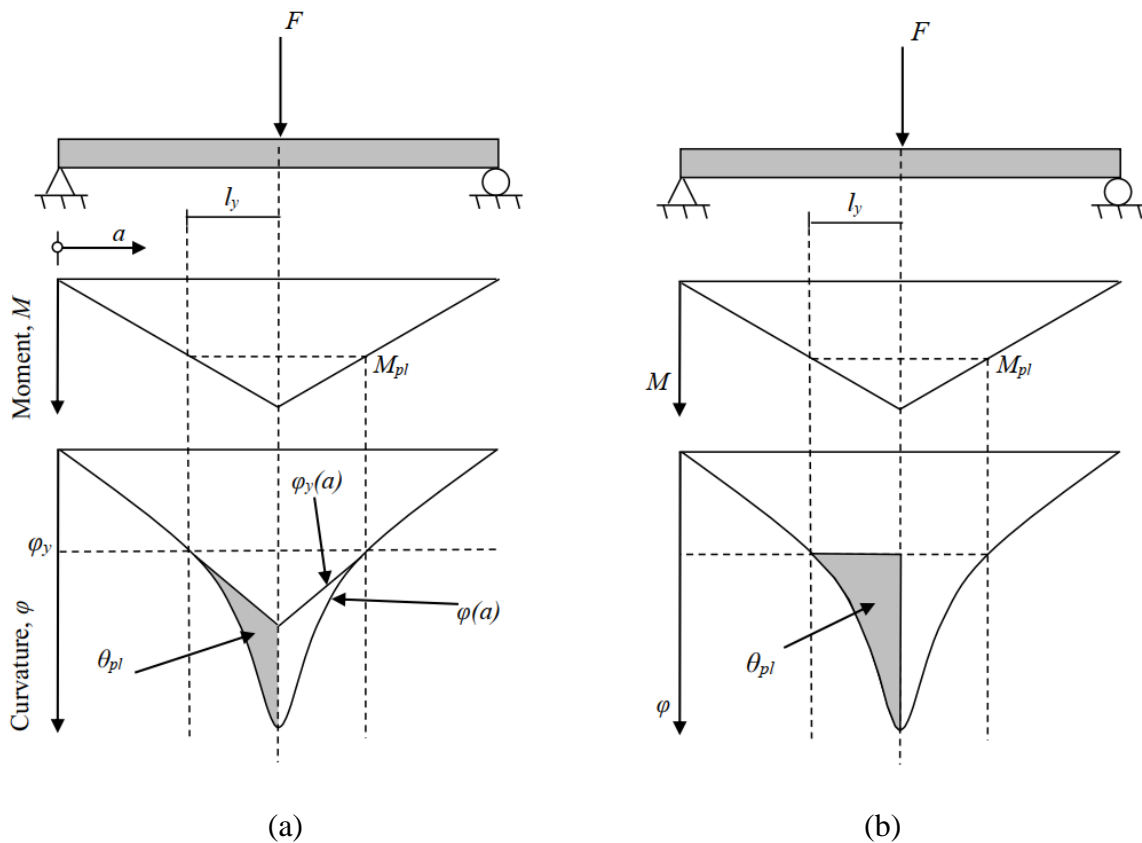
Figure 4.4   *Schematic representation of different simplified models to determine plastic rotation capacity. (a) Model with variable elastic curvature along l_y and (b) Model with constant elastic curvature along l_y. Modified from Lozano and Makdesi (2017).*

4.3 Methods to predict plastic rotation capacity of RC

Plastic deformation capacity can be determined using different proposed methods. These methods use different load type such as point load or uniformly distributed load and different loading rate whether it is impact load or static load. In this section methods to predict the plastic rotation capacity of RC independent of FRP strengthening will be discussed based on the information from Johansson and Laine (2012) and Engström (2015).

4.3.1 Plastic rotation according to Eurocode 2

The method proposed in Eurocode 2 is intended to be used for a static type of point load at mid span. The design plastic rotation is obtained from Figure 4.5 depending on the ratio of the height of compressive zone in the ultimate state, x_u, and the effective height of cross section, d, which is expressed $\frac{x_u}{d}$ together with concrete strength class and reinforcing steel class.
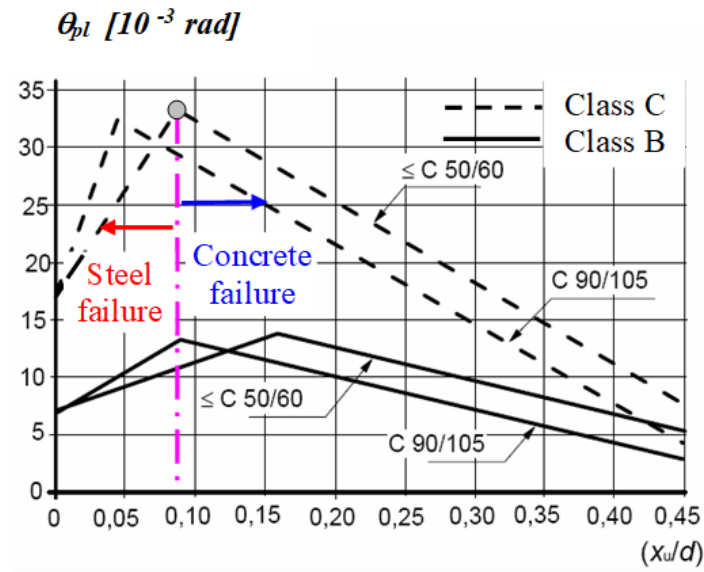
Figure 4.5   Plastic rotation capacity according to Eurocode 2 (Modified from Johansson and Laine, 2012).

The plastic rotation capacity can be directly obtained from Figure 4.5 if the condition shear slenderness $\lambda = 3$ is satisfied. Otherwise the rotation capacity θ_{pld} obtained from Figure 4.5 should be modified by a factor k_λ which can be calculated as

$$k_\lambda = \sqrt{\frac{\lambda}{3}} \tag{4.8}$$

$$\lambda = \frac{x_0}{d} \tag{4.9}$$

where x_0 = distance between the considered maximum moment section and adjacent zero

moment section after plastic redistribution, i.e. the final moment distribution

d = effective depth

λ can also be calculated as

$$\lambda = \frac{M_{Ed}}{V_{Ed} \cdot d} \tag{4.10}$$

where M_{Ed} = design bending moment

V_{Ed} = design shear resistance

θ_{pld} is limited by the ultimate steel strain ε_{sud} for smaller ratio of $\frac{x_u}{d}$ and increase with increasing $\frac{x_u}{d}$. For higher $\frac{x_u}{d}$ ratio θ_{pld} is limited by ultimate concrete strain ε_{cu} and decrease with increase of $\frac{x_u}{d}$ ratio as indicated in Figure 4.5.

4.3.2 Plastic rotation according to BK25

Johansson and Laine (2012) thoroughly presents the BK25 method for computing plastic rotation capacity which is proposed in Fortifikationsförvaltningen. This method is intended to be used for uniformly distributed impulse loading. A model which is used to illustrate this method is shown in Figure 4.6 based on (Johansson and Laine, 2012).
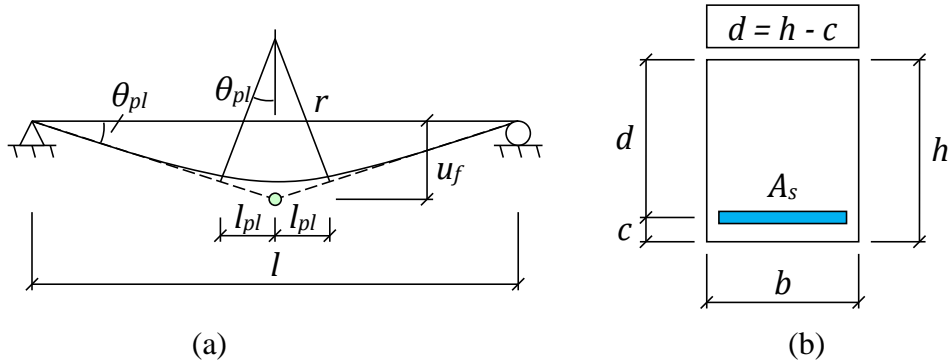
Figure 4.6 *(a) Model for plastic rotation capacity and (b) its cross section. Inspired by Johansson and Laine (2012).*

For a constant curvature r, the equivalent plastic hinge length, l_{pl}, can be calculated as

$$l_{pl} = 0.5 \cdot d + 0.15 \cdot l \tag{4.11}$$

The rotation capacity can be calculated from the plastic hinge length as

$$\theta_{pl} = \frac{l_{pl}}{r} \tag{4.12}$$

The radius of curvature at ultimate moment can be calculated as following

$$\left(\frac{1}{r}\right)_u = \frac{\varepsilon_{cu}}{x_u} = \frac{\varepsilon_s}{d - x_u} \tag{4.13}$$

Where ε_{cu} and ε_s are ultimate concrete and steel strain along the plastic hinge length l_{pl} respectively.

A stress-strain relationship in ultimate state for a reinforced concrete beam subjected to bending moment, is shown in Figure 4.7.
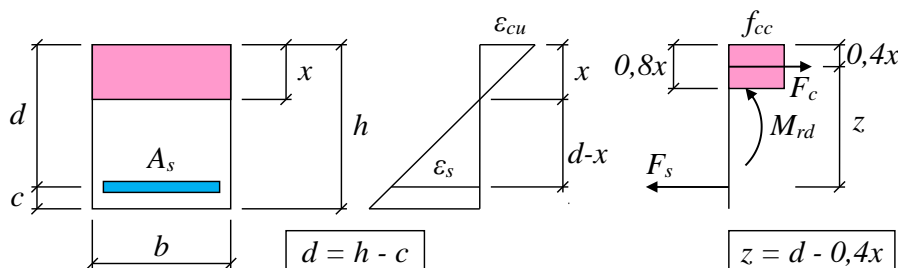
Figure 4.7 *RC beam cross section subjected to bending moment (Johansson and Laine, 2012).*

For horizontal equilibrium, $F_s = F_c$

$$0.8 \cdot x \cdot f_c = A_s \cdot f_y \tag{4.14}$$

With the reinforcement ratio

$$\rho = \frac{A_s}{b \cdot d} \tag{4.15}$$

And the mechanical reinforcement ratio, ω_s, as

$$\omega_s = \frac{A_s}{b \cdot d} \cdot \frac{f_y}{f_{cc}} \tag{4.16}$$

The height of the compressive zone x and the ratio $\frac{x}{d}$ can be calculated as

$$x = \frac{1}{0.8} \cdot \rho \cdot d \frac{f_y}{f_{cc}} = \frac{\omega_s \cdot d}{0.8} \tag{4.17}$$

$$\frac{x}{d} = \frac{\omega_s}{0.8} \tag{4.18}$$

The limiting failure mode can be gained from the expression

$$\omega_{s,crit} = \frac{0.8 \cdot \varepsilon_{cu}}{\varepsilon_{cu} + \varepsilon_s} \tag{4.19}$$

For $\omega_s > \omega_{s,crit}$, the failure will be due to crushing of concrete and the plastic rotation is expressed as

$$\theta_{pl} = \frac{l_p}{r} = \frac{0.8 \cdot \varepsilon_{cu}}{\omega_s}(0.5 \cdot d + 0.15 \cdot l) = \frac{0.4 \cdot \varepsilon_{cu}}{\omega_s}\left(1 + 0.3 \cdot \frac{l}{d}\right) \tag{4.20}$$

For $\omega_s < \omega_{s,crit}$, the governing failure mode will be due to rupture of reinforcement and the plastic rotation is expressed as

$$\theta_{pl} = \frac{l_p}{r} = \frac{0.8 \cdot \varepsilon_s}{d \cdot (0.8 - \omega_s)}(0.5 \cdot d + 0.15 \cdot l) = \frac{0.4 \cdot \varepsilon_s}{0.8 - \omega_s}\left(1 + 0.3 \cdot \frac{l}{d}\right) \tag{4.21}$$

4.3.3 Plastic rotation capacity from test results

Jönsson and Stenseke (2018) and Lozano and Makdesi (2017) presents the determination of plastic rotation capacity from experimental results of static test. In a deformation-controlled test, displacement will increase for a decreasing load after reaching the ultimate load until the ultimate plastic curvature is reached. Plastic rotation is initiated when yielding is reached and continue until attaining the maximum plastic deformation for a certain percentage value of the ultimate load on the descending branch of the load–displacement curve as illustrated in Figure 4.8.
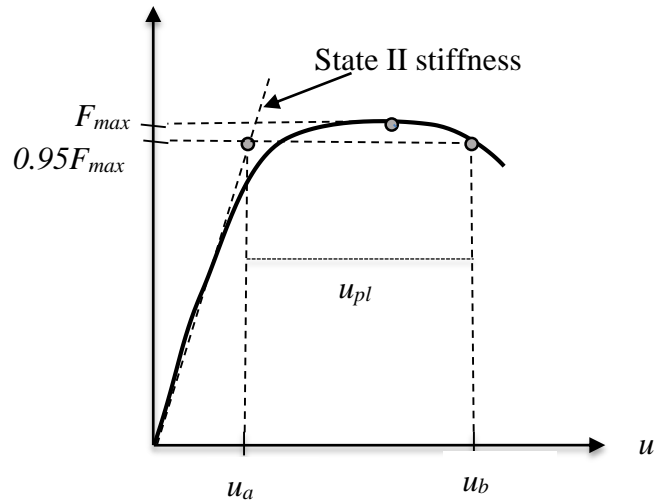
Figure 4.8   Response of deformation-controlled test with rotation capacity 95 % of the ultimate load (Jönsson and Stenseke, 2018).

The plastic rotation capacity $\theta_{pl.x\%}$ can be determined from the deformation, u_b, at a certain percentage of the ultimate load *(x % / 100)*. F_{max} on the descending branch, and the elastic deformation, $u_{a,}$ from the load-displacement curve.
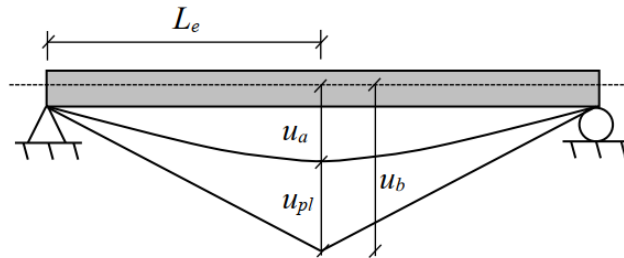
Figure 4.9   Response of elastic and plastic deformation measured from experiments (Lozano and Makdesi, 2017).

For a simply supported beam loaded with a point load at the middle of the beam, with length L_e being the distance between the plastic hinge and the support of the beam, see Figure 4.9. The plastic rotation can be determined as

$$\theta_{pl,x\%} = \frac{u_{b,x\%} - u_{a,x\%}}{L_e} = \frac{u_{pl,x\%}}{L_e} \tag{4.22}$$

5 FRP Strengthening of Reinforced Concrete

As mentioned in Section 1.1 strengthening RC with FRP has become a widely used method in recent years. FRP material is advantageous due to high strength to weight ratio, light weight, high stiffness and its corrosion resistance (Wu and Eamon, 2017). Even though the initial cost of FRP strengthening is relatively high, it is advantageous because of its ease to installation and relatively lower maintenance cost for the whole life time of heavy structures due to its durability (Zoghi, 2014). Numerous studies states FRP strengthening of RC structures results in increase of flexure, and shear resistance in beams, slabs and girders, and increase of confining compression and seismic resistance in columns (Smith and Teng, 2002), (Nordin, 2003), (Pantelides, 2004) and (Wu and Eamon, 2017).

Moreover, it also improves the performance during service load slightly and ultimate strength remarkably. The crack width is also reduced (El-Hacha et al., 2001).
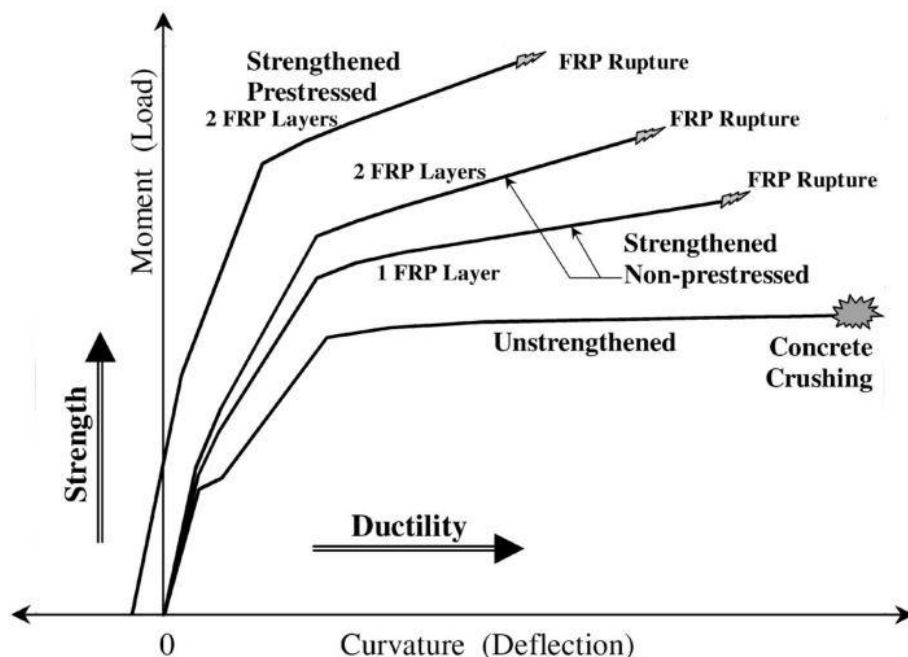
Figure 5.1   Load–deflection relations for RC beams strengthened with prestressed and non-prestressed FRP layers (El-Hacha et al., 2001).

RC structures shows a more brittle failure when it is strengthened with FRP. This needs to be addressed according to El-Hacha et al. (2001) by ensuring the failure happen after yielding of steel but before crushing of concrete. How the FRP can affect the behaviour of RC structures can be seen in Figure 5.1. This figure illustrates load-deflection relations for reinforced concrete beams which are strengthened by a different amount of FRP layers and one is also prestressed. It shows that the FRP strengthened beams have higher load capacity and are less ductile compared with the strengthened RC beam. Additional layers of FRP laminates increase this kind of behaviour and this behaviour is also increased by prestressing the FRP layers.

5.1 Properties and classification of FRP

FRP can be classified as carbon, glass, aramid, and basalt fibre and is available in different grades and classification. Except for glass fibre, FRP material is known to have anisotropic material property (Wu and Eamon, 2017).

Carbon fibre has higher modulus of elasticity and strength, lower weight, very good fatigue resistance, higher chemical and thermal resistance and is more expensive. It is used in strengthening all types of structural members in RC structures (Wu and Eamon, 2017). Glass fibre is the most widely used FRP material because of its lower cost. It has moderate strength and weight and relatively lower stiffness and modulus of elasticity. Aramid fibre is known to be widely used in aerospace and military. Basalt fibre is a relatively new FRP composite produced from volcanic basalt and have a very good thermal and chemical resistance and low cost (Wu and Eamon, 2017). Specific properties of FRP materials can vary based on the manufacturer. Some typical FRP materials and their mechanical properties are presented in Table 5.1.

Table 5.1   Approximated FRP material properties modified from (Wu and Eamon, 2017).

Fibre type	Fibre Identification	Tensile modulus [GPa]	Tensile strength [MPa]	Failure strain [%]	Poisson's ratio [-]
Basalt		93	3000	3.2	
Glass	E - Glass	72	3400	4.8	0.2
	S - Glass	87	4300	5.0	0.22
Aramid	Kevlar 49	131	3600	2.8	0.35
	Technora	70	3000	4.6	0.35
Carbon	T-300	230	3700	1.4	0.2
	P-100	6.0	3000	0.32	0.2
	AS-4	248	4000	1.65	0.2

FRP can be found in different forms such as bars, sheets and strips or prestressed tendons. Bars and tendons are used in a newly built concrete while the sheets are mostly used in retrofitting existing structures or as additional strengthening in tension for newly built structure.

5.2 Failure modes of externally bonded FRP reinforcement

Numerous researches state there are several types of failures in externally bonded FRP beams (Camata et al., 2006), (Teng et al., 2003) and (Zoghi, 2014). These failures are generally classified in two groups:

- Failures that do not result from lack of composite action which includes failure due to
  - crushing of concrete
  - yielding of steel rebars before rupture of FRP plate
  - rupture of FRP prior to yielding of steel rebar or ultimate concrete strain
  - shear failure
- Failures induced due to lack of composite actions i.e. debonding failures. (Wu and Eamon, 2017) subdivided this failure mode in to

- plate end debonding
- intermediate crack induced debonding

Different failure modes are illustrated in Figure 5.2.
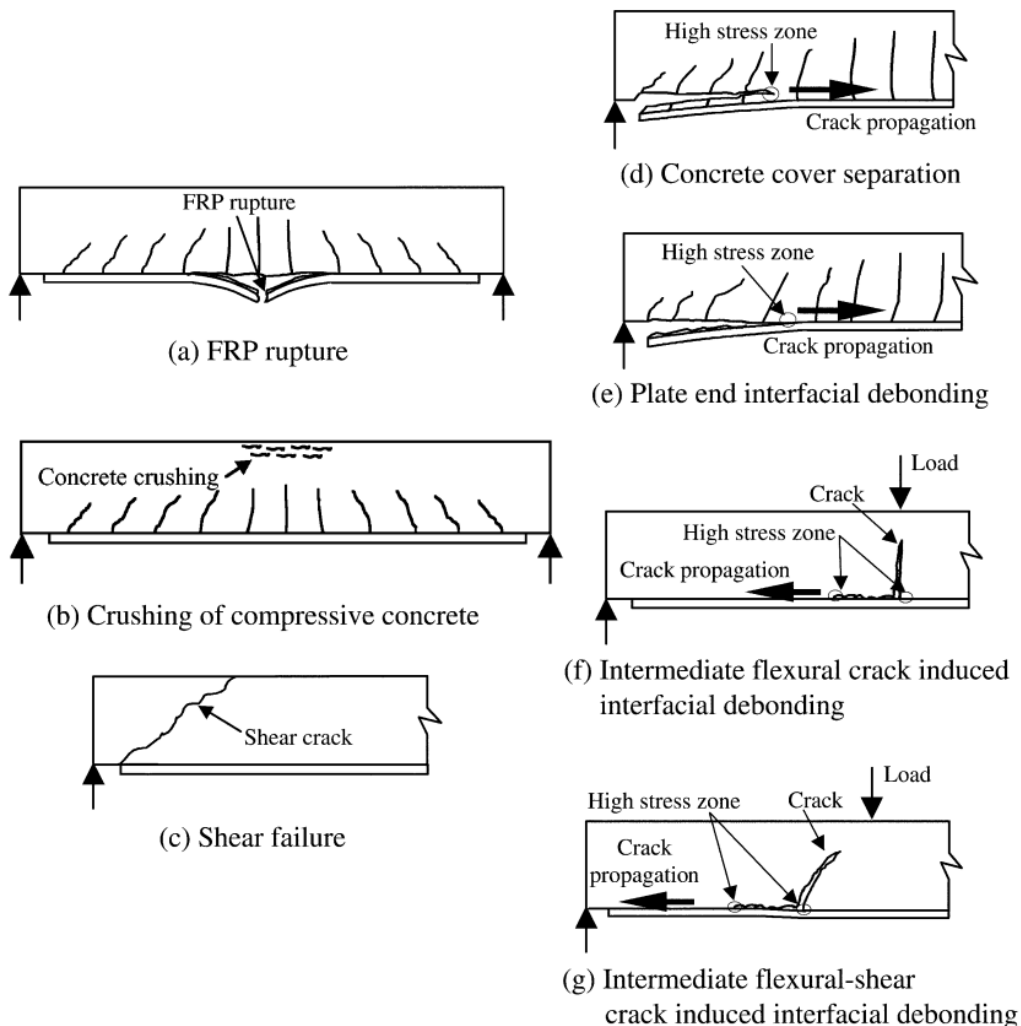
Figure 5.2   Failure types for FRP plated RC beams (Teng et al., 2003).

In case of intermidiate flexural crack induced interfacial debonding, when cracks are initiated in the tension zone, the tensile stress in the concrete will transfer to the FRP plate and when the load is increased further the tensile stress both in the concrete and the FRP will increase and debonding will occur as a result of increasing interfacial stress between the FRP and concrete interface (Teng et al., 2003).

According to Teng et al. (2003) shear failure and plate end debonding (concrete cover separation and plate end interfacial debonding) are very brittle failures and should be avoided by using e.g. u jackets/wrapping or fibre anchors. Teng et al. (2003) states for sections strengthed in bending adding u jackets at the end of the bonding will enhance the shear strength and reduce the risk of end plate debonding since the shear force and the resulting bond stress between the concrete and the FRP will be larger near the support. Furthermore, if u jackets are distibuted all over the span it can also increase the ductility of IC debonding and bending strength of the section (Teng et al., 2003).
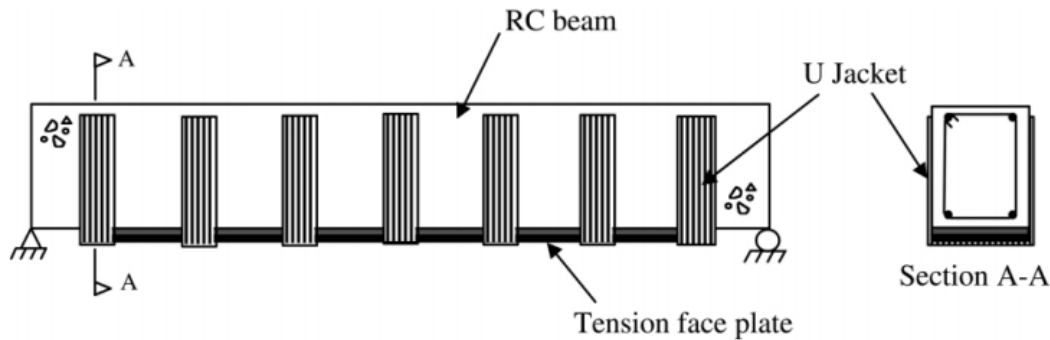
Figure 5.3   Combined use of tensile strengthening and u jacketing (Teng et al., 2003).

5.3   Structural response of FRP strengthened RC structures

According to Teng et al. (2003), many researches state that the most common failure mode of FRP strengthened RC structures is debonding or bond slip failure which results in a brittle failure mode. The plastic deformation throughout the failure process depends on different features such as; debonding modes, stiffness of resin/adhesive, stiffness and type of FRP material, bond strength between concrete and resin and ratio of FRP to RC member width (Wu and Eamon, 2017). According to (Camata, 2006) even if the FRP strengthening significantly increase the flexural resistance in ultimate state the ductility might be reduced due to debonding of FRP reinforcement.

According to (Wu and Eamon, 2017) and (Oehlers and Mohamed, 2009), the rotation of FRP plated RC is limited by certain factors to constitute a moment-rotation, *(M/θ)*, relation. These factors include

- softening of concrete
- slip during rupture of reinforcement or FRP
- shear failure across the crack plane
- steel reinforcement or FRP debonding

Oehlers and Mohamed (2009) states that the rotation capacity at the crack front can decrease significantly if rupture of FRP takes place before concrete sliding failure. The probability of rupture of reinforcing steel before rupture of FRP is low for ductile steel. However, there's a chance of steel rebar rupture or slip for low ductility rebars prior to FRP rupture (Oehlers and Mohamed, 2009).

Even though different results can be gained under different scenarios and failure modes, results from previous investigations by (Camata, 2006) is presented for intermediate debonding and FRP rupture failure mode considering it is more relevant to the scope of this study.

Camata (2006) performed displacement control tests until failure on simply supported beams using a four point bending configuration for three FRP strengthened beams and one unstrengthened reference beam, see Figure 5.4.
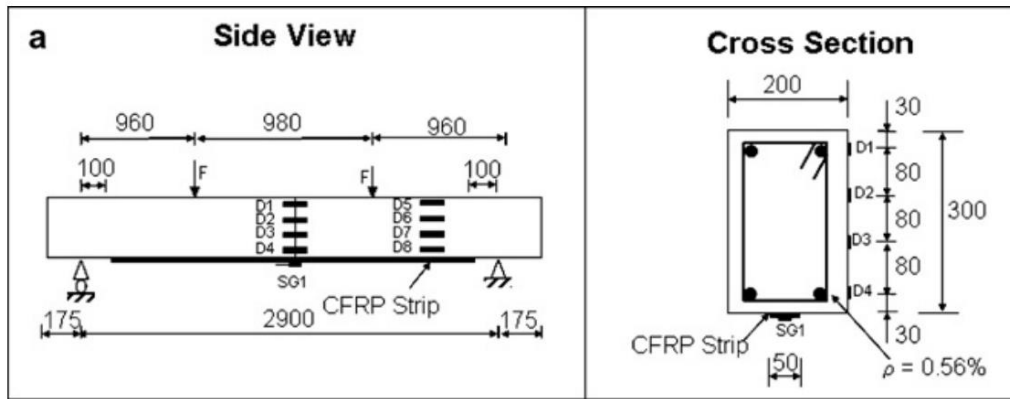
(a)   (b)

Figure 5.4   (a) Geometry and test set up and (b) cross section from Camata (2006).

The failure mode that was exhibited on this test was intermediate debonding due to high interfacial stress between the concrete and the resin, resulting in some concrete remained attached to the FRP plate during debonding. In Figure 5.5, it is shown that for the ascending branch a higher ultimate load is achieved when reaching point D. This is when debonding of the FRP took place, which resulted in a sudden drop to a load capacity that corresponds to the plastic platue of the unstrengthened beam. It can be seen that after debonding the beams show similar load deflection curve or similar structural response with the reference beams. Hence, this result shows an increased ultimate load for strengthened beam and the area under load displacement curve for FRP strengthen beams might increase if the final displacement is the same for both strengthened and test beams. Moreover, larger energy can be consumed by the structure before the final failure is attained if the latter case holds true. Camata (2006) states that FRP strengthening has resulted in decrease of ductility compared with the strengthened samples. The ductility is computed as the ratio of energy consumed in the system at final failure, E_U and the energy consumed at first yield E_y.
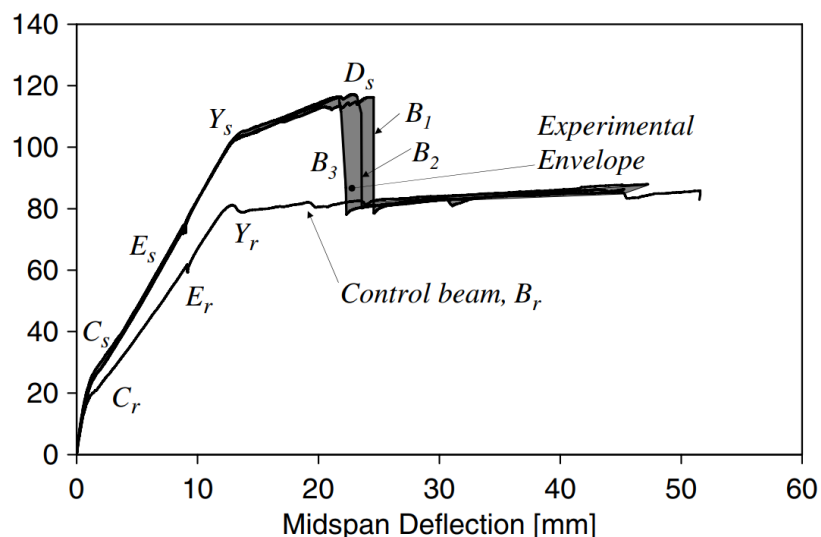
Figure 5.5   Load–midspan deflection for FRP strengthen and unstrengthened control beam (Br) from Camata (2006).

5.4   Flexural strengthening

Different guidelines propose a variety of design procedures for the design of FRP strengthen concrete structures. Wu and Eamon (2017) gives an overview of different approaches using reduction factors to maintain ductility. According to Wu and Eamon (2017) it is often enough to increase the strength of the structure by 40 %, though many researchers suggest FRP strengthening can increase the flexural strength by more than 100 %. (Huanga et al, 2019) have also presented different guidelines for design of concrete structures strengthened by FRP. In this section different guidelines for flexural design of FRP strengthen RC structures are presented based on Wu and Eamon (2017), Huanga and Zhoua (2019) and Täljsten and Gabriel (2016).

5.4.1   Flexural design procedure according to Fib

The model used for RC cross section strengthened with FRP and stress-strain distribution is shown in Figure 5.6.
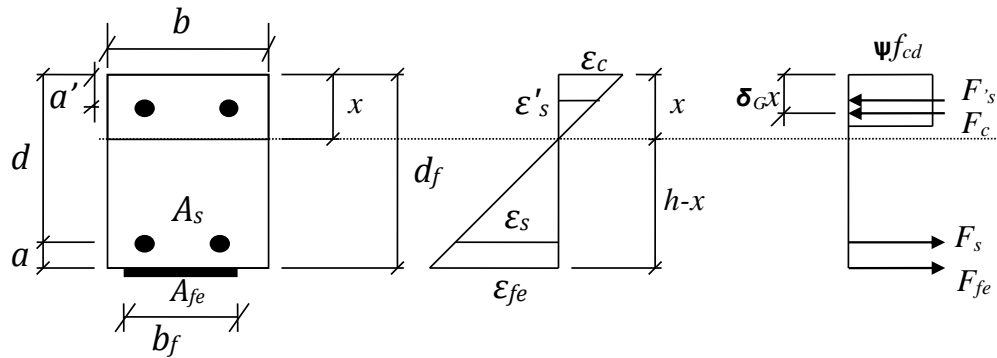
Figure 5.6   Cross section and stress-strain distribution, Fib T5.1 (Huanga and Zhoua, 2019).

According to Huanga and Zhoua (2019), Fib T5.1 2019 proposes the estimation of design moment capacity as

$$M = A_s f_{yd} \cdot (d - \delta_G \cdot x) + A_f E_f \varepsilon_f \cdot \left(d_f - \delta_G \cdot x\right) + A'_s E_s \varepsilon'_s \cdot (\delta_G \cdot x - a') \qquad (5.1)$$

The depth of the neutral axis x, see Figure 5.6, can be calculated as

$$0.5 \cdot \psi \cdot f_c \cdot b \cdot x = A_s \cdot f_{yd} + A_f \cdot E_f \cdot \varepsilon_f \qquad (5.2)$$

Where $f_{yd} = f_y$ assuming the yielding of steel will be the first failure mode. If the failure mode is concrete crushing the value for stress block parameters are given as

$\psi = 0.8$

$\delta_G = 0.4$

For failure modes of FRP rupture or concrete crushing the stress block parameters of concrete are given as

$$
\Psi = \begin{cases} 1000 \cdot \varepsilon_c \left(0.5 - 1000 \cdot \dfrac{\varepsilon_c}{12}\right), for\ \varepsilon_c \leq 0.002 \\ 1 - \dfrac{2}{3000 \cdot \varepsilon_c}, for\ 0.002 \leq \varepsilon_c \leq 0.0035 \end{cases}
\tag{5.3}
$$

$$
\delta_G = \begin{cases} \dfrac{8 - 1000 \cdot \varepsilon_c}{4 \cdot (6 - 1000 \cdot \varepsilon_c)}, for\ \varepsilon_c \leq 0.002 \\ \dfrac{1000 \cdot \varepsilon_c \cdot (3000 \cdot \varepsilon_c - 4) + 2}{2000 \cdot \varepsilon_c \cdot (3000 \cdot \varepsilon_c - 2)}, for\ 0.002 \leq \varepsilon_c \leq 0.0035 \end{cases}
\tag{5.4}
$$

5.4.2 Flexural design procedure according to ACI

The model used for RC cross section strengthen with FRP and stress strain distribution is shown in Figure 5.7.
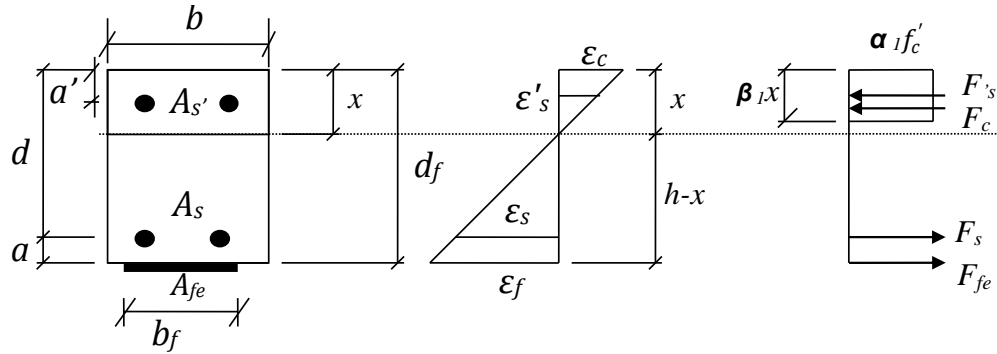
Figure 5.7   Cross section and stress-strain distribution ACI 440.2R (Huanga and Zhoua, 2019).

According to ACI 440.2R the design moment for the FRP strengthened section in tension can be calculated as

$$
M_n = A_s \cdot f_s \cdot \left(d - \frac{\beta_1 \cdot x}{2}\right) + \phi \cdot A_{fe} \cdot f_{fe} \cdot \left(d_f - \frac{\beta_1 \cdot x}{2}\right)
\tag{5.5}
$$

The height of the neutral axis x, see Figure 5.7, can be calculated as

$$
x = \frac{A_s \cdot f_s + \phi \cdot A_{fe} \cdot f_{fe}}{\alpha_1 \cdot f_c' \cdot \beta_1 \cdot b}
\tag{5.6}
$$

The concrete block parameter α_1 and β_1 are given as

$$
\alpha_1 = 0.8
$$

$$
\beta_1 = \begin{cases} 0.85, f_c' \leq 28\ MPa \\ 0.85 - 0.007(f_c' - 28), f_c' > 28\ MPa \end{cases}
\tag{5.7}
$$

where M = design moment capacity

A_s and A_{fe} = area of steel and FRP respectively

f_s and f_{fe} = section capacity of steel and FRP respectively

f_c' = concrete compression strength

$d - \frac{\beta_1 x}{2}$ and $d_f - \frac{\beta_1 x}{2}$ = lever arms to the compression zone

ϕ = reduction factor calculated from steel strain ε_s

$$\phi = \begin{cases} 0.9, for \ \varepsilon_s \geq 0.005 \\ 0.65 + \dfrac{0.25(\varepsilon_s - \varepsilon_{sy})}{0.005 - \varepsilon_{sy}}, for \varepsilon_{sy} < \varepsilon_s < 0.005 \\ 0.65 \ for \ \varepsilon_s \geq 0.005 \end{cases} \qquad (5.8)$$

Where recommended value for ϕ is 0.85.

ACI 440.2R recommend limiting the allowable strain of FRP to 90 % of the ultimate strain to avoid failure due to debonding or detachment of FRP plate.

$$\varepsilon_{fd} = 0.41 \cdot \sqrt{\frac{f_c'}{n \cdot E_f \cdot t_f}} \leq 0.9 \cdot \varepsilon_{fu} \qquad (5.9)$$

where E_f = tensile modulus of FRP

t_f = nominal thickness of FRP

f_c' = concrete compressive strength

ε_{fd} = design FRP strain

ε_{fu} = ultimate FRP strain

End peeling is also another factor that influence the flexural capacity of a strengthened member. According to ACI440.2R a transverse anchorage should be provided if the shear, V_u, at the termination point of FRP is greater than 2/3 of the concrete shear strength, V_c.

5.4.3 Flexural design procedure according to kompositförstärkning av betong

The model used for RC cross section strengthened with FRP and stress-strain distribution is shown in Figure 5.8.
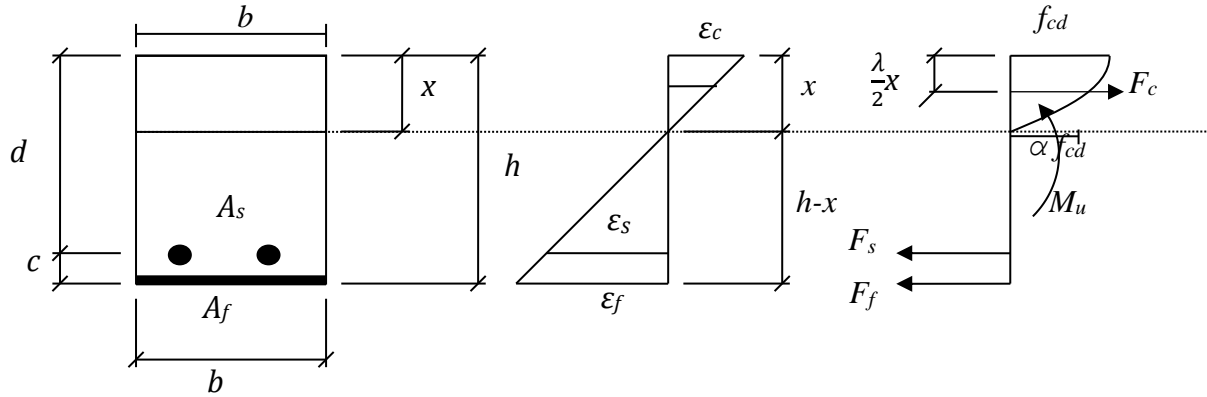
Figure 5.8   Cross section and stress-strain distribution (Björn, 2016).

For a section as shown in Figure 5.8, the design moment for the FRP strengthened section in tension can be calculated as

$$M = A_s f_{yd} \cdot \left(d - \frac{\lambda}{2} \cdot x \right) + A_f E_f \varepsilon_f \cdot \left(h - \frac{\lambda}{2} x \right) \tag{5.10}$$

The height of the neutral axis x, see Figure 5.8 can be calculated as

$$x = \frac{A_s \cdot f_y + E_f \varepsilon_f A_{fe}}{\eta \cdot f_{cd} \cdot b} \tag{5.11}$$

where $\lambda = 0.8$ for $f_{ck} \leq 50 MPa$

           $\eta = 1$ for $f_{ck} \leq 50 MPa$

           $\varepsilon_f =$ design FRP strain

           $M =$ design moment capacity

           A_s and $A_{fe} =$ area of steel and FRP respectively

           $f_{yd} =$ section capacity of steel

           $f_{cd} =$ concrete compression strength

The recommend limiting the allowable strain of FRP to 90 % of the ultimate strain to avoid failure due to debonding or detachment of FRP plate.

$$\varepsilon_{fd} = 0.41 \cdot \sqrt{\frac{f_{cd}}{n \cdot E_f \cdot t_f}} \leq 0.9 \cdot \varepsilon_{fu} \tag{5.12}$$

where E_f = tensile modulus

t_f = nominal thickness

f_c' = concrete compressive strength

ε_{fd} = design FRP strain

ε_{fu} = ultimate FRP strain

5.4.4   Flexural design procedure according to AASHTO

This design approach assumes a perfect bond between concrete, steel reinforcement and FRP material for externally bonded RC members. For FRP material the stress-strain relation is taken as linear elastic until failure and bi linear response for steel reinforcement considering elastic behaviour until yielding and plastic response until failure beyond yield stress. The concrete strain is limited to 0.005 for concrete/FRP interface while the compressive concrete strain is limited to 0.003. The concrete compression stress distribution, f_c, can be calculated as

$$f_c = \frac{2 \cdot (0.9 \cdot f_c')(\varepsilon_c/\varepsilon_0)}{1 + (\varepsilon_c/\varepsilon_0)^2} \tag{5.13}$$

$$\varepsilon_0 = 1.71 \cdot \frac{f_c'}{E_c} \tag{5.14}$$

where ε_0 = corresponds to the maximum concrete strain at stress-strain curve

ε_c = concrete strain

f_c' = specific concrete compressive strength, not more than 55 MPa.

The factored resistance, Mr, for RC beams externally bonded with FRP on the tension side can be calculated as

$$Mr = 0.9 \cdot [A_s f_s \cdot (d_s - K_{2c}) + A_s' f_s' \cdot (K_{2c} - d_s')] + \phi_{FRP} T_{FRP} \\ \cdot (d_f - K_{2c}) \tag{5.15}$$

where ϕ_{FRP} = resistance factor, equal to 0.85

$T_{FRP} = n \cdot b_{FRP} \cdot N_b$

n = number of FRP plates

N_b = FRP strength per unit width, assumed to be 1.07

6 Discrete Model for Dynamic Loading

This chapter will treat discrete model for dynamic loading which is the theory behind the dynamic predictions, in Section 8.2.1. It will describe the basic behind a Single Degree of Freedom (SDOF) system and how it can be transformed into a Two Degree of Freedom (2DOF) system that can treat dynamic loading and calculate predictions for the dynamic experimental testing that were conducted in this thesis. This chapter is based on literature from Johansson and Laine (2012) and previous year's thesis's made in cooperation between Norconsult and Chalmers about impact loading.

6.1 SDOF system

SDOF system is a simple system consisting of a mass, m, which is subjected by an external force, $F(t)$, which cause displacement, u. This system include an internal resistance, $R(u)$, and a damping coefficient, c, see Figure 6.1. The damping coefficient, c, will be excluded in following calculations since it's only during a short time the mass will be subjected by a load when studying impulse loading. Moreover, it's also a good estimation to make since in this case only the maximum deflection is of interest.
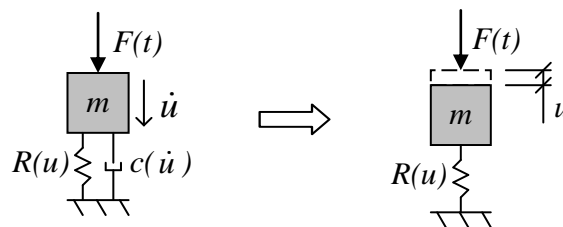
Figure 6.1   Schematic figure illustrating a SDOF system of a mass, m, subjected by an external force, F(t). The first figure illustrates the system including damping coefficient, c(u), and the second figure illustrate a simplified model where it's not included (Johansson and Laine, 2012).

6.2 Transformation factors

To get equivalent SDOF systems for a structure, it needs to be transformed using transformation factors. This section will treat the transformation factors needed for the kind of impulse load that the experimental testing in this thesis have conducted. The transformation factors used consider, mass, stiffness and external load.

6.2.1 Transformation of beam into equivalent SDOF system

When studying a beam that's statically loaded and show linear elastic behaviour, it can be assumed that the displacement will be increased by a factor α, see Figure 6.2. Furthermore, the deformation shape is the same independently of the magnitude of the load which makes it possible to choose only one point to study the deformation, it is called system point. This system point is usually placed where the deformation is at largest or at the midpoint of the beam. The deflection in this point is denoted u_s and it should be equal to the deflection in the SDOF system. Hence, $u_s = u_{SDOF}$.
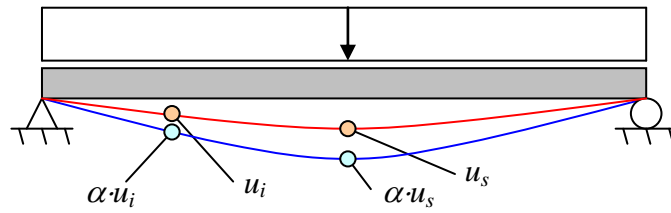
Figure 6.2   Schematic figure illustrating a beam subjected to a uniform load. It shows a linear elastic behaviour, so the displacement can be increased with a factor α along the whole beam. (Johansson and Laine, 2012).

In order to transform the beam into a SDOF system, transformation factors will be used. κ_m consider the transformation due to mass, κ_F the force and κ_k the stiffness. An illustration for the factors affected by this transformation is shown in Figure 6.3.
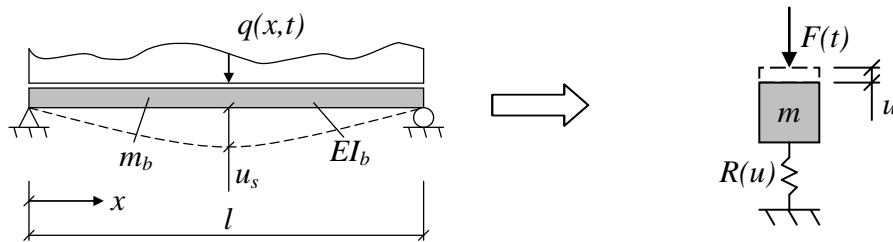
Figure 6.3   Transformation of the beam into an equivalent SDOF system, stiffness of the beam EI_b can also be denoted as k_b (Johansson and Laine, 2012).

Following equations show how these transformation factors are included in the calculations

$$m = \kappa_m \cdot m_b \tag{6.1}$$

$$F = \kappa_F \cdot F_b \tag{6.2}$$
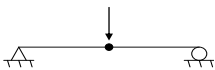
$$k = \kappa_k \cdot k_b \tag{6.3}$$

$$\kappa_{mF} = \frac{\kappa_m}{\kappa_F} \tag{6.4}$$

where m_b = mass of the beam [kg]

k_b = stiffness of the beam [N/m]

F_b = external force [N]

κ = transformation factor [-]

The magnitude of these transformation factors that's of interest for three point bending with simply supported beam are also dependent on whether the beam is showing elastic or plastic behaviour, see Table 6.1.

Table 6.1   Transformation factors for three point bending of a simply supported beam (Johansson and Laine, 2012).

	Strain range	κ_m	κ_F	κ_k	κ_{mF}
	Elastic	0.486	1.000	1.000	0.486
	Plastic	0.333	1.000	1.000	0.333

6.2.2 Transformation of drop weight into equivalent SDOF system

The drop weight will need to be treated as a bar, when transformed into a SDOF system. This is because it will experience axial displacement, see Figure 6.4. The system point in this case is placed at largest deformation which is at the bottom of the bar, where it will hit the surface of the beam. Lovén and Svarvarsdóttir (2016) have presented a detailed description about the transformation of a drop weight into a SDOF system and this section is based on that information.
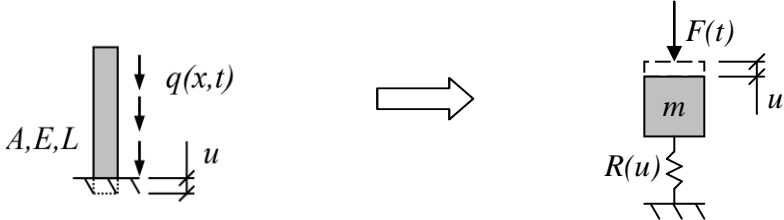
Figure 6.4   Transformation of the drop weight into an equivalent SDOF system (Johansson and Laine, 2012).

There are two ways to treat the drop weight when transforming it into an equivalent SDOF system and that is to consider it as a rigid bar or rigid surface. Rigid bar mean that the drop weight is seen as a rigid body which is very stiff compared with the impacted beam surface and rigid surface mean that the beam surface is considered to be the rigid body. The description that is the most accurate is that the drop weight is a rigid bar, however, in real it is something in-between these two extreme cases. The transformation factors used are the same as for the beam with values corresponding to Table 6.2 for a rigid bar, which mean they all equal 1.000.

Table 6.2   Transformation factors for the drop weight which is considered as a bar in this thesis (Jönsson and Stenseke, 2018).

Case	κ_m	κ_F	κ_k	κ_{mF}
Rigid surface:	0.333	0.500	0.500	0.667
Rigid bar:	1.000	1.000	1.000	1.000

6.3 2DOF system

The two equivalent SDOF systems of the beam and drop weight need to be coupled into a 2DOF system, see Figure 6.5. Figure 6.5 show that mass m_1 correspond to the mass of the drop weight and mass m_2 corresponds to the mass of the beam. R_1 and R_2 are the internal resistances of the drop weight and beam, respectively. These names of the constants will be used in the calculations for the dynamic predictions. Moreover, with this system it is possible to use the equation of motion for 2DOF systems to predict the behaviour of the beam and drop weight.
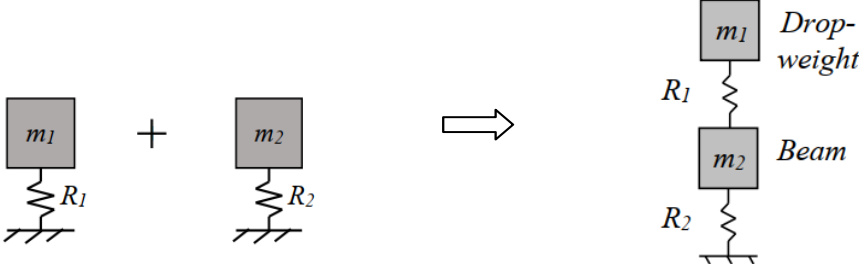
Figure 6.5   *Coupling of the equivalent SDOF systems for the drop weight and the beam into a 2DOF system (Johansson and Laine, 2019).*

6.4 Equation of motion

To understand the equation of motion, we will study a free body in a SDOF spring-mass system, see Figure 6.6. The free-body in Figure 6.6 is subjected by an external force, $F(t)$, that cause an acceleration, a, and displacement, u. This force is resisted by static and dynamic reaction forces, which respectively are the result of spring stiffness, k, and damping coefficient, c.
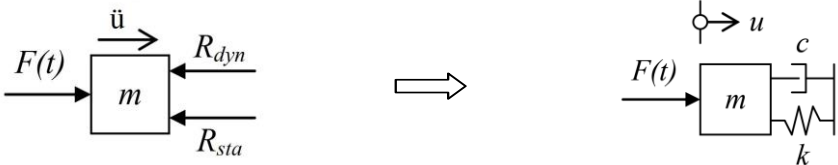
Figure 6.6   *SDOF system for a free body that is subjected to a dynamic loading (Johansson and Laine, 2012).*

The equation of motion is based on Newton's second law (Johansson and Laine, 2012). For a SDOF system with a particle with mass, m, which is subjected by an external force, Newton's second law gives Equation (6.5) (Ljung et al., 2015).

$$F = m \cdot \ddot{u} \tag{6.5}$$

where F = external force [N]

m = mass [kg]

$\ddot{u}$ = acceleration [m/s^2]

Figure 6.6 is also affected by a spring stiffness and damping coefficient, those are non-negative constants (Ljung et al., 2015). When applying Newton's second law for this system we get following equation

$$F - R_{sta} - R_{dyn} = m \cdot \ddot{u} \qquad (6.6)$$

where $\quad R_{sta}$ = static reaction force [N]

$\qquad\qquad R_{dyn}$ = dynamic reaction force [N]

It is assumed that there is a linear elastic response, then the constitutive equations for the spring and dampener is following (Ljung et al., 2015)

$$R_{sta} = k \cdot u \qquad (6.7)$$

$$R_{dyn} = c \cdot \dot{u} \qquad (6.8)$$

where $\quad k$ = spring stiffness [N/m]

$\qquad\qquad c$ = damping coefficient [Ns/m]

$\qquad\qquad u$ = displacement [m]

$\qquad\qquad \dot{u}$ = velocity [m/s]

Furthermore by combining Equations (6.6), (6.7) and (6.8), we get the final statement for the equation of motion in Equation (6.9). Velocity is the derivative of displacement and acceleration is the second derivative of displacement.

$$m\ddot{u} + c\dot{u} + ku = F(t) \qquad (6.9)$$

6.4.1 Equation of motion for 2DOF systems

The equation of motion will be applied on the 2DOF system presented in Section 6.3. This gives a free body diagram which is illustrated in Figure 6.7.
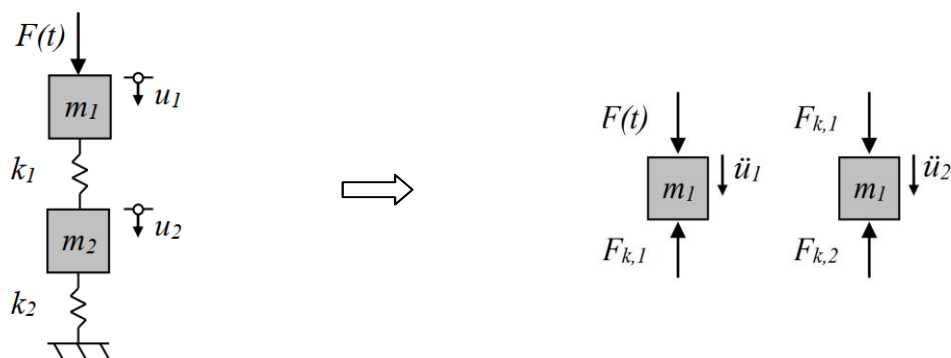

Figure 6.7   *2DOF system for a free body diagram that is subjected to a dynamic loading (Johansson and Laine, 2012).*

Newton's second law of force equilibrium gives following

$$F_1(t) - F_{k,1} = m_1 \cdot \ddot{u}_1 \tag{6.10}$$

$$F_2(t) - F_{k,2} = m_2 \cdot \ddot{u}_2 \tag{6.11}$$

constitutive relations give

$$m_1 \ddot{u}_1 + k_1(u_1 - u_2) = F_1(t) \tag{6.12}$$

$$m_2 \ddot{u}_2 - k_1 u_1 + (k_1 + k_2)u_2 = F_2(t) \tag{6.13}$$

writing these equations as a matrix yields

$$\begin{bmatrix} m_1 & 0 \\ 0 & m_2 \end{bmatrix}\begin{bmatrix} \ddot{u}_1 \\ \ddot{u}_2 \end{bmatrix} + \begin{bmatrix} k_1 & -k_1 \\ -k_1 & k_1 + k_2 \end{bmatrix} = \begin{bmatrix} F_1(t) \\ F_2(t) \end{bmatrix} \tag{6.14}$$

Introducing the transformation factors results in following

$$\begin{bmatrix} \kappa_{m,1} m_1 & 0 \\ 0 & \kappa_{m,2} m_2 \end{bmatrix}\begin{bmatrix} \ddot{u}_1 \\ \ddot{u}_2 \end{bmatrix} + \begin{bmatrix} \kappa_{k,1} k_1 & -\kappa_{k,1} k_1 \\ -\kappa_{k,1} k_1 & \kappa_{k,1} k_1 + \kappa_{k,2} k_2 \end{bmatrix} = \begin{bmatrix} \kappa_{F,1} F_1(t) \\ \kappa_{F,2} F_2(t) \end{bmatrix} \tag{6.15}$$

This expression can also be written as

$$\boldsymbol{m\ddot{u} + ku = F(t)} \tag{6.16}$$

6.4.2 Beam and drop weight

Transformation factors from Section 6.2 are introduced in Equations (6.1), (6.2) and (6.3). There are no external forces, $F_i(t)$, that is considered to affect the beam and drop weight. The impulse load is instead introduced as an initial velocity affecting the beam and the drop weight at impact zone. Both bodies will obtain a displacement and an acceleration. Depending on whether it's elastic response or elasto-plastic response following equations will be used.

For elastic response

$$\kappa_{mF,2}\begin{bmatrix} \alpha_m m_1 & 0 \\ 0 & m_2 \end{bmatrix}\begin{bmatrix} \ddot{u}_1 \\ \ddot{u}_2 \end{bmatrix} + \begin{bmatrix} k_1 & -k_1 \\ -k_1 & k_1 + k_2 \end{bmatrix} = \begin{bmatrix} 0 \\ 0 \end{bmatrix} \tag{6.17}$$

where

$$\alpha_m = \frac{\kappa_{m,1}}{\kappa_{m,2}} \tag{6.18}$$

and for elasto-plastic response

$$\kappa_{mF,2}\begin{bmatrix} \alpha_m m_1 & 0 \\ 0 & m_2 \end{bmatrix}\begin{bmatrix} \ddot{u}_1 \\ \ddot{u}_2 \end{bmatrix} + \begin{bmatrix} R_1 & -R_1 \\ -R_1 & R_1 + R_2 \end{bmatrix} = \begin{bmatrix} 0 \\ 0 \end{bmatrix} \tag{6.19}$$

The internal resistance for the case of elastic response is determined as

$$R_i(u) = k_i \cdot u_{el} \tag{6.20}$$

and for elasto-plastic

$$R_i(u) = \begin{cases} F_i & if & u = 0 \\ R_{m,i} & if & u > 0 \end{cases} \tag{6.21}$$

However, in the case of the drop weight some additional factors need to be considered. The drop weight will at a time be moving away from the beam and in that case there will be tension in the spring between the two bodies. This will not happen, since at that time there's no connection between the two bodies and therefore for the drop weight Equation (6.21) is modified into

$$R_1 = \begin{cases} k_i \cdot u & if & u_1 \le u_{el,1} \\ R_{m,i} & if & u_1 > u_{el,1} \\ 0 & if & u_1 \le 0 \end{cases} \tag{6.22}$$

Internal resistance and stiffness of the beam are calculated as

$$R_2 = \frac{4 \cdot M_u}{l_2} \tag{6.23}$$

$$k_2 = \frac{48 \cdot E_{cm}I_{II}}{l^2} \tag{6.24}$$

where $\quad M_u$ = maximum moment in ultimate limit state [Nm]

$\quad\quad\quad l$ = length of the beam [m]

$\quad\quad\quad E_{cm}$ = modulus of elasticity for concrete [Pa]

$\quad\quad\quad I_{II}$ = stiffness of the beam in state II [m^4]

Furthermore, the internal resistance of the beam is affected by its self-weight. Figure 6.8 show the relation between the internal resistances of the beam, $R_{m,2} = R_2$.
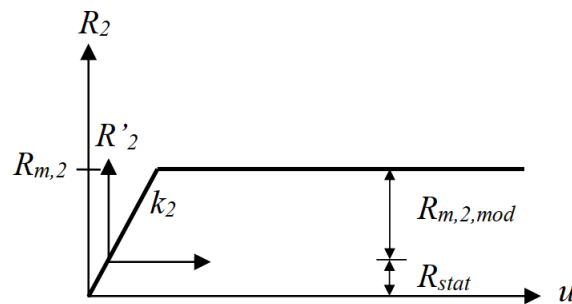

Figure 6.8   *Illustration showing the internal resistance of the beam and the different denotions (Jönsson and Stenseke, 2018).*

The effect of the self-weight, g_{beam}, is calculated according to

$$R_{stat} = \frac{g_{beam} \cdot l}{2} \tag{6.25}$$

which give

$$R_{m,2,mod} = R_{m,2} - R_{stat} \tag{6.26}$$

6.5 Central difference method

Central difference method is an explicit method to solve a second order differential equation i.e. equation of motion. Figure 6.9 illustrates a scheme of how it's done.

The velocity is expressed as

$$\dot{u}_i = \frac{u_{i+1} - u_{i-1}}{2\Delta t} \tag{6.27}$$

and the acceleration is

$$\ddot{u}_i = \frac{u_{i+1} - 2u_i + u_{i-1}}{(\Delta t)^2} \tag{6.28}$$
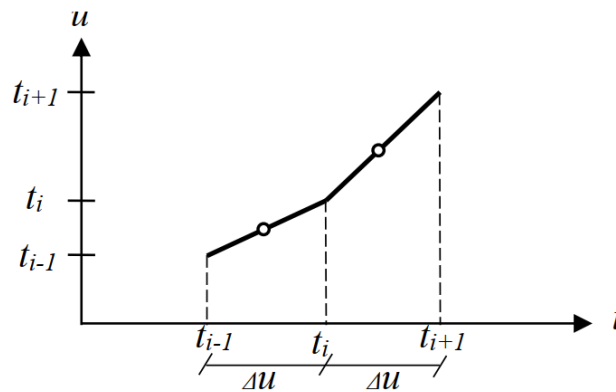
Figure 6.9   *Illustration showing the way that the theory behind central difference method is used (Jönsson and Stenseke, 2018).*

If Equations (6.27) and (6.28) are put in the equation of motion, it gives

$$\boldsymbol{M}\frac{\boldsymbol{u}_{i+1} - 2\boldsymbol{u}_i + \boldsymbol{u}_{i-1}}{(\Delta t)^2} + \boldsymbol{K}\boldsymbol{u}_i = \boldsymbol{F}_i(t) \tag{6.29}$$

u_i and u_{i-1} are assumed to be known, so by introducing initial conditions u_{i+1} can be found. The initial conditions used are

$$\boldsymbol{u}(0) = \boldsymbol{u}_0 \tag{6.30}$$

$$\ddot{\boldsymbol{u}}(0) = \ddot{\boldsymbol{u}}_0 \tag{6.31}$$

$$\ddot{\boldsymbol{F}}(0) = \ddot{\boldsymbol{F}}_0 \tag{6.32}$$

and when i equal zero the solution is expressed as

$$\boldsymbol{u}_{i+1} = (\Delta t)^2 \boldsymbol{M}^{-1}\left(\boldsymbol{F}_i(t) - \left(\boldsymbol{K} - \frac{2}{(\Delta t)^2}\boldsymbol{M}\right)\boldsymbol{u}_i - \frac{1}{(\Delta t)^2}\boldsymbol{M}\boldsymbol{u}_{i-1}\right) \tag{6.33}$$

When using this method it is of importance that the time step, $\varDelta t$, is not too large, cause that will give misguiding results as the iterations increase. To establish this the time step should be smaller than

$$\varDelta t_{crit} = \frac{2}{\omega_{max}} = \frac{T_n}{\pi} \tag{6.34}$$

where ω_{max} = highest eigenfrequency [s^{-1}]

T_n = smallest time period [s]

Furthermore according to Johansson and Laine (2012) there might be of interest to use a smaller time step. This would be that it should be smaller than 1 % of the load duration, t_1, as seen

$$\varDelta t_{crit} \leq \begin{cases} \varDelta t_{crit} \\ \dfrac{t_1}{100} \end{cases} \tag{6.35}$$

7 Experimental Description

In this experiment a total of 19 beams were used for dynamic and static tests. The first 18 beams were classified in three groups, each group consisting of six beams. Afterwards, each group of six beams were provided with 1 layer or 3 layers of FRP strengthening and six beams were left without FRP strengthening to be used as reference beams. From a total of 18 beams half of them were subjected to impact loading with drop heights of 4 m, 3.5 m, and 3 m, followed by a static three point bending test to determine the remaining residual capacity. The other half of the beams were subjected to only static three point bending until failure. The method used was deflection control method. The 19th beam was subjected to only static loading with a different support condition, using flat steel squares on top of the rollers. This beam was used for comparison of support condition on the stiffness response. The concrete was manufactured in two batches with the same recipe. The naming and classification of the beams are based on batches, FRP reinforcement and loading condition, see Table 7.1.

Table 7.1   Naming of beams according to batches, loading condition and FRP layers.

Beam no.	Batch no.	FRP layer	Load type	Test day	Beam name
1	1	-	Static	27	01-B1-FRP0-S
2	1	-	Static	27	02-B1-FRP0-S
3	2	-	Static	27	03-B2-FRP0-S
4	1	-	Impulse 4 m + Static	26 + 28	04-B1-FRP0-D4
5	2	-	Impulse 3.5 m + Static	26 + 28	05-B2-FRP0-D3.5
6	2	-	Impulse 3 m + Static	26 + 28	06-B2-FRP0-D3
7	1	1	Static	27	07-B1-FRP1-S
8	1	1	Static	27	08-B1-FRP1-S
9	2	1	Static	27	09-B2-FRP1-S
10	1	1	Impulse 4 m + Static	26 + 28	10-B1-FRP1-D4
11	2	1	Impulse 3.5 m + Static	26 + 28	11-B2-FRP1-D3.5
12	2	1	Impulse 3 m + Static	26 + 28	12-B2-FRP1-D3
13	1	3	Static	27	13-B1-FRP3-S
14	1	3	Static	27	14-B1-FRP3-S
15	2	3	Static	28	15-B2-FRP3-S
16	1	3	Impulse 4 m + Static	26 + 28	16-B1-FRP3-D4
17	2	3	Impulse 3.5 m + Static	26 + 28	17-B2-FRP3-D3.5
18	2	3	Impulse 3 m + Static	26 + 28	18-B2-FRP3-D3
19	1	-	Static – square supports	28	19-B1-FRP0-S

7.1 Preparation of moulds and reinforcement

The moulds that were used in previous year's master thesis by Andersson and Pettersson (2019), were reused in this study. The geometry of the beam is shown in Figure 7.1
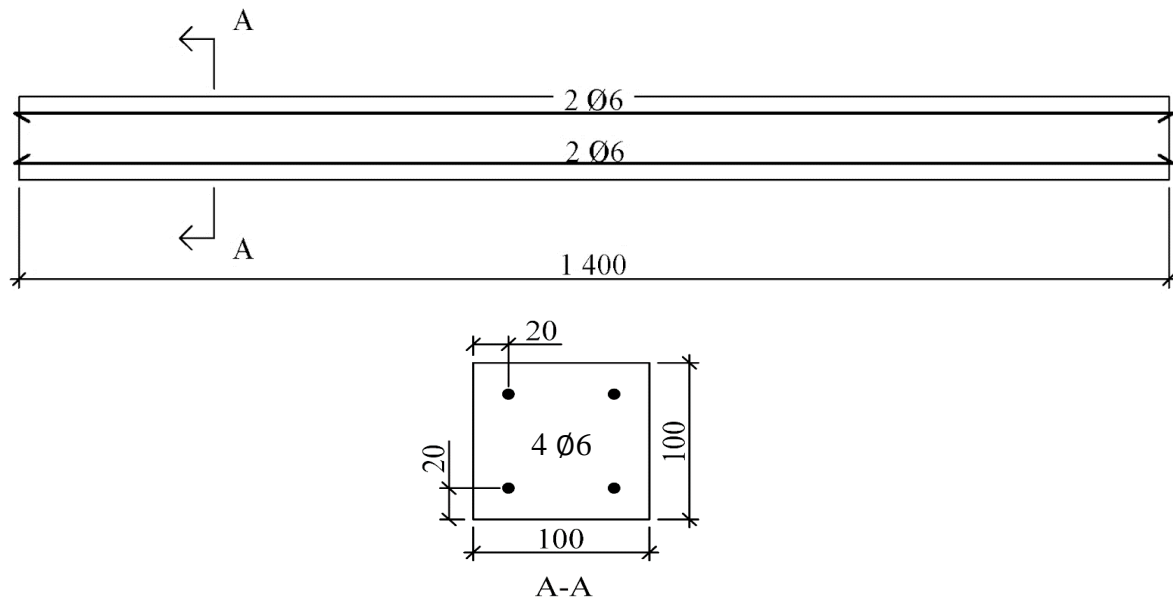

Figure 7.1   Geometry and reinforcement arrangement of the beams (Jönsson and Stenseke, 2018).

The frame was made of timber parts that were screwed together. The frames had part-holes on the opposite ends to give space and support for the rebars. The inner dimensions of the frame gave a cross-section of 100×100 mm^2 and a length of 1 400 mm. For the compressive and tensile material tests, plastic cubes with inner dimensions of $150 \times 150 \times 150$ mm^3 were used. Steel cubes with the same dimensions but with an additional notch on one of the sides were used for wedge splitting tests. The moulds were cleaned by removing old concrete and dust, and then lubricated using oil to make it easier to remove the beams out of the moulds later on.

Figure 7.2   Sample of moulds showing bored holes to give space and support for rebars.

Reinforcement bars with 6 mm nominal diameter and specification K500C-T were cut in a length of 1 410 mm allowing 5 mm on each side to be placed in the holes to prevent movement of rebars while preparing and casting the beams see Figure 7.2. To maintain a concrete cover of 17 mm the rebars were placed with a distance of 20 mm from the surface of the mould to the center of the reinforcement bars.

Wooden blocks were used as spacers to keep a correct and uniform spacing between the bottom of the mould and the bottom reinforcement and between the top and the bottom reinforcement. With spacing of one third of the mould length, short rebars were placed on top of the mould. Then the main rebars were hanged on these rebars using steel wires in order to prevent misplacing and to keep the rebars at the desired position, see Figure 7.3.

It was Lozano and Makdesi (2017) who observed that the reinforcement would bend down and lose position due to the self-weight of the rebars and the additional weight from the concrete during casting. This method with steel wire were used by Jönsson and Stenseke (2018). After their testing was done, they saw their beams apart to measure the position of the reinforcement to confirm it kept its position after casting. It was confirmed by them that this is a good method, so it is assumed that the result is the same in this case since similar moulds and same nominal rebar diameter are used.
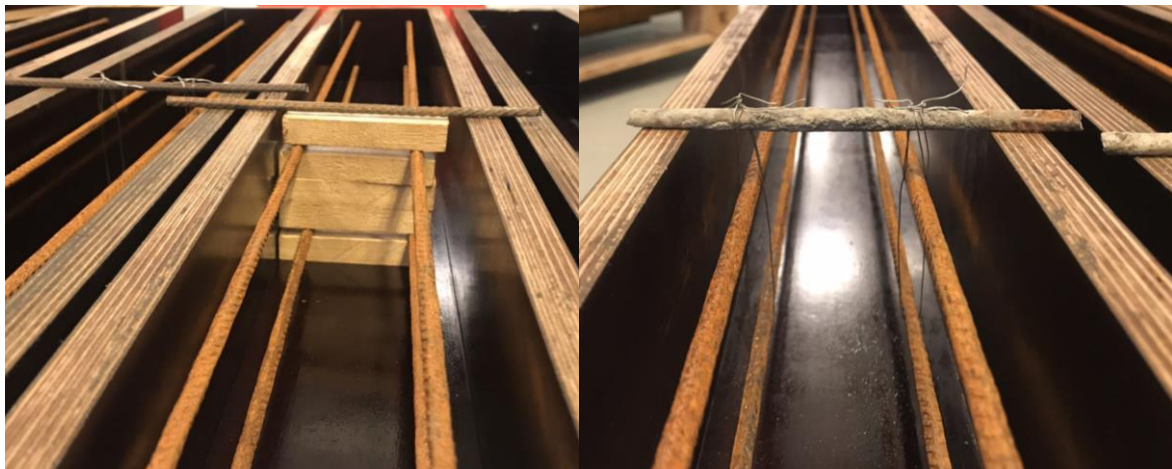
Figure 7.3   Arrangement of reinforcement to maintain the desired spacing.

7.2   Manufacturing of concrete

The beams are manufactured at Chalmers structural engineering laboratory based on a recipe developed by Ingemar Löfgren, Thomas Concrete Group AB. The ratio used in this recipe is shown in Table 7.2. The concrete mix was done aiming at normal concrete with strength of C40/50 and water-cement ratio of 0.45.

Figure 7.4   Moisture analyser for sand and stones.

A moisture analyser, see Figure 7.4, was used to measure how much percentage of moist there were in the sand and in the stones that were used for the manufacturing of concrete. Depending on the amount of moisture the recipe was adjusted to get the correct water-cement ratio. The moisture analyser weighs the material then it heats up to dry out the moisture. During the process, by the loss of weight it calculates the percentage of lost moisture and shows the result in a graph. When the graph plane out it implies that the moisture have dried out and the value of initial moisture content can be read. This was done for some examples of sand and stones, and the most representative values was used respectively, see Table 7.2.

Table 7.2   Recipe for one batch of concrete for the beams, one batch is 175 litre.

Material	Supplier	Moisture [%]	Quantity [kg]
Byggcement CEM II/A-LL 42.5R	Cementa	-	71.8
Sand 0/8 Sköllunga	Ucklums Grus	7.76	180.6
Stone 8/16 Vikan	Skanska	1.13	153.1
Mater Glenium 51/18	BASF	-	0.9
Master Set R 401 Lent	BASF	-	0.2
Water	-	-	17.7

Because of size limit, the mixing was done in two batches. Six cubes from each batch were casted for compression and tensile tests and three cubes for wedge splitting tests, i.e., a total of 15 cubes were used for cube tests. Concrete was poured to the moulds by using buckets and vibrator rod was used to compact the concrete as shown in Figure 7.5. After casting, the surface was levelled and covered by plastic cover.
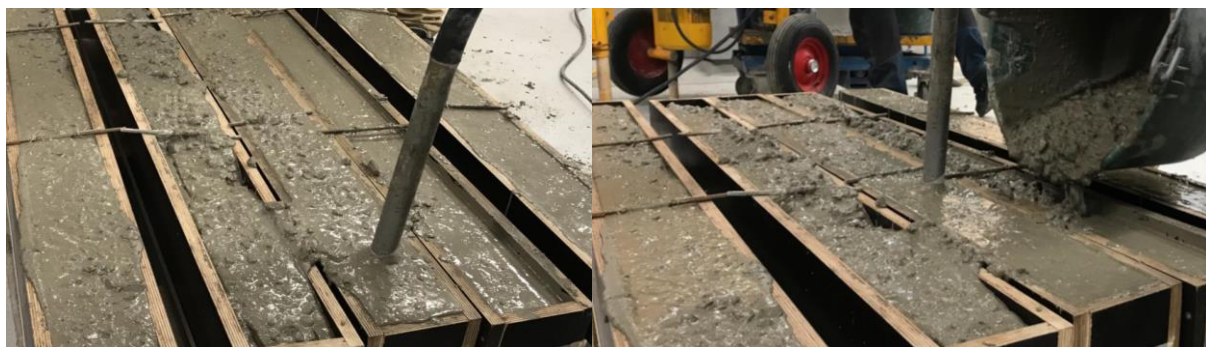

Figure 7.5   Casting and compacting of concrete.

7.3   Demoulding

Demoulding of cubes was done on day one after casting and they were directly placed into water for curing. The concrete beams were demoulded eight days after casting. The beams were given names B1 for batch one and B2 for batch two while demoulding. After demoulding, preparation of the beams before applying epoxy and aramid fibre was done by removing oil and dust from the surface of the beams to make sure the bond between the concrete and resin will not be affected by an oily surface and dirt. Only bottom surface of the beams, where FRP would be attached, was prepared by rubbing the surface using a wire brush. Dust was then removed by using fabric and a vacuum cleaner.

Figure 7.6   Surface preparation of beams for FRP strengthening.

7.4   Preparation and applying FRP

External strengthening was done by binding FRP sheets to the concrete surface using resin. The type of FRP material that was used was S&P A-sheet 120, which is a unidirectional aramid fibre fabric with high strength and toughness provided by a supplier S&P Clever Reinforcement Company AG. Kevlar has a good fatigue and heat resistance. When it is exposed to high temperature the stiffness decreases as the temperature increases but is able to retain most of its original strength after exposure to high temperature. Kevlar has a sensitive behaviour when it comes to moisture and certain chemicals like some acids and alkalis (Wu and Eamon, 2017).The resin used was "S&P Resin 55HP" (impermeable) and S&P Resicem HP (vapour permeable) from the same supplier. The mixing of the resin was made according to the specification.

Figure 7.7   S&P A-sheet 120 used in the experiment (from the S&P A-sheet 120 manual).

The specification provided by the supplier for the mechanical properties and resin consumption are given in Table 7.3 and Table 7.4 respectively.

Table 7.3   Mechanical properties of S&P A-sheet 120 according to S&P Clever Reinforcement Company AG.

S&P A-Sheet 120 Aramid fibre sheet for structural reinforcement		
Technical data unidirectional	**Unit**	**A-Sheet 120 290 g/m**
Elastic modulus	kN/mm²	≥ 120
Tensile strength	N/mm²	$\geq 2\ 900$
Fibre weight	g/m²	290
Weight per unit area of sheet	g/m²	320
Density	g/cm³	1.45
Elongation at rupture	%	2.5
Design thickness (fibre weight/density), longitudinal	mm	0.20
Theoretical design cross-section Width: 1000 mm, longitudinal	mm²	200
Reduction factor y for the design (manual lamination / UD sheet)	-	1.3 (recommended by S&P)
Tensile force (elongation at break) Width: 1000 mm	kN, longitudinal	440
Tensile force for dimensioning (flexural strength) Width: 1000 mm at $\varepsilon = 0.6$ %	kN, longitudinal	105
Tensile force for dimensioning (axial load) Width: 1000 mm at $\varepsilon = 0.4$ %	kN, longitudinal	70

Table 7.4   Consumption of S&P A-sheet 120 according to S&P Clever Reinforcement Company AG.

Product	S&P Resin 55 Hp (impermeable)	S&P Resin Hp (vapour permeable)
S&P A-Sheet 120 290 g/m²	700 – 1 000 g/m²	1 200 – 1 600 g/m²
The material consumption depends on the flatness and the roughness of the substrate. The actual consumption could be higher.		

Based on the geometry of the beams, the aramid sheet was prepared in length of 1 200 mm and 100 mm width. Six beams were strengthened with 1 layer FRP and another six beams were strengthened with 3 layers of FRP. The FRP was placed at a distance of 100 mm from both edges of the beam.
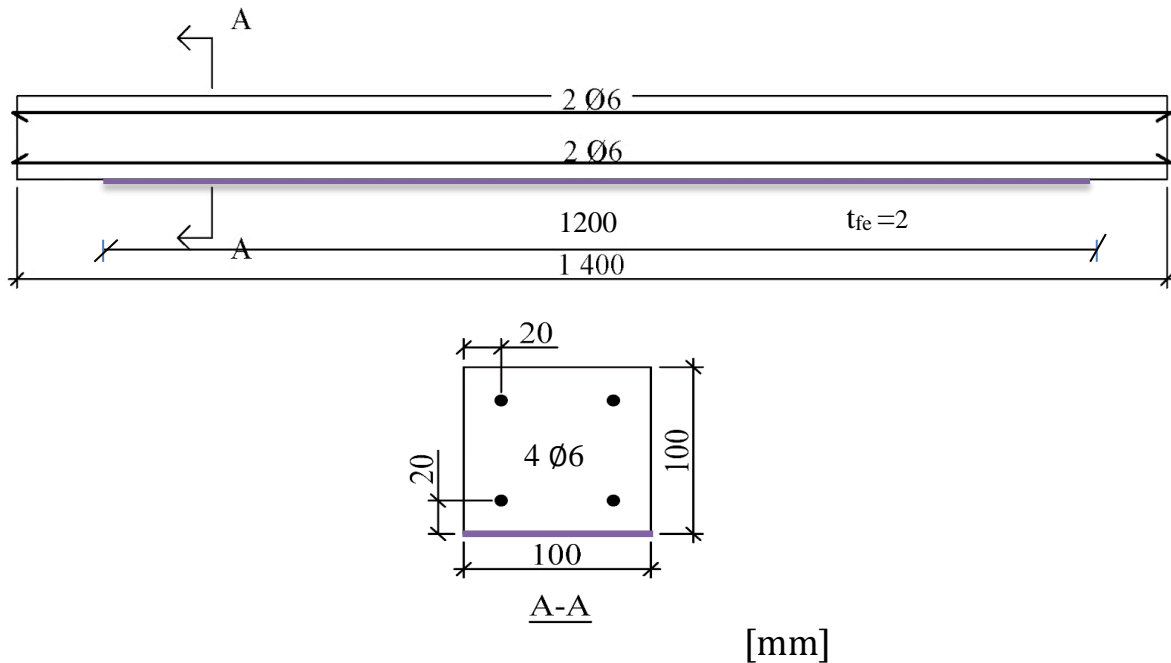
Figure 7.8   Geometry of FRP strengthened RC beam.

The epoxy was mixed according to the specification and applied on the concrete surface. Afterwards one layer of FRP was placed and a roller was used to attach the FRP more firmly and to remove any air bubbles between the resin and the FRP sheet. For the beams with three layers of FRP sheets, they were applied in the same way by putting resin between the sheets and placing layers one after each other.

For the application of FRP a temporary ventilated tent was put up in the Chalmers structural laboratory to meet safety regulations while using resin. Application of FRP was done by associate professor Reza Haghani. The set up and application of FRP is shown in Figure 7.9.
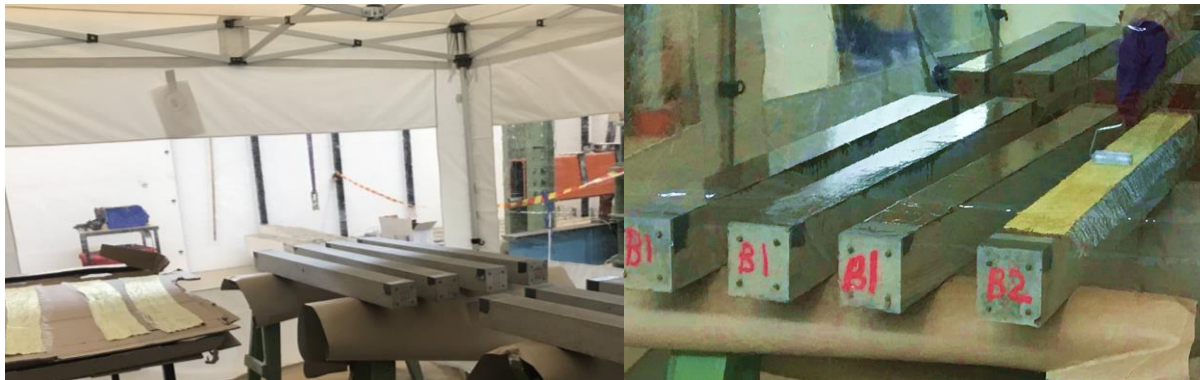

Figure 7.9   Set up and application of FRP strengthening.

7.5 Painting of beams

To create a plain white background the beams were first painted white, but some beams had droplets from the epoxy on the surface, that came from binding the FRP. Therefore, additional layers of white paint were applied to cover the spots and create uniform white background. Afterwards black dots were applied to create a random pattern that gives good results while analysing the footages from DIC and static camera in GOM Correlate 2019.

Figure 7.10   Illustration showing the painting pattern for beam 01-B1-FRP0-S.

7.6 Material testing for concrete

The material tests carried out were cube compressive test, tensile splitting test and wedge splitting test (WSP). The compressive strength and tensile strength of concrete were determined in accordance with (CEN, 2009e) and (CEN, 2009f), respectively. The concrete density was determined in accordance with (CEN, 2009g). The estimation of fracture energy from WST was done in accordance with Tschegg (1991). For compressive tests and tensile splitting tests, six cubes were used for each test with three cubes from batch one and three cubes from batch two at the age of 26 days after casting. For the WST three cubes were used from both batches at the age of 28 days after casting.

7.7 Material testing for reinforcement

Tensile tests for six specimens of reinforcement were tested by using a MTS 380 machine, see Figure 7.11. They had a nominal diameter of 6 mm, same as for the reinforcement used for the concrete beams in the experiments. They were cut at a length of 400 mm, of which 50 mm in each end was used for the machine to grip, resulting in an effective length of 300 mm. An extensometer of model MTS 634.25F-24 was used for the first 15 mm of deformation since it gives a more accurate result for the initial strain. The stress-strain curve shows where this happened since the applied force was stopped for a short time. The continued strain was calculated by the material data extracted from the machine. The most wanted results from these tests were to extract the yield strength, tensile strength, ultimate strain and modulus of elasticity for the steel bars and to find the mean value of the tested specimen. These tests were done in accordance to CEN (2016), deformation speed was 5 mm/min for stage I and 120 mm/min for stage II. 4 mm of deformation were used in the tests for the change in speed, at this time yielding strength had passed which met the CEN (2016) requirement.

Figure 7.11   Setup for the reinforcement testing in a MTS 380 machine with an extensometer attached to measure strain.

7.8   Dynamic tests

The testing for the drop weight impact were performed first, 26 days after casting. The beams were simply supported and the drop weight was cylindrical steel rod with rounded tip. The dynamic testing for the beams were conducted at Chalmers structural engineering laboratory.

7.8.1   Test set-up

The beams were simply supported on rollers as shown in Figure 7.12 and Figure 7.13. The rollers were cut at the bottom and fixed in a fixture with a span length of 1 300 mm. The drop weight were released at the midpoint of the beam.
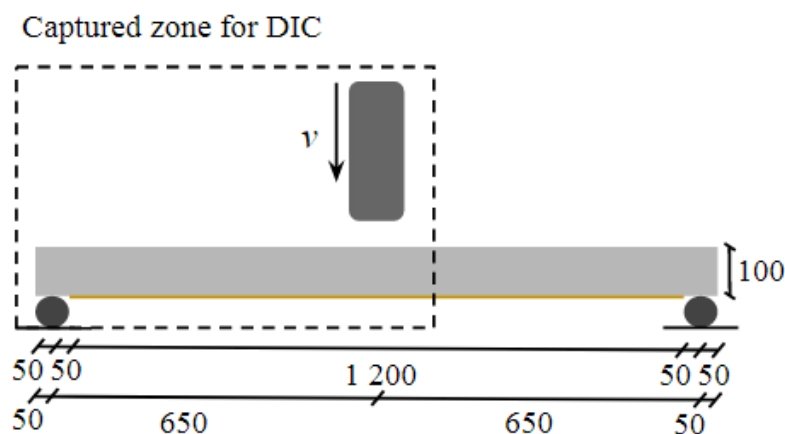

Figure 7.12   Illustration showing schematic figure of the test set-up and dimensions [mm] for dynamic testing.

Figure 7.13   Illustration showing test set up for dynamic testing.

The drop weight was painted in the same black and white pattern as the beams to make it possible for the results from the DIC cameras to be read and analysed. It was tied up in a rope and placed in vertical guiding rails which kept it in place, see Figure 7.13. The drop weight would be hauled up to the desired height by the rope and then released from the rope to fall down to hit the beam. The geometry for the drop weight were a diameter of 80 mm and a height of 500 mm, see Figure 7.14. Its weight was 20 kg. The rounded part at the tip gives a radius of 200 mm.

For all dynamic testing the beams were only subjected to drop weight impact once, but to different drop height depending on specimen. The drop heights used were 3 m, 3.5 m and 4 m.
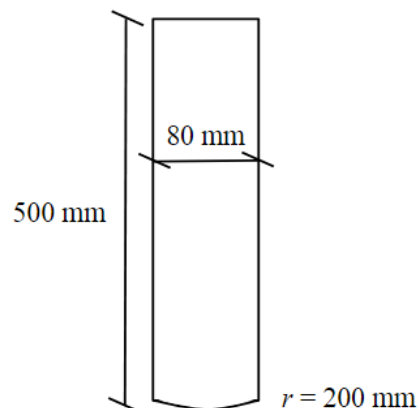

Figure 7.14   Schematic illustration of the dimensions [mm] for the drop weight.

7.8.2   Digital image correlation

Digital Image Correlation (DIC) is a technique to analyse a large number of images and from them extract results such as deflection, strain fields and velocity as examples. Two different high speed cameras were used for the impact testing. One of the cameras (camera 1) captured 40 000 frames per second (frp), while the other (camera 2) capsured 5 000 frp. Camera 1 filmed

approximately half of the beam in the middle, while camera 2 filmed the left-hand side of the beam.

The aim of camera 1 was to analyse the drop weight impact during the tests to get more accurate measures for the acceleration and thus a better estimation of the impact force, which is calculated from the accelerations. Camera 2 was used to analyse the beam behaviour and therefore the results from this camera have mainly been used in this thesis. Camera 2 was also the same type of camera that was used in previous years drop weight impact tests, see Andersson and Pettersson (2019).

The images from the high speed cameras were processed and analysed in GOM Correlate 2019. A DIC facet analysis were performed to find the most appropriate settings for facet size and point distance, see Appendix C. Detailed information about the cameras used can be seen in Table 7.5 and Table 7.5.

Table 7.5   Camera specifications for camera 1.

High speed camera	Photron SAZ
Distance from front of the beam to camera house	2000 mm
Zoom	Nikon 50 mm lens
Resolution	1024x400 pixels
Spatial scale	Calibrated with 40 mm measuring scale → 40 mm = 54 pixel → 1 pixel = 0.7407 mm
Approximate measuring area	819x320 mm
Frame rate	40000 fps (every 0.025 ms)
Shutter	1/50000
Trigging	Manual trigging with "centre trigger"

Table 7.6   Camera specifications for camera 2.

High speed camera	Photron SA4
Distance from front of the beam to camera house	2000 mm
Zoom	Nikon 50 mm lens
Resolution	1024x400 pixels
Spatial scale	Calibrated with 40 mm measuring scale → 40 mm = 54 pixel → 1 pixel = 0.7407 mm
Approximate measuring area	819x320 mm
Frame rate	5000 fps (every 0.2 ms)
Shutter	1/7000
Trigging	Manual trigging with "centre trigger" which approximately capture 1 s before and 1 s after impact

7.9   Static tests

For the static testing, three point bending tests on simply supported beams were performed on day 27 and 28 after casting. The static tests for the beams were also conducted at Chalmers structural engineering laboratory.

7.9.1   Test set-up

The beams were simply supported on rollers with a span length of 1 300 mm as shown in Figure 7.15 and Figure 7.16, and the rollers were placed on stiff steel plates. In the three point bending tests were the load was applied in the centre of the beam. The load was applied as deformation controlled, using a roller placed perpendicular to the beam.
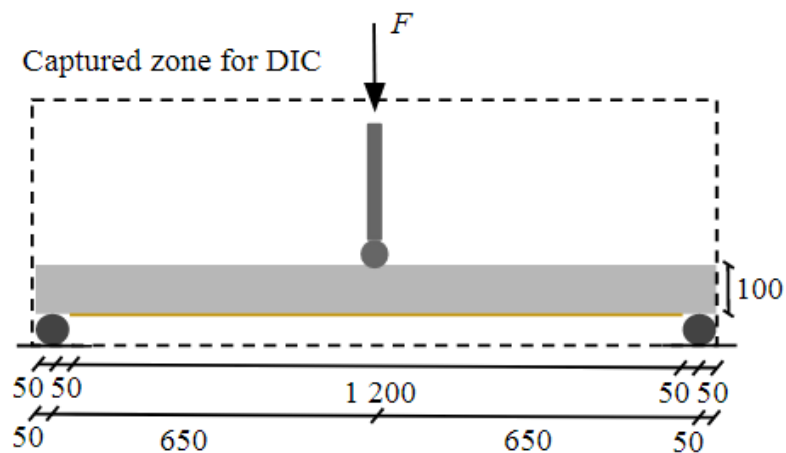

Figure 7.15   Illustration showing schematic figure of the test set-up and dimensions [mm] for static testing.

Figure 7.16   Photo of test set up with DIC equipment in the background.

After loading of 3 kN the force was unloaded and then reloaded again. This was done to eliminate possible imperfections and to make sure that the initial stiffness was captured correctly. Deformation speed was set to be the same for all static tests, which was 2 mm/min for the first 10 mm deflection and then it continued with 10 mm/min until rupture of

reinforcement was reached. However, the reinforcement didn't rupture for beam 14-B1-FRP3-S, instead the beam exeperinced some kind of shear crack and large plastic deformation. The test stopped when the machine reached its maximum deformation limit.

Beam 19-B1-FRP0-S was without FRP strengthening and only subjected to static loading. The reason for this test was to examine the support condition for the beam and to see if the response changes with a different set up for the supports. Instead of only using the roller supports, in this case square steel plates were placed on top of the roller supports. Beam 19-B1-FRP0-S then lay freely supported on top of them see Figure 7.17.

Figure 7.17   Illustration of test set up for support condition for beam 19-B1-FRP0-S.

7.9.2   Digital image correlation

Two cameras were used for the static testing. Both were placed in front of the middle of the beam, one slightly to the right hand side and the other slightly to the left hand side. This set up makes it possible to get a 3D view over the surface of the beam and to get more accurate results. The cameras covered the whole beam, including both supports. The distance between the front of the beam and the camera house was 1 350 mm. The frames were processed and analysed in GOM Correlate 2019.

8 Analytical and Numerical Predictions

In this section calculations for estimation of response of the beams for both static and dynamic loading cases are presented. The static predictions include calculations for the load capacity, cracking moment, load-deflection curves and the plastic rotation capacity. The dynamic predictions focus on the 2DOF calcualtions for displacement-time curve for the beam and the velocity-time curve for the drop weight. These predictions are compared with the experimental results in Chapter 10.

8.1 Static response

Static response of beams for the geometry illustrated in Figure 8.1 and Figure 8.2 are calculated based on Engström (2013), Engström (2015). Material parameters extracted from experimental results which are tabulated in Section 9.1 are used in prediction calculation. Load capacity in ultimate limit state and theoretical load vs. deformation are the presented responses for unstrengthen, 1 and 3 layers FRP strengthened beams for three point bending. Furthermore, plastic rotation capacity for refrence beam is also presented.

8.1.1 Load capacity

Load capacity in ultimate limit state is done for unstrengthened reference beams and FRP strengthened beams.

8.1.1.1 Load capacity for reference beam

For the determination of the load capacity in ULS it is assumed that ultimate compressive strain, ε_{cu} = 3.5 ‰, is reached and steel reinforcement is yielding. In addition, it is assumed that compressive zone follows idealized parabolic stress-strain relation and the strain distribution follows linear relationship, see Figure 8.1.
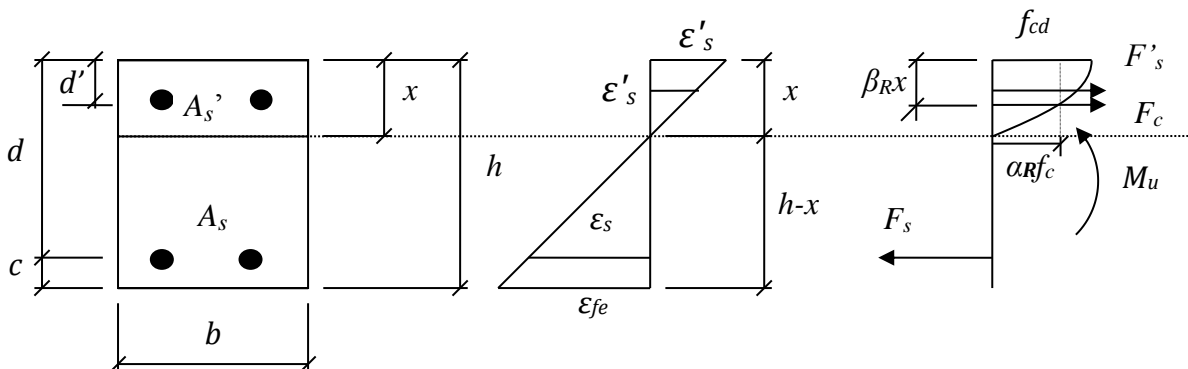

Figure 8.1   Assumed stress-strain relationship in ULS. Modified from Lozano and Makdesi (2017).

Assuming the neutral axis is located below the top reinforcement, the equilibrium conditions in ULS can be expressed as

$$\alpha_R \cdot f_{cd} \cdot b \cdot x + \sigma_s' \cdot A_s' = \sigma_s \cdot A_s \qquad (8.1)$$

where σ_s = stress in bottom reinforcement [Pa]

σ_s' = stress in top reinforcement [Pa]

A_s = area of bottom reinforcement [m²]

A_s' = area of top reinforcement [m²]

$\alpha_R \cdot f_{cd}$ = mean stress of concrete in compression [Pa]

However, the neutral axis was found to be located above the centre of gravity of the top reinforcement which means the top reinforcement is subjected to tensile reinforcement, which was also observed by Andersson and Pettersson (2019) for the same geometry of beams. Thus Equation (8.1) was modified as

$$\alpha_R \cdot f_{cd} \cdot b \cdot x = \sigma_s \cdot A_s + \sigma_s' \cdot A_s' \tag{8.2}$$

$$M_u = \alpha_R \cdot f_{cd} \cdot b \cdot x(d - \beta_R \cdot x) - \sigma_s' \cdot A_s'(d - d') \tag{8.3}$$

where the stress block resultant, α_R and location of stress block resultant, β_R are taken as

$$\alpha_R = 0.81 \tag{8.4}$$

$$\beta_R = 0.42 \tag{8.5}$$

The corresponding steel strains at ULS and yielding is checked as

$$\varepsilon_s = \frac{d - x}{x} \cdot \varepsilon_{cu} \tag{8.6}$$

$$\varepsilon_s' = \frac{d' - x}{x} \cdot \varepsilon_{cu} \tag{8.7}$$

where ε_s = strain in bottom reinforcement [-]

ε_s' = strain in top reinforcement [-]

ε_{cu} = ultimate strain in concrete [-]

The reinforcement stresses were determined from stress–strain relationships using a bilinear relation as

$$\sigma_s = \begin{cases} E_{sm} \cdot \varepsilon_s & if \ \varepsilon_s \leq \varepsilon_{sy} \\ f_{ym} + \dfrac{\varepsilon_s - \varepsilon_{sy}}{\varepsilon_{su} - \varepsilon_{sy}} \cdot (f_{tm} - f_{ym)} & if \ \varepsilon_s > \varepsilon_{sy} \end{cases} \tag{8.8}$$

where E_{sm} = modulus of elasticity of reinforcement [Pa]

f_{ym} = yielding stress in reinforcement [Pa]

f_{tm} = tensile stress in reinforcement [Pa]

ε_{sy} = yielding strain in reinforcement [-]

ε_{su} = ultimate strain in reinforcement [-]

The ultimate load is then calculated from the calculated ultimate moment as

$$F_u = \frac{4 \cdot M_u}{L} \tag{8.9}$$

The resulting ultimate load and moment capacity are presented in Table 8.1 for two cases. One is when the top reinforcement is neglected and considered it is subjected to compressive stress while the other is when top reinforcement is subjected to tensile stress as described previously in this section.

Table 8.1   Ultimate moment and load capacity of reference beams in ULS for different reinforcement cases using yield strength of reinforcement steel.

Reinforcement considered	M_u[kNm]	F_u [kN]
Only bottom reinforcement	2.5	7.6
Top and bottom reinforcement	2.6	8.1

8.1.1.2 Load capacity for FRP strengthened beams

To calculate the ultimate load capacity in ULS for FRP strengthened beams simplification is made by assuming there would be a perfect bond between FRP and concrete and between FRP layers, i.e, neglecting the effect of bond strength. The prediction was made by considering the assumptions and procedure stated in section 8.1.1.1 and section 5.4.3. It is assumed that in ultimate compressive strain, ε_{cu} = 3.5 ‰, is reached and steel reinforcement is yielding. In addition, it is assumed that compressive zone follows idealized parabolic stress strain relation and the strain distribution follows linear relationship, see Figure 8.2. The strain in FRP is limitted according to strain limit recomnded in Section 5.4.1 to avoid debonding.
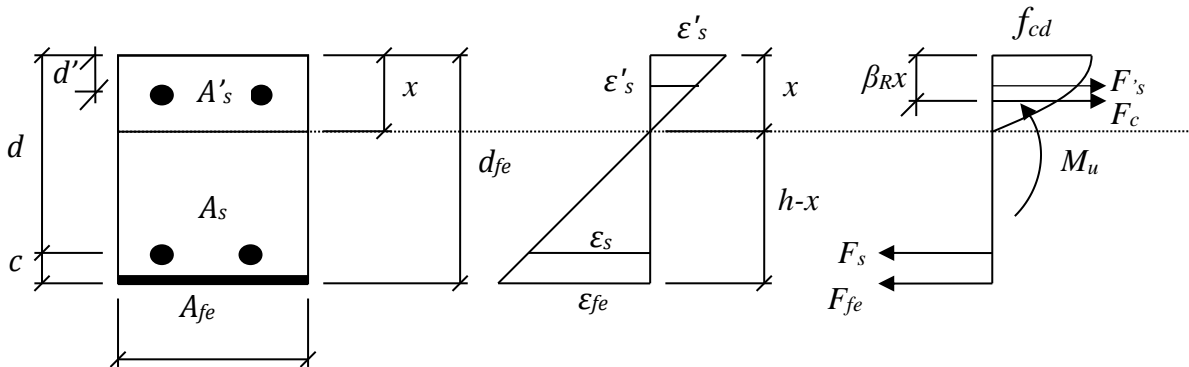

Figure 8.2   Assumed stress strain relationship in ULS for strengthened beams. Modified from Lozano and Makdesi (2017) and Huanga and Zhoua (2019).

For FRP strengthened beam assuming the top reinforcement will be in the compressive zone, the equilibrium conditions in ULS can be expressed as

$$\alpha_R \cdot f_{cd} \cdot b \cdot x + \sigma_s' \cdot A_s' = \sigma_s \cdot A_s + \sigma_{fe} \cdot A_{fe} \tag{8.10}$$

$$M_u = \alpha_R \cdot f_{cd} \cdot b \cdot x(x - \beta_R \cdot x) + A_s' \cdot E_{sm} \cdot \varepsilon_s' \cdot (x - d') + f_{yd} \cdot A_s \cdot (d - x) + + \varepsilon_{fe} \\ E_{fe} * A_{fe}(d_{fe} - x) \tag{8.11}$$

Where the stress block resultant, α_R and location of stress block resultant, β_R are taken as

$$\alpha_R = 0.8 \tag{8.12}$$

$$\beta_R = 0.4 \tag{8.13}$$

The corresponding steel strains at ULS and yielding is checked as

$$\varepsilon_s = \frac{d - x}{x} \cdot \varepsilon_{cu} \tag{8.14}$$

$$\varepsilon_s' = \frac{x - d'}{x} \cdot \varepsilon_{cu} \tag{8.15}$$

The strain at FRP is limitted as

$$\varepsilon_{fd} = 0.41 \cdot \sqrt{\frac{f_{cd}}{n \cdot E_{fe} \cdot t_f}} \leq \varepsilon_{fu} \tag{8.16}$$

where $\quad \varepsilon_{fu} =$ ultimate strain in FRP [-]

$\varepsilon_{fe} =$ strain in FRP [-]

$E_{fe} =$ modulus of elasticity of FRP [Pa]

$n =$ number of FRP layers

$t =$ tickness of FRP

The ultimate load is then calculated from the calculated ultimate moment as

$$F_u = \frac{4 \cdot M_u}{L} \tag{8.17}$$

The resulting ultimate load and moment capacity are presented in Table 8.2 for 1 layer and 3 layers of FRP strengthening.

Table 8.2   Ultimate moment and load capacity of reference beams in ULS for different reinforcement cases considering yield strength.

Reinforcement considered	M_u [kNm]	F_u [kN]
1 layer FRP	5.2	15.8
3 layers FRP	8.8	27.2

8.1.2   Cracking moment

The cracking moment is calculated from the mean flexural tensile concrete strength and moment of inertia in state I as

$$M_{cr} = \frac{f_{ct.fl} \cdot I_{Ife}}{h/2} \tag{8.18}$$

where $f_{ct.fl}$ = mean flexural tensile concrete strength [Pa]

I_{Ife} = moment of inertia in state I including FRP section [m⁴]

h = height of beam [m]

The resulting cracking force and cracking moment are presented in Table 8.3 for 1 layer and 3 layers of FRP strengthening.

Table 8.3   Moment and load at cracking for unstrengthened, 1 layer and 3 layers FRP strengthening beams.

Beam type	M_{cr} [kNm]	F_{cr} [kN]
Unstrengthened	0.89	2.7
1 layer FRP	0.91	2.8
3 layer FRP	0.94	2.9

8.1.3   Load-deflection curves

Load-deflection relations were done by creating stiffness until cracking and from cracking until reaching ultimate load for a trilinear response and by only considering stiffness in state II for a bilinear response. After reaching ultimate load the beam was assumed to be plastic. The stiffness is calculated from moment of inertia *I* as

$$K = \frac{48 \cdot E_{cm} \cdot I_I}{L^3} \tag{8.19}$$

Where *I* is replaced with I_I or I_{II} to calculate stiffness in state I and state II. The calculation for the stifness can be seen in Appendix O.

The stiffness between cracking and ultimate load was calculated as the ratio between the difference in ultimate load and cracking load and the difference of deflection for the corresponding loads.

The calculated stiffness and estimated response using bilinear and trilinear load-deflection curve are presented in Table 8.4 and Figure 8.3 to Figure 8.5.

Table 8.4   Estimated stiffness for different types of beams.

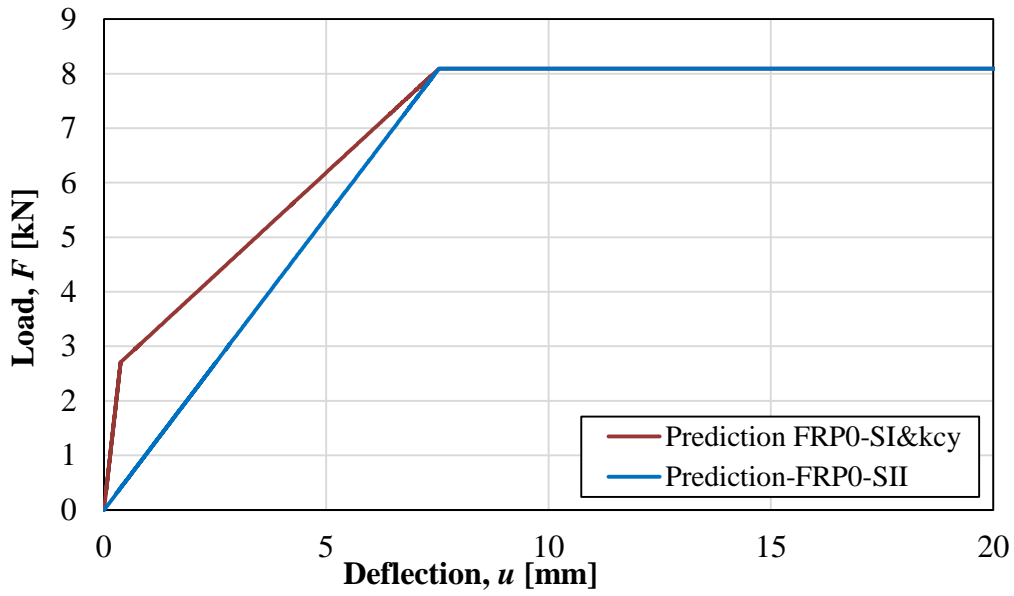| Beam type	k_I[MN/m]	k_{cy}[MN/m]	k_{II}[MN/m]
unstrengthened	6.68	0.75	1.07
1 layer FRP	6.80	1.19	1.39
3 layer FRP	7.06	1.82	1.98

Figure 8.3   Load-deflection curve for unstrengthened beams.
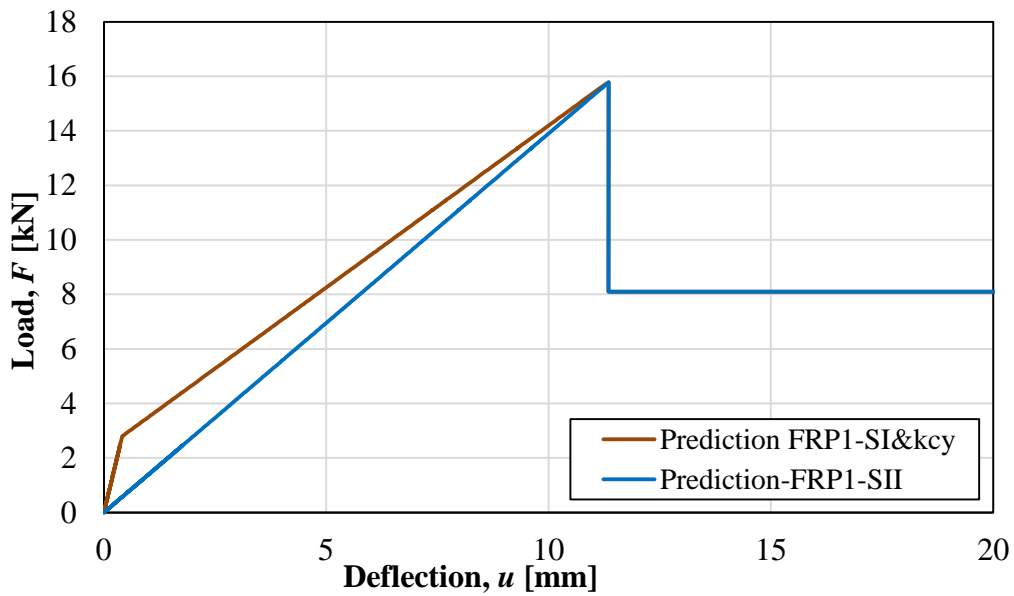

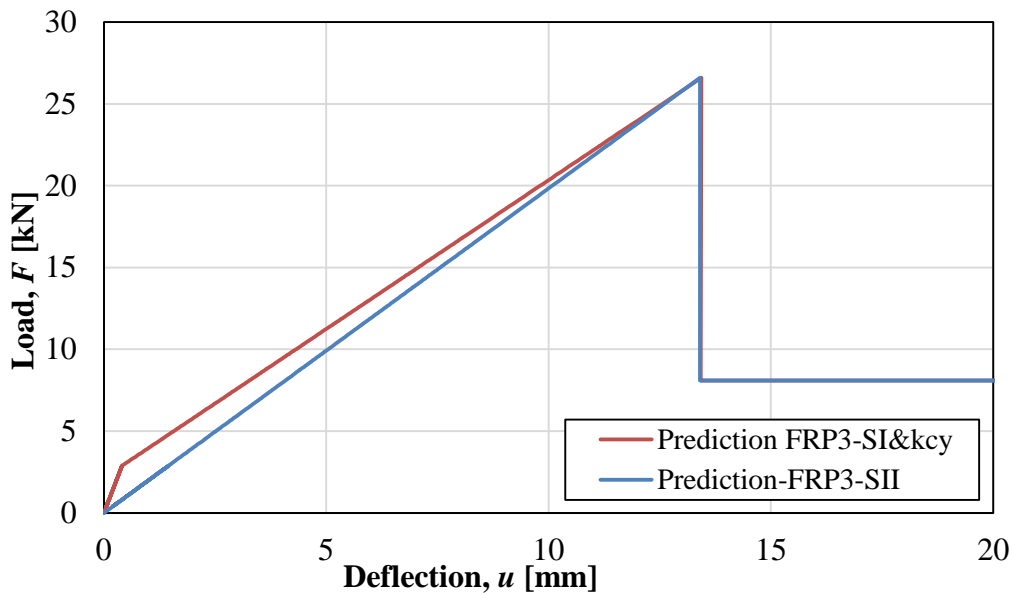*Figure 8.4   Load-deflection curve for 1 layer FRP strengthening.*

Figure 8.5   Load-deflection curve for 3 layers FRP strengthening.

8.1.4   Plastic rotation capacity

The prediction for rotation capacity is done using recommendations according to Eurocode 2 and Bk25 as stated in Section 4.3. However, the case of top reinforcement being in the compression zone is not fulfilled, the calculations are based disregarding the top reinforcement. The calculation is done in Mathcad prime 5 and presented in Appendix O.

8.1.4.1   Plastic rotation according to Eurocode 2

Plastic rotation is predicted in accordance with Section 4.3.1 and results are presented in Table 8.5.

Table 8.5   Predicted Plastic rotation capacity and plastic deformation according to Eurocode 2.

Beam type	θ_{pl} [rad]	u_{pl} [mm]
Unstrengthened	0.026	16.6

8.1.4.2   Plastic rotation according to BK25

Plastic rotation is predicted in accordance with Section 4.3.2 and results are presented in Table 8.6.

Table 8.6   Predicted plastic rotation capacity and plastic deformation according to BK25.

Beam type	θ_{pl} [rad]	u_{pl} [mm]
Unstrengthened	0.98	63.4

8.2 Dynamic response

Dynamic response of beams for the geometry illustrated in Figure 7.8, Figure 7.12 and Figure 7.14 are calculated based on Chapter 6 and equations presented in this chapter. Material parameters extracted from experimental results which are tabulated in Section 9.1 are used in prediction calculation. 2DOF predictions have been done for unstrengthened beams subjected to different drop heights to find deflection-time relation for the beam and velocity-time relation for the drop weight. The drop heights used in the calculations have been adjusted to the measured ones, i.e. 3.97 m, 3.44 m and 2.94 m, that are presented in Section 9.2. Additionally, calculations for initial shear velocities are included in this section.

8.2.1 2DOF predictions

The theories and equations the 2DOF predictions are based on are explained in Chapter 6 and the results are calculated in the software programme Matlab R2017b, based on a script created by Lozano and Makdesi (2017). The Matlab script is presented in Appendix N. The 2DOF predictions were only calculated for the reference beams. It would be of interest to do it for the FRP strengthened RC beams too but the force-deflection relation used to describe the structural response in the Matlab script was not suitable for this and therefore, a prediction was not made for the FRP strengthened beams.

8.2.1.1 Input data

The initial velocities at impact for the drop weight were calculated from the dynamic testing experiments and are the average value between time -2.0 ms and 0.0 ms, from the values seen in Figure 9.13 to Figure 9.15 in Section 9.2.3. The used velocities for the predictions for drop height 4 m, 3.5 m and 3 m and the initial velocities calculated from Equation (8.20) with the measured drop heights from the testing are presented in Table 8.7.

$$v_{0,calc.} = \sqrt{2 \cdot g \cdot h} \tag{8.20}$$

where $v_{0,calc.}$ = predicted initial velocity [m/s]

     g = gravitational metric system [kg·m·s^{-2}]

     h = measured drop height [m]

Table 8.7   Initial velocity of drop weight at impact depending on drop height measured from the experimental testing and the predicted values from before testing.

Drop height [m]	Initial velocity, v_0 [m/s]	Calculated initial velocity, $v_{0,calc.}$ [m/s]
4.0	8.5	8.8
3.5	8.0	8.2
3.0	7.4	7.6

Two different values for the internal resistance of the beam, R_2, were studied. The predicted value is calculated in Section 8.1.1.1 and the measured value is calculated based on the experimental results. This latter was done by finding the maximum deformation from the dynamic testing and use this in combination with the average force-deflection relation obtained in the static testing. The internal work were then analysed. To find an estimation of measured R_2 the maximum deformation from dynamic testing was used as maximum deformation capacity in the static results. Using the predicted state II stiffness of the beam and the same amount of internal work, generated by the average force-deflection relation in the static test, an equivalent load capacity could be determined that were used to represent the measured value of R_2 when using a simplified bi-linear relation, see Figure 8.6. Consequently, the average value for R_2 from the unstrengthened beams were used as the measured R_2 in following predictions. To get this result an estimation was made to use the average value from the three drop heights, from the results from dynamic testing, since the difference in deformation result in only small changes when comparing the internal work from the static tests.

The beam stiffness in state II, k_{II}, is calculated in Section 8.1.3 and is here denoted as k_2. The moment of inertia for the beam used in this section is calculated also for state II, I_{II}. These input data are presented in Table 8.8.
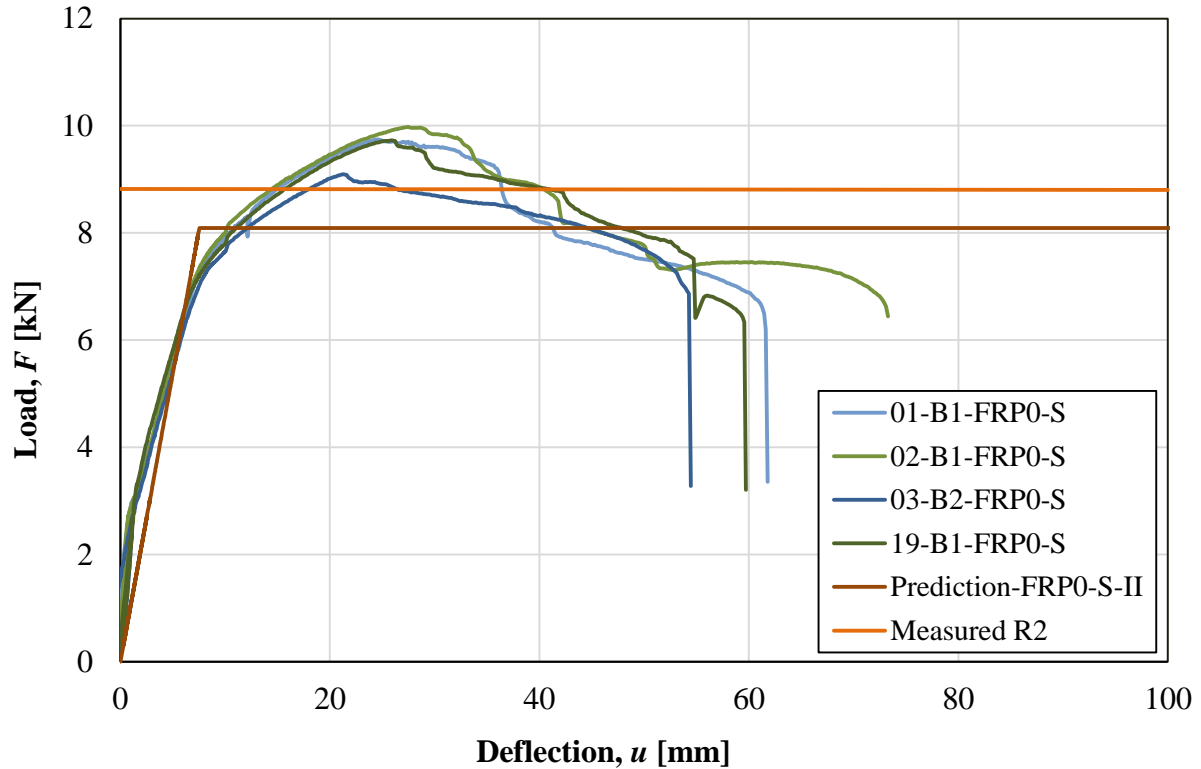
Figure 8.6   *Internal resistance of the beam, R_2, for the measured value is shown in the figure as a horizontal line, along with the experimental results from the static testing of unstrengthened beams subjected to static loading only, and the calculated bi-linear response for unstrengthen beams subjected to static loading which illustrate the predicted R_2 as the maximum load.*

Table 8.8   *Internal resistance, stiffness and moment of inertia for the beam.*

$R_{2,predicted}$ [kN]	$R_{2,measured}$ [kN]	k_2 [MN/m]	I_{II} [m^4]
8.10	8.80	1.07	$1.42 \cdot 10^{-6}$

The values for internal resistance of the drop weight, R_1, and stiffness of the spring between drop weight and the beam, k_1, are based on a study conducted by Andersson and Pettersson (2019). The stiffness of the spring is calculated in accordance to Hertz contact theory and R_1 is found through a convergence analysis. A constant, k_1, was calculated using Equation (8.21) and by using this constant, the impact force dependent on the deformation at the impact zone was found and illustrated as a graph with Equation (8.22), see Appendix M.

$$k_1 = \frac{4 \cdot \sqrt{r_1}}{3} \left[\frac{1 - v_1^2}{E_1} + \frac{1 - v_2^2}{E_2} \right]^{-1} \tag{8.21}$$

$$F_1 = k_1 \cdot \delta^{3/2} \tag{8.22}$$

where	F_1 = impact force [N]

k_1 = constant [-]

δ = deformation at impact zone [m]

r_1 = radius of the rounded tip of the drop weight [m]

v_1 = Poisson's ratio for the drop weight [-]

v_2 = Poisson's ratio for the beam [-]

E_1 = modulus of elasticity for the drop weight (steel) [Pa]

E_2 = modulus of elasticity for the beam (concrete) [Pa]

From the graph of the impact force, the value for R_1 was read and a secant was calculated and from that stiffness k_1 was found. A convergence analysis, see Appendix L, made it possible to find the most appropriate graph and the chosen values for R_1 and k_1 are presented in Table 8.9.

*Table 8.9	Internal resistance of the drop weight and stiffness of the spring between drop weight and beam.*

R_1 [kN]	k_1 [MN/m]
50	258

8.2.1.2   Result

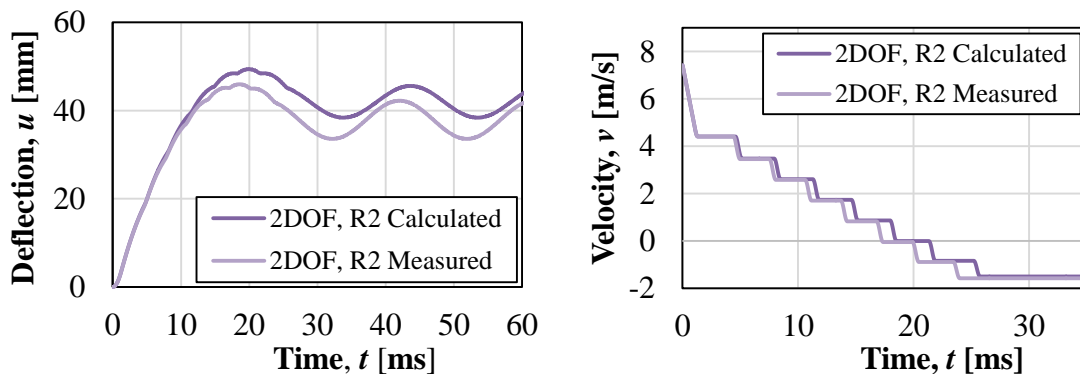The results of the 2DOF predictions are presented in Figure 8.7 to Figure 8.9.
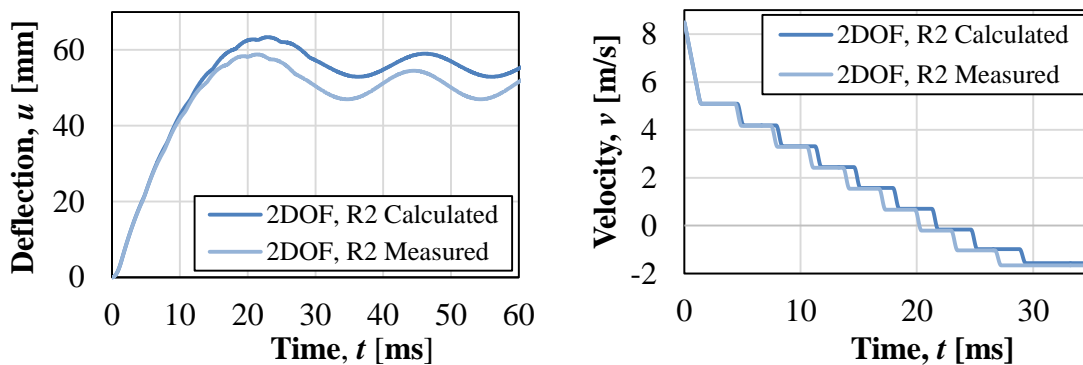
*Figure 8.7	Illustration of the deflection-time relation for the beam and velocity-time relation for the drop weight. Results are illustrated for beams subjected to 4 m drop weight impact and using the calculated internal resistance of the beam and the measured internal resistance of the beam.*
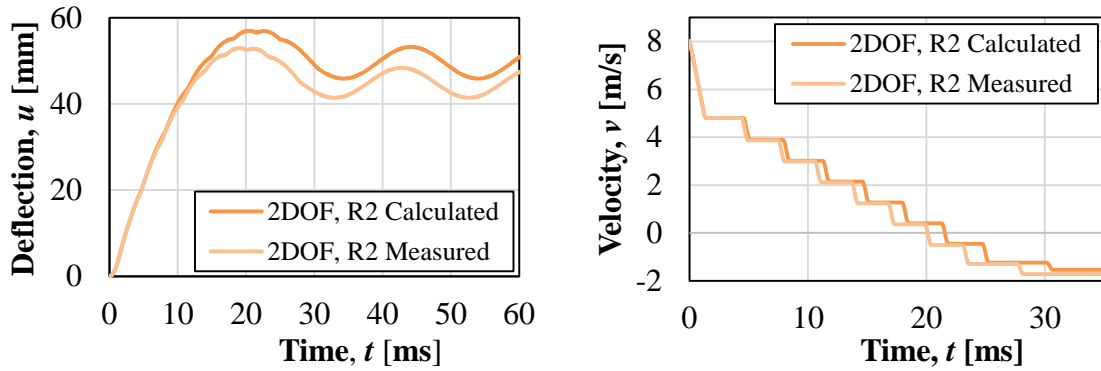
Figure 8.8   *Illustration of the deflection-time relation for the beam and velocity-time relation for the drop weight. Results are illustrated for beams subjected to 3.5 m drop weight impact and using the calculated internal resistance of the beam and the measured internal resistance of the beam.*

Figure 8.9   *Illustration of the deflection-time relation for the beam and velocity-time relation for the drop weight. Results are illustrated for beams subjected to 3 m drop weight impact and using the calculated internal resistance of the beam and the measured internal resistance of the beam.*

8.2.1.3 Comparison

For the deflection-time relationship of the beam it shows for all drop heights that the calculated internal resistance of the beam, R_2, results in higher deflections compared with the measured value. Time for maximum deflection is also shifted and occur later for the calculated R_2. The decrease in drop height result with decrease in deflection. The shape in all cases are similar, first the maximum deflection is reached and then the deflection oscillate uniformly with a lower maximum value of the curve.

The velocity-time relationship for the drop weight also result in higher values with the calculated internal resistance of the beam, with similar difference for all drop heights. The difference between the drop heights are slightly smaller maximum values when the drop height decrease. The curve also reaches its constant final value for the velocity faster with decreasing drop height.

8.2.2 Initial shear velocity

Shear wave propagation for dynamically loaded structures can be explained in an active and inactive portion of the beam, of where it takes time, t_0, for the active part to span the whole beam (Yi et al., 2016), see Figure 8.10.

Inactive | Active | Inactive

Figure 8.10   Illustration of the active and inactive part of a beam subjected to drop weight impact (Jönsson and Stenseke, 2018).

Time t_0 can be calculated as

$$t_0 = \frac{L_0}{2 \cdot v_s} \tag{8.23}$$

where L_0 = span of the beam [m]

   v_s = velocity for stress waves in the concrete [m/s]

Shear velocity can be calculated as follow

$$v_s = \sqrt{\frac{G}{\rho}} \tag{8.24}$$

where G = shear modulus [Pa]

   ρ = density of concrete [kg/m³]

Shear modulus is calculated as

$$G = \frac{E}{2 \cdot (1 + v)} \tag{8.25}$$

where E = modulus of elasticity [Pa]

   v = Poisson's ratio [-]

Table 8.10   Calculation of impact propagation time for the active part of the beam to span the whole beam for unstrengthen RC beams.

L_0 [m]	$\rho_{concrete}$ [kg/m³]	E [GPa]	v [-]	G [GPa]	v_s [m/s]	t_0 [ms]
1.3	2 432	34.7	0.2	14.5	2 438	0.27

Input used for the calculation of the time that it takes for the active portion to span the whole beam can be seen in Table 8.10 and also the final result which is 0.27 ms.

9 Experimental Results

This chapter presents results gained from the material tests, dynamic tests, and static tests together with comparison of structural response among different loading conditions and beam types giving emphasis on how FRP strengthening affects the response for different parameters of interest.

9.1 Material testing

The material tests are done for hardened concrete strength and reinforcement strength parameters as described in Section 7.6 and Section 7.7.

9.1.1 Concrete material tests

Mean cylindrical compressive strength, mean tensile strength from splitting tests, density, fracture energy and modulus of elasticity are determined from the tests in accordance with Section 6.7 and Section 2.2.1. Summarized material properties are presented in Table 9.1 to Table 9.3, and a detailed result is shown in Appendix A. The specimen has been numbered one to three, depending on test order and they are also named depending on batch specimen with B1 and B2. These are the material parameters that are used in calculations, except for the mean splitting tensile strength, $f_{ctm,sp}$, since it's much higher capacities when compared with calculated tensile strength according to Eurocode 2. A minor scatter is seen in results from both batches for both compressive and tensile tests.

Table 9.1   Material properties of hardened concrete from compressive test results at the age of 26 day.

Batch	Specimen ID	Cylindrical compressive strength f_{cm} [MPa]	Density ρ [kg/m³]	Modulus of elasticity E_{cm} [GPa]
1	B1_1	45.5	2 399	34.6
	B1_2	45.7	2 449	34.7
	B1_3	45.8	2 408	34.7
2	B2_1	46.9	2 448	35.9
	B2_2	43.4	2 435	34.1
	B2_3	45.9	2 453	34.7
Average		**45.5**	**2 432**	**34.7**

Table 9.2   Tensile strength of hardened concrete from splitting test at the age of 26 days.

Batch	Specimen ID	Mean splitting tensile strength $f_{fctm,sp}$ [MPa]
1	B1_1	6.3
	B1_2	5.9
	B1_3	5.9
2	B2_1	5.7
	B2_2	5.7
	B2_3	5.9
Average		**5.9**

Table 9.3   Fracture energy of hardened concrete from wedge splitting test at the age of 28 days.

Specimen ID	G_F [Nm/m^2]
1	63.2
2	58.4
3	57.8
Average	**59.8**

9.1.2   Reinforcement

Proof stress, ultimate stress, ultimate strain, modulus of elasticity and the ratio between ultimate stress and proof stress are determined from the tests in accordance with Section 7.7. The average values for the reinforcement were then calculated and are being used in calculations. Material properties are presented in Table 9.4 and a stress-strain graph is illustrated in Appendix B. The specimen have been numbered from one to six, depending on test order. A minor scatter is seen in results for the reinforcement, though they can be assumed to be reasonable since there could be local imperfections.

Table 9.4   Material parameters of reinforcement from test results.

Specimen ID	$f_{0.2}$ [MPa]	f_u [MPa]	ε_{su} [‰]	E_s [GPa]	$f_u/f_{0.2}$ [-]
1	540	658	85	201	1.22
2	548	662	85	193	1.21
3	548	671	92	204	1.22
4	544	654	84	183	1.20
5	537	656	87	208	1.22
6	542	661	90	186	1.22
Average	**543**	**660**	**87**	**196**	**1.22**

9.2 Dynamic testing

In this section experimental results from drop weight impact tests are presented. Images from the high speed cameras are analysed in GOM Correlate 2019. As it is stated in Section 7.8.2, two cameras were used during the tests, camera 1 and camera 2, the results presented here are analysed from images of camera 2 mainly. However, a comparison of velocities for footages of both cameras is performed in order to get an overview of the accuracy of the results.

Drop height of 4 m, 3.5 m and 3 m was not maintained due to measurement errors of 30 mm to 60 mm which has resulted in a slight variation of results compared with the initial predicted velocities. Hence, it has to be noted that 4 m, 3.5 m and 3 m drop heights stand for 3.97 m, 3.44 m and 2.94 m respectively, in reality.

The results that will be discussed in this chapter include the deformation over time, applied force and impulse, deformed shape of the beams, initial velocity, and the strain field.

9.2.1 Midpoint deflection over time

To determine the deflection-time relationship for the beams, surface points were created at the mid span and support of each beam. Then the resulting deformation for each point was extracted and relative midpoint deflection was taken as the difference between the midpoint and support deflection.

In the deflection-time chart in between around 3 ms and 5 ms, depending on the type of FRP strengthening used, disturbances which arise from the lifting up and returning back of the beam from the support are encountered. These were also observed in a previous project by Andersson and Pettersson (2019).

The deflection-time relationship for beams with different amount of FRP strengthening and different drop height is presented in this section. In addition, how the FRP strengthening has affected the maximum deformation is also discussed and presented by making comparisons between the reference beams and FRP strengthened beams for the same drop height of impact.

9.2.1.1 Beams with same amount of FRP strengthening

In this section, beams with the same amount of FRP strengthening, i.e. groups of unstrengthened, 1 layer and 3 layers FRP strengthened beams, subjected to drop weight impact of 4 m, 3.5 m and 3 m are presented. Initial velocity, maximum deflection and plastic deformation are also presented in the same manner.

Midpoint deflection for the first 60 ms after impact for reference beams subjected to drop weight impact of 4 m, 3.5 m and 3 m are presented in Figure 9.1. Maximum deflection, plastic deformation and initial velocity for reference beams subjected to drop weight impact of 4 m, 3.5 m and 3 m are also presented in Table 9.5.
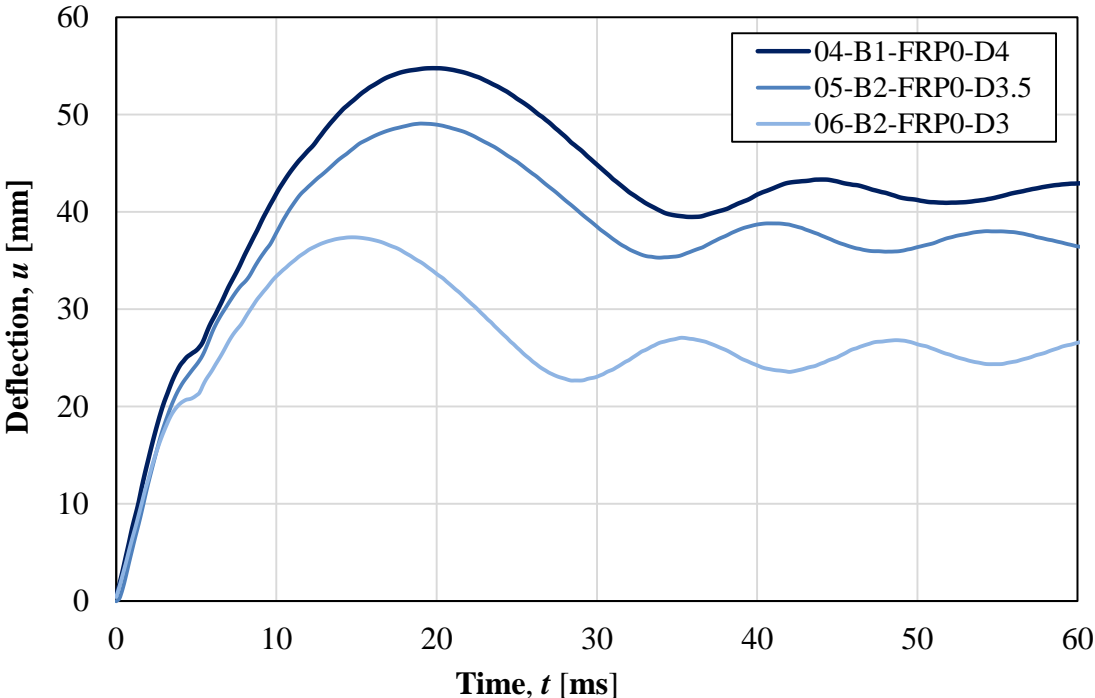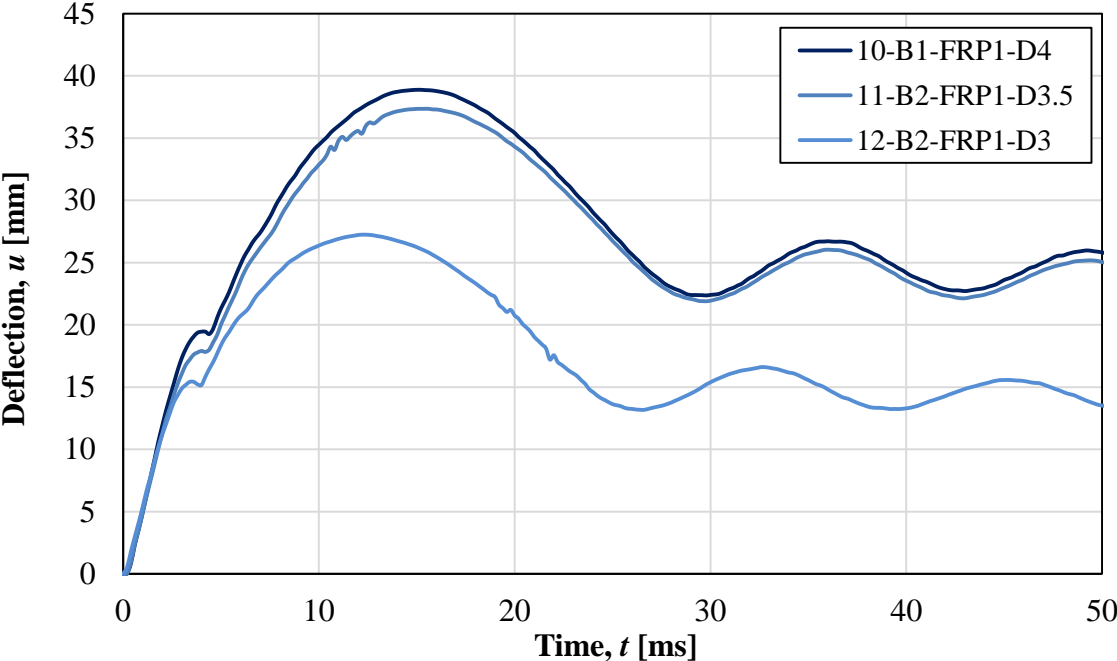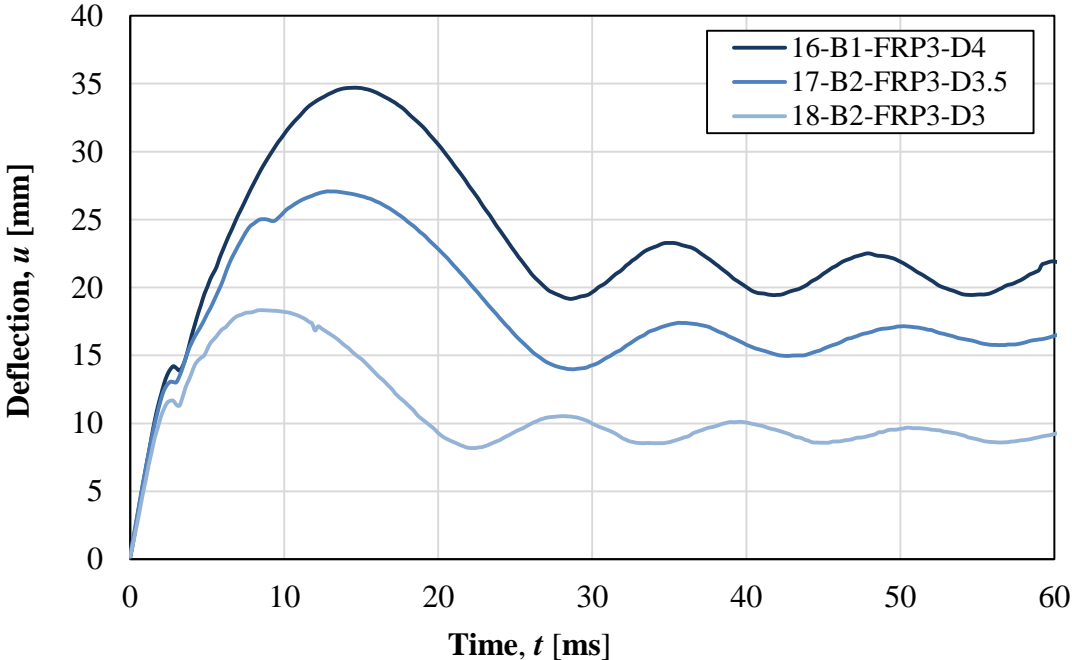

Figure 9.1   Midpoint deflection for reference beams subjected to 4 m, 3.5 m and 3 m drop weight impact.

Table 9.5   Maximum deflection, plastic deformation and initial velocity of reference beams subjected to drop weight impact of 4 m, 3.5 m and 3 m.

Beam	Number of FRP layers	Drop height [m]	u_{max} [mm]	u_{pl} [mm]	v_o [m/s]
04-B1-FRP0-D4	-	4.0	54.8	42.9	8.5
05-B2-FRP0-D3.5	-	3.5	49.1	38.2	7.9
06-B2-FRP0-D3	-	3.0	37.4	24.7	7.5

Midpoint deflection for the first 50 ms after impact for 1 layer FRP strengthened beams subjected to drop weight impact of 4 m, 3.5 m and 3 m are presented in Figure 9.2.

Figure 9.2   Midpoint deflection for 1 layer FRP strengthened beams subjected to 4 m, 3.5 m and 3 m drop weight impact.

Maximum deflection, plastic deformation, and initial velocity for 1 layer FRP strengthened beams subjected to drop weight impact of 4 m, 3.5 m and 3 m are presented in Table 9.6.

Table 9.6   Maximum deflection, plastic deformation, and initial velocity for 1 layer FRP strengthened beams subjected to drop weight impact of 4 m, 3.5 m and 3 m.

Beam	Number of FRP layers	Drop height [m]	u_{max} [mm]	u_{pl} [mm]	v_o [m/s]
10-B1-FRP1-D4	1	4.0	38.9	25.1	8.6
11-B2-FRP1-D3.5	1	3.5	37.4	24.4	8.1
12-B2-FRP1-D3	1	3.0	27.2	15.1	7.5

Midpoint deflection for the first 60 ms after impact for 3 layers FRP strengthened beams subjected to drop weight impact of 4 m, 3.5 m and 3 m height are presented in Figure 9.3.

Figure 9.3   *Midpoint deflection for 3 layers FRP strengthened beams subjected to 4 m, 3.5 m and 3 m drop weight impact.*

Maximum deflection, plastic deformation, and initial velocity for 3 layers FRP strengthened beams subjected to drop weight impact of 4 m, 3.5 m and 3 m are presented in Table 9.7.

Table 9.7   *Maximum deflection, plastic deformation, and initial velocity for 3 layers FRP strengthened beams subjected to drop weight impact of 4 m, 3.5 m and 3 m.*

Beam	Number of FRP layer	Drop height [m]	u_{max} [mm]	u_{pl} [mm]	v_o [m/s]
16-B1-FRP3-D4	3	4.0	34.7	21.9	8.4
17-B2-FRP3-D3.5	3	3.5	27.1	16.2	8.1
18-B2-FRP3-D3	3	3.0	18.3	9.9	7.4

9.2.1.2 Beams with different amount of FRP strengthening

Midpoint deflection for the first 50 ms after impact for unstrengthened reference beams, 1 layer and 3 layers FRP strengthened beams subjected to 4 m drop weight impact is presented in Figure 9.4.
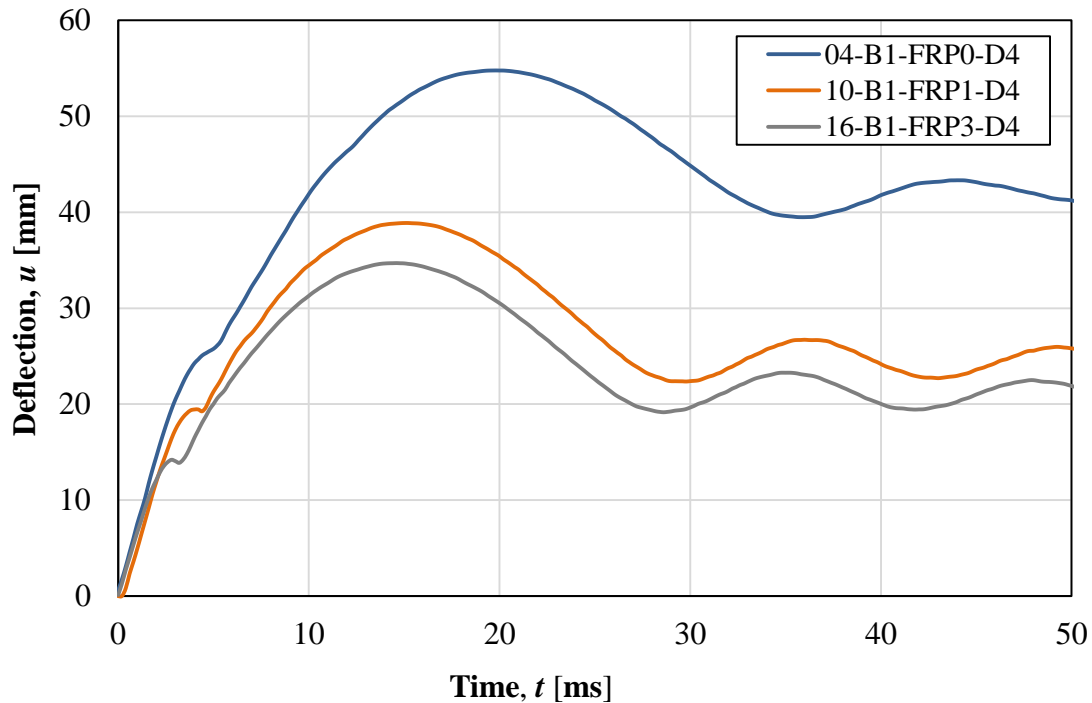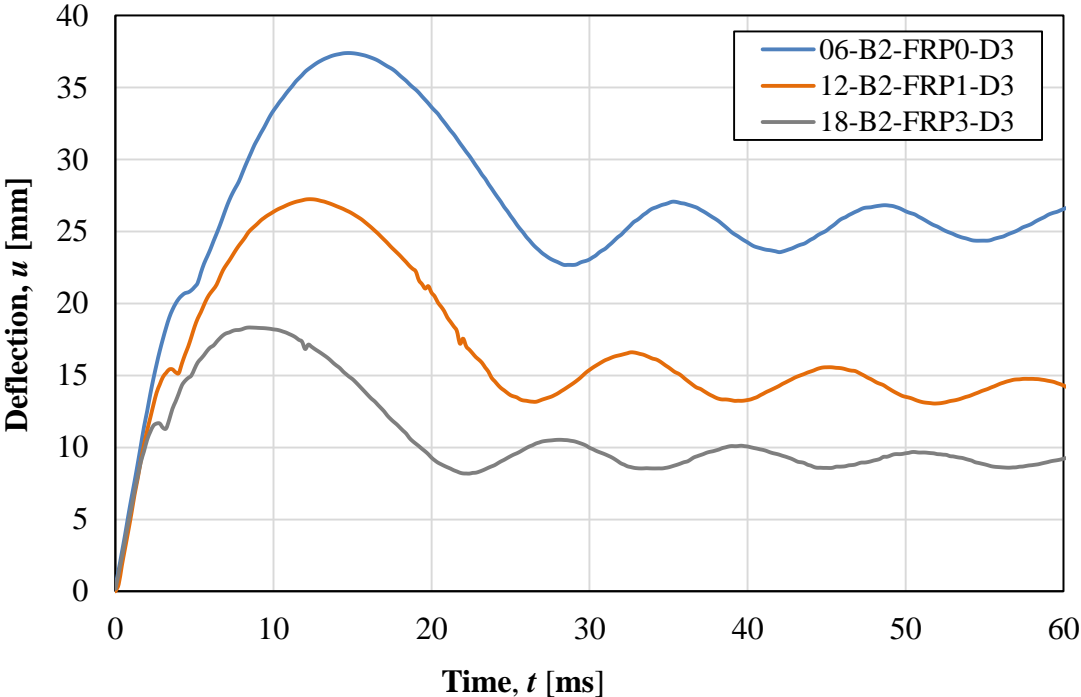

Figure 9.4   Midpoint deflection for reference beam, 1 layer and 3 layers FRP strengthened beams subjected to 4 m drop weight impact.

Maximum deflection, plastic deformation, and initial velocity for reference beams, beams strengthened with 1 layer FRP and 3 layers FRP subjected to drop weight impact of 4 m are presented in Table 9.8.

Table 9.8   Maximum deflection, plastic deformation, and initial velocity for unstrengthened, 1 layer and 3 layers FRP strengthened beams subjected to drop weight impact of 4 m height.

Beam	Number of FRP layers	Drop height [m]	u_{max} [mm]	u_{pl} [mm]	v_o [m/s]
04-B1-FRP0-D4	-	4.0	55	42	8.5
10-B1-FRP1-D4	1	4.0	39	25	8.6
16-B1-FRP3-D4	3	4.0	35	22	8.4

Midpoint deflection for the first 60 ms after impact for reference beams, beams strengthened with 1 layer and 3 layers of FRP subjected to drop weight impact of 3.5 m is presented in Figure 9.5.
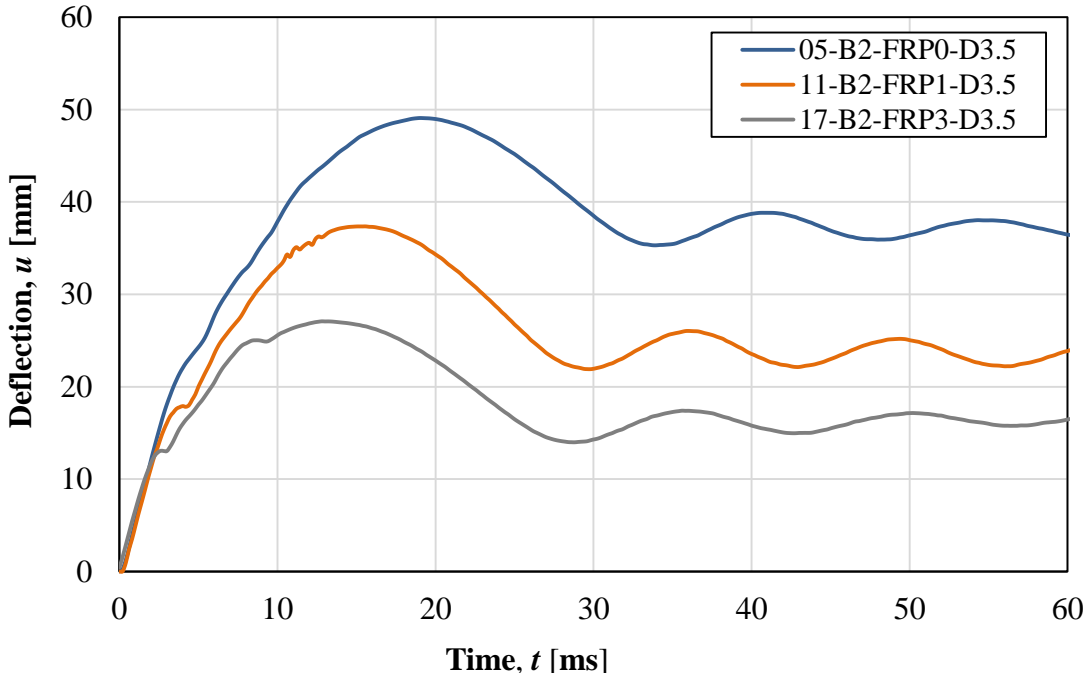
Figure 9.5   *Midpoint deflection for reference beam, 1 layer and 3 layers FRP strengthened beams subjected to 3.5 m height drop weight impact.*

Maximum deflection, plastic deformation, and initial velocity for reference beams, beams strengthened with 1 layer and 3 layers of FRP subjected to drop weight impact of 3.5 m are presented in Table 9.9.

Table 9.9   *Maximum deflection, plastic deformation, and initial velocity for unstrengthened, 1 layer and 3 layers FRP strengthened beams subjected to drop weight impact of 3.5 m height.*

Beam	Number of FRP layers	Drop height [m]	u_{max} [mm]	u_{pl} [mm]	v_o [m/s]
05-B2-FRP0-D3.5	-	3.5	49	38	7.9
11-B2-FRP1-D3.5	1	3.5	37	24	8.1
17-B2-FRP3-D3.5	3	3.5	27	15	8.1

Midpoint deflection for the first 60 ms after impact for reference beams with no FRP, beams strengthened with 1 layer and 3 layers of FRP subjected to drop weight impact of 3 m height is presented in Figure 9.6.

Figure 9.6   Midpoint deflection for unstrengthened, 1 layer and 3 layers FRP strengthened beams subjected to 3 m drop weight impact.

Maximum deflection, plastic deformation, and initial velocity for unstrengthened, 1 layer and 3 layers of FRP strengthened beams subjected to drop weight impact of 3 m height are presented in Table 9.10.

Table 9.10   Maximum deflection, plastic deformation, and initial velocity for unstrengthened, 1 layer and 3 layers FRP strengthened beams subjected to drop weight impact of 3 m.

Beam	Number of FRP layers	Drop height [m]	u_{max} [mm]	u_{pl} [mm]	v_o [m/s]
06-B2-FRP0-D3	-	3.0	37	25	7.4
12-B2-FRP1-D3	1	3.0	27	15	7.5
18-B2-FRP3-D3	3	3.0	18	10	7.4

9.2.1.3   Comparison of maximum deflection and plastic deformation

From the test results it is observed that midpoint deflection and plastic deformation have decreased as the layers of FRP strengthening increases. Decrease of maximum deflection and plastic deformation is presented by comparing the deflection of unstrengthened reference beams with 1 layer and 3 layers FRP strengthened beams subjected to the same height of drop weight impact. This is tabulated in Table 9.11 to Table 9.13.

Table 9.11   Comparison of maximum deflection and plastic deformation for beams with different amount of FRP strengthening vs. unstrengthened beam subjected to 4 m drop weight impact.

Beam	Number of FRP layer	u_{max} [mm]	u_{pl} [mm]	Decrease of u_{max} [%]	Decrease of u_{pl} [%]
04-B1-FRP0-D4	-	54.8	42.4		
10-B1-FRP1-D4	1	38.9	25.1	29	41
16-B1-FRP3-D4	3	34.7	21.9	37	48

Table 9.12   Comparison of maximum deflection and plastic deformation for beams with different amount of FRP strengthening vs. unstrengthened beam subjected to 3.5 m drop weight impact.

Beam	Number of FRP layer	u_{max} [mm]	u_{pl} [mm]	Decrease of u_{max} [%]	Decrease of u_{pl} [%]
05-B2-FRP0-D3.5	-	49.1	38.2		
11-B2-FRP1-D3.5	1	37.4	24.4	24	36
17-B2-FRP3-D3.5	3	27.1	15.1	45	61

Table 9.13   Comparison of maximum deflection and plastic deformation for beams with different amount of FRP strengthening vs. unstrengthened beam subjected to 3 m drop weight impact.

Beam	Number of FRP layer	u_{max} [mm]	u_{pl} [mm]	Decrease of u_{max} [%]	Decrease of u_{pl} [%]
06-B2-FRP0-D3	-	37.4	24.7		
12-B2-FRP1-D3	1	27.2	15.1	27	39
18-B2-FRP3-D3	3	18.3	9.9	51	60

9.2.2   Maximum force and impulse

To extract acceleration and velocity of drop weight first a surface area over the middle of the drop weight was created by taking a smaller section in GOM Correlate. Arithmetic mean acceleration and velocity for that surface was computed and used in the calculations.

Force was then computed from mean acceleration. The impulse was calculated as the integral of peak force over time under the force-time curve by taking a section where the maximum force had registered.

For force-time diagrams an adjustment was made by making the maximum force registered at time 0.0 ms in order to make the comparison between beams visible. Since the time steps that were used here are relatively large some data points might not have been registered by the DIC camera. Therefore, it has to be kept in mind that the maximum values extracted using this method are not the exact maximum values; rather they are just approximate results. This was also observed by Andersson and Pettersson (2019). This effect is more noticeable for results of the impulse.

9.2.2.1 Beams with same amount of FRP strengthening

In this section, impact force over time for the same group of beams, i.e. unstrengthened, 1 layer and 3 layers FRP strengthened beams subjected to different height of drop weight impact are presented individually for each group.

Maximum force of drop weight and impulse under the peak force calculated as stated in Section 3.1 are presented in Table 9.14 to Table 9.16 for unstrengthened, 1 layer and 3 layers FRP strengthened beams subjected to different drop weight impact heights respectively.

Applied force vs. time relationship for unstrengthened beams subjected to drop weight impact of 4 m, 3.5 m and 3 m drop height is presented in Figure 9.7.
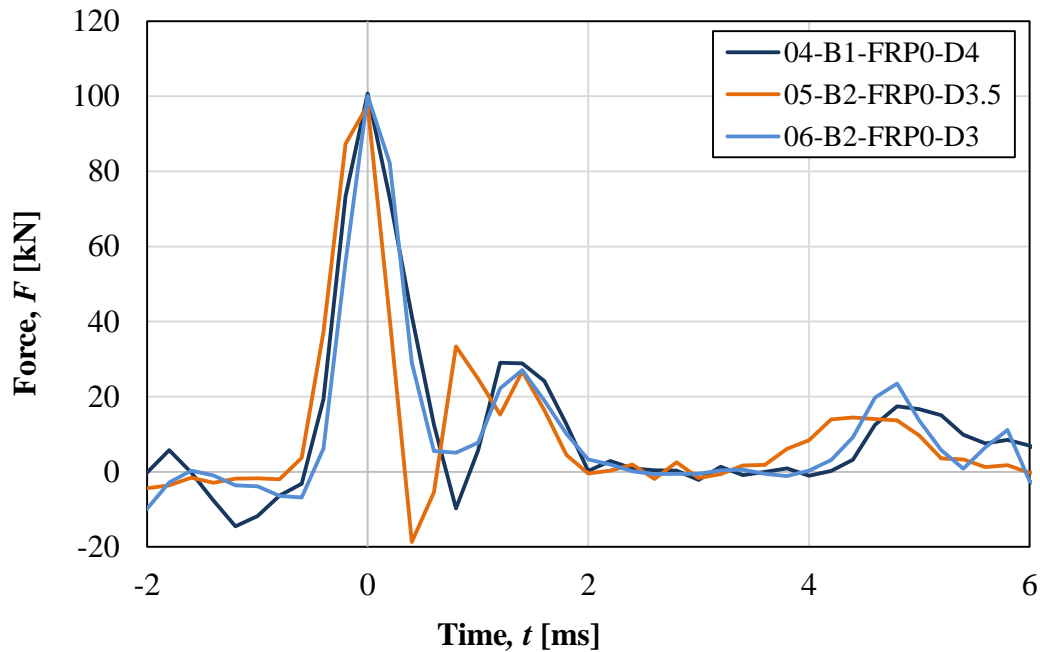
Figure 9.7   *Applied force for reference beams subjected to drop weight impact of 4 m, 3.5 m and 3 m drop height.*

Table 9.14   *Maximum applied force and impulse for reference beams subjected to drop weight impact of 4 m, 3.5 m and 3 m height.*

Beam	Drop height [m]	F_{max} [kN]	Impulse [Ns]
04-B1-FRP0-D4	4.0	101	62
05-B2-FRP0-D3.5	3.5	98	51
06-B2-FRP0-D3	3.0	100	53

Applied force vs. time relationship for 1 layer FRP strengthened beams subjected to drop weight impact of 4 m, 3.5 m and 3 m drop height is presented in Figure 9.8.
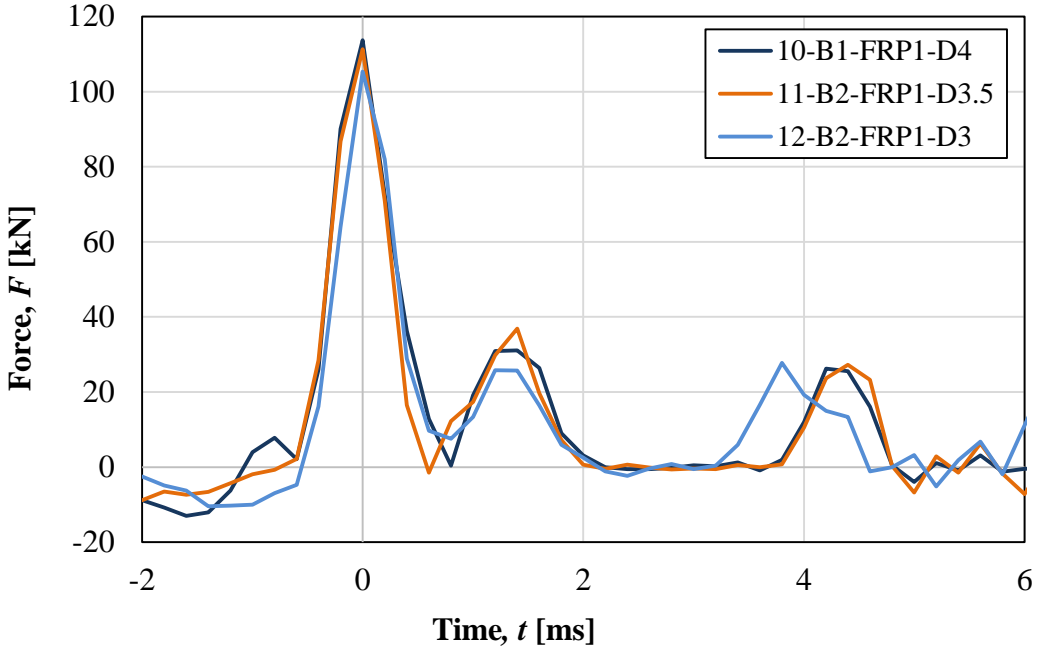
Figure 9.8   Applied force for 1 layer FRP strengthened beams subjected to drop weight impact of 4 m, 3.5 m and 3 m drop height.

Table 9.15   Maximum applied force and impulse for 1 layer FRP strengthened beams subjected to drop weight impact of 4 m, 3.5 m and 3 m drop height.

Beam	Drop height [m]	F_{max} [kN]	Impulse [Ns]
10-B1-FRP1-D4	4.0	114	73
11-B2-FRP1-D3.5	3.5	111	61
12-B2-FRP1-D3	3.0	105	59

Applied force for 3 layers FRP strengthened beams subjected to drop weight impact of 4 m, 3.5 m and 3 m drop height are presented in Figure 9.7.
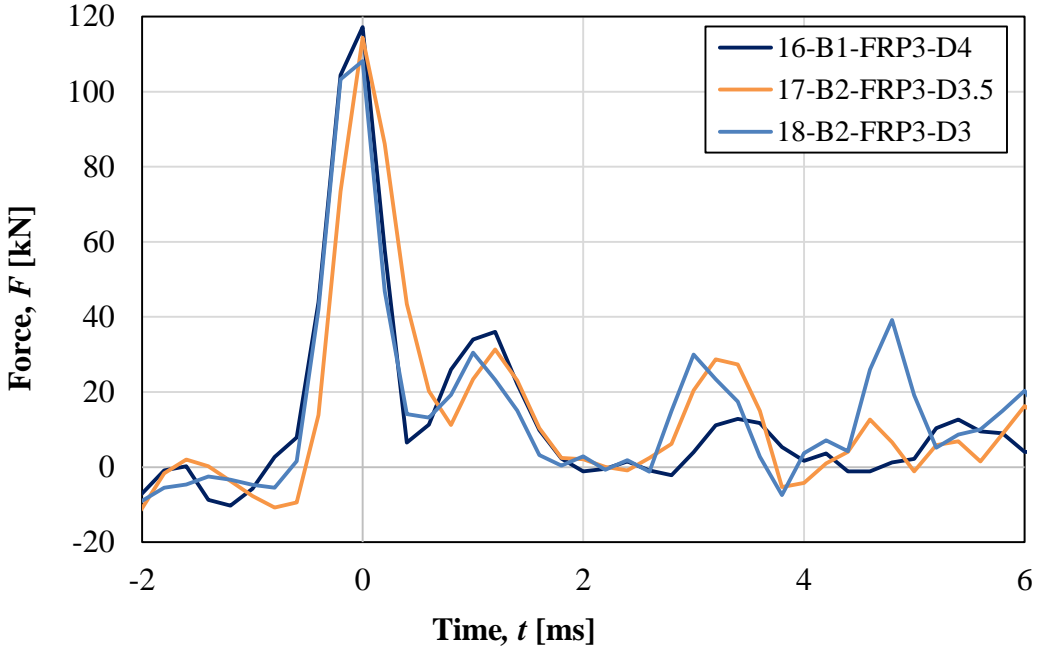
Figure 9.9   *Applied force for 3 layers FRP strengthened beams subjected to drop weight impact of 4 m, 3.5 m and 3 m drop height.*

Table 9.16   *Maximum applied force and impulse for 3 layers FRP strengthened beams subjected to drop weight impact of 4 m, 3.5 m and 3 m drop height.*

Beam	Drop height [m]	F_{max} [kN]	Impulse [Ns]
16-B1-FRP3-D4	4.0	117	73
17-B2-FRP3-D3.5	3.5	114	65
18-B2-FRP3-D3	3.0	108	57

9.2.2.2 Beams with different FRP strengthening subjected to same drop height impact

In this section, impact force over time for beams with different FRP strengthening, i.e. unstrengthened, 1 layer and 3 layers FRP strengthened beams subjected to the same height of drop weight impact are presented.

Applied force for unstrengthened, 1 layer and 3 layers FRP strengthened beams subjected to 4 m drop weight impact are presented in Figure 9.7. Maximum force and impulse for the same beams are also presented in Table 9.17.
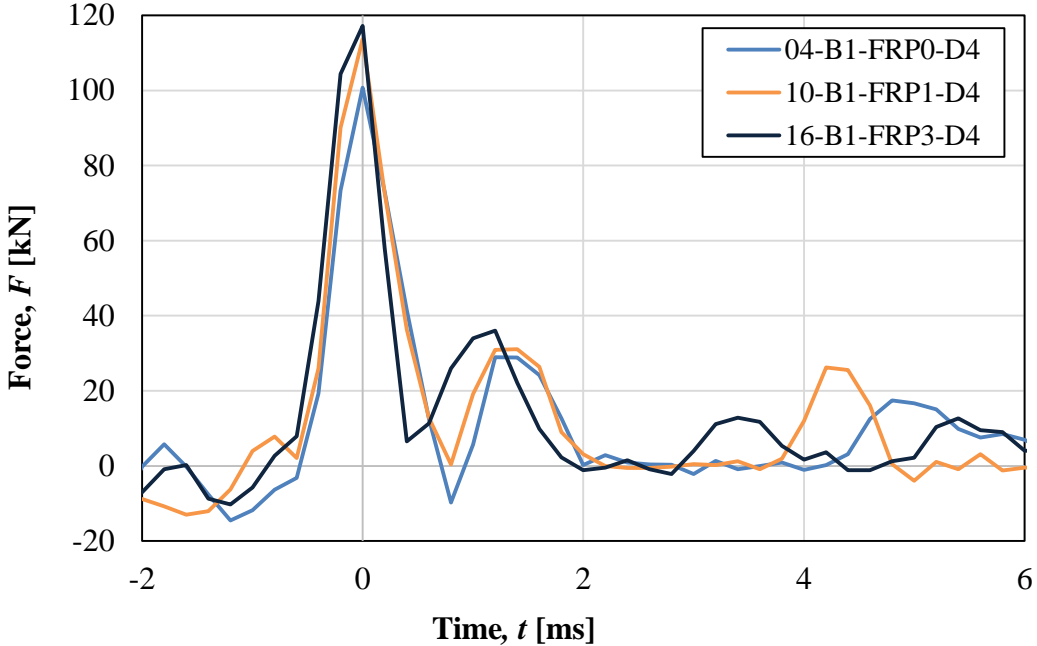
Figure 9.10   Applied force for unstrengthened, 1 layer and 3 layers FRP strengthened beams subjected to 4 m drop weight impact.

Table 9.17   Maximum applied force and impulse for unstrengthened, 1 layer and 3 layers FRP strengthened beams subjected to 4 m drop weight impact.

Beam	Number of FRP layer	F_{max} [kN]	Impulse [Ns]
04-B1-FRP0-D4	-	101	62
10-B1-FRP1-D4	1.0	114	73
16-B1-FRP3-D4	3.0	117	69

Applied force for unstrengthened, 1 layer and 3 layers FRP strengthened beams subjected to 3.5 m drop weight impact are presented in Figure 9.11. Maximum force and impulse for the same beams subjected to drop weight impact of 3.5 m are also presented in Table 9.18.
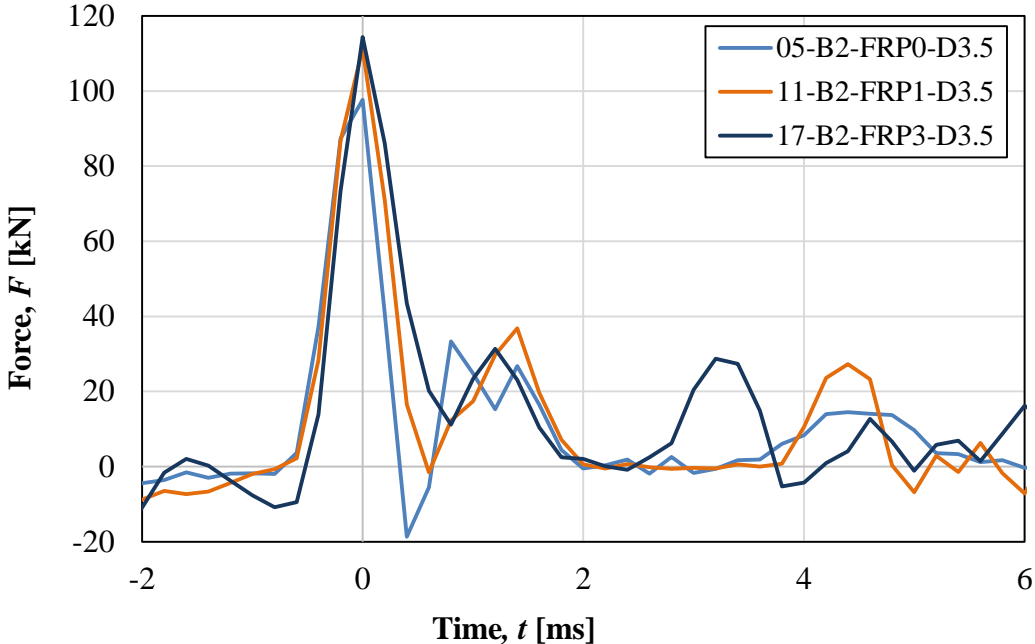
Figure 9.11   Applied force for unstrengthened, 1 layer and 3 layers FRP strengthened beams subjected to 3.5 m drop weight impact.

Table 9.18   Maximum applied force and impulse for unstrengthened, 1 layer and 3 layers FRP strengthened beams subjected to 3.5 m drop weight impact.

Beam	Number of FRP layer	F_{max} [kN]	Impulse [Ns]
05-B2-FRP0-D3.5	-	98	51
11-B2-FRP1-D3.5	1.0	111	63
17-B2-FRP3-D3.5	3.0	114	65

Applied force for unstrengthened, 1 layer and 3 layers FRP strengthened beams subjected to 3 m drop height impact are presented in Figure 9.12. Maximum force and impulse for the same beams subjected to drop weight impact of 3 m are also presented in Table 9.19.
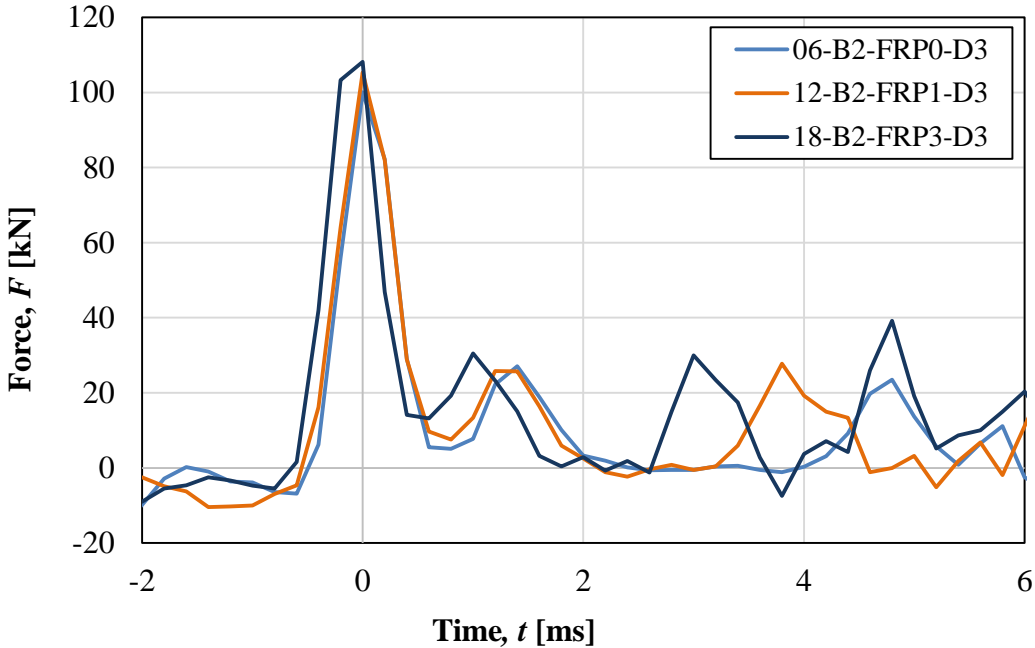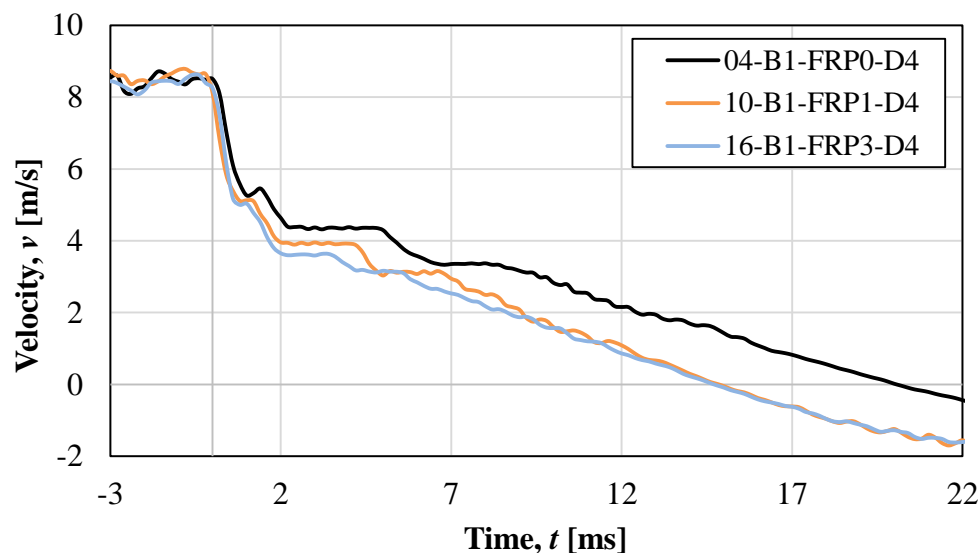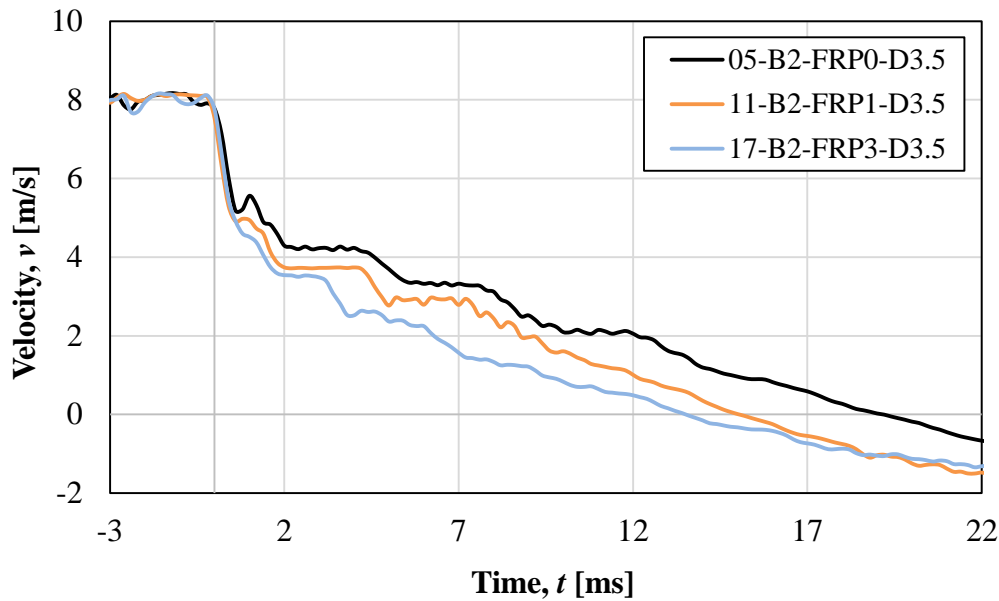

Figure 9.12   Applied force for unstrengthened, 1 layer and 3 layers FRP strengthened beams subjected to 3 m drop weight impact.

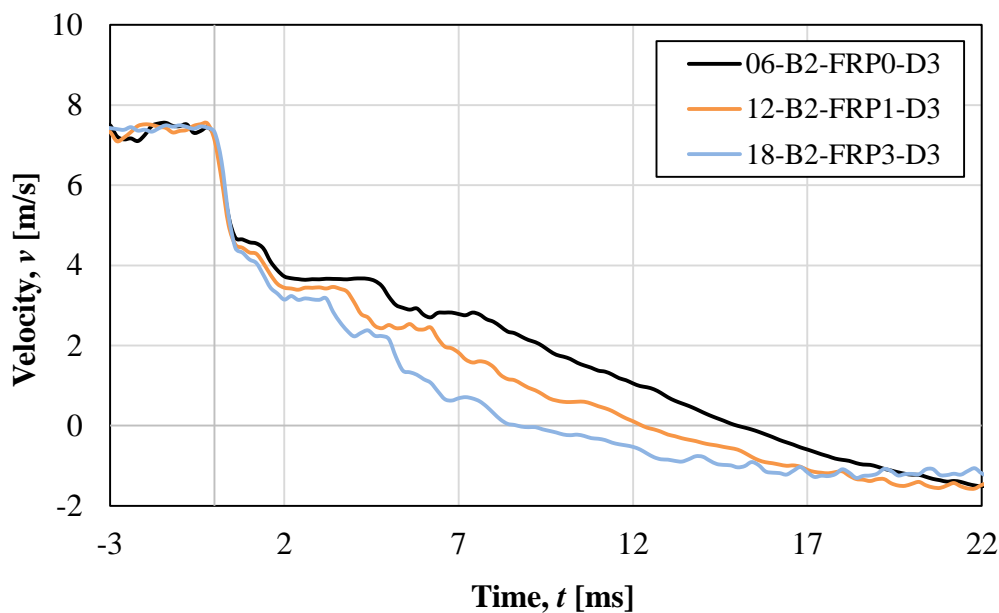*Table 9.19   Maximum applied force and impulse for unstrengthened, 1 layer and 3 layers FRP strengthened beams subjected to 3 m drop weight impact.*

Beam	Number of FRP layers	F_{max} [kN]	Impulse [Ns]
06-B2-FRP0-D3	-	100	53
12-B2-FRP1-D3	1.0	105	59
18-B2-FRP3-D3	3.0	108	57

9.2.2.3   Comparison of maximum force and impulse

From the test results it is shown that the maximum load capacity has increased as the layer of FRP strengthening increases. Moreover, for impulse it's only for drop height 3.5 m that the impulse increase as the layer of FRP strengthening increases. For the other drop heights, the increase of impulse is the most for the 1 layer FRP strengthened beam.

Increment of maximum force is presented in percentage comparing the maximum applied force of unstrengthened beams with 1 layer and 3 layers FRP strengthened beams subjected to the same drop height impact. This is presented in Table 9.20 to Table 9.22.

Table 9.20   Comparison of maximum applied force for beams with different FRP strengthening vs. the unstrengthened beam subjected to 4 m drop weight impact.

Beam	Number of FRP layers	F_{max} [kN]	Impulse [Ns]
04-B1-FRP0-D4	-	101	-
10-B1-FRP1-D4	1	114	12.9
16-B1-FRP3-D4	3	117	15.8

Table 9.21   Comparison of maximum applied force for beams with different FRP strengthening vs. the unstrengthened beam subjected to 3.5 m drop weight impact.

Beam	Number of FRP layer	F_{max} [kN]	Increase of F_{max} [%]
05-B2-FRP0-D3.5	-	98	-
11-B2-FRP1-D3.5	1	111	13.3
17-B2-FRP3-D3.5	3	114	16.3

Table 9.22   Comparison of maximum applied force for beams with different FRP strengthening vs. the unstrengthened beam subjected to 3 m drop weight impact.

Beam	Number of FRP layer	F_{max} [kN]	Increase of F_{max} [%]
06-B2-FRP0-D3	-	100	-
12-B2-FRP1-D3	1	105	5.0
18-B2-FRP3-D3	3	108	8.0

Increment of impulse is presented in percentage comparing the impulse of unstrengthened beams with 1 layer and 3 layers FRP strengthened beams subjected to the same drop height impact. This is presented in Table 9.23 to Table 9.25.

Table 9.23   Comparison of impulse for beams with different FRP strengthening vs. the unstrengthened beam subjected to 4 m drop weight impact.

Beam	Number of FRP layer	Impulse [Ns]	Increase of Impulse [%]
04-B1-FRP0-D4	-	62	-
10-B1-FRP1-D4	1	73	17.7
16-B1-FRP3-D4	3	69	11.3

Table 9.24   *Comparison of impulse for beams with different FRP strengthening vs. the unstrengthened beam subjected to 3.5 m drop weight impact.*

Beam	Number of FRP layer	Impulse [Ns]	Increase of Impulse [%]
05-B2-FRP0-D3.5	-	51	-
11-B2-FRP1-D3.5	1	63	23.5
17-B2-FRP3-D3.5	3	65	27.5

Table 9.25   *Comparison of impulse for beams with different FRP strengthening vs. the unstrengthened beam subjected to 3 m drop weight impact.*

Beam	Number of FRP layer	Impulse [Ns]	Increase of Impulse [%]
06-B2-FRP0-D3	-	53	-
12-B2-FRP1-D3	1	59	11.3
18-B2-FRP3-D3	3	57	7.5

9.2.3   Velocity of drop weight

The velocity of drop weight for beams with different amount of FRP strengthening subjected to same height of drop weight impact is presented in Figure 9.13 to Figure 9.15. From the velocity-time relation, it can be observed that as the layer of FRP strengthening increases the drop weight velocity after impact slows down faster.

Figure 9.13   *Velocity of drop weight for unstrengthened, 1 layer and 3 layers FRP strengthened beams subjected to 4 m drop weight impact.*

Figure 9.14   Velocity of drop weight for unstrengthened, 1 layer and 3 layers FRP strengthened beams subjected to 3.5 m drop weight impact.

Figure 9.15   Velocity of drop weight for unstrengthened, 1 layer and 3 layers FRP strengthened beams subjected to 3 m drop weight impact.

In order to compare velocity results gained from camera 1 and camera 2, velocity for drop weight impact of 3.5 m is presented in Figure 9.16. Trend lines are used to show the velocity from camera 1 more clearly. In Figure 9.16, it's shown that camera 1, denoted by C1, gives results containing a higher amount of noise and trend lines are therefore used to show the velocity from camera 1 more clearly. Even though camera 1 uses a higher frame rate and gives a more precise result for the velocity of drop weight, it can be concluded that camera 2 also gives a good approximation by comparing the velocities from both cameras.
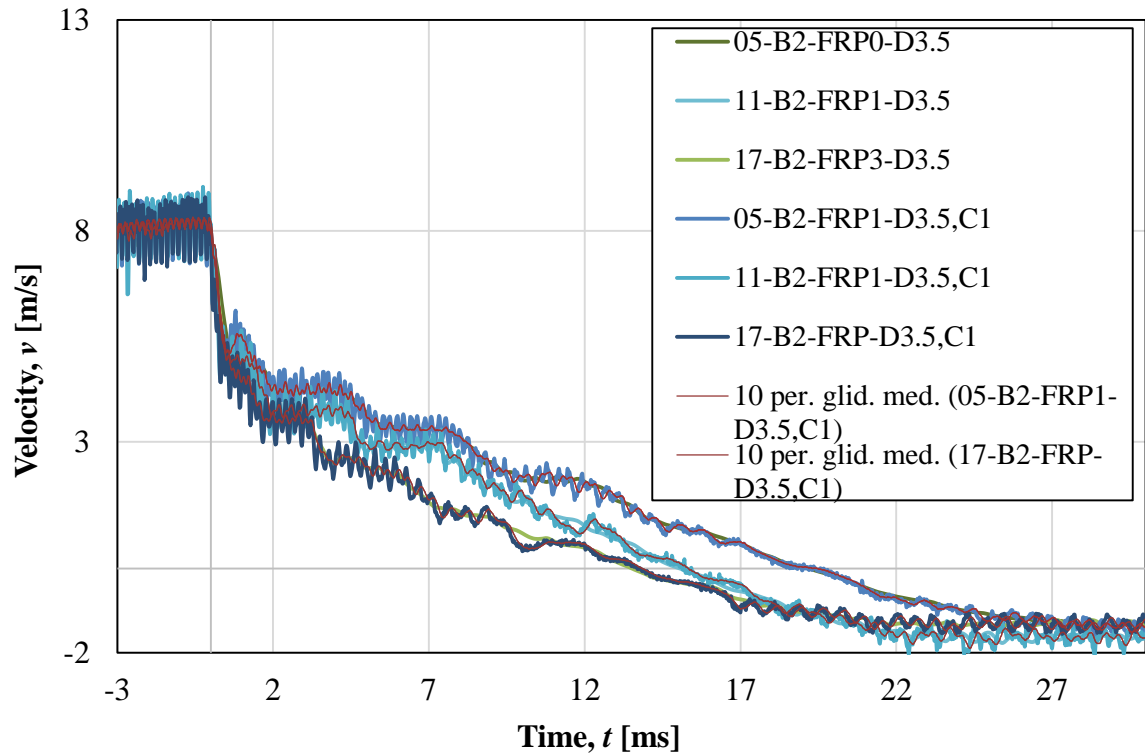
Figure 9.16   Velocity of drop weight for unstrengthened, 1 layer and 3 layers FRP strengthened beams subjected to 3.5 m drop weight impact from images of camera 1 and camera 2.

9.2.4   Deformed shape

The deformed shape in the longitudinal direction of the beams are presented in this section. The results are extracted from high speed camera 2 and display somewhat more than half of the beam. In GOM Correlate, a single section was constructed, i.e. a result line in the middle of the beam, parallel to the horizontal axis, from which the deflection was extracted. The coordinate system show coordinate x in the length direction of the beam and deflection as y-axis. It is of interest to see how the shape of deflection initiates along the beam and develops to get an impression on how the load transfers in the beam after impact. Therefore, the first 2 ms were studied with an interval of 0.2 ms. To get a better understanding of how the deformed shape develops the relative deflection was also studied. This would show how the beams active and inactive parts changes with time.

Camera 2 only have data for every 0.2 ms and therefore some information is lost in between each data point. A lot happen with the beam during the first 0.2 ms of impact and therefore it is of interest to have more data points during this period of time. The different beams have different data points which mean that it is not possible to get the first data at exact 0.2 ms after the time of impact for every beam. An approximation has been done to find the data point which is closest to 0.2 ms for every beam separately. This means that there will be some difference in the results when comparing the deflection. The results for the small deflections that initially shows will also be more affected to possible noise, which also can affect the results at time 2.0 ms after impact.

Camera 1, which have more data points, only display the middle of the beam, therefore it is not possible to use these results to illustrate the deformed shape along the beam. However, a study

has been made to compare the results from camera 1 and camera 2 to find out a more exact time for when the impact was initiated. Camera 1 and 2 were not synchronised in time, so the initial impact from both cameras were found by studying the change in deflections along the beam. The results from the deformed shape were compared with each other and with the additional data points from camera 1 more exact values for time of impact could be established, see Table 9.26. Results for the other beams subjected to impulse loading are presented in Appendix E and Appendix F.

Table 9.26   Estimated times from camera 1 for 0.2 ms after impact, for beams subjected to drop weight impact of 4 m drop height.

Beam	Time [ms]
04-B1-FRP0-D4	0.185
10-B1-FRP1-D4	0.209
16-B1-FRP3-D4	0.284

9.2.4.1   Deflection over the beam

Beam 04-B1-FRP0-D4, 10-B1-FRP1-D4 and 16-B1-FRP3-D4 are presented with their deformed shape in this section. Hence, one unstrengthened beam, one with 1 layer FRP and one with 3 layers FRP strengthening, all with drop height of 4 m. These beams are considered to be representative of their kind. However, the results of all beams are presented in Appendix E and Appendix F. There were some differences when comparing different number of FRP strengthening and unstrengthened which are presented in Figure 9.17 to Figure 9.19. Coordinate *x* starts at the left hand side support of the beam and stop a little to the right of the midpoint of the beam. The support and middle of the beam are marked with dashed lines to better illustrate the behaviour along the beam.
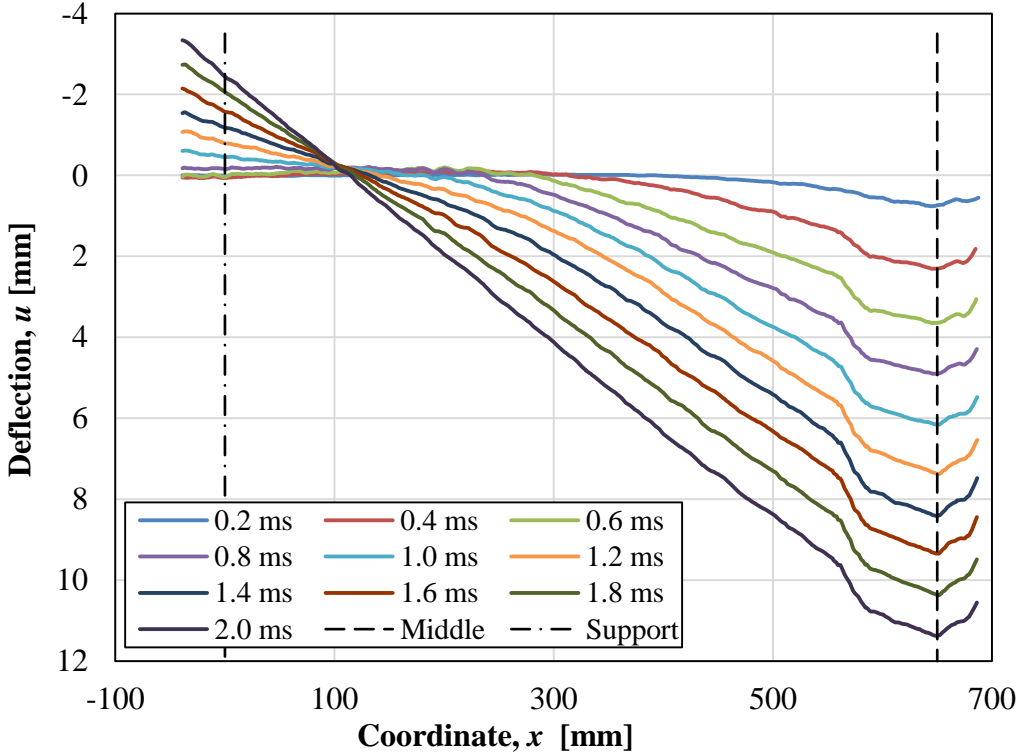
Figure 9.17   Deformed shape for the initial 2 ms of the drop weight impact illustrating the behaviour in deflection for beam 04-B1-FRP0-D4.
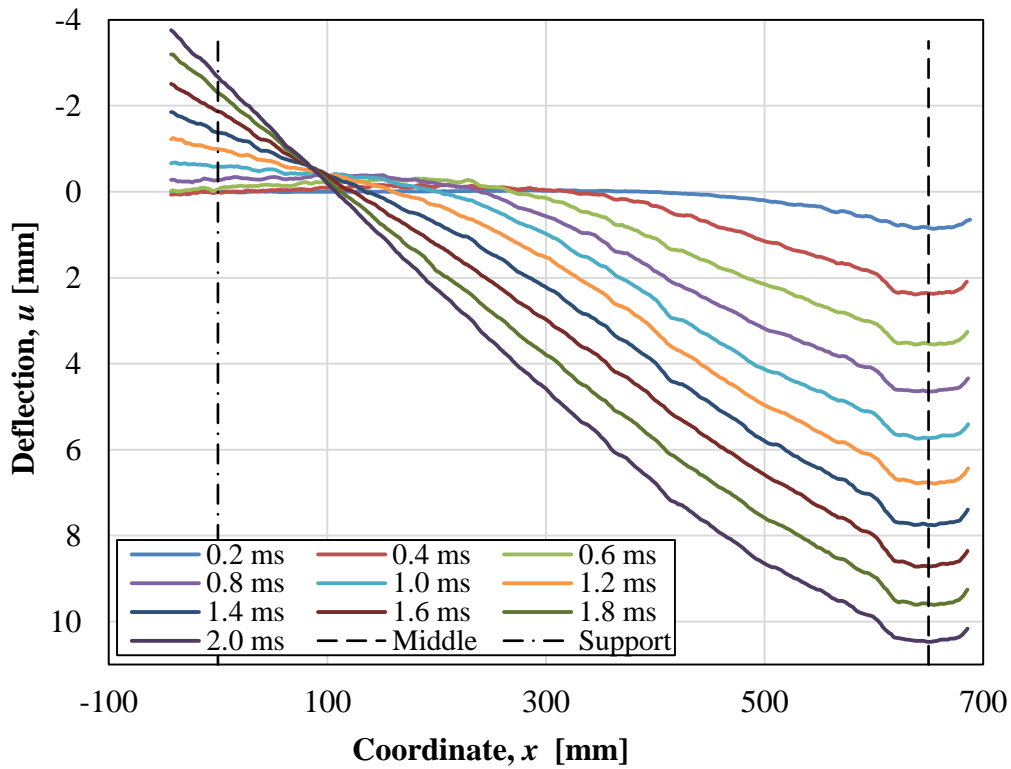
Figure 9.18   Deformed shape for the initial 2 ms of the drop weight impact illustrating the behaviour in deflection for beam 10-B1-FRP1-D4.
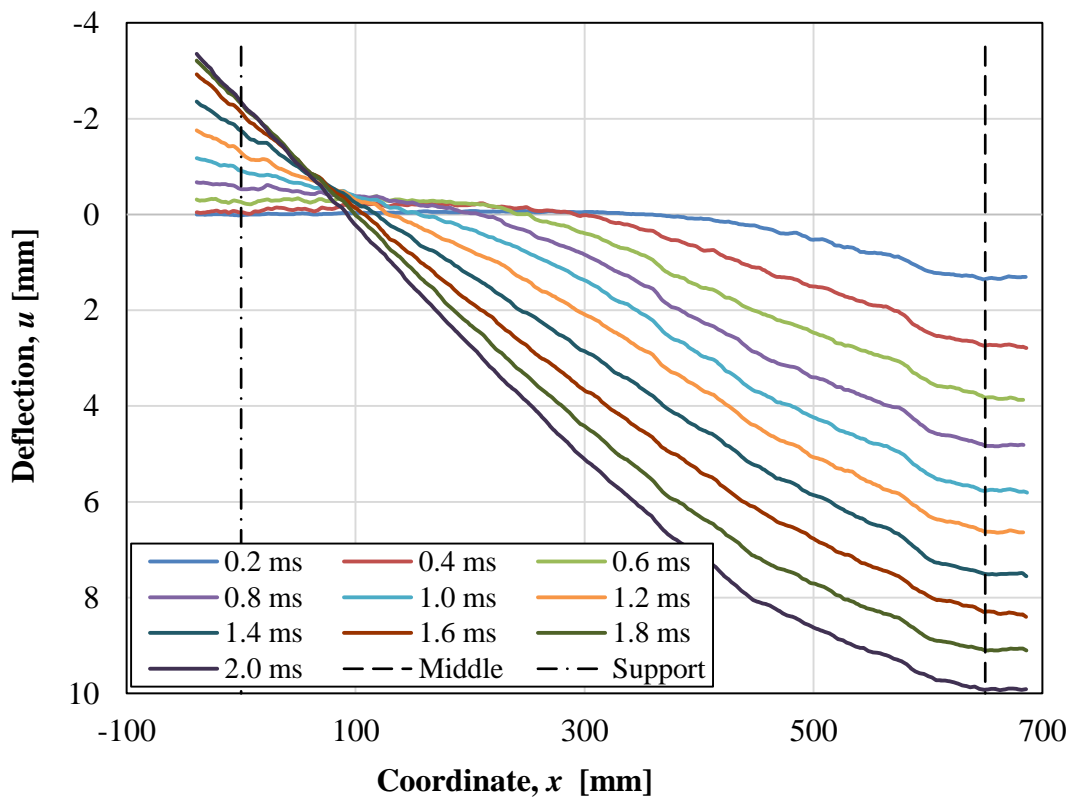
Figure 9.19   Deformed shape for the initial 2 ms of the drop weight impact illustrating the behaviour in deflection for beam 16-B1-FRP3-D4.

9.2.4.2 Relative deflection over the beam

Beam 04-B1-FRP0-D4, 10-B1-FRP1-D4 and 16-B1-FRP3-D4 are presented with their deformed shape as relative displacement, normalized to the maximum value for each time step. Hence, one unstrengthen beam, one with 1 layer FRP and one with 3 layers FRP strengthening, all with drop height of 4 m. These beams are considered to be representative of their kind. However, the results of all beams are presented in Appendix E and Appendix F. There were some differences when comparing different number of FRP strengthening and unstrengthened which are presented in Figure 9.20 to Figure 9.22. Coordinate x starts at the left hand side support of the beam and continue until a little after the middle. The support and middle of the beams are marked to better illustrate the behaviour.
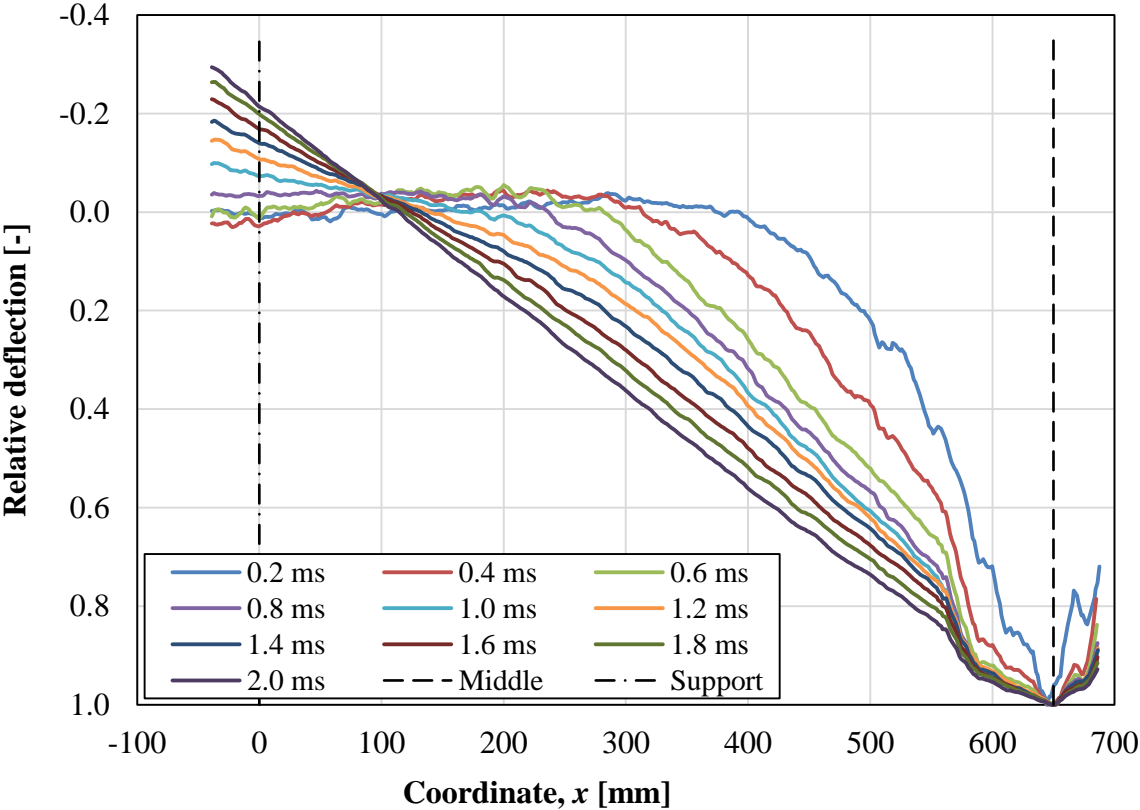
Figure 9.20   Deformed shape for the initial 2 ms of the drop weight impact illustrating the behaviour in relative deflection for beam 04-B1-FRP0-D4.
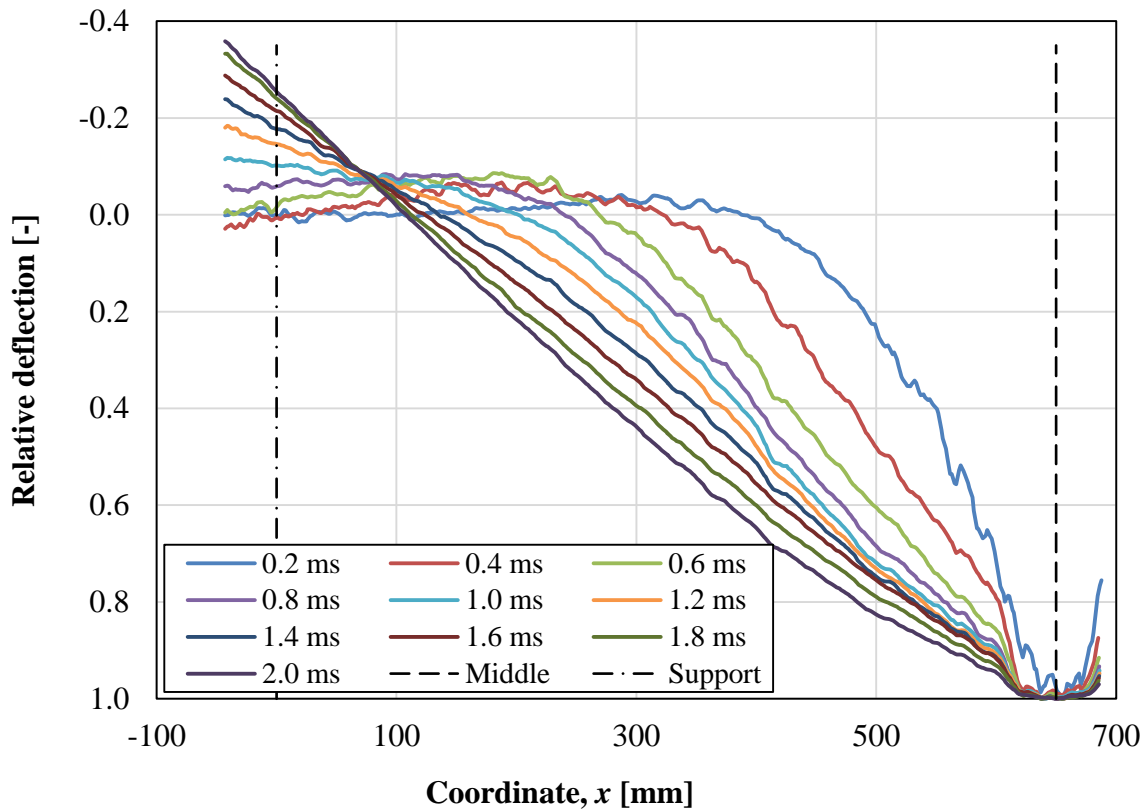
Figure 9.21   *Deformed shape for the initial 2 ms of the drop weight impact illustrating the behaviour in relative deflection for beam 10-B1-FRP1-D4.*
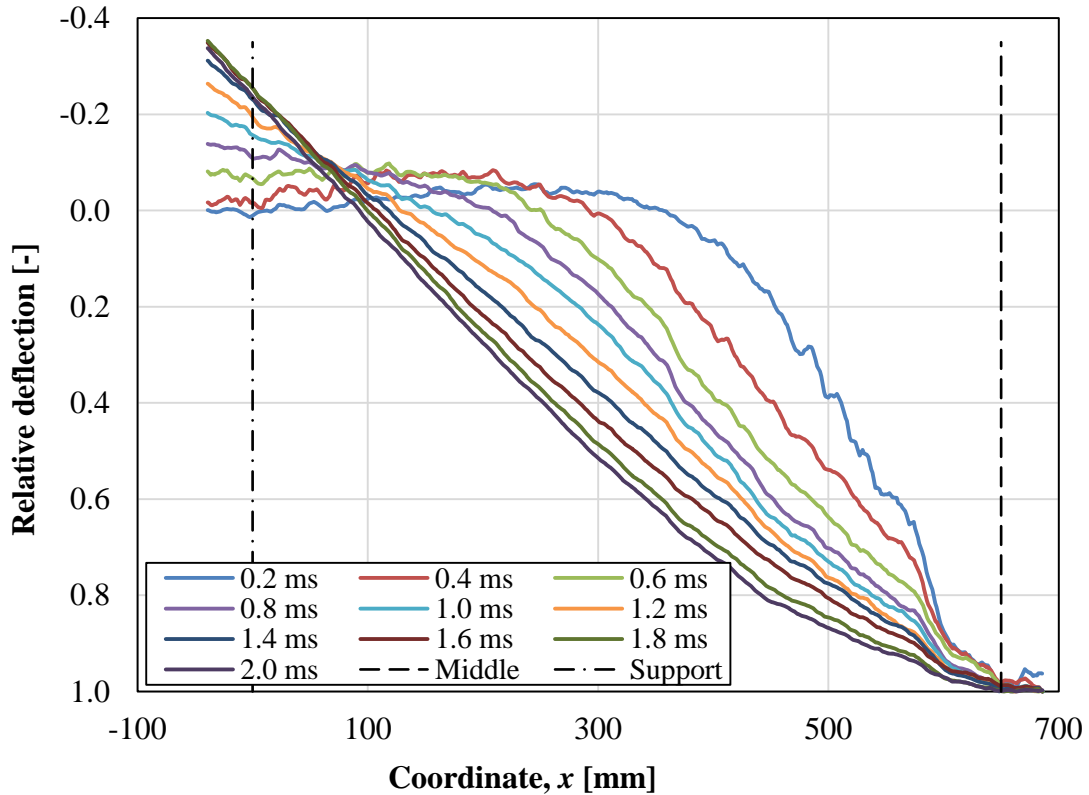
Figure 9.22   *Deformed shape for the initial 2 ms of the drop weight impact illustrating the behaviour in relative deflection for beam 16-B1-FRP3-D4.*

9.2.4.3 Comparison

The graphs in Section 9.2.4.1 shows that the impact loading does not affect the whole beam at once, initially only a small part of the beam deform. However, with time the whole beam will deform due to the impact force. Before that happens, the beam will behave as fully fixed and in the transition point between the active and the inactive part of the beam, there will be tension in the upper part of the beam, causing cracks.

In Section 9.2.4.1 the deformed shape of beam 04-B1-FRP0-D4 is more triangular compared with beam 10-B1-FRP1-D4 and beam 16-B1-FRP3-D4. Beam 16-B1-FRP3-D4 has a more parabolic shape. Furthermore, it can be explained that the unstrenghtened beam has developed a plastic hinge in the middle of the beam, whereas the beam strengthened with 3 layers FRP has not and instead show a more elastic behaviour. This behaviour can also be seen in the other beams subjected to drop weight impact, see Appendix E and Appendix F.

In Section 9.2.4.2 the same behaviour can be observed by looking at the maximum relative deflection. It shows clearly that the deformed shape for the beam with 3 layers of FRP have a more round shape and it becomes more triangular when not strengthened.

9.2.5 Propagation velocity of initial deflection

To improve the understanding about the initial behaviour of the deformed beam and how the force propagates through the beam, the propagation velocity of the initial deflection was also studied. The same beams that were presented with their deformed shape in Section 9.2.4 will be presented here, i.e. 04-B1-FRP0-D4, 10-B1-FRP1-D4 and 16-B1-FRP3-D4. It were of interest to study the first 2 ms and results for every 0.2 ms were calculated.

9.2.5.1 Calculation of velocity

The velocity of initial deflection was calculated as

$$v = \frac{x(t_2) - x(t_1)}{t_2 - t_1} \tag{9.1}$$

where v = velocity of initial deflection [m/s]

            $x(t_1)$ = coordinate x at t_1 [m]

            $x(t_2)$ = coordinate x at t_2 [m]

            t_1 = time 1 [s]

            t_2 = time 2 [s]
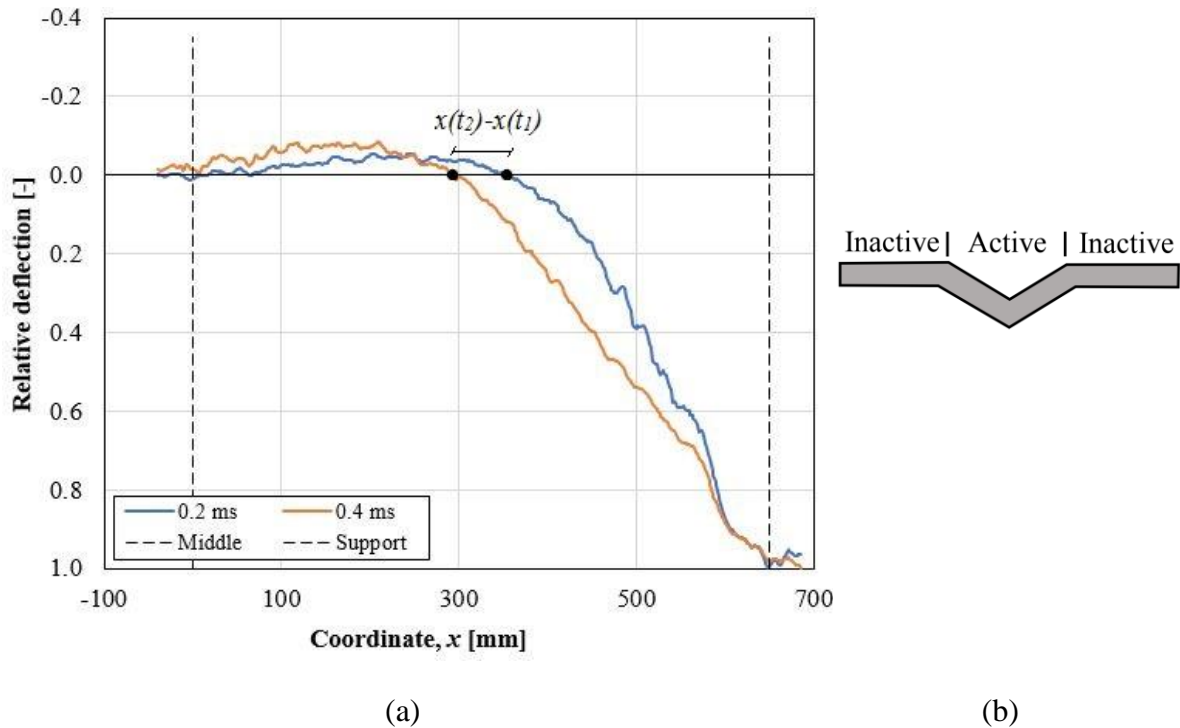
Figure 9.23   a) Transition point between active and inactive part of the beam. b) Schematic illustration of the active and inactive part of a beam subjected to drop weight impact (Jönsson and Stenseke, 2018).

Figure 9.23 illustrates how the position of t_1 and t_2 were found. What is of interest is to know where the active part of the beam starts for the different time steps. Dividing the difference in position for coordinate x with the time step gives the velocity of initial deflection. The first value to be presented is for 0.4 ms. This is because the impact does not happen at the exact time 0.0 ms so it will likely give wrong values for the propagation velocity at 0.0 to 0.2 ms.

The results for the beams subjected to a drop height of 4 m are tabulated in Table 9.27 and the results for the other beams subjected to impulse loading are presented in Appendix H. It can be seen that the beam without FRP strengthening has the highest propagation velocity at 0.4 ms and that it decreases with increasing number of FRP strengthening. With time the velocity decreases fast at start for all three beams then it increase before it decreases again and later stabilises. The increase in speed that occur between 0.8 ms and 1.2 ms was also noticed by Andersson and Pettersson (2019). It can be because of noise in the results or it could indicate that this is the time when the beam starts to lift from the support, hence affect the behaviour. In Section 9.2.3 when studying the velocity of drop weight this behaviour can be observed as well. The active part span the whole beam when the velocity of initial deflection stabilises (Andersson and Pettersson, 2019). For the tests carried out in this experimental study, this occurs at 1.2 ms for beam 04-B1-FRP0-D4 and 16-B1-FRP3-D4, and 1.4 ms for beam 10-B1-FRP1-D4.

Table 9.27   Velocity of initial deflection for the deformed shape of beams subjected to a drop weight impact of 4 m.

Beam	04-B1-FRP0-D4	10-B1-FRP1-D4	16-B1-FRP3-D4
Time [ms]	Propagation velocity of initial deformation [m/s]		
0.4	395	352	320
0.6	159	258	234
0.8	223	136	186
1.0	266	198	266
1.2	222	204	130
1.4	31	111	55
1.6	44	74	56
1.8	31	56	37
2.0	19	37	42

9.2.5.2   Comparison with results from other studies

Another way to study the velocity of initial deflection is by calculating its average value. Johansson et al. (2019) have studied the impact propagation effects along RC beams and the method used to study the velocity of initial deflection will be followed in this thesis too. This is done by using Equation (9.1) like before, but in this case time 1 will be at 0.2 ms for all cases whereas only time 2 changes depending on the studied time, thereby it will give an average value for the velocity. The effective span length for each time step, which is the active part of the beam, were determined and divided with the height of the beam. The average propagation velocity is sensitive to span/depth ratio therefore it is of interest to study this connection by plotting it in a diagram (Isaac et al., 2017).

The results for the beams subjected to 4 m drop height impact are illustrated in Figure 9.24 and the results for the other beams subjected to impact loading are presented in Appendix H. These results show a more uniformly decrease in shear velocity compared with previous values for the velocity of initial deflection. However, the increase in speed that occurred between 0.8 ms and 1.2 ms are here instead accounted for more as a slower decrease in velocity in time. By observing Figure 9.24 it shows a non-linear response for the forces propagation in time in velocity. This non-linear behaviour is also observed in the deformed shape of the beam when illustrating the deflection in different time steps.
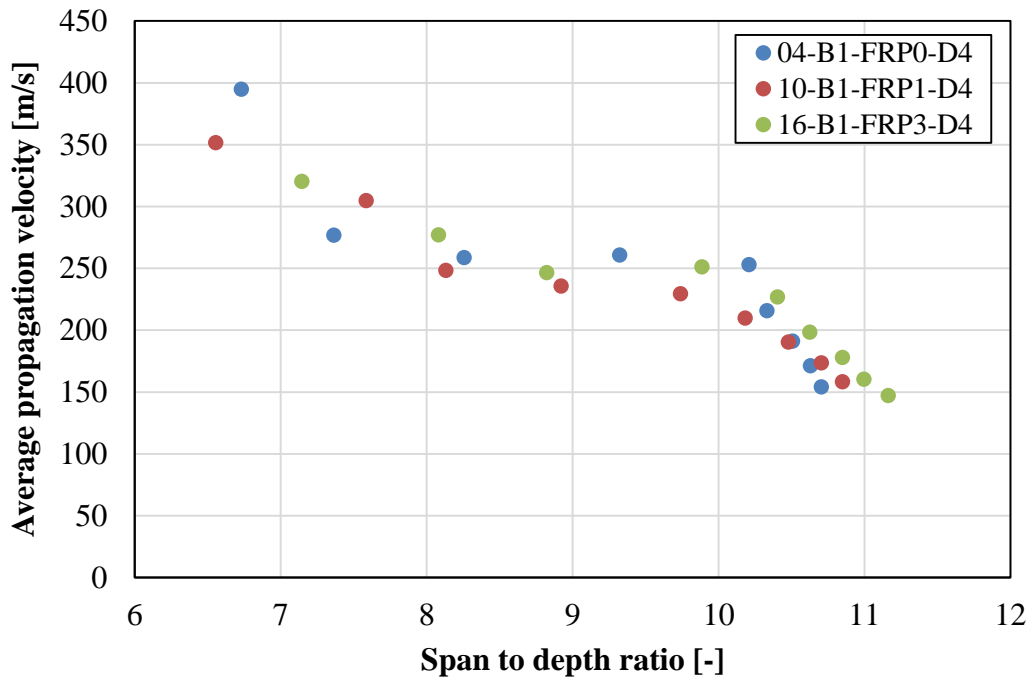
Figure 9.24 Average propagation velocity for the initial 2 ms of the drop weight impact, starting with values for 0.4 ms and continues with time steps of 0.2 ms for the beams subjected to 4 m drop height impact.

The results from Ulzurrun et al. (2019) are presented in Figure 9.25. Beam 12, 13 and 14 are presented in Jönsson and Stenseke (2018) and have a cross section of 100 x 100 mm^2 with span length of 1 m and are subjected to a drop weight of 20 kg and drop height of 5 m. These results are illustrated for a span to depth ratio as low as almost 3. This shows that the velocities are much higher, more than 1 200 m/s, at this lower span to depth value and then decrease fast until the curve plane out to later again decrease faster with non-linear response.

This is a similar behaviour that is observed for the experimental results conducted in this master thesis. The differences are that Figure 9.24 display values that level out between eight to ten span to depth ratio which is earlier than the results reached by Ulzurrun et al. (2019). This could however depend on the different geometries and drop heights of the beams. Ulzurrun et al. (2019) does also have a more clear non-linear shape in their results and this could depend on the higher number of information points that are presented in Figure 9.25.
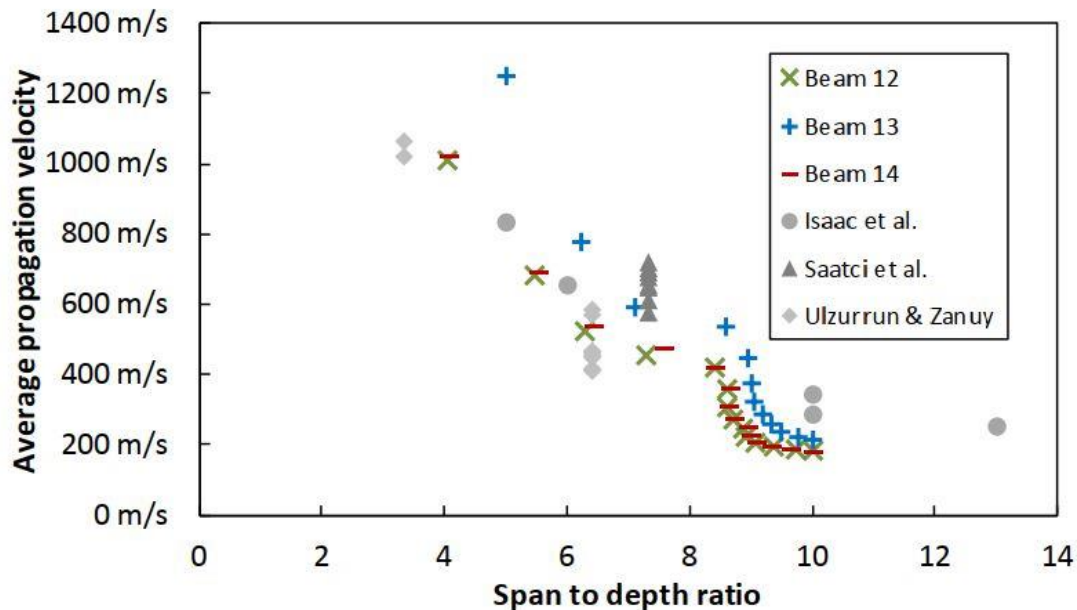
Figure 9.25   Average propagation velocity for impact loaded RC beams with same geometry for beams 12, 13 and 14 which were subjected to a drop weight of 20 kg at drop height 5 m. These results are from a study conducted by Ulzurrun et al. (2019).

9.2.6   Strain field

Strain field and its initial behaviour have been analysed and are presented in this section. It's major strains and high strain values corresponds approximately to real cracks. Section 9.2.6.1 presents the results for the three beams that were subjected to 4 m drop height impact, one beam is unstrengthened and two beams are strengthened with 1 and 3 layers of FRP, respectively. This will show how FRP affect the resulting strain field (crack pattern) when being dynamically loaded. In Section 9.2.6.2 the other beams that were subjected to drop height impact will be presented to compare the effect of different drop heights.

The results are extracted from GOM Correlate. The colour scale has been analysed and the settings that show most strains without too much noise have been chosen to 1 % - 2 %, it is also presented in the tables. Where the colour becomes white in the beams shows open cracks or spalling of concrete and GOM Correlate can no longer get any information from these regions.

9.2.6.1   Beams subjected to 4 m drop weight impact

Strain fields for the first 2.0 ms and strain field for maximum deflection are illustrated in Table 9.28 to Table 9.30 for one unstrengthened reference beam and beams with 1 layer and 3 layers FRP strengthening, subjected to 4 m drop weight impact.

Table 9.28   Strain field illustrated for beam 04-B1-FRP0-D4 when subjected to drop weight impact of 4 m.
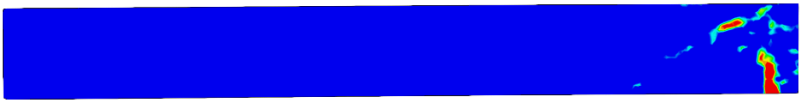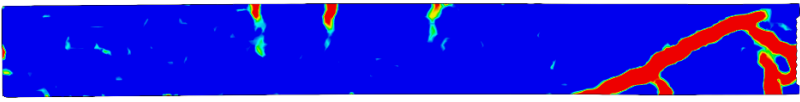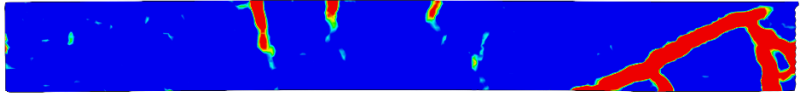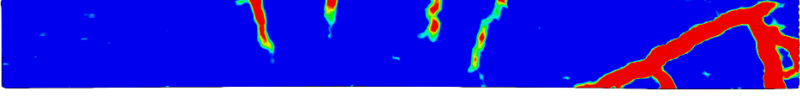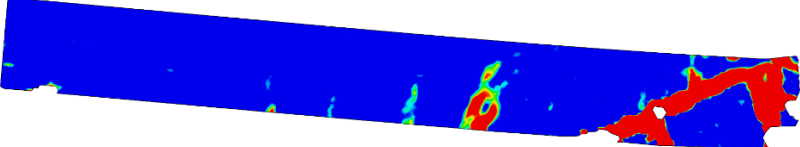
Time [ms]	Beam 04-B1-FRP0-D4
0.2	
0.4	
0.6	
0.8	
1.0	
2.0	
Time when reaching u_{max} 20.0	
Scale	1 %　　　　　　　　　　　　　　　　　2 %

Table 9.29   Strain field illustrated for beam 10-B1-FRP1-D4 when subjected to drop weight impact of 4 m.
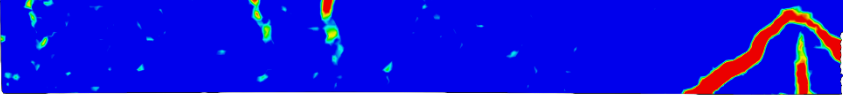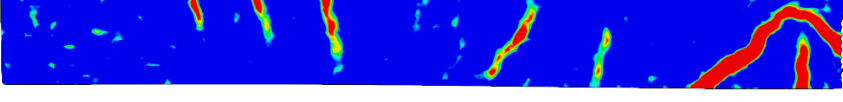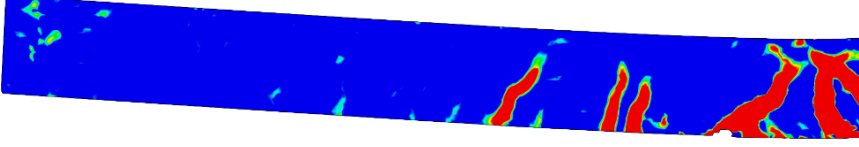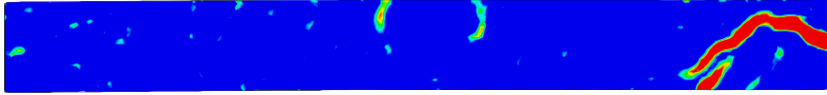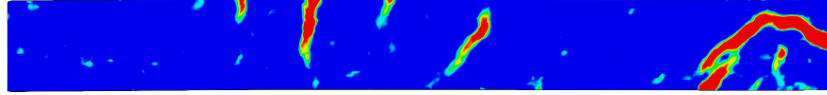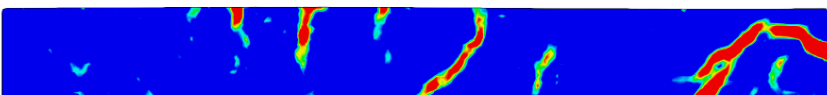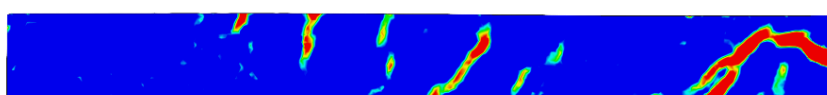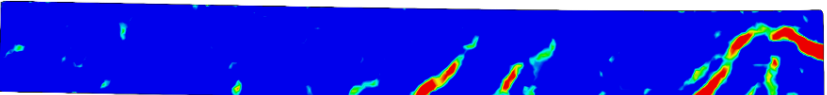
Time [ms]	Beam 10-B1-FRP1-D4
0.2	
0.4	
0.6	
0.8	
1.0	
2.0	
Time when reaching u_{max} 15.4	
Scale	1 % ▬▬▬▬ 2 %

Table 9.30   Strain field illustrated for beam 16-B1-FRP3-D4 when subjected to drop weight impact of 4 m.

Time [ms]	Beam 16-B1-FRP3-D4
0.2	
0.4	
0.6	
0.8	
1.0	
2.0	
Time when reaching u_{max} 14.6	
Scale	1 % [color scale] 2 %

9.2.6.2 Beams subjected to 3.5 m and 3 m drop weight impact

Strain fields for the first 2.0 ms and strain field for maximum deflection are illustrated in Table 9.31 to Table 9.33 for the beams subjected to 3.5 m and 3 m drop weight impact.

Table 9.31   Strain field illustrated for two reference beams subjected to 3.5 m and 3 m drop weight impact.
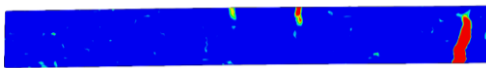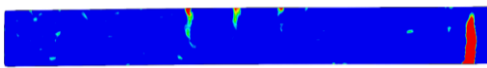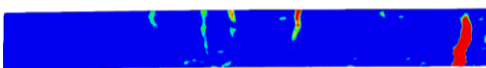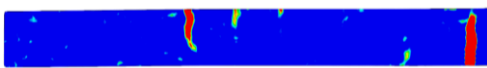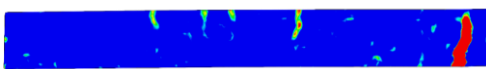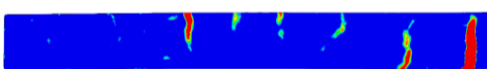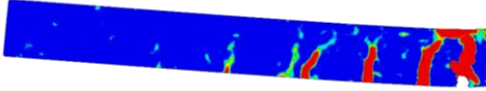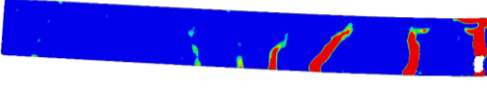
Time [ms]	Beam 05-B2-FRP0-D3.5	Beam 06-B2-FRP0-D3
0.2		
0.4		
0.6		
0.8		
1.0		
2.0		
Time when reaching u_{max}	19.0 ms	15.0 ms
Scale	1 % 2 %	

Table 9.32   Strain field illustrated for two beams strengthened with 1 FRP layer subjected to 3.5 m and 3 m drop weight impact.
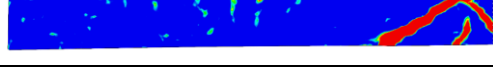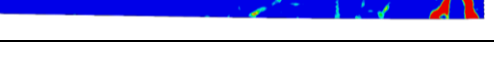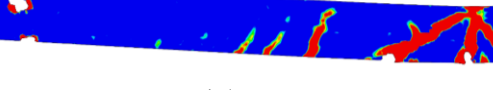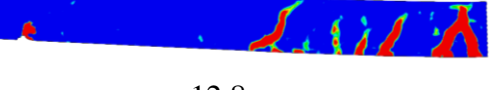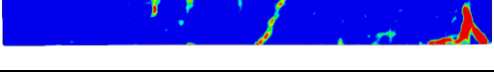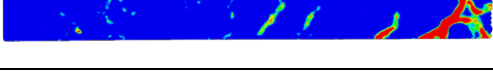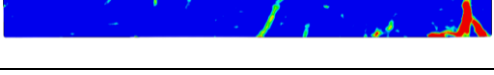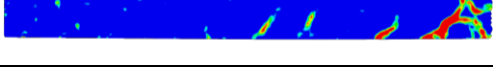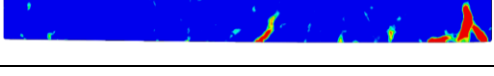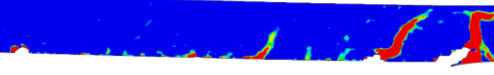
Time [ms]	Beam 11-B2-FRP1-D3.5	Beam 12-B2-FRP1-D3
0.2		
0.4		
0.6		
0.8		
1.0		
2.0		
Time when reaching u_{max}	15.6 ms	12.8 ms
Scale	1 % 2 %	

Table 9.33   Strain field illustrated for two beams strengthened with 3 FRP layers subjected to 3.5 m and 3 m drop weight impact.

Time [ms]	Beam 17-B2-FRP3-D3.5	Beam 18-B2-FRP3-D3
0.2		
0.4		
0.6		
0.8		
1.0		
2.0		
Time when reaching u_{max}	 14.4 ms	 8.4 ms
Scale	1 % 2 %	

9.2.6.3 Comparison

High strain values corresponds approximately to real cracks. The first strain to appear are close to impact zone, bending cracks and diagonal shear cracks from the bottom of the beams. Table 9.28 to Table 9.30 illustrates this clearly for the beams subjected to 4 m drop height. When the drop height decrease, the diagonal shear cracks at impact zone decrease as well and can no longer be seen in the strain field. However, it show when the beams are strengthened with different layers of FRP.

After approximately 0.6 ms top cracks occur, positioned in between the middle of the beam and the support. These cracks seems to be developed undependent of the drop height and show similar results for unstenghtened and FRP strengnthened beams. However, the strains show more clearly when the drop height is increased. Furhermore, as the impact force propagates along the beam, these top cracks will close and by the time 2.0 ms after impact are no longer visible in the strain field.

Between time 2.0 ms after impact and the time when maximum deflection is reached, the bending cracks and diagonal shear cracks in the bottom of the beams are developed further. Moreover, the strain field show that these cracks also distribute away from the impact zone but are still centered toward the middle of the beam.

9.3 Static testing

In this section static test results for beams loaded only statically and beams that were subjected to impact loading prior to static loading are presented.

For only statically loaded beams load-deflection relationship, ultimate moment, stiffness in state I and tangent stiffness in state II are presented. The maximum load capacity of beams with different amount of FRP strengthening is presented in comparison with load capacity of unstrengthened reference beams. Furthermore, remaining residual capacity for all types of impacted beams is presented and comparison is made between the responses in different FRP strengthening.

Maximum deflection, $u_{50\%FRmax}$, is in all cases taken as the deformation at the descending branch of load-deflection curve that corresponds to a load level of 50 % of the average maximum load $(0.5 \cdot F_{Rmax} = 4.9 \text{ kN})$, where F_{Rmax} is the average maximum load for the unstrengthened reference beams subjected to static load only.

Plastic deformation and internal work for statically loaded beams and beams subjected to dynamic and static loading are finally presented and discussed.

9.3.1 Only statically loaded beams

In this section test results for three group of beams with different amount of FRP strengthening, i.e. unstrengthened, 1 layer and 3 layers of FRP strengthening, subjected to only static loading is presented. Load-deflection relationship, comparison of maximum load capacity, rotation capacity and strain fields of the beams are presented.

9.3.1.1 Load–deflection relation

Load-deflection relationship for unstrengthen, 1 layer and 3 layers of FRP strengthened beams subjected to static loading only is presented in Figure 9.26.
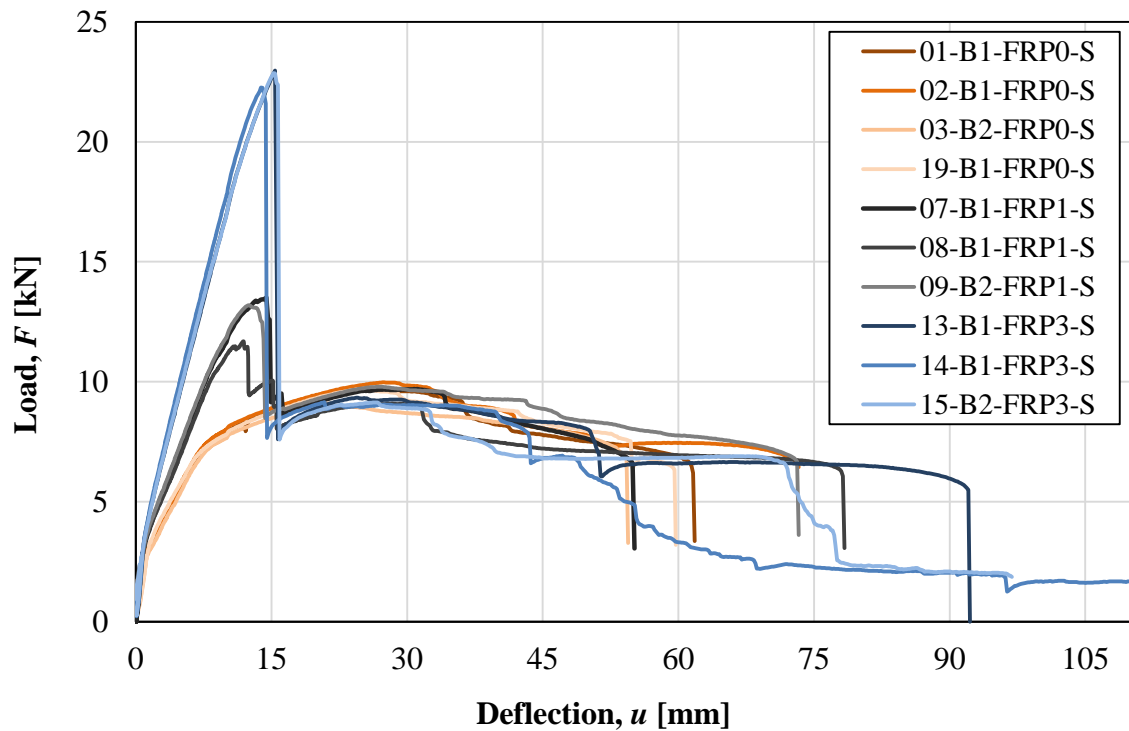
Figure 9.26   Load-deflection relation for unstrengthened, 1 layer and 3 layers FRP strengthened beams under static loading.

Ultimate load capacity, maximum moment, maximum deflection at failure and stiffness at state I and state II for unstrengthened, 1 layer FRP strengthened and 3 layers FRP strengthened beams are presented in Table 9.34 to Table 9.36.

Table 9.34   Maximum deflection, ultimate load, ultimate moment, and stiffness for unstrengthened beams loaded statically.

Beam	Number of FRP layer	u_{max} [mm]	F_{max} [kN]	M_u [kNm]	k_I [MN/m]	k_{II} [MN/m]
01-B1-FRP0-S	-	62	9.7	3.3	3.35	0.93
02-B1-FRP0-S	-	73	10.0	3.2	3.02	0.96
03-B2-FRP0-S	-	54	9.1	3.0	2.05	0.90
19-B1-FRP0-S	-	60	9.7	3.2	2.17	0.99
Average		**62**	**9.6**	**3.2**	**2.6**	**0.9**

Table 9.35   Maximum deflection, ultimate load, ultimate moment, and stiffness for 1 layer FRP strengthened beams loaded statically.

Beam	Number of FRP layer	u_{max} [mm]	F_{max} [kN]	M_u [kNm]	k_I [MN/m]	k_{II} [MN/m]
07-B1-FRP1-S	1	55	13.5	4.4	3.58	1.23
08-B1-FRP1-S	1	78	11.7	3.8	3.63	1.14
09-B2-FRP1-S	1	73	13.2	4.3	3.43	1.20
Average		**69**	**12.8**	**4.2**	**3.5**	**1.2**

*Table 9.36   Maximum deflection, ultimate load, ultimate moment, and stiffness for 3 layers
            FRP strengthened beams loaded statically.*

Beam	Number of FRP layer	u_{max} [mm]	F_{max} [kN]	M_u [kNm]	k_I [MN/m]	k_{II} [MN/m]
13-B1-FRP3-S	3	92	23.0	7.5	3.9	1.6
14-B1-FRP3-S	3	55	22.3	7.2	3.8	1.7
15-B2-FRP3-S	3	74	22.9	7.4	3.9	1.6
Average		**74**	**22.7**	**7.4**	**3.9**	**1.6**

9.3.1.2 Comparison of maximum load and maximum deflection capacity

Comparison of maximum load and deformation capacity for beams with different amount of FRP strengthening are presented in Table 9.37. It can be seen that in Figure 9.26, all strengthened beams except for beam 08-B1-FRP1-S exhibited debonding around the same deflection of 15 mm. After debonding the load shows a sudden drop and the beams tend to have a similar behaviour to that of unstrengthened beams and follow more or less the same load deflection plateau. Beams 14-B1-FRP3-S and beam 15-B2-FRP3-S shows a behaviour of some kind of shear failure and experience a larger deformation without rupture of reinforcement bar in case of beam 14-B1-FRP3-S.

Comparison of applied force and maximum deflection is done using average maximum force and average maximum deflection for each beam type. Both 1 layer and 3 layers FRP of strengthening resulted in increased maximum force and deflection capacity. It is observed that increase of load capacity is significantly higher for beams strengthened with 3 layers of FRP compared with 1 layer strengthening. This is illustrated in Table 9.14 by comparing the increase of load and deformation capacity between unstrengthened and 1 layer strengthening as well as the increase between unstrengthened 3 layers of strengthening.

*Table 9.37   Comparison of average maximum load and deflection in reference to
            unstrengthened beams for statically loaded beams.*

Beam type	Average F_{max} [kN]	Average u_{max} [mm]	Increase of F_{max} [%]	Increase of u_{max} [%]
Reference beam	9.7	62		
1 layer FRP strengthening	12.8	69	32	11
3 layers FRP strengthening	22.7	74	133	18

9.3.1.3 Plastic rotation capacity

Plastic rotation capacity at different load levels for statically loaded beams are calculated according to Section 4.3.3 from test results and is presented in Table 9.38 to Table 9.40. For the calculation of rotation capacity at different load levels, $\theta_{pl,x\%}$, the maximum load level that is used as 100 % load level is the average maximum force for unstrengthened beams (F_{max} = 9.7 kN). This choice is made since the maximum force for strengthened beams are too high and exhibits a sudden drop immediately after debonding, which is a value far from the plastic plateau that the beams follow after debonding. Furthermore, the same maximum force is also used for the reference beams in order to make the comparison of the effect of FRP strengthening on plastic rotation capacity realistic.

Table 9.38   Plastic rotation capacity at different load levels for unstrengthened beams subjected to static loading only.

Beam	Number of FRP layer	$\theta_{pl,100\%}$ [mrad]	$\theta_{pl,95\%}$ [mrad]	$\theta_{pl,90\%}$ [mrad]	$\theta_{pl,85\%}$ [mrad]	$\theta_{pl,80\%}$ [mrad]
01-B1-FRP0-S	-	19.2	54.3	41.5	45.7	54.0
02-B1-FRP0-S	-	25.2	36.2	41.9	50.6	56.8
03-B2-FRP0-S	-	17.2	34.2	50.8	61.7	67.5
Average		**20.5**	**41.6**	**44.7**	**52.7**	**59.4**

Table 9.39   Plastic rotation capacity at different load levels for 1 layer FRP strengthened beams subjected to static loading only.

Beam	Number of FRP layer	$\theta_{pl,100\%}$ [mrad]	$\theta_{pl,95\%}$ [mrad]	$\theta_{pl,90\%}$ [mrad]	$\theta_{pl,85\%}$ [mrad]	$\theta_{pl,80\%}$ [mrad]
07-B1-FRP1-S	1	26.4	34.2	50.8	61.7	67.5
08-B1-FRP1-S	1	32.7	32.7	34.5	36.1	43.1
09-B2-FRP1-S	1	27.5	50.0	56.2	64.2	77.5
Average		**28.9**	**39.0**	**47.2**	**54.0**	**62.7**

Table 9.40   Plastic rotation capacity at different load levels for 3 layers FRP strengthened beams subjected to static loading only.

Beam	Number of FRP layer	$\theta_{pl,100\%}$ [mrad]	$\theta_{pl,95\%}$ [mrad]	$\theta_{pl,90\%}$ [mrad]	$\theta_{pl,85\%}$ [mrad]	$\theta_{pl,80\%}$ [mrad]
13-B1-FRP3-S	3	_	27.9	41.5	56.9	64.9
14-B1-FRP3-S	3	-	27.3	46.8	50.2	54.0
15-B2-FRP3-S	3	24.0	26.3	35.3	37.1	40.3
Average		**24.0**	**27.2**	**41.2**	**48.1**	**53.1**

Comparison of average plastic rotation for the three groups of beams at different load levels is presented. It is shown that beams strengthened with 1 layer of FRP shows similar results of plastic rotation capacity whereas 3 layers of FRP has exhibited a somewhat lower plastic rotation capacity. However, since two of three beams in this set experienced shear type of failure the deformation that was registered at 50 % of F_{Rmax} were smaller than for the other beams.
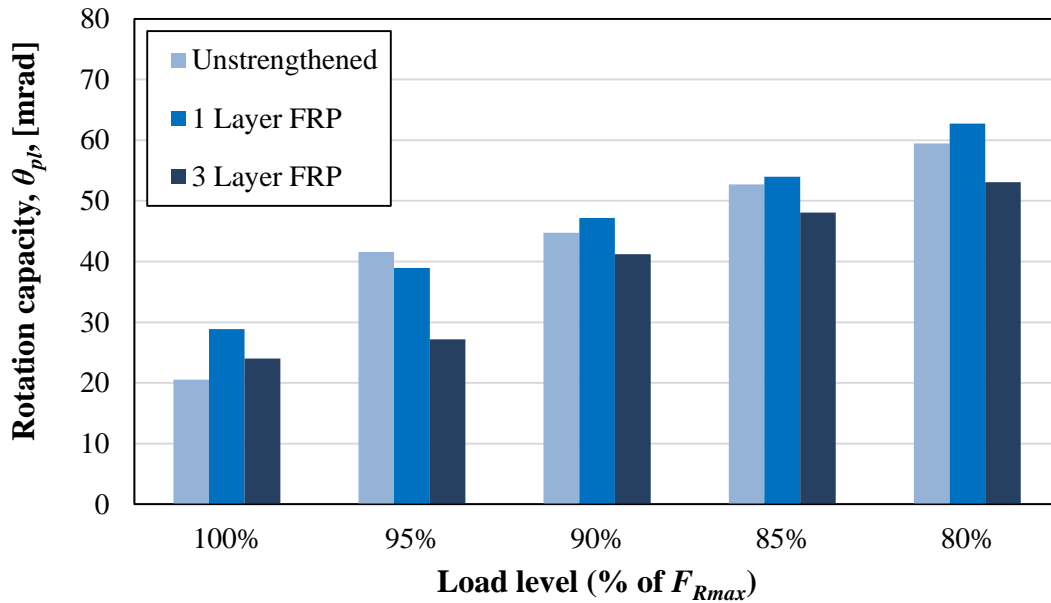
Figure 9.27 *Comparison of rotation capacity at different load levels for unstrengthened, 1 layer and 3 layers FRP strengthened beams.*

9.3.1.4 Internal work

Internal work at different load levels, $W_{pl,x\%}$, for unstrengthened, 1 and 3 layers FRP strengthened beams subjected to static loading only is calculated using a method stated in Section 3.5 and is presented in Table 9.41 to Table 9.43. The load level is taken in the same way as it was done for plastic rotation capacity in Section 9.3.1.3. The average total internal work, W_{tot}, under force-deflection curve until reaching a deflection $u_{50\%FRmax}$ and average total internal work, $W_{tot,fail}$, until final failure by rupture of reinforcement bars are presented and compared in Figure 9.29. From Figure 9.28 and Figure 9.29, it can be seen that the internal work at different levels and the total internal work have increased as the amount of FRP strengthening increases. In addition, in some beams approximations were made for levels of 100 % and 95 % if the load level does not much with the exact load levels of the FRP strengthened beams after debonding.

Table 9.41 *Internal work at different load levels for unstrengthen beams subjected to static loading only.*

Beam	$W_{pl,100\%}$ [J]	$W_{pl,95\%}$ [J]	$W_{pl,90\%}$ [J]	$W_{pl,85\%}$ [J]	$W_{pl,80\%}$ [J]	$W_{tot,50\%FRmax}$ [J]	$W_{tot,fail}$ [J]
01-B1-FRP0-S	113	228	250	272	316	491	491
02-B1-FRP0-S	153	223	255	305	338	582	582
03-B2-FRP0-S	97	193	284	341	370	427	427
Average	**121**	**215**	**263**	**306**	**341**	**500**	**500**

Table 9.42   Internal work at different load levels for 1 layer FRP strengthened beams subjected to static loading only.

Beam	$W_{pl,100\%}$ [J]	$W_{pl,95\%}$ [J]	$W_{pl,90\%}$ [J]	$W_{pl,85\%}$ [J]	$W_{pl,80\%}$ [J]	$W_{tot,50\%FRmax}$ [J]	$W_{tot,fail}$ [J]
07-B1-FRP1-S	176	249	274	326	380	488	488
08-B1-FRP1-S	35	198	209	219	258	602	602
09-B2-FRP1-S	182	322	359	404	476	639	639
Average	**131**	**256**	**281**	**316**	**371**	**576**	**576**

Table 9.43   Internal work at different load levels for 3 layers FRP strengthened beams subjected to static loading only.

Beam	$W_{pl,100\%}$ [J]	$W_{pl,95\%}$ [J]	$W_{pl,90\%}$ [J]	$W_{pl,85\%}$ [J]	$W_{pl,80\%}$ [J]	$W_{tot,50\%FRmax}$ [J]	$W_{tot,fail}$ [J]
13-B1-FRP3-S	-	229	313	401	447	790	790
14-B1-FRP3-S	-	212	330	352	376	520	661
15-B2-FRP3-S	202	221	277	291	311	650	707
Average	**202**	**221**	**307**	**348**	**378**	**653**	**720**
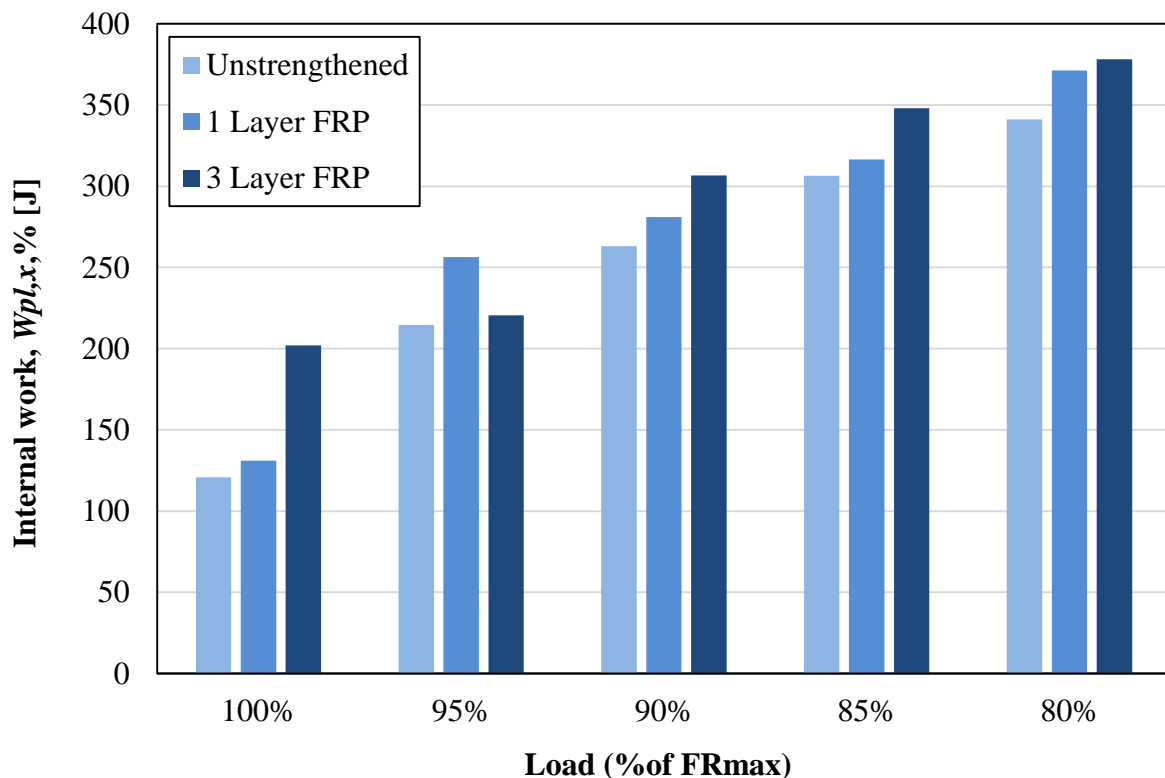
Figure 9.28   Internal work at different load levels for unstrengthened, 1 layer and 3 layers FRP strengthened beams.
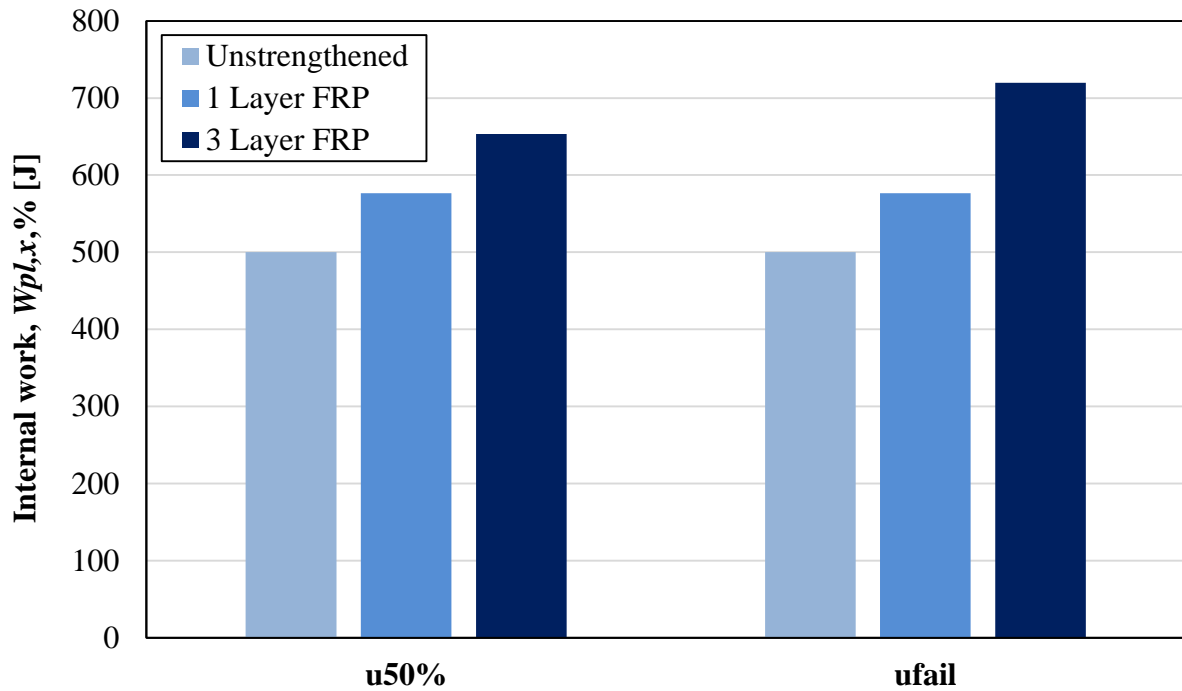
Figure 9.29   *Comparison of average internal work at load corresponds to $u_{50\%FRmax}$ and final deformation u_{fail} for unstrengthened, 1 layer and 3 layers FRP strengthened beams.*

9.3.1.5 Change of support condition

The extra beam 19-B1-FRP0-S was subjected to static loading only to examine the response, up to maximum load, with a different set up for the supports. This was conducted by using freely laid square steel plates on top of the roller supports, see Figure 7.17. The experimental results show that this support condition give similar results as the other reference beams, see Figure 9.30.
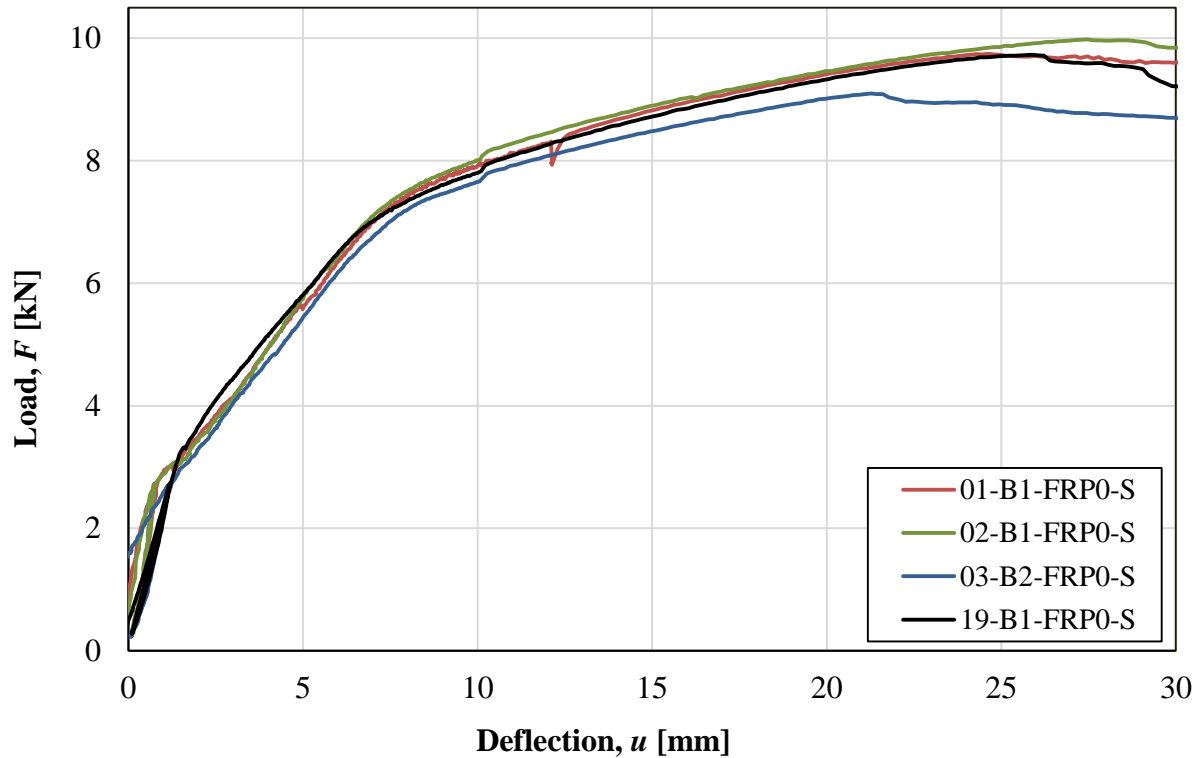
Figure 9.30   Load-deflection relation for unstrengthened beams under static loading up to maximum load.

9.3.2   Static response of impact loaded beams

In this section test results and comparison of results for beams with different FRP strengthening are presented. The results presented include load-deformation relationship, internal work, and strain field.

For load-deflection curves in beams previously subjected to dynamic loading, deflection is given as the total deflection resulted from both tests by taking into consideration the plastic deformation resulted from impact loading. Maximum deformation, $u_{50\%FRmax}$, is given in the same manner as stated in Section 9.3, i.e., for a load level of 50 % of F_{Rmax}. The total internal work is also calculated as the area under the load-deflection curve until reaching the maximum deformation, $u_{50\%FRmax}$.

9.3.2.1   Response of different types of beams

In this section load-deflection relationship for unstrengthened, 1 layer and 3 layers FRP strengthened beams subjected to an impact of drop-weight from the same drop-height are presented in three sets.

Load-deflection curve for unstrengthened, 1 layer and 3 layers FRP strengthened beams, all subjected to 4 m drop height impact prior to static loading, is presented Figure 9.31. Maximum deflection, ultimate load and internal work are tabulated in Table 9.44. It is observed that the remaining residual capacity and internal work increased significantly when using FRP strengthening. Further, the plastic deformation obtained from impact loading also decreased considerably as a result of FRP strengthening. Comparing beam 10-B1-FRP3-D4 (1 layer FRP) and 16-B1-FRP3-D4 (3 layers FRP), the former happened to have a higher residual load

capacity, maximum deformation capacity and internal work. This could be due to a smaller degree of compression zone damage in beam 10-B1-FRP3-D4 since the deformation resulted from the impact load was smaller than expected see Section 9.2.1. Additional reason could be that a higher imulse load was absorbed in the section in case of 3 layers of FRP strengthened beam during impact loading prior to static loading which resulted in a more severe damage in 3 layer FRP strengthened beam. Generally, beams strengthened with 1 and 3 layers of FRP obtained an increase of remaining residual capacity and internal work compared with the reference beam.

Figure 9.31   Load-deflection relation for unstrengthened, 1 layer and 3 layers FRP strengthened beams subjected to 4 m drop weight impact prior to static loading.

Table 9.44   Maximum deflection, maximum load and internal work for beams subjected to 4 m drop weight impact prior to static loading.

Beam	Number of FRP layer	$u_{50\%FRmax}$ [mm]	F_{max} [kN]	W_{tot} [J]
04-B1-FRP0-D4	-	87	6.9	260
10-B1-FRP1-D4	1	105	9.2	545
16-B1-FRP3-D4	3	88	8.9	492

Load-deflection curve for unstrengthened, 1 layer and 3 layers FRP strengthened beams subjected to 3.5 m drop height impact prior to static loading is presented in Figure 9.32. Maximum deflection, ultimate load and total internal work are tabulated in Table 9.45. Beam 17-B2-FRP3-D3.5 (3 layers FRP) has shown a strange structural behaviour by failing at a lower load level compared with the other two beams as shown in Figure 9.32. The deformation capacity and total internal work for 1 layer FRP strengthening has resulted to be higher than that of unstrengthen beam.
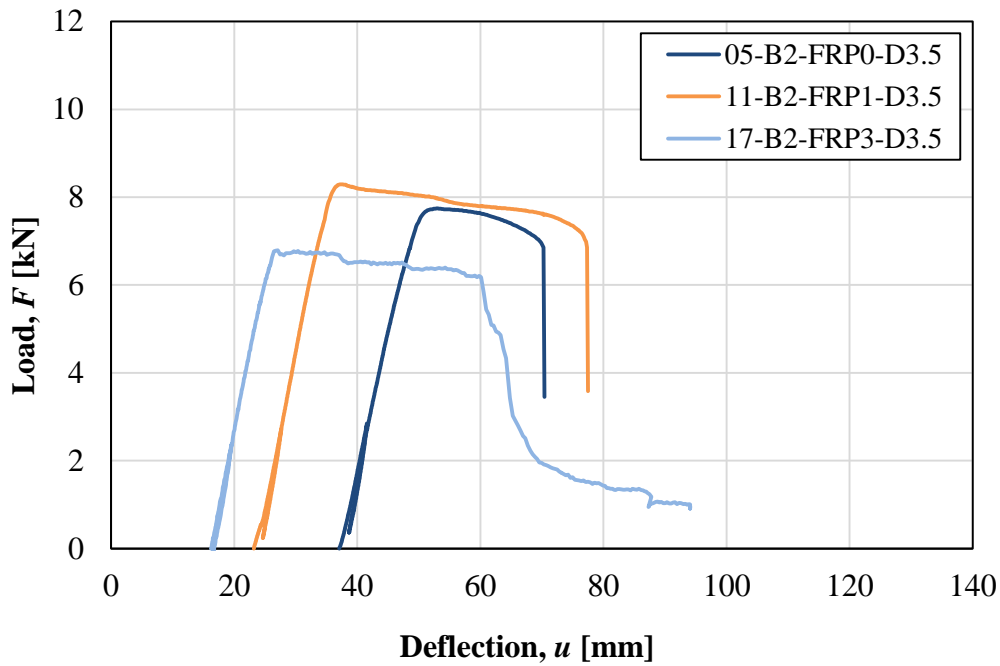
Figure 9.32   Load-deflection relation for unstrengthened, 1 layer and 3 layers FRP strengthened beams subjected to 3.5 m drop height impact prior to static loading.

Table 9.45   Maximum deflection, maximum load and internal work for beams subjected to 3.5 m drop height impact prior to static loading.

Beam	Number of FRP layer	$u_{50\%FRmax}$ [mm]	F_{max} [kN]	W_{tot} [Nm]
05-B2-FRP0-D3.5	-	70	7.7	204
11-B2-FRP1-D3.5	1	77	8.3	379
17-B2-FRP3-D3.5	3	63	6.8	271

Load-deflection curve for unstrengthened, 1 layer and 3 layers FRP strengthened beams subjected to 3 m drop weight impact prior to static loading is presented Figure 9.33. Maximum deflection, ultimate load and total internal work are tabulated in Table 9.46. Looking at Figure 9.33 and Table 9.46 the deformation capacity and remaining residual strength of the beams increased slightly as the amount of FRP strengthening increases. While the internal work for beams with FRP strengthening has shown a significant amount of increment.
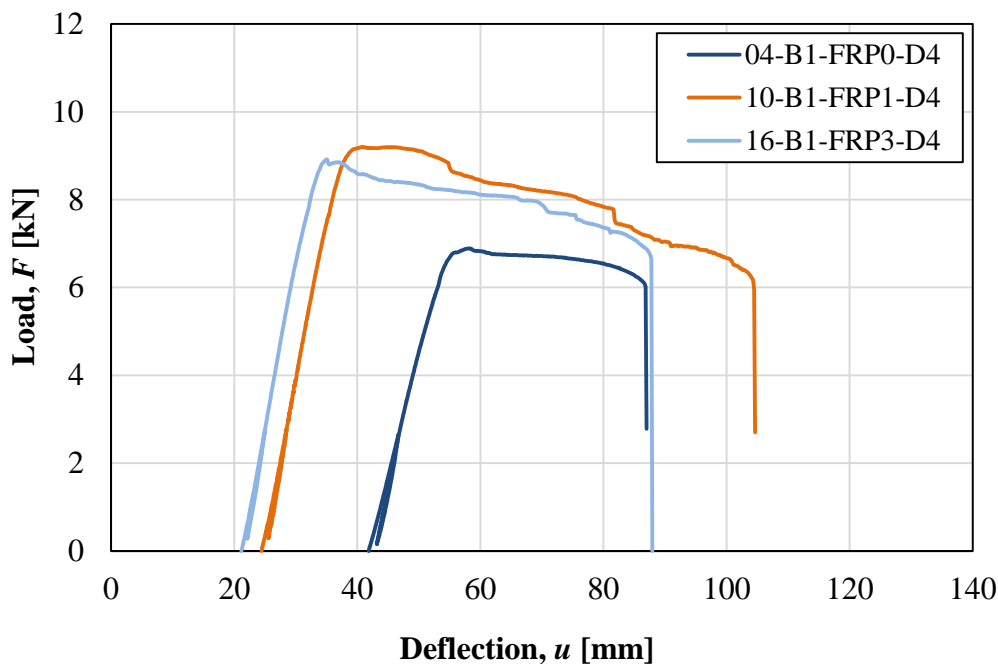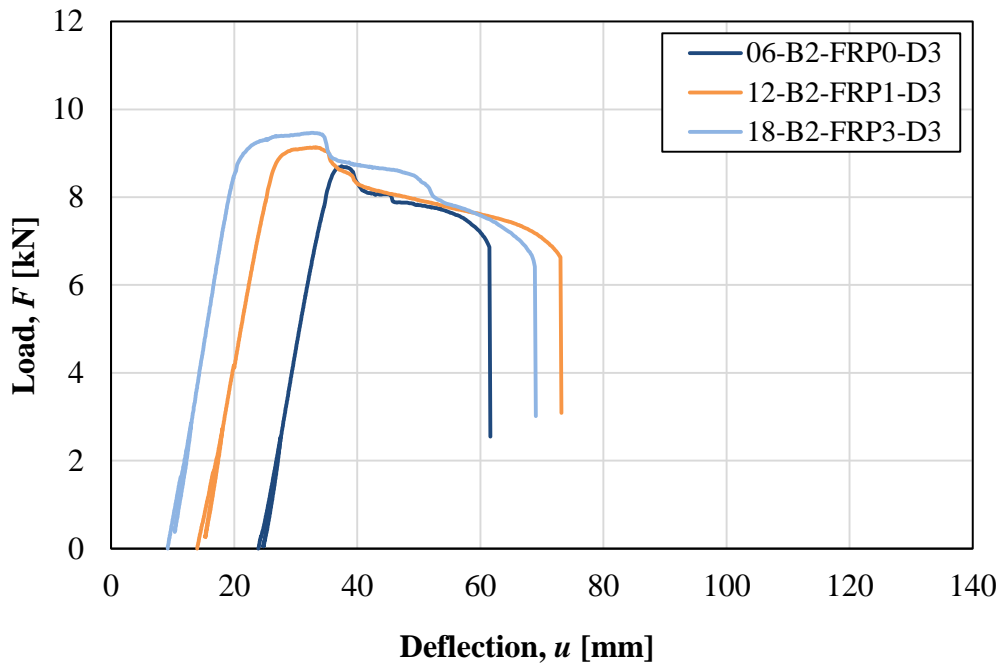
Figure 9.33 Load-deflection relation for unstrengthened, 1 layer and 3 layers FRP strengthened beams subjected to 3 m drop height impact prior to static loading.

Table 9.46 Maximum deflection, maximum load and internal work for beams subjected to 3.5 m drop height impact prior to static loading.

Beam	Number of FRP layer	$u_{50\%FRmax}$ [mm]	F_{max} [kN]	W_{tot} [Nm]
06-B2-FRP0-D3	-	62	8.7	255
12-B2-FRP1-D3	1	73	9.1	429
18-B2-FRP3-D3	3	69	9.5	460

9.3.2.2 Static response of previously impacted and only statically loaded beams

Beams that were loaded only statically are compared with beams of their type that were subjected to different drop weight impact prior to static loading. The comparison is presented in three sets for each type of strengthening.

For all three sets of beams, it can be seen that impacted beams exhibited a lower load capacity than only statically loaded beams and they tend to share the same behaviour with the unloading branch of only statically loaded beams. It is also observed that when height of drop weight increases the remaining residual capacity is reduced and maximum deformation increased except for beams with three layers of strengthening due to failing in shear type of failure.

Unstrengthened beams that were loaded only statically are presented in Figure 9.34 together with same type of beams that were exposed to 4 m, 3.5 m and 3 m drop height impact loading prior to static loading. Maximum deflection, ultimate load and moment together with total internal work from static loading tests are tabulated in Table 9.47.

Figure 9.34   Load-deflection relation for unstrengthened beams subjected to only static loading and drop weight impact of 4 m, 3.5 m and 3 m prior to static loading.

Table 9.47   Maximum deflection, maximum load and maximum moment and total internal work for unstrengthened beams subjected to only static loading and dynamic loading prior to static loading (for only statically loaded beams the average values are presented).

Beam	Drop height [m]	$u_{50\%FRmax}$ [mm]	F_{max} [kN]	M_u [kNm]	W_{tot} [J]
Only statically loaded	-	62	9.7	3.2	500
04-B1-FRP0-D4	4.0	87	6.9	2.2	260
05-B2-FRP0-D3.5	3.5	70	7.7	2.5	204
06-B2-FRP0-D3	3.0	62	8.7	2.8	255

1 layer FRP strengthened beams that were loaded only statically are presented together with the same type of beams that were exposed to 4 m, 3.5 m and 3 m drop height impact loading prior to static loading in Figure 9.34. Maximum deflection, ultimate load and moment together with total internal work are tabulated in Table 9.48.
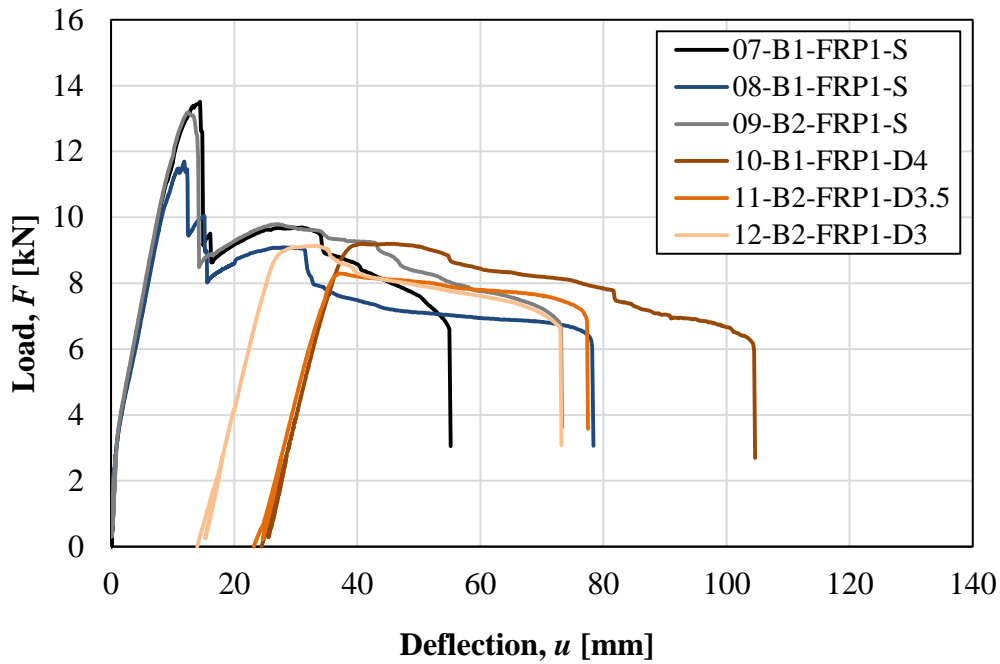
Figure 9.35   Load-deflection relation for 1 layer FRP strengthened beams subjected to only static loading and drop weight impact of 4 m, 3.5 m and 3 m prior to static loading.

Table 9.48   Maximum deflection, maximum load and maximum moment and total internal work for 1 layer strengthened beams subjected to only static loading and dynamic loading prior to static loading (for only statically loaded beams the average values are presented).

Beam	Drop height [m]	$u_{50\%FRmax}$ [mm]	F_{max} [kN]	M_u [kNm]	W_{tot} [J]
Only statically loaded	-	69	12.8	4.2	576
10-B1-FRP1-D4	4.0	105	9.2	3.0	545
11-B2-FRP1-D3.5	3.5	77	8.3	2.7	379
12-B2-FRP1-D3	3.0	73	9.1	3.0	429

The 3 layers FRP strengthened beams that were loaded only statically are presented with the same type of beams that were exposed to 4 m, 3.5 m and 3 m drop height impact loading prior to static loading in Figure 9.34. Maximum deflection, ultimate load and moment together with total internal work are tabulated in Table 9.49.

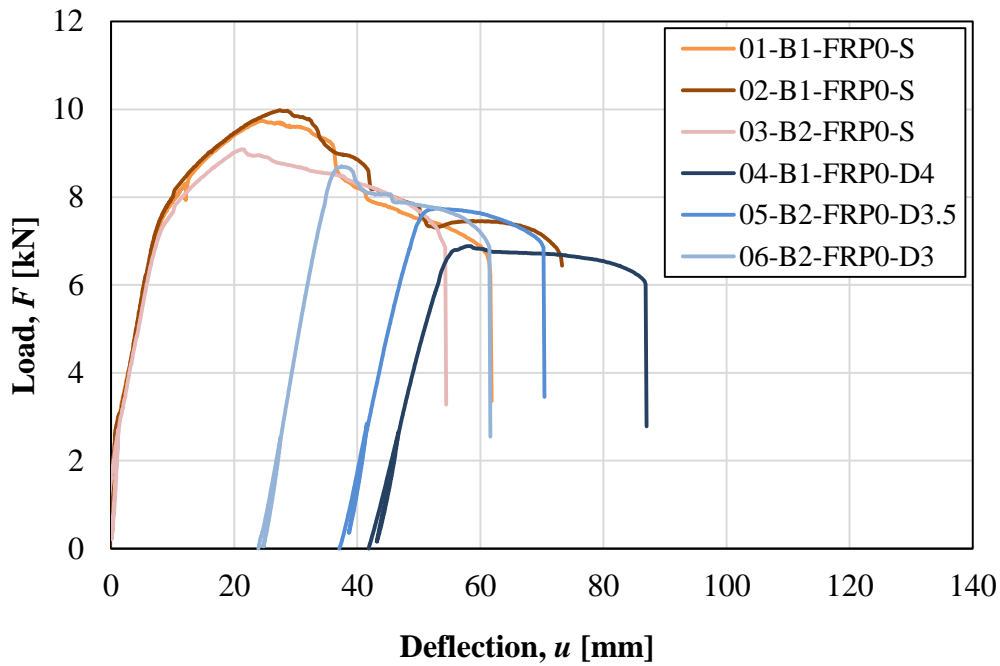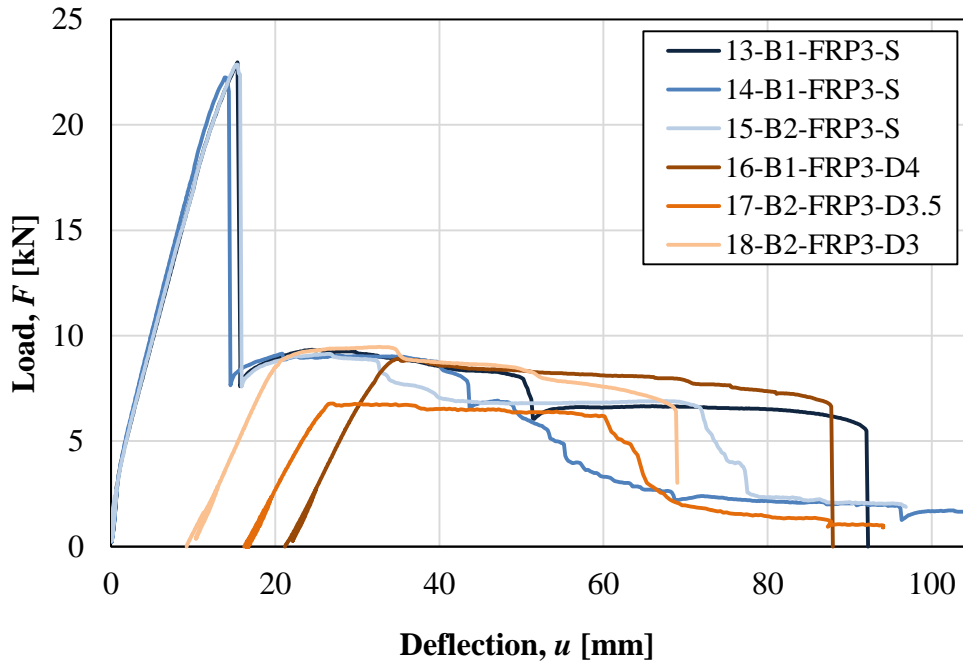*Figure 9.36   Load-deflection relation for 3 layers FRP strengthened beams subjected to only static loading and drop weight impact of 4 m, 3.5 m and 3 m prior to static loading.*

Table 9.49   Maximum deflection, maximum load and maximum moment and total internal work for 3 layers strengthened beams subjected to only static loading and dynamic loading prior to static loading (for only statically loaded beams the average values are presented).

Beam	Drop height [m]	$u_{50\%FRmax}$ [mm]	F_{max} [kN]	M_u [kNm]	W_{tot} [J]
Only statically loaded	-	74	22.7	7.4	701
16-B1-FRP3-D4	4.0	88	8.9	2.9	492
17-B2-FRP3-D3.5	3.5	63	6.8	2.2	271
18-B2-FRP3-D3	3.0	69	9.5	3.1	460

9.3.2.3   Approximation and comparison of internal work

To see how the impact loading influenced the internal work approximate calculation is done by adding a section of internal work, W_{imp} It is calculated from the only statically loaded beams to compensate for the loss due to drop weight impact. It is assumed that the previously impacted beams would have exhibit the same amount of internal work with similar kind of beams that were loaded only statically until its curve coincides with the unloading branch of the only statically loaded beam. This approximated internal work is illustrated in Appendix K and is calculted as

$$W_{imp+stat} = W_{imp} + W_{pl,stat} \tag{9.2}$$

Where $W_{pl,stat}$ is calculated as internal work under the load-deflection curve for statically loaded impacted beams after the point where it coincides with the unloading branch of only statically loaded beam of the same kind. Finally, a comparison is made between $W_{tot,stat}$ and $W_{imp+stat}$ and

is presented in Table 9.50 to Table 9.52. Where $W_{tot,stat}$ is the average total internal work for only statically loaded beams. This is the same methodology used by Andersson and Pettersson (2019). It can be concluded that FRP strengthening do not have negative effect on internal work except for 17-B2-FRP3-D3.5. It is observed that due to FRP strengthening the amount of energy that is absorbed by the beams is not reduced significantly even for 3 layer FRP strengthening.

Table 9.50   *Approximation and comparison of internal work for unstrengthened impacted beams loaded statically vs. only statically loaded beams. (W_{imp} and $W_{imp+stat}$ average values for only statically loaded beams).*

Beam	W_{imp} [J]	$W_{pl,stat}$ [J]	$W_{imp+stat}$ [J]	$W_{tot,stat}$ [Nm]	$\dfrac{W_{imp+stat}}{W_{tot,stat}}$
04-B1-FRP0-D4	447	204	652	500	1.30
05-B2-FRP0-D3.5	409	147	556	500	1.11
06-B2-FRP0-D3	299	195	494	500	0.99

Table 9.51   *Approximation and comparison of internal work for 1 layer FRP strengthened impacted beams loaded statically vs. only statically loaded beams. (W_{imp} and $W_{imp+stat}$ taken as average values for only statically loaded beams).*

Beam	W_{imp} [J]	$W_{pl,stat}$ [J]	$W_{imp+stat}$ [J]	$W_{tot,stat}$ [Nm]	$\dfrac{W_{imp+stat}}{W_{tot,stat}}$
10-B1-FRP1-D4	338	485	823	576	1.42
11-B2-FRP1-D3.5	332	319	651	576	1.13
12-B2-FRP1-D3	250	362	613	576	1.06

Table 9.52   *Approximation and comparison of internal work for 3 layers FRP strengthened impacted beams loaded statically vs. only statically loaded beams. (W_{imp} and $W_{imp+stat}$ is taken as average values for only statically loaded beams).*

Beam	W_{imp} [J]	$W_{pl,stat}$ [J]	$W_{imp+stat}$ [J]	$W_{tot,stat}$ [Nm]	$\dfrac{W_{imp+stat}}{W_{tot,stat}}$
16-B1-FRP3-D4	375	431	806	701	1.15
17-B2-FRP3-D3.5	331	215	546	701	0.78
18-B2-FRP3-D3	257	403	660	701	0.94

9.3.3 Strain field

Strain fields have been analysed and are presented in this section. The beams will be presented in the order of the reference beams first, then the strengthened with 1 layer FRP and last the beams strengthened with 3 layers FRP. This section will show the difference in behaviour depending on what loading history the beams have, statically or statically and dynamically loaded, number of FRP strengthening and drop height for the beams that's been subjected to dynamic loading.

The results are extracted from GOM Correlate and major strains are the ones studied, high strain values corresponds approximately to real cracks. The colour scale have been analysed and the settings that show most strains without too much noise have been chosen to 0.2 %-2 %, it is also presented in the tables. Where the colour becomes white in the beams shows open cracks or spalling of concrete and GOM Correlate can no longer get any information from these regions.

The whole beam will be illustrated with its strain field at two times, first when it reach its maximum force and then right before failure. For the beams that's been subjected to dynamic loading prior to these tests there will be an additional picture presented of the beam that show its deformed shape before the static tests begin.

9.3.3.1 Reference beams

The reference beams, not strengthened with FRP, are presented with its strain field in Table 9.53 and Table 9.54. The tables also include maximum force, deflection at that time and maximum deflection.

Table 9.53   Strain field under static loading at time for maximum force and at time for maximum deflection illustrated for reference beams and beam 19-B1-FRP0-S subjected to static loading only.
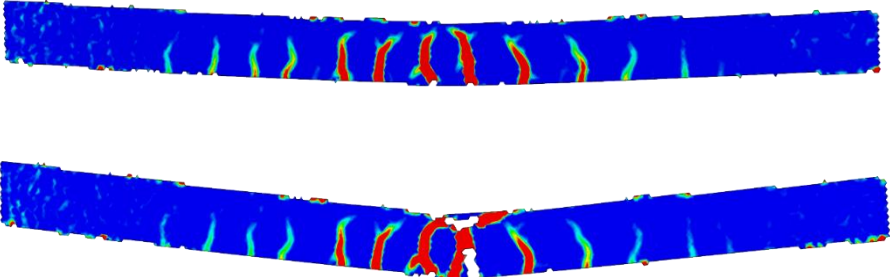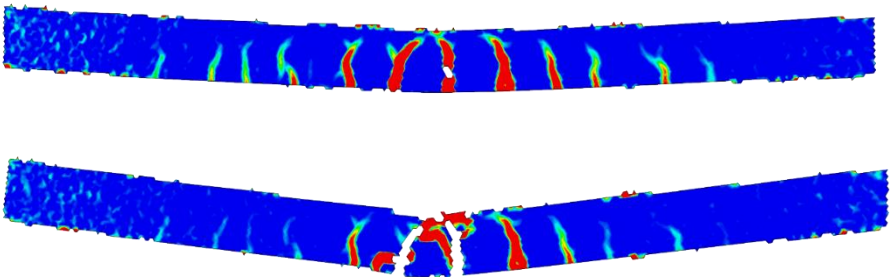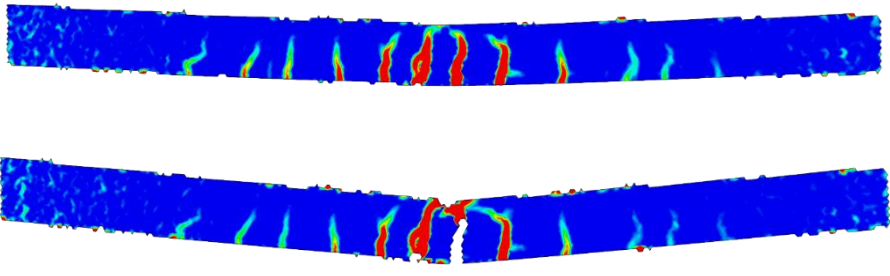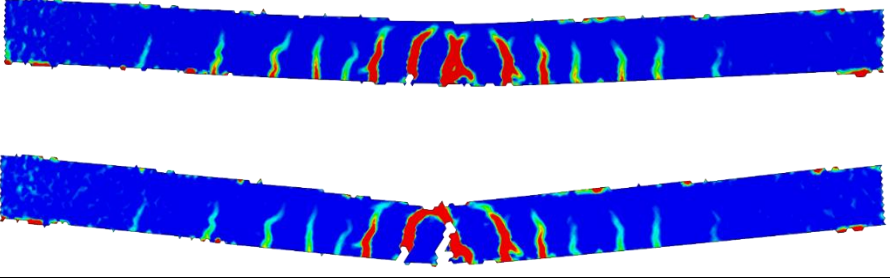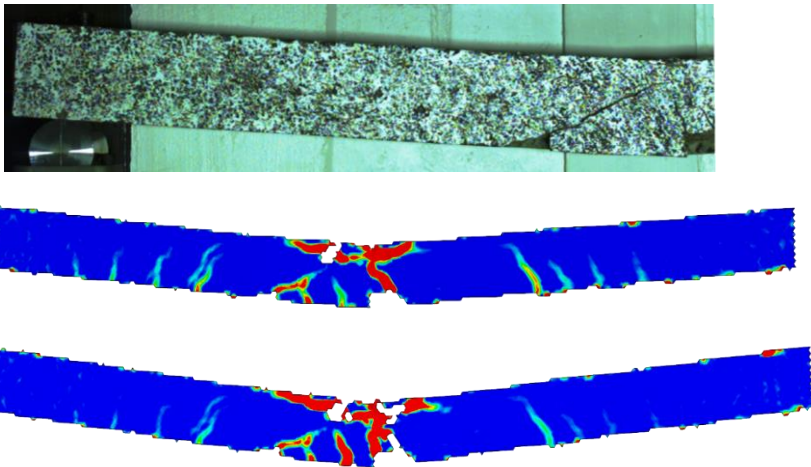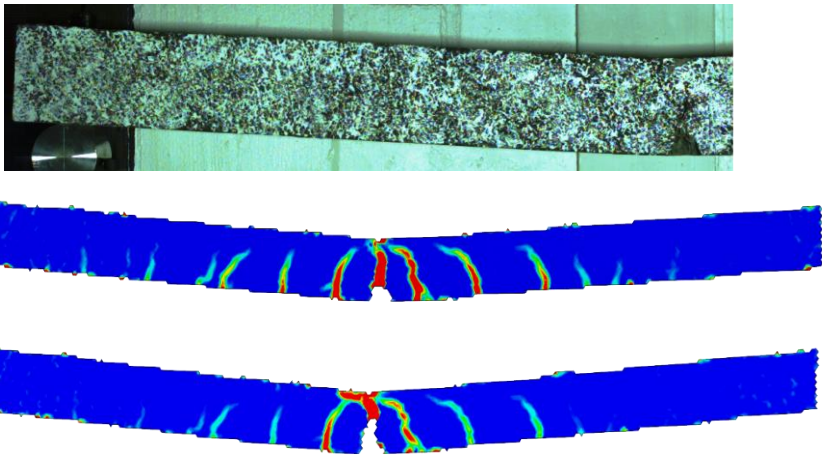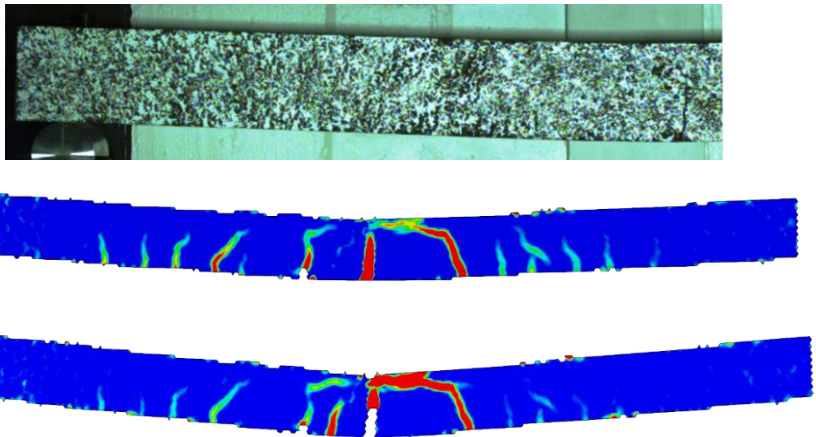
01-B1-FRP0-S F_{max} = 9.7 kN u_{Fmax} = 24.6 mm u_{max} = 61.8 mm	
02-B21FRP0-S F_{max} = 10.0 kN u_{Fmax} = 27.5 mm u_{max} = 73.3 mm	
03-B2-FRP0-S F_{max} = 9.1 kN u_{Fmax} = 21.3 mm u_{max} = 54.4 mm	
19-B1-FRP0-S F_{max} = 9.7 kN u_{Fmax} = 25.9 mm u_{max} = 59.8 mm	
Scale	**0.2 %** ▬▬▬▬▬▬▬▬ **2 %**

Table 9.54   *Strain field under static loading at time for maximum force and at time for*
              maximum deflection illustrated for reference beams subjected to dynamic
              loading before static loading. A photo of the damaged beam before static loading
              is also presented.

04-B1-FRP0-D4	
F_{max} = 6.9 kN u_{Fmax} = 58.1 mm u_{max} = 87.0 mm	
05-B2-FRP0-D3.5	
F_{max} = 7.7 kN u_{Fmax} = 53.1 mm u_{max} = 70.4 mm	
06-B2-FRP0-D3	
F_{max} = 8.7 kN u_{Fmax} = 37.4 mm u_{max} = 61.6 mm	
Scale	**0.2 %** **2 %**

9.3.3.2 Beams strengthened by 1 layer FRP

The beams strengthened with 1 layer FRP, are presented with their strain field in Table 9.55 and Table 9.56. The tables also include maximum force, deflection at that time and maximum deflection. The data for beam 08-B1-FRP1-S was unfortunately lost, therefore no strain fields can be illustrated for this beam.

Table 9.55   Strain field under static loading at time for maximum force and at time for maximum deflection illustrated for beams strengthened by 1 layer FRP and subjected to static loading only.
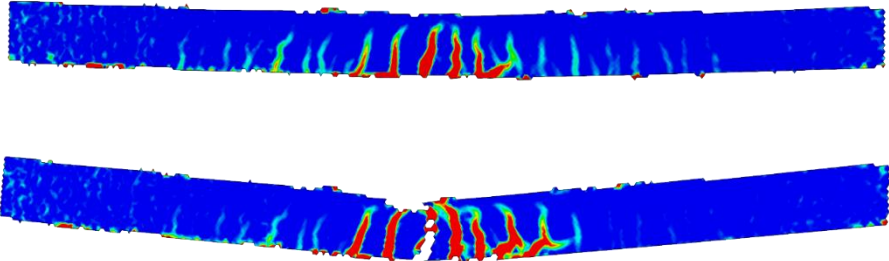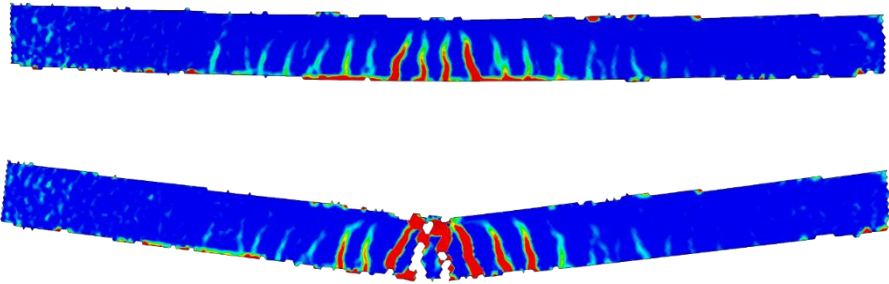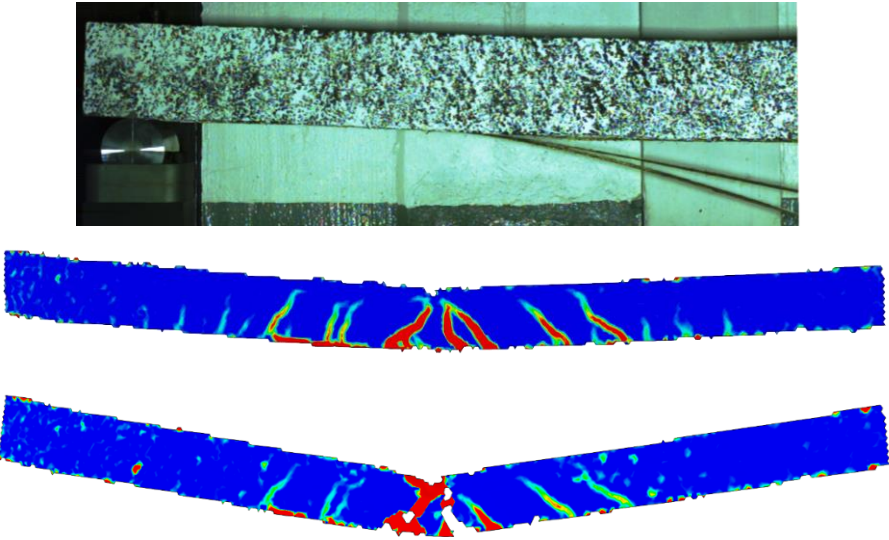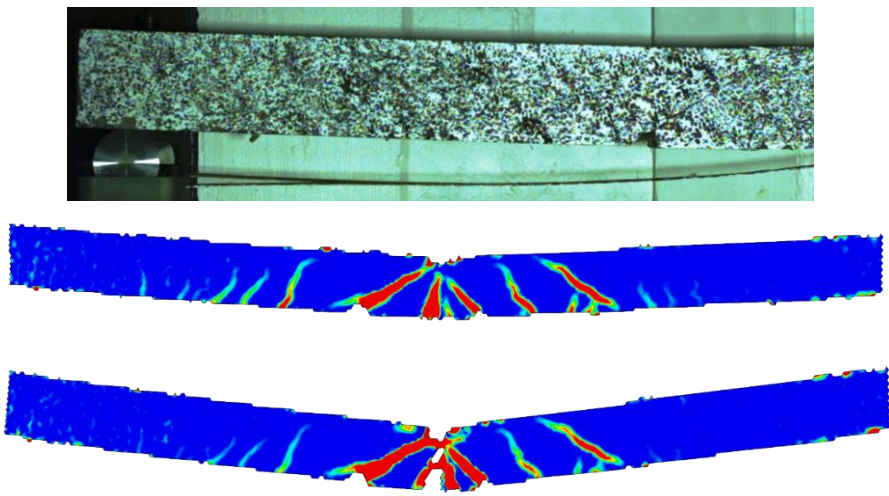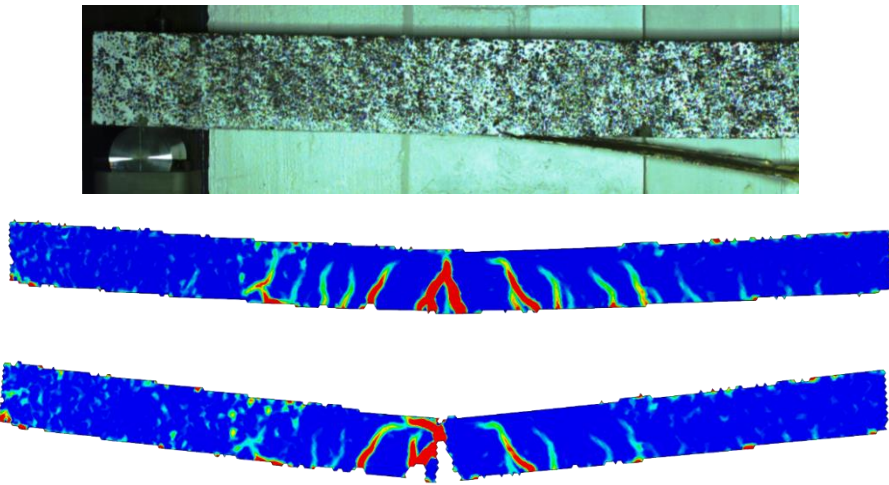
07-B1-FRP1-S F_{max} = 13.5 kN u_{Fmax} = 14.4 mm u_{max} = 55.2 mm	
08-B1-FRP1-S F_{max} = 11.7 kN u_{Fmax} = 11.9 mm u_{max} = 78.4 mm	- -
09-B2-FRP1-S F_{max} = 13.2 kN u_{Fmax} = 12.5 mm u_{max} = 73.3 mm	
Scale	**0.2 %** **2 %**

Table 9.56   Strain field under static loading at time for maximum force and at time for maximum deflection illustrated for beams strengthened by 1 layer FRP and subjected to dynamic loading before static loading. A photo of the damaged beam before static loading is also presented.

10-B1-FRP1-D4 F_{max} = 9.2 kN u_{Fmax} = 41.0 mm u_{max} = 104.6 mm	
11-B2-FRP1-D3.5 F_{max} = 8.3 kN u_{Fmax} = 37.3 mm u_{max} = 77.5 mm	
12-B2-FRP1-D3 F_{max} = 9.1 kN u_{Fmax} = 33.3 mm u_{max} = 73.2 mm	
Scale	**0.2 %** ▬▬▬▬▬▬ **2 %**

9.3.3.3 Beams strengthened by 3 layers FRP

The beams strengthened with 3 layers FRP, are presented with its strain field in Table 9.57 and Table 9.58. The tables also include maximum force, deflection at that time and maximum deflection.

Table 9.57 Strain field under static loading at time for maximum force and at time for maximum deflection illustrated for beams strengthened by 3 layers FRP and subjected to static loading only.
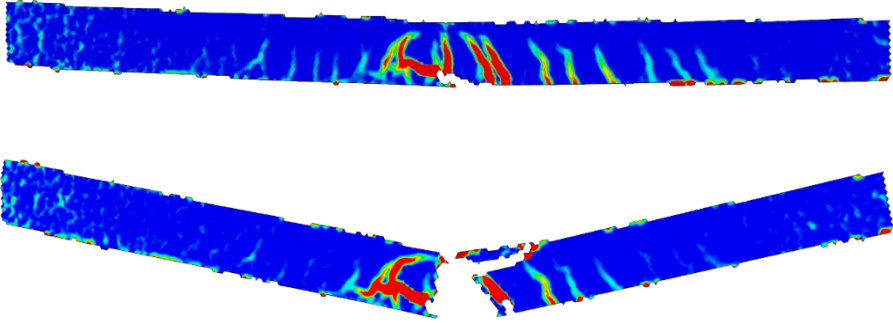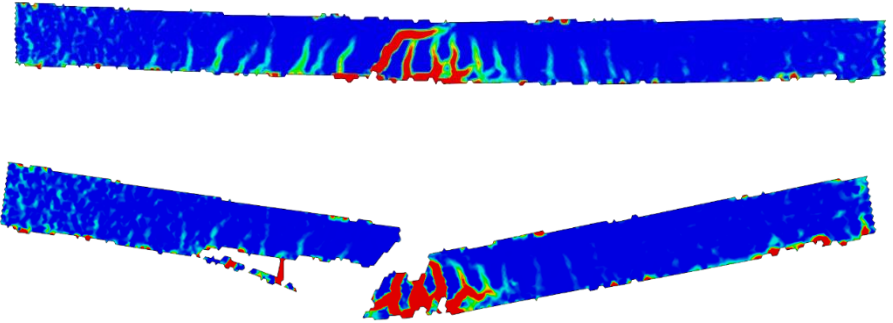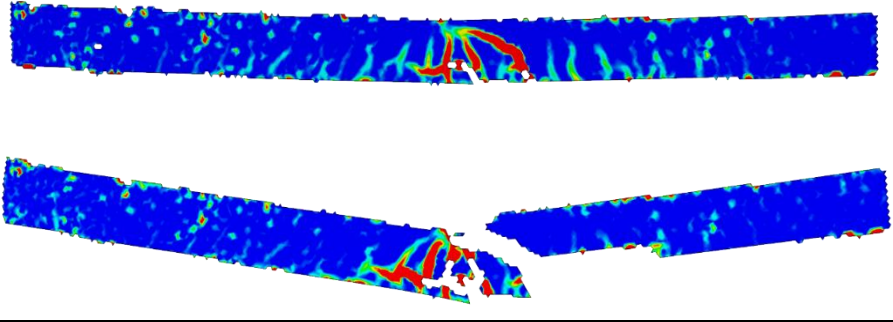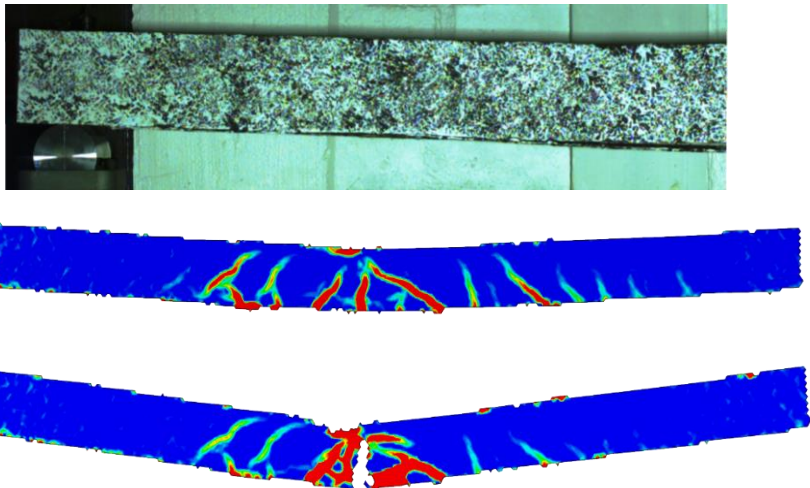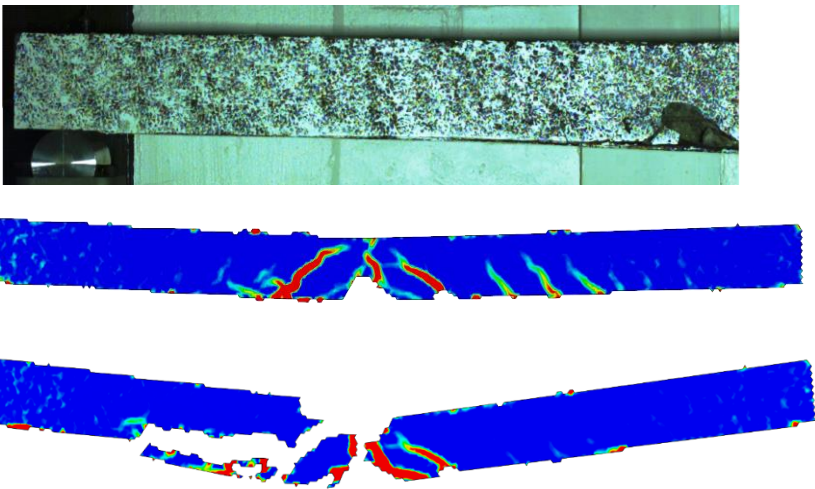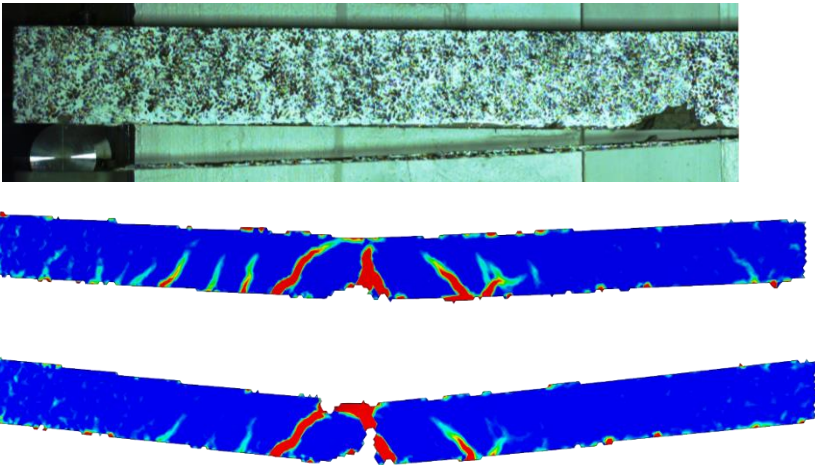
13-B1-FRP3-S F_{max} = 23 kN u_{Fmax} = 15.4 mm u_{max} = 92.1 mm	
14-B1-FRP3-S F_{max} = 22.3 kN u_{Fmax} = 13.8 mm u_{max} = 119.3 mm	
15-B2-FRP3-S F_{max} = 22.9 kN u_{Fmax} = 15.2 mm u_{max} = 96.9 mm	
Scale	**0.2 %** **2 %**

Table 9.58   Strain field under static loading at time for maximum force and at time for
maximum deflection illustrated for beams strengthened by 3 layers FRP and
subjected to dynamic loading before static loading. A photo of the damaged beam
before static loading is also presented.

16-B1-FRP3-D4	
F_{max} = 8.9 kN u_{Fmax} = 35.1 mm u_{max} = 88.0 mm	
17-B2-FRP3-D3.5	
F_{max} = 6.8 kN u_{Fmax} = 26.7 mm u_{max} = 94.0 mm	
18-B2-FRP3-D3	
F_{max} = 9.5 kN u_{Fmax} = 32.7 mm u_{max} = 69.0 mm	
Scale	0.2 % ▬▬▬ 2 %

9.3.3.4 Comparison

A clear difference can be seen when comparing the different layers of FRP strengthened beams with the reference beams. The three reference beams subjected to static loading only and beam 19-B1-FRP0-S, which was also unstrengthened and only subjected to static loading, showed a similar behaviour with uniformly distributed bending cracks along the beam with largest cracks in the middle of the beam. All strains appear at the bottom of the beams and develops upward. When the major crack in the middle appear the smaller strains closer to the support becomes smaller. This can be observed when comparing the two stages of time when the strain fields are illustrated.

The reference beams show a slight scatter in result for the beams that were previously subjected to drop weight impact. Beam 04-B1-FRP0-D4 with a drop height of 4 m showed some local damage at the top of the beam where the load was applied since large cracks appeared at that place. Beam 05-B2-FRP0-D3.5 and 06-B2-FRP0-D3 that was subjected to 3.5 m and 3 m drop height respectively, had a more similar pattern that looked more like the strain field illustrated for the reference beams subjected to static loading only. However, the strains were not as uniformly distributed along the beam and the localised strains obtained closer to the support were smaller. The reason for the difference in behaviour for the reference beams subjected to impact load prior to these tests can be observed in the pictures showing the initial cracks before loaded statically. Beam 04-B1-FRP0-D4 had developed larger cracks from the dynamic testing compared with the other two beams.

The beams strenghtened by 1 layer of FRP and only loaded statically showed smaller strains compared with the reference beams. The distance between the cracks were closer and they were more centred to the middle of the beam. Beam 10-B1-FRP1-D4 and 11-B2-FRP1-D3.5 were also strenghtened by 1 layer FRP, but also subjected to drop weight impact with height 4 m and 3.5 m respectively. The strain fields in these beams had a more distinct inclination toward the centre of the applied force, this is best illustrated in the pictures at time of maximum force. For beam 12-B2-FRP1-D3 which had a smaller drop height of 3 m, this behaviour was not as clear.

For the beams strengthened with 3 layers of FRP and subjected to only static loading, the same behaviour as for the strengthening of 1 layer FRP could be observed at the start. Furthermore it caused some kind of shear failure for beam 14-B1-FRP3-S and 15-B2-FRP3-S, starting from the top of the beam due to local crushing of concrete. This kind of shear crack also appeared for beam 17-B2-FRP3-D3.5 that was subjected to 3.5 m drop height prior to static loading. Beam 16-B1-FRP3-D4 and 18-B2-FRP3-D3 showed similar behaviour in strain field to each other. The strains were more concentrated to the middle part of the beam and were inclined toward the point of load. At maximum deflection the smaller strains did not show anymore, but the strains in the middle increased further.

9.3.4 Crack width

Maximum crack width were extracted from GOM Correlate from the static testing to examine the effects when strengthening with FRP. The beams subjected to only static loading were studied in this case. The beams strengthened with 3 layers of FRP developed large plastic deformations which made it difficult to determine the width of the resulting cracks since the spalling of concrete and open cracks caused loss of data points. The data for beam 08-B1-FRP1-S was lost, hence no results for this beam is shown.

Table 9.59   Maximum crack width for the beams subjected to static loading only.

Beam	Maximum crack width [mm]
01-B1-FRP0-S	7.2
02-B21FRP0-S	8.1
03-B2-FRP0-S	8.0
19-B1-FRP0-S	7.8
07-B1-FRP1-S	7.5
08-B1-FRP1-S	-
09-B2-FRP1-S	4.9
13-B1-FRP3-S	-
14-B1-FRP3-S	-
15-B2-FRP3-S	-

There are only two beams strengthened with FRP that gives reliable results for the maximum crack width, see Table 9.59. Beam 07-B1-FRP1-S shows a similar maximum crack width as the unstrengthened beams but slightly smaller than most, whereas beam 09-B2-FRP1-S has a significantly smaller maximum crack width.

The debonding occured at approximate the same time for both beam 07-B1-FRP1-S and beam 09-B2-FRP1-S. It is marked in the graph where this happen with a dashed line. Both beams show rather similar behaviour in crack width when debonding, see Figure 9.37.
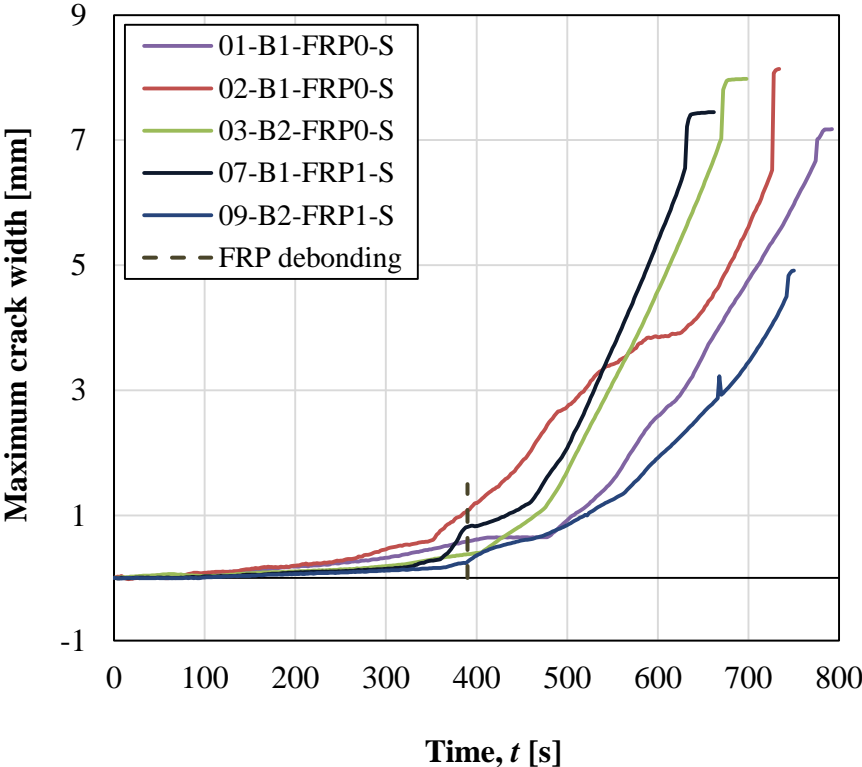
Figure 9.37   Development of maximum crack width for reference beams and beams strengthened with 1 layer FRP, subjected to static loading only.

10 Comparison of Experimental Results with Predictions

Predictions for the experimental results are in this chapter compared with the actual results that were received from the experimental testing of both dynamic response and static response.

10.1 Dynamic response

Experimental results presented in Section 9.2 are compared with the predicted results in Section 8.2. The results that are compared are the 2DOF calculations for deflection-time relation for the beams and velocity-time relation for the drop weight. Additional, the propagation velocity for the beam is compared with the velocity of initial deflection. Two different values for the internal resistance of the beam, R_2, were studied in the cases of deflection-time and velocity-time relation. The predicted value is calculated in Section 8.1.1.1 and the measured value is the average value, for values above 8 kN, from the experimental testing of the unstrengthened beams subjected to static loading only, presented in Section 9.3.1.1.

10.1.1 Deflection-time relation for the beam

The comparison between predicted values and experimental results of deflection-time curve for reference beams subjected to drop heights 4 m, 3.5 m and 3 m are presented in Figure 10.1 to Figure 10.3. Maximum deflection and plastic deformation for each drop height of the predictions and the experimental results for unstrenghtened beams are tabulated in Table 10.1 and Table 10.2.
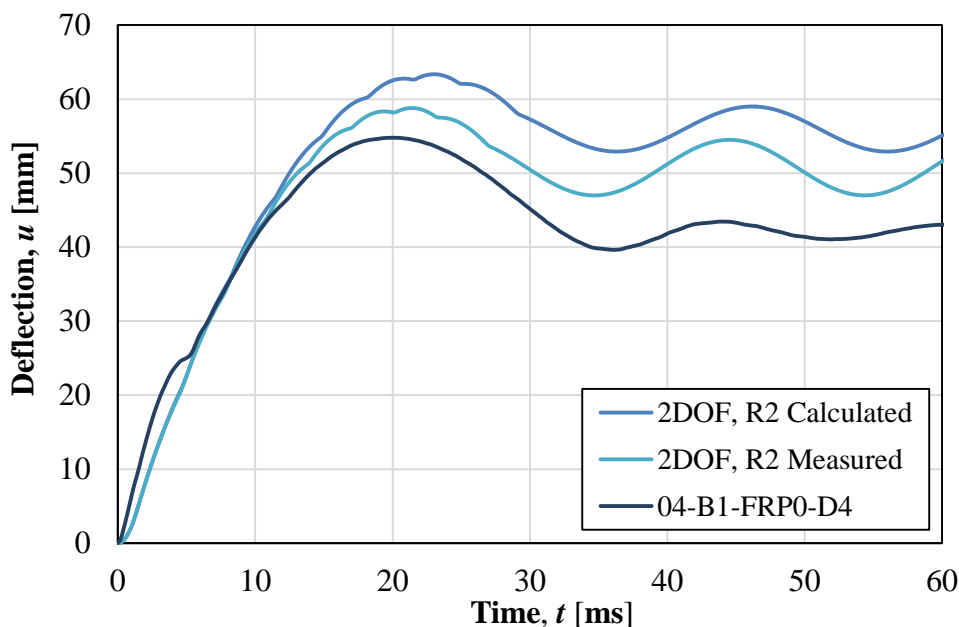
Figure 10.1   Experimental and predicted deflection-time relation for unstrengthened beams subjected to 4 m drop height.
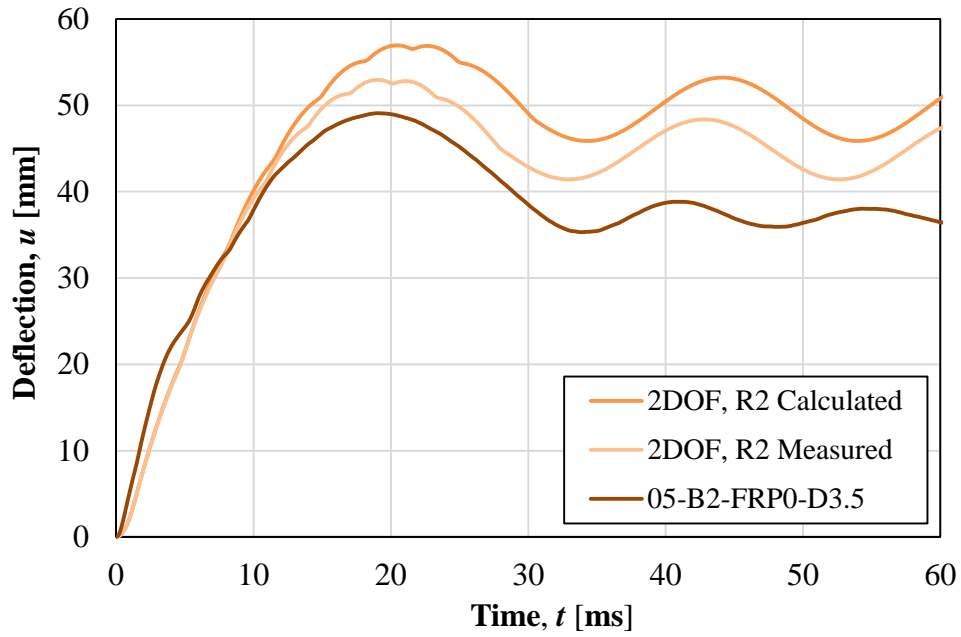
Figure 10.2   Experimental and predicted deflection-time relation for unstrengthened beams subjected to 3.5 m drop height.
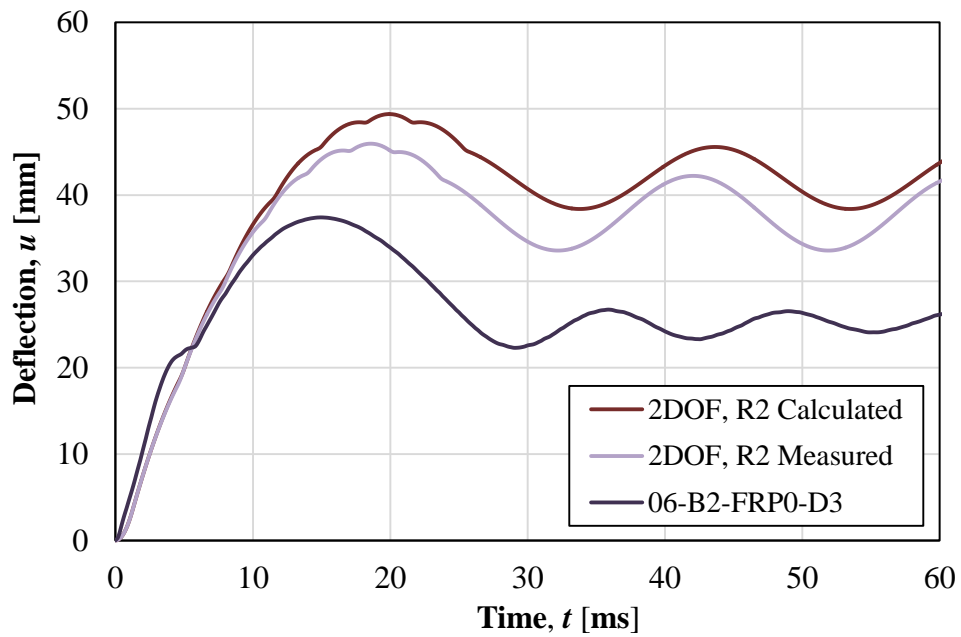
Figure 10.3   Experimental and predicted deflection-time relation for unstrengthened beams subjected to 3 m drop height.

Table 10.1   Comparison of maximum deflection for unstrengthened beams subjected to different drop heights.

Drop height [m]	u_{max} [mm] for experimental result	u_{max} [mm] for $R_{2,calculated}$	u_{max} [mm] for $R_{2,measured}$
4.0	54.8	63.4	58.8
3.5	49.1	56.9	53.0
3.0	37.4	49.4	46.0

Table 10.2   Comparison of plastic deformation for unstrengthened beams subjected to different drop heights.

Drop height [m]	u_{pl} [mm] experimental result	u_{pl} [mm] $R_{2,calculated}$	u_{pl} [mm] $R_{2,measured}$
4.0	42.9	56.0	50.7
3.5	38.2	49.5	44.9
3.0	24.7	42.0	37.9

Figure 10.1 to Figure 10.3 show that the calculated value for the internal resistance of the beam, R_2, results in values that are too conservative. The results for the prediction with measured R_2 show values in-between the calculated R_2 and experimental results from the dynamic testing for drop heights of 4 m and 3.5 m. However, for the 3 m drop height the deflection-time relation show larger differences when comparing predictions with the experimental results. Moreover, for all drop heights the time for the peak is shifted to the right for the measured R_2 and even further for the calculated R_2.

10.1.2 Velocity-time for the drop weight

The comparison between predicted values and experimental results of velocity-time curve for the drop weight subjected to drop heights 4 m, 3.5 m and 3 m are presented in Figure 10.4 to Figure 10.6.
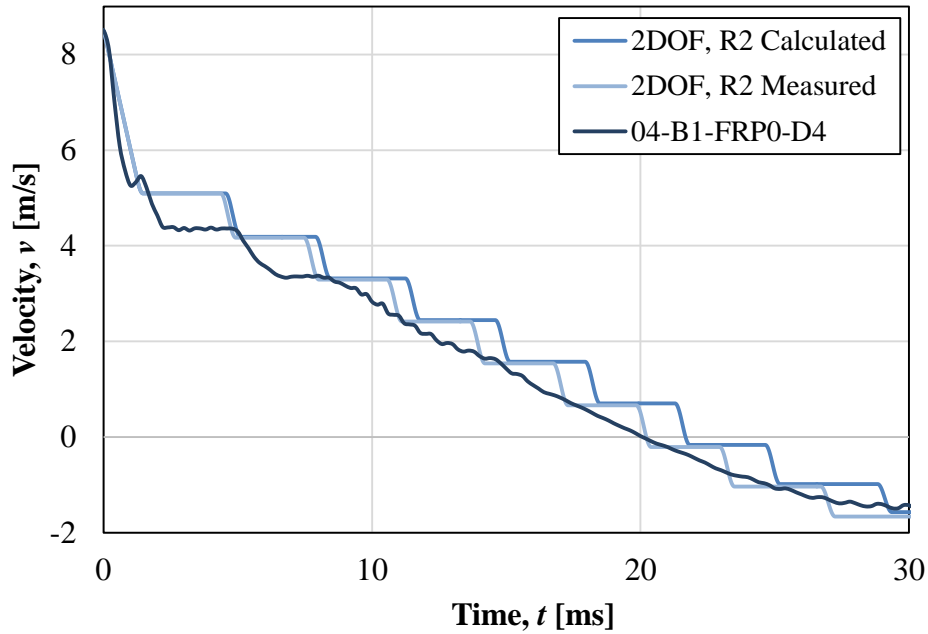
Figure 10.4   Experimental and predicted velocity-time relation for the drop weight subjected to 4 m drop height.
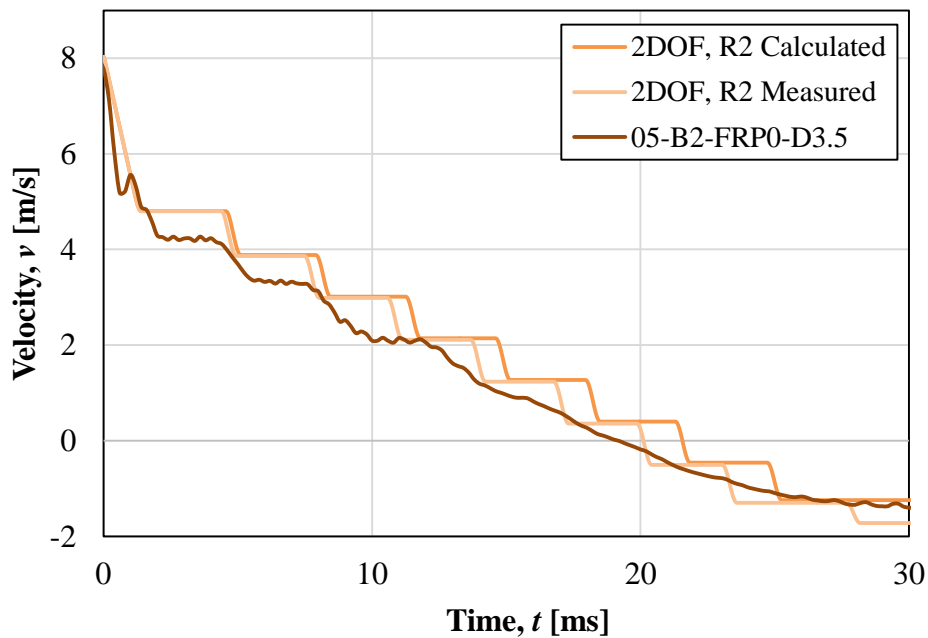
Figure 10.5   Experimental and predicted velocity-time relation for the drop weight subjected to 3.5 m drop height.
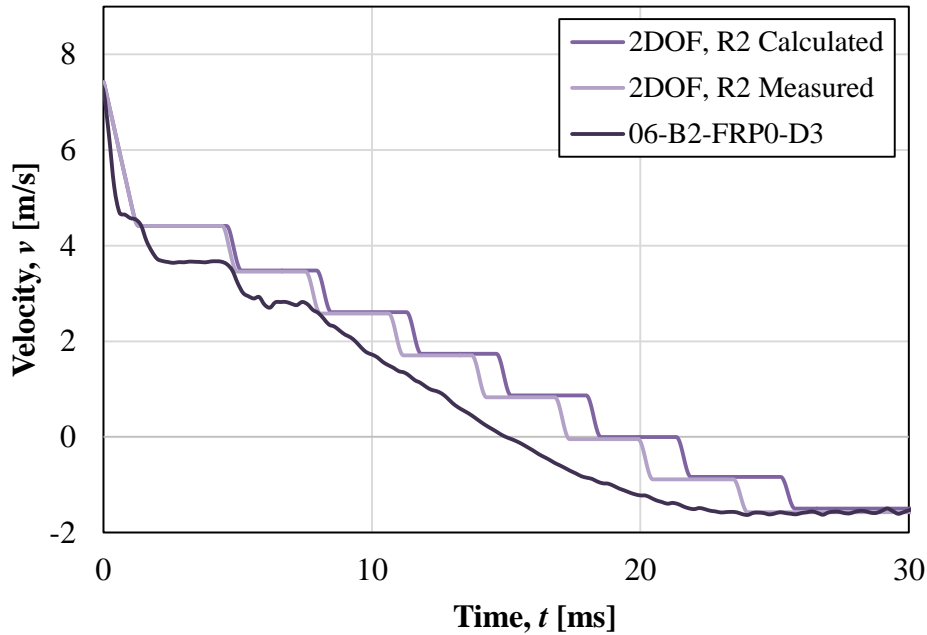
Figure 10.6 Experimental and predicted velocity-time relation for the drop weight subjected to 3 m drop height.

The velocity-time relationship is slightly overestimated the whole way for all drop heights, more for the drop height of 3 m.

10.1.3 Propagation velocity

The predicted shear velocity was calculated to be 2 438 m/s in Section 8.2.2, which gives the impact propagation time of 0.27 ms for the active part to span the whole beam. This is approximately a 4 - 5 times smaller value compared with the values from the velocity of initial deflection for the deformed shape which were 1.2 ms for beam 04-B1-FRP0-D4 and 16-B1-FRP3-D4, and 1.4 ms for beam 10-B1-FRP1-D4, see Section 9.2.5.1. These observations were also made by Andersson and Pettersson (2019) and Jönsson and Stenseke (2018) in previous years theses about impact loading.

The predictions based on Yi et al. (2016) assume that the shear velocity is the velocity for stress waves in concrete. By studying the calculated velocity of initial deflection for the deformed beam, it can be seen that those velocities are much smaller than the predicted velocity, see Table 9.27. This was also observed by Ulzurrun et al. (2019), which had average propagation velocities in the range of 250 – 1 250 m/s, see Figure 9.25.

10.2 Static response

Experimental results presented in Section 9.3 are compared with the predicted results in Section 8.1. From load-deflection relation, the results from prediction have resulted in overestimation of ultimate load and stiffness, especially in case of FRP strengthening.

10.2.1 Load-deformation response

Load deflection response for experimental and test results of reference beams are presented in Figure 10.7 and Figure 10.8. Figure 10.7 presents comparison for only statically loaded beams where Figure 10.8 presents comparison for beams subjected to drop weight impact of 3 m prior to static loading together with predicted response in state II for a cracked state.
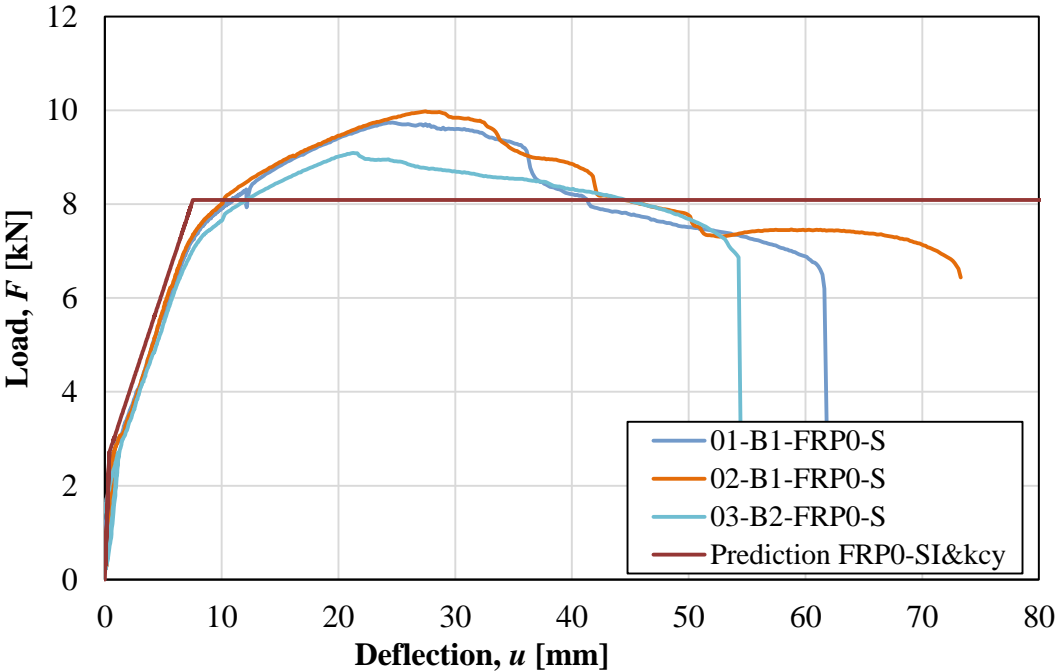
Figure 10.7   Experimental and predicted load-deflection relation for unstrengthened beams subjected to only static loading.

Load-deflection relation for experimental and test results for reference beams are presented in Figure 10.7.
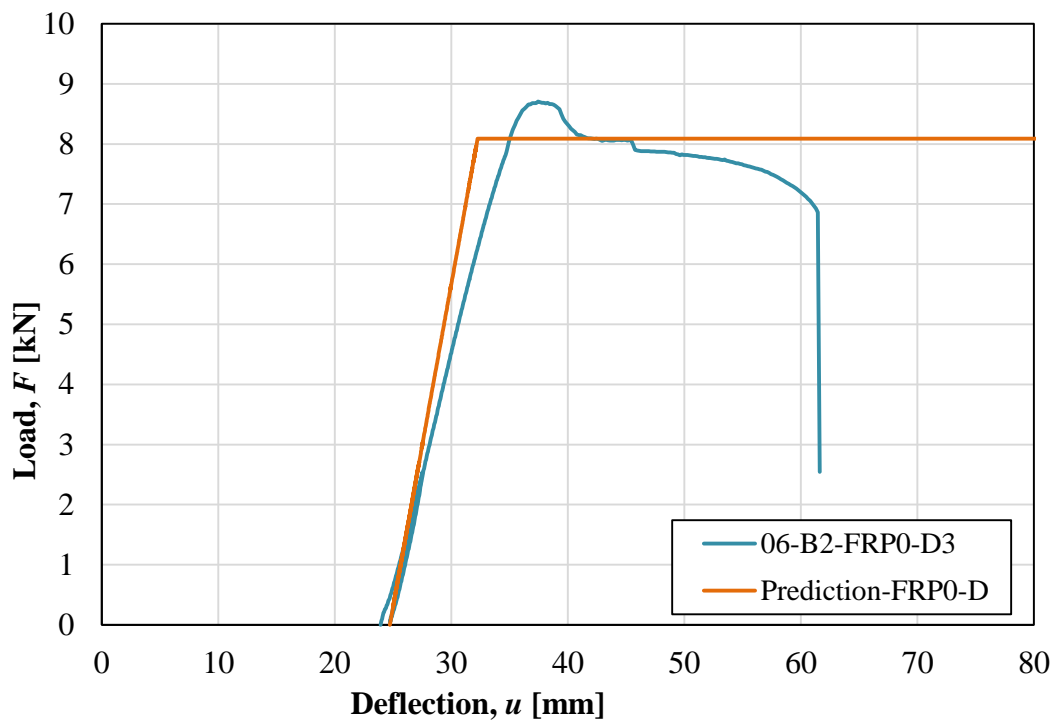
Figure 10.8   Experimental load-deflection relation and predicted load-deflection relation in state II for unstrengthened beams subjected to impact loading of 3 m prior to static loading.

The predicted stiffness and load capacity for strengthened beams in both cases are somewhat overestimated. This variation can be the result of not reaching the estimated capacity due to early debonding of FRP sheets initiated due to intermediate interfacial debonding resulted from weak bond strength. The prediction calculation estimates failure due to concrete crushing and a higher load capacity. However, the load deformation curve does exhibit such behaviour. Hence, this prediction is an approximate calculation since bond strength is not included in the calculation.

Load-deflection relation for experimental results of only statically loaded beams and predicted results for 1 layer FRP strengthened reference beams are presented in Figure 10.9.
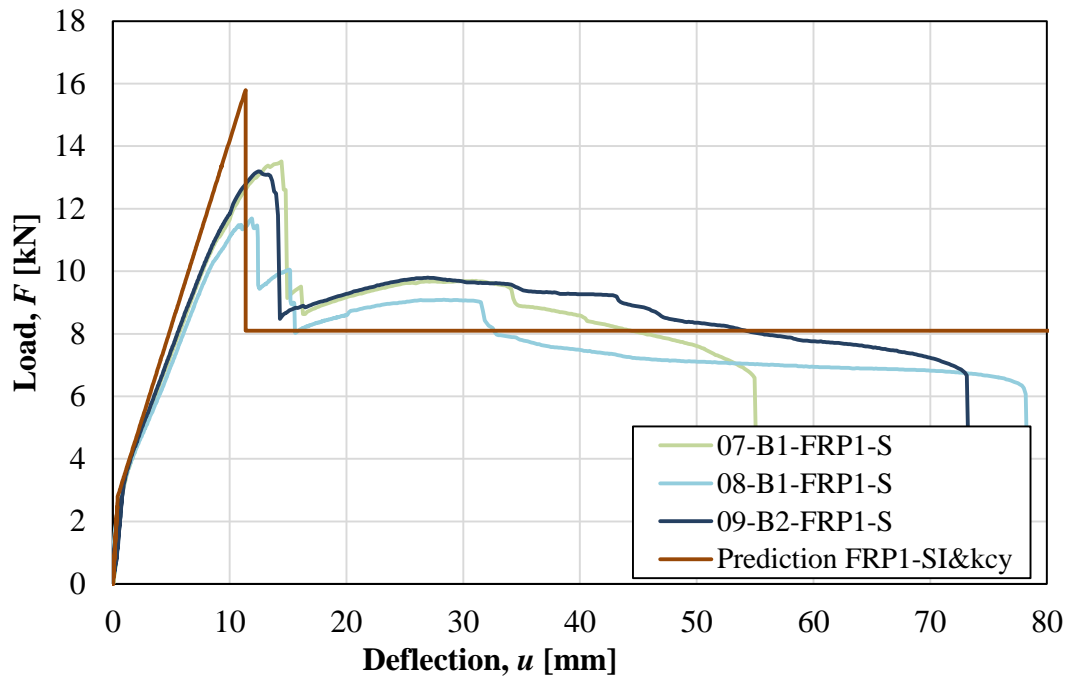
Figure 10.9   Experimental and predicted load-deflection relation for 1 layer FRP strengthened beams subjected to only static loading.

Load-deflection relation for beam subjected to drop weight impact of 3.5 m prior to static loading together with predicted load-deflection relation in state II for the unstrengthened beam is presented in Figure 10.11.
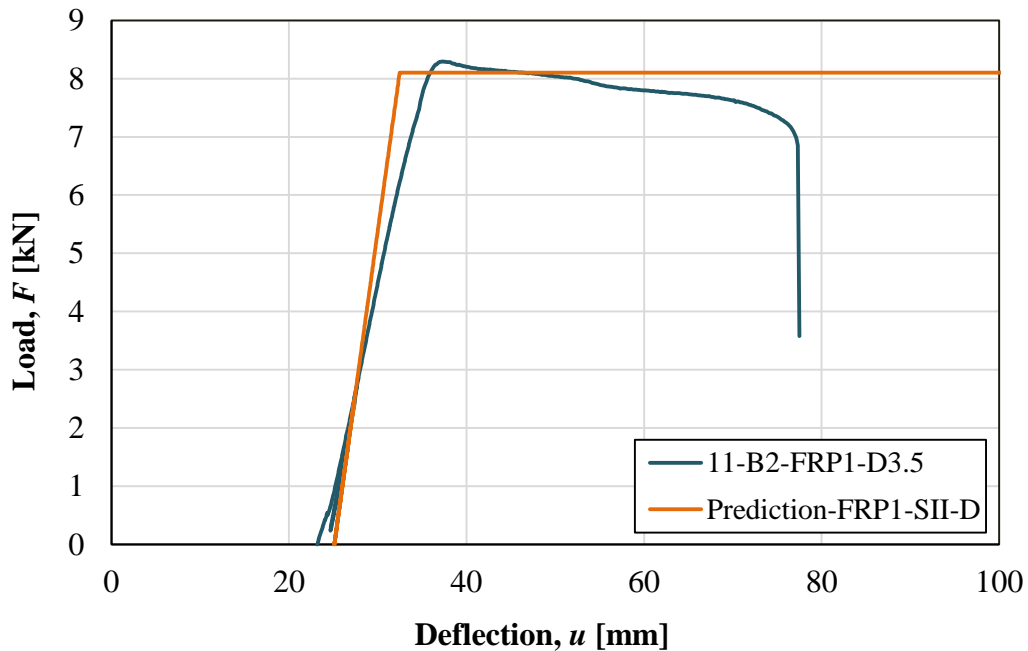
Figure 10.10 Experimental and predicted load-deflection relation in state II for 1 layer FRP strengthened beams subjected to impact loading of 3.5 m prior to static loading.

Load-deflection relation from experimental and test results for 3 layer FRP strengthened reference beams is presented in Figure 10.11.
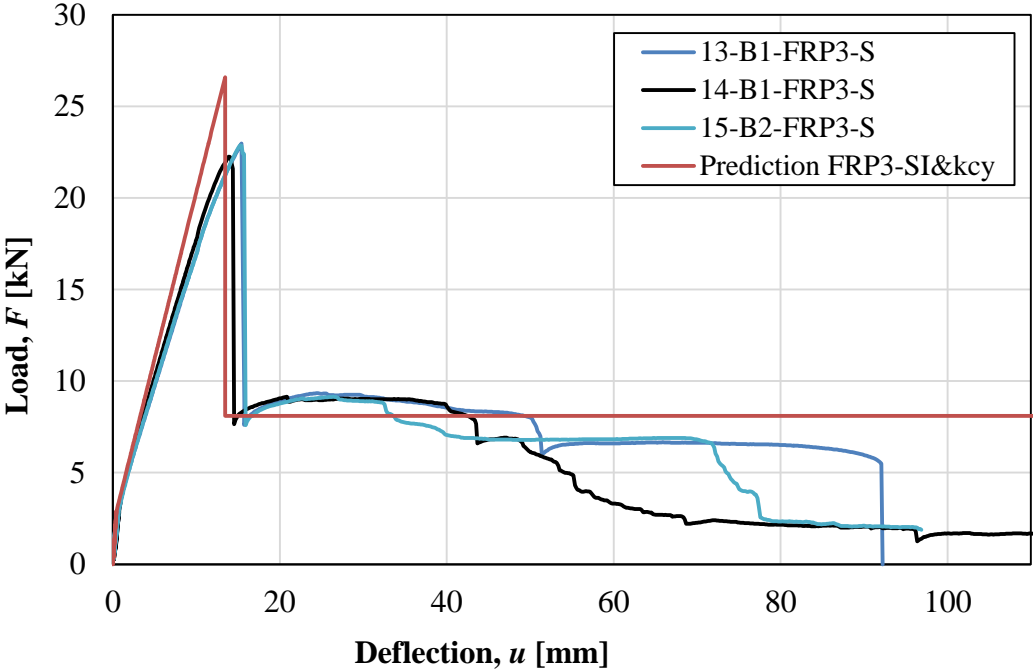
Figure 10.11 Experimental and predicted load-deflection relation for 3 layers FRP strengthened beams subjected to only static loading.

Load-deflection relationship for 3 layers FRP strengthened beams subjected to drop weight impact of 3.5 m prior to static loading are presented in Figure 10.12.
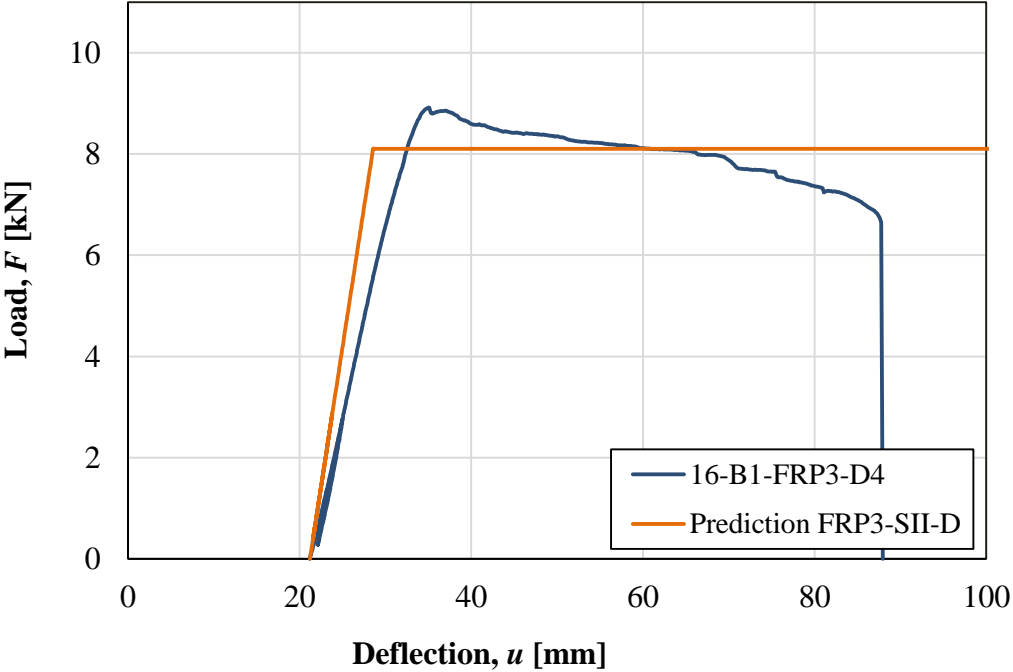
Figure 10.12 Predicted load-deflection relation in state II and experimental load-deflection relation for 3 layers FRP strengthened beam subjected to impact loading of 4 m height prior to static loading.

10.2.2 Plastic rotation capacity

Plastic rotation capacity predicted according to Section 8.1.4 is presented in comparison with rotation capacity from test results. The predicted results presented here are only for reference beams. It can be seen that predicted results according to Eurocode 2 are closer to test results for 100 % load level where BK25 prediction differs much from exeperimental results. The reason for this can be that Eurocode 2 assumes simply supported beam loaded with a point load at the middle which is a similar case with the load type of this experiment. On the other hand, BK25 asssumes a uniformly distributed loading case.
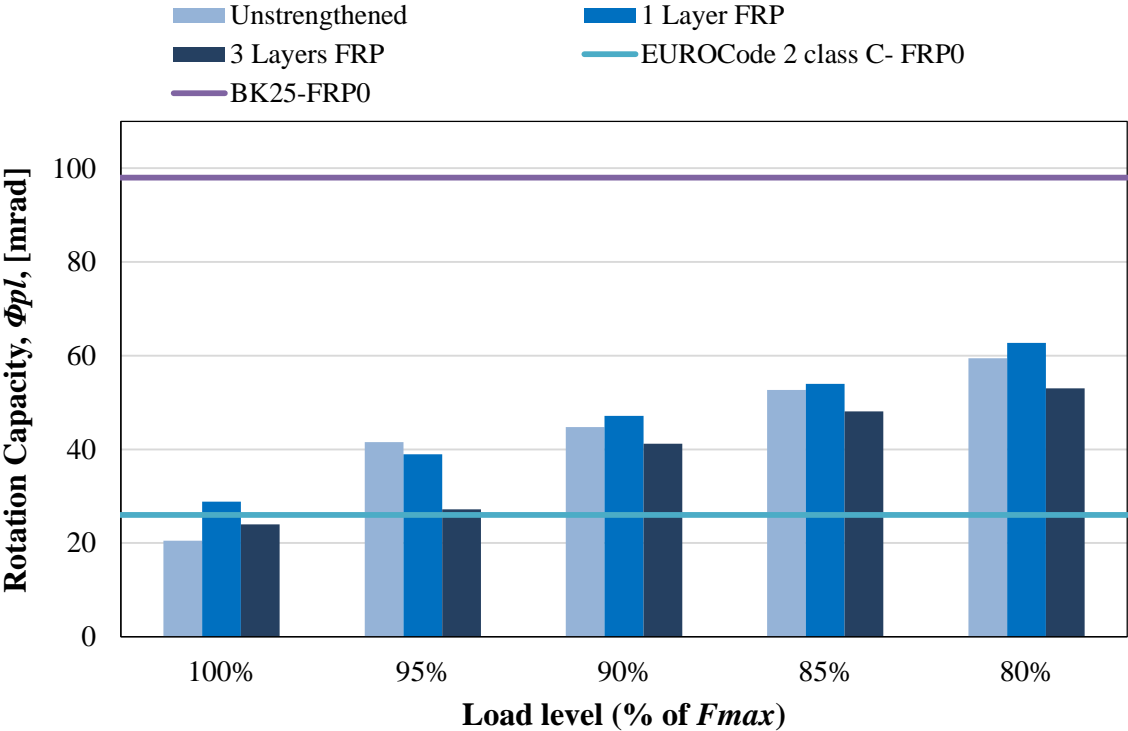
Figure 10.13 Predicted rotation capacity according to Eurocode 2 and BK25 and experimental rotation capacity for different load levels of unstrengthened, 1 layer and 3 layers FRP strengthened beams subjected to static loading.

11   Discussion

In this chapter general observations and experiences during this thesis work are discussed. It mainly includes the test procedures and analysis of the test results.

In order to avoid the differences in material properties that can be obtained due to manufacturing of concrete in two batches, the intention was to buy a good quality self-compacting concrete from concrete manufacturing company mixed in one huge batch. Nevertheless, two attempts were tried but not possible to finish due to various reasons. This has also affected the time plan for casting of concrete. Consequently, the concrete was manufactured in two batches at Chalmers structural engineering laboratory. However, the divergence of material properties from the two batches were minor and can be considered to have negligible effect on the properties of test specimen.

Material tests for FRP material properties and evaluation of bond strength were not carried out due to problems with the adhesive after attaching the FRP to the concrete beams. The adhesive started hardening, which initiated boiling in the bucket of unused epoxy. Therefore, it was not feasible to continue the procedure. In addition, because of Covid-19 outbreak it was not possible to do the FRP material tests afterwards. While cutting the kevlar, there were difficulties to keep the geometry in the desired length and width, since proper instrument for cutting of the FRP was not available at the time. However, the effect was considered to be minor.

Despite the fact that a high speed camera, i.e. camera 1, with a higher frame rate was used, the lighting used during the set up was not satisfactory to extract and analyse the footages from camera 1. Therefore, the results were almost exclusively extracted from the camera with a lower frame rate i.e. camera 2. The results obtained from camera 2 were good approximation and gave acceptable outputs. However, some data points might be missing as a result of larger time steps, which could be the case in beam 05-B2-FRP0-D3.5. For this particular beam it was noticed that the acceleration to calculate the impact force was smaller when compared with beam 06-B2-FRP0-D3. Which in return results in a higher increase of force and impulse for drop weight impact of 3.5 m compared with 4 m drop weight impact.

Time of impact for each beam was established in Section 9.2.4 when studying the deformed shape from the dynamic testing. Due to missing data points, time of impact is not exactly the same for all beams. By making comparison of results from DIC camera 1 and 2, it could be approximated that time 0.2 ms after impact differed between 0.150 ms and 0.287 ms for the different cases. This result does not influence the shape of initial behaviour much for the beams. However, if the values are compared between the beams, then some variations are noticed.

As it was pointed out in previous years by Jönsson and Stenseke (2018) and Andersson and Pettersson (2019), capturing only half of the beam gives a higher resolution for the analysis of results. Therefore, only one half of the beam was captured by DIC cameras. However, due to the limitation of not capturing the other symmetry, it was not possible to detect the debonding behaviour of FRP in all cases except for two specimens. This problem could be fixed by using two similar high speed cameras capturing one half of the beam each. It would result in high resolution of the pictures and the behaviour of the whole beam would be possible to be analysed.

The 2DOF model is a simplified numerical calculation to predict the behaviour of the dynamic loading for deflection-time relation of the beam and velocity-time relation of the drop weight. It gives too conservative results when using the calculated internal resistance of the beam, so another method was tried to get a more accurate value from the experimental results. However, the results calculated by using larger measured internal resistance of the beam still gave too conservative results compared with the experimental results for deflection-time relation of the beam. The results for the velocity-time relation of the drop weight were closer to the

experimental results. Moreover, the initial velocity used was described from the experimental results to get a better estimation since it was slightly smaller than the calculated values.

The material properties used in the 2DOF model were the ones from the material testing which are based on static loading. Since the behaviour of materials can be different for impulse load this can also be a factor which affect the numerical predictions for the dynamic loading. As mentioned before in Section 8.2.1, the dynamic predictions were not made for the FRP strengthened beams since the force-deflection relation used to describe the structural response in the 2DOF Matlab script was not suitable for this.

From all 3 layers FRP strengthened beams, including impulse loaded, half of them encountered shear type of failure during the static testing due to a higher stiffness of the beams in the tensile zone. Increased shear capacity, using for e.g. stirrups would probably have resulted in higher plastic rotation and larger internal work could have been obtained. In the FRP strengthened beams, after attaining a higher maximum load, the load deformation curve exhibits a sudden drop when debonding occurs, and taking the recommended load levels of the maximum force to calculate internal work and plastic rotation were not possible because of a very high maximum load that attained in FRP strengthened beams. Therefore, since the response after debonding follows a similar plateau with the reference beam, the maximum load was taken as the average maximum force of the reference beam. Which resulted in the mismatch of desired load in some cases, so approximation had to be done. However, this approximation was believed to give a reasonable result.

The predicted ultimate capacity of the reference beams in static testing were lower compared with the experimental results, which was also observed by Jönsson and Stenseke (2018) and Andersson and Pettersson (2019). This can be due to the conservative calculation method used for the predictions. On the other hand, the predicted ultimate load capacity for FRP strengthening was found to be higher than the experimental results, which can be due to the fact that the bond strength was not accurately considered in the design calculation and the prediction instead estimated failure due to concrete crushing. However, the test results show failure due to debonding before the predicted capacity was reached, which might be initiated due to not achieving the optimum bond strength. A more precise prediction calculation taking into consideration of every aspects would give a better estimation.

The extra beam 19-B1-FRP0-S which was subjected to static loading only was an extra test specimen used to examine the support condition's effect on the initial response and maximum load capacity of the beam. This was conducted by using square steel plates on top of the roller supports. The experimental results showed that this support condition gave similar results as the other reference beams so it could be concluded that the used roller supports were a good set up for the static testing used for this kind of experiment.

12 Conclusions

The aim of this thesis is to increase the understanding of structural response of FRP strengthened RC beams subjected to impact and static loading. Only static loading and impact loading followed by static loading were carried out for a total of 19 beams, of where one third of the beams were strengthened by 1 layer FRP and one third by 3 layers FRP strengthening.

From the literature survey and experimental results, it is observed that FRP strengthening results in a promising effect on the structural response of RC beams; i.e. a significant decrease of midpoint deflection and plastic deformation during impact loading. An increased effect was gained with increased amount of FRP strengthening. The impact force and impulse also increased as a result of FRP strengthening. For static testing, the ultimate load capacity increased with FRP strengthening, where the effect was considerably higher for increased amount of FRP strengthening. Furhermore, the deflection at failure i.e. at the rupture of reinforcement also increased with FRP strengthening.

The amount of internal work and the deformation capacity to absorb a higher energy are of most interest in impact loaded structures. Initially the FRP added a substantial amount to the internal of the structure. However, at a certain stage , debonding of the FRP occurred, and this positive effect disappeared when the response went back to that of the unstrengthened beam instead.The rotation capacity was evaluated for the cases with debonded FRP and it was observed that the rotation capacity for 1 layer FRP strengthening was found to be slightly higher between 90 % and 80 % load level, while 3 layers FRP strengthening resulted in a lower plastic rotation in all cases. Even though the rotation capacity was not increased in 3 layers of FRP strengthening, the total internal work at failure increased slightly in all FRP strengthening cases. This increase is due to the elastic internal work gained due to a higher load capacity before debonding occurred. Therefore, it can be concluded that FRP strengthening had a positive effect. From the approximation of internal work a significant increase was not observed; rather the obtained results were close to each other. However, it cannot be regarded as negative effect.

The residual capacity of FRP strengthened beams increased in all cases except for one beam that encountered a shear failure, which can be regarded as a scatter. The deformation capacity of both reference beams and FRP strengthened beams increased for beams previously subjected to impact load.

A simplified 2DOF model was used to predict the response of the reference beams subjected to impact load. The 2DOF system showed reasonable results in behaviour but some differences. It resulted in larger deformations compared with the experimental results. This is because the beams were predicted to be weaker than they actually were.

The high speed cameras for the dynamic testing and the DIC analysis are powerful tools to receive and analyse the structural response of the beams after the experimental testing. The behaviour of the beams showed the development of bending cracks in strain field for the impulse and statically loaded beams. Shear failure can also be expected in beams with high amount of FRP strengthening. It can be concluded though, that this type of phenomenon was observed in the tests. The results from the dynamic testing show that a lot happen during the initial 2.0 ms as the impact wave propagates along the beam.

Initially for the impulse loaded beams the behaviour for the deformed shape showed that the beams behave as fully fixed before the active part span the whole beam. This results in tension on the upper part and cause top cracks to appear and disappear. After the active part span the whole beam, it behave as simply supported due to the support condition for the testing.

13 Future Studies

This thesis focused on FRP strengthened RC beams subjected to impact loading. What seem to be the most interesting to do as future studies is to develop the experimental testing with the increased knowledge obtained from this thesis. It would be valuable to look at other types of FRP strengthening and to try different adhesives. In this study debonding of the FRP strengthening occurred before the aramid fibre reached its maximum tensile capacity. Therefore, with a stronger bond between the adhesive and concrete of the beam, it would be of interest to study the effect on the plastic deformation capacity. However, it could also result in failure due to shear cracks since the FRP strengthening only strengthen the beam in bending. Shear cracks developed due to similar reasons were also observed in this experimental study, therefore providing shear strengthening would be interesting.

It would also be of interest to study the amount of reinforcement in the beams. Furthermore, the geometry of the beams are also of interest to try different dimensions. However, due to limitations of the set up for the dynamic testing this would be more difficult to achieve. Much work would be needed to make this work, but it would be valuable to test these experiments in larger dimensions to see if the behaviour of the beams are similar to the testing conducted in this thesis and the theses made in previous years.

Larger dimensions of the beams and test set up would also result in interest to experiment more with different weights and drop heights of the drop weight. The strength and composition of the concrete could also be experimented more with. Like in this thesis, it was used a concrete with higher strength compared with previous years theses which resulted in less damage at impact zone for the drop weight.

Numerical methods for the predictions of impact load could be studied to try to find better estimations of the structural behaviour of the beams. The 2DOF model used in this thesis could be refined to include more detailed material properties and different FEA models could also be included.

14 References

Al-Emrani, M., Engström, B., Johansson, M., Johansson, P. (2011). *Bärande konstruktioner: Del 2*, Chapter B7-B11. Chalmers University of Technology, Gothenburg.

Al-Emrani, M., Engström, B., Johansson, M., Johansson, P. (2013). *Bärande konstruktioner: Del 1*, Chapter B1-B6. Chalmers University of Technology, Gothenburg.

Ali, M., Oehlers, D., Haskett, M., Wu, C. (2009). *Influence of bond on the hinge rotation of FRP plated beams*. Adelaide University South Australia 5005, Australia.

Andersson, J., Antonsson, A. (2015). *Design with Regard to Collision Impact – Comparison between 2DOF and FE Analysis for Collision Impact on Concrete Slabs*. (Master's thesis, Chalmers University of Technology, Institution of Architecture and Civil Engineering, Gothenburg).

Andersson, M., Pettersson, E., (2019). *Reinforced Concrete Beams Subjected to Drop-Weight Impact – Experimental study about the influence of reinforcement properties on the structural response*. (Master's thesis, Chalmers University of Technology, Institution of Architecture and Civil Engineering, Gothenburg).

Blanksvärd, T., Täljsten, B., Sas, G. (2015). *Kompositförstärkning av betong*. Luleå University of Technology, Luleå.

Boverket (2004). *Boverkets handbok om betongkonstruktioner, BBK 04*. Boverket.

Burström, P. (2007). *Byggnadsmaterial: Uppbyggnad, tillverkning och egenskaper.* Studentlitteratur AB, Lund.

Camata, G., Spacano, E., Zarnic R. (2016). *Experimental and nonlinear finite element studies of RC beams strengthened with FRP plates*. University of Ljubljana, Slovenia.

CEN (2005). *SS*-EN 1992-1-1: 2005: Design of concrete structures - Part 1-1: General rules and rules for buildings. European Committee for Standardization.

   – (2009a). *SS*-EN 12350-1: 2009: Testing fresh concrete - Part 1: Sampling. European Committee for Standardization.

   – (2009c). *SS*-EN 12350-7: 2009: Testing fresh concrete - Part 7: Air-content - Pressure methods. European Committee for Standardization.

   – (2009d). *SS-EN 12390-2: 2009: Testing hardened concrete - Part 2: Making* and curing *specimens for strength tests*. European Committee for Standardization.

   – (2009e). *SS*-EN 12390-3: 2009: Testing hardened concrete - Part 3: Compressive strength of test specimens. European Committee for Standardization.

   – (2009f). *SS*-EN 12390-6: 2009: Testing hardened concrete - Part 6: Tensile splitting strength of test specimens. European Committee for Standardization.

   – (2009g). *SS*-EN 12390-7: 2009: Testing hardened concrete - Part 7: Density of hardened concrete. European Committee for Standardization.

Chen, J., Smith, S., Teng. J., Yao, J. (2003). *Intermediate Crack Induced Debonding in RC Beams and Slabs*. Construction and Building Materials, 17(6-7), 447-462.

Dahlblom, O., Olsson, K. (2015). *Strukturmekanik: Modellering och analys av ramar och fackverk.* Studentlitteratur AB, Lund.

Eamon, C., Wu, C. (2017). *Strengthening of Concrete Structures using Fiber Reinforced Polymers (FRP).* Wayne State University, Michigan.

Ekengren, B., Jansson, H., Johansson, M., Leppänen, J. (2014). *Beräkning av impulsbelastade konstruktioner*. Myndigheten för samhällsskydd och beredskap, Karlstad.

Ekengren, B., Jansson, H., Johansson, M., Leppänen, J. (2014). *Seminarium om impulsbelastade konstruktioner*. Myndigheten för samhällsskydd och beredskap, Karlstad.

Ekengren, B., Johansson, M., Leppänen, J., Laine, L. (2005). *Dynamsk Lastpåverkan – Referensbok*. Räddningsverket, Karlstad.

Engström, B. (2014). *Restraint cracking of reinforced concrete.* Chalmers University of Technology, Gothenburg.

Engström, B. (2015). *Design and analysis of continuous beams and columns.* Chalmers University of Technology, Gothenburg.

Fib Bulletin Vol.90 (2019). *Externally Applied FRP reinforcement for concrete structures*. DCC Document Competence Center Siegmar Kästl e. K., Germany.

Isaac, P., Darby, A., Ibell, T., Evernden, M. (2017). *Experimental investigation into the force propagation velocity due to hard impacts on reinforced concrete members*. University of Bath, department of Architecture and Civil Engineering, Bath.

Johansson, M. (2000). *Structural Behaviour in Concrete Frame Corners of Civil Defence Shelters.* (PhD thesis. Chalmers University of Technology, Department of Structural Engineering, Gothenburg).

Johansson, M. (2012). *Beräkningsanvisning för strukturrespons: Central differencemetod.* Dokument B03-102 from MSBs series "Beräkning av impulsbelastade konstruktioner", 2014.

Johansson, M., Laine, L. (2012). *Bebyggelsens motståndsförmåga mot extrem dynamisk belastning, Del 3 – Kapacitet hos byggnader.* Swedish Civil Contingencies Agency, Gothenburg.

Ulzurrun, G., Johansson, M., Rempling, R., Zanuy, C. (2019). *Impact propagation effects along reinforced concrete beam*. IABSE Symposium 2019, Guimarães.

Jönsson, J., Stenseke, A. (2018). *Concrete Beams Subjected to Repeated Drop-Weight Impact and Static Load: Assessment of structural response in experimental testing and predicted response with numerical analyses.* (Master's thesis, Chalmers University of Technology, Institution of Architecture and Civil Engineering, Gothenburg).

Ljung, C., Saabye Ottosen, N., Ristinmaa, M. (2007). *Hållfasthetslära: Allmänna tillstånd.* Studentlitteratur AB, Lund.

Ljung, C., Saabye Ottosen, N., Ristinmaa, M. (2007). *Introduktion till hållfasthetslära: Enaxliga tillstånd.* Studentlitteratur AB, Lund.

Lovén, J., Svarvarsdóttir, E. (2016). *Concrete Beams Subjected to Drop Weight Impact – Comparison of experimental data and numerical modelling*. (Master's thesis, Chalmers University of Technology, Institution of Architecture and Civil Engineering, Gothenburg).

Lozano Mendoza, F., Makdesi Aphram, J. (2017). *Concrete Beams Subjected to Drop-Weight Impact and Static Load: Structural behavior and plastic rotation capacity from experiments and finite element analysis.* (Master's thesis, Chalmers University of Technology, Institution of Architecture and Civil Engineering, Gothenburg).

Munther, M., Runebrant, J., (2018). *Structural Response of Concrete Beams Subjected to Drop Weight Impact – A parametric study using numerical modelling*. (Master's thesis, Chalmers University of Technology, Institution of Architecture and Civil Engineering, Gothenburg).

Nordin H. (2003). *Fibre Reinforced polymers*. Luleå University of Technology, Luleå.

Nyström, U., (2006). *Design with regard to explosions*. (Master's thesis, Chalmers University of Technology, Institution of Architecture and Civil Engineering, Gothenburg).

Pantelides, C., Duffin, J., Reaveley, L. (2004). *Design of FRP jackets for seismic strengthening*. 13th world conference on earthquake engineering, Vancouver.

Plem E. (1981). *The rotation capacity of plastic hinges in reinforced concrete beams*. Lund inistitute of technology, Lund.

Smith, S., Teng, J. (2002). *FRP-strengthened RC beams. I: review of debonding strength*. The Hong Kong Polytechnic University, Hong Kong.

Smith, S., Teng, J. (2004). *FRP- Strengthened RC beams.II: assessment of debonding strength models*. The Hong Kong Polytechnic University, Hong Kong.

S&P Clever Reinforcement Company (n. d.). *S&P A-Sheet 120 – Aramid fibre sheet for structural reinforcement*. A Simpson Strong-Tie Company, Seewen.

Xiaoxu H., Yingwu Z., Feng X., Yufei W., Lili S., Ningxu H. (2019). *Reliability-based design of FRP flexural strengthened reinforced concrete*. National Natural Science Foundation of China, Shenzhen Basic Research Project, China.

Zoghi, M. (Eds.). (2014). *The International Handbook of FRP Composites in Civil Engineering*. Taylor & Francis Group, Boca Raton.

A Appendix – Material Properties of Concrete

Compressive and tensile tests for concrete were carried out 26 days after casting of concrete and wedge splitting tests were performed 28 days after casting. The results from compressive and tensile material tests are shown in Table A.1 and Table A.2.

Table A.1 Results from concrete compressive tests at the age of 26 days.

Batch	Specimen ID	Length [mm]	Width [mm]	Height [mm]	Weight [g]	Density [kg/m^3]	Load [kN]	f_{cc} [MPa]
1	B1_1	150	150	150	8 095	2 399	1 278	56.8
	B1_2	150	150	150	8 267	2 449	1 285	57.1
	B1_3	150	150	150	8 127	2 408	1 288	57.2
2	B2_1	150	150	150	8 262	2 448	1 320	58.7
	B2_2	150	150	150	8 217	2 435	1 222	54.3
	B2_3	150	150	150	8 278	2 453	1 291	57.4

Table A.2 Results from tensile splitting tests at the age of 26 days.

Batch	Specimen ID	Length [mm]	Width [mm]	Height [mm]	Weight [g]	Density [kg/m^3]	Load [kN]	$f_{ct,sp}$ [MPa]
1	B1_1	150	150	150	8 117	2 405	158	7.03
	B1_2	150	150	150	8 246	2 443	148	6.58
	B1_3	150	150	150	8 260	2 447	149	6.61
2	B2_1	150	150	150	8 274	2 452	141	6.27
	B2_2	150	150	150	8 266	2 449	142	6.31
	B2_3	150	150	150	8 237	2 441	148	6.59

Wedge splitting tests were performed to determine the fracture energy, G_F, of the concrete. Three specimens were tested named 1-3 and the geometry is tabulated in Table A.3. The relation between splitting load, F_{sp}, and CMOD are illustrated in Figure A.1 and from this relation the fracture energy could be calculated as the area under the curve divided with the area of the cross section. The results are presented in Table A.4.

Table A.3 Geometry for wedge splitting tests.

Specimen ID	Length [mm]	Height [mm]	Area [mm^2]	Weight [g]
1	150	75.6	11 367	7 938
2	150	76.0	11 379	7 936
3	150	75.9	11 343	7 859
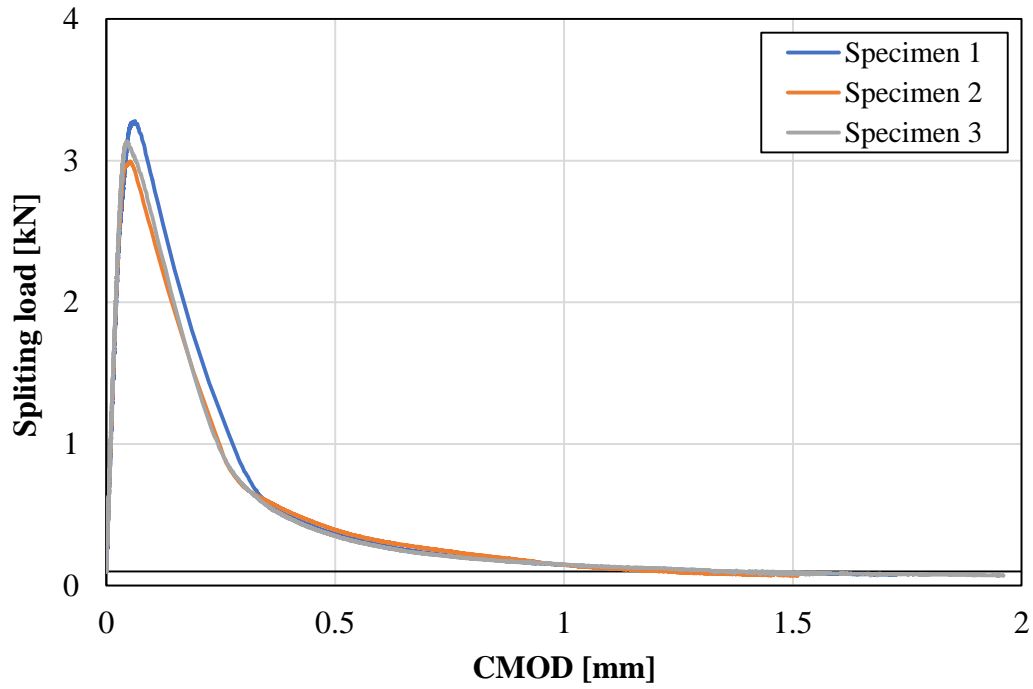
Figure A.1   *Splitting load, F_{sp}, plotted against CMOD from the wedge splitting tests conducted at 28 days after casting of concrete.*

Table A.4   *Results from wedge splitting tests at the age of 28 days.*

Specimen ID	G_F [Nm/m²]	Maximum F_{sp} [kN]	Maximum CMOD [mm]
1	63.2	3.18	1.73
2	58.4	2.89	1.51
3	57.8	3.04	1.96

B   Appendix – Material Properties of Reinforcement

Six tests were performed for tensile testing of reinforcement and the names are given as 1-6. The stress-strain curve for the reinforcement used in the experiments are presented in Figure B.1 and the material parameters are presented in Table B.1.
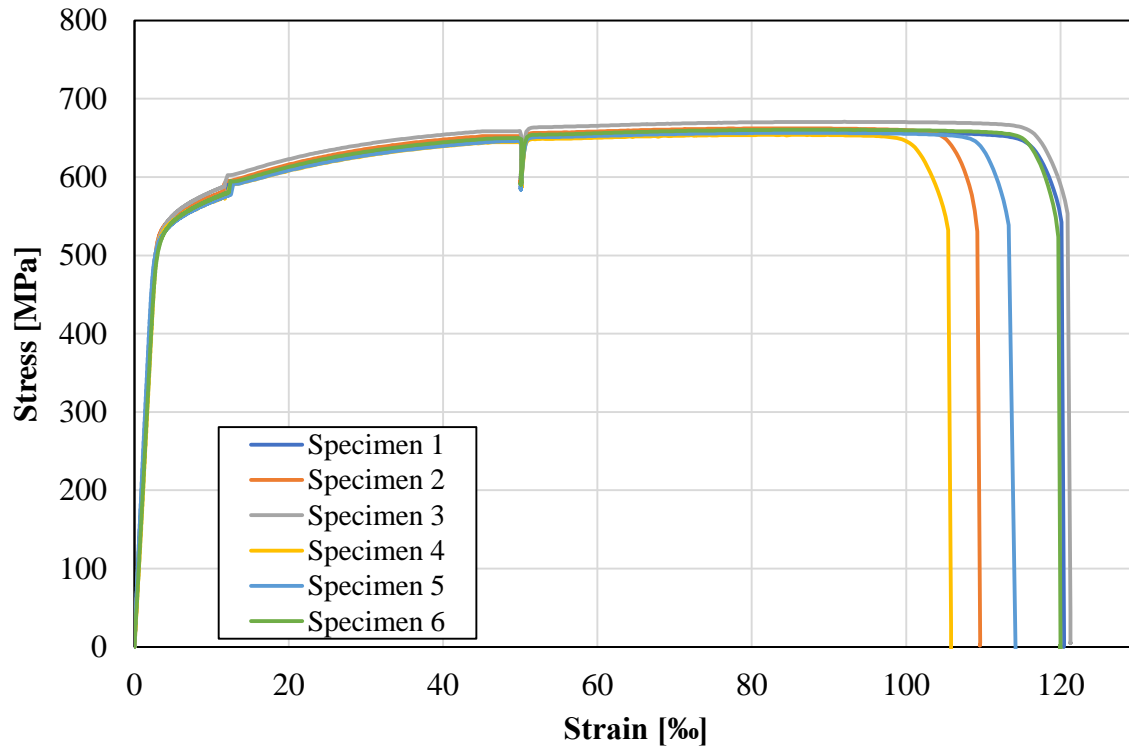
Figure B.1   Stress-strain relation for reinforcement.

Table B.1   Material parameters of reinforcement from test results.

Specimen ID	$f_{0.2}$ [MPa]	f_u [MPa]	ε_{su} [‰]	E_s [GPa]	$f_u/f_{0.2}$ [-]
1	540	658	85	201	1.22
2	548	662	85	193	1.21
3	548	671	92	204	1.22
4	544	654	84	183	1.20
5	537	656	87	208	1.22
6	542	661	90	186	1.22
Average	**543**	**660**	**87**	**196**	**1.22**

C   Appendix – DIC Facet Analysis

Settings for point distance and facet size were chosen based on an analysis of strain field made on beam 16-B1-FRP3-D4 from the impact loaded testing. The results were used for both the static and dynamic test results. Facet size is the length of one side of each facet and point distance is the distance between the middle of two facets, see Figure C.1. Point distance 5-20 pixels were analysed with different facet sizes to see which figure show the most accurate results without too much noise, see Table C.1 to Table C.4. From the results of the DIC facet analysis it was decided to use point distance 5 pixels and facet size 15 pixels.

A triangular mesh is used in GOM Correlate 2019 and it is based on the chosen facet size and point distance. The strain field was displayed as major strains and was compared with reference stage. Interpolation size was chosen to 1 and high accuracy computation was used.
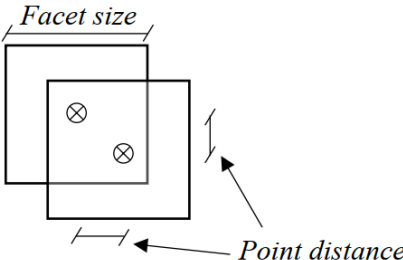
Figure C.1   Illustration of facet size and point distance, from Jönsson and Stenseke (2018).

Table C.1   Strain field with point distance 5 pixels and different facet sizes.

Facet size [pixels]	Point distance: 5 pixels
10	
15	
20	
25	
Scale	**1 %** ▬▬▬▬▬▬▬▬▬ **5 %**

Table C.2   Strain field with point distance 10 pixels and different facet sizes.

Facet size [pixels]	Point distance: 10 pixels
15	
20	
25	
Scale	1 % ▬▬▬▬▬▬▬▬▬▬▬ 5 %
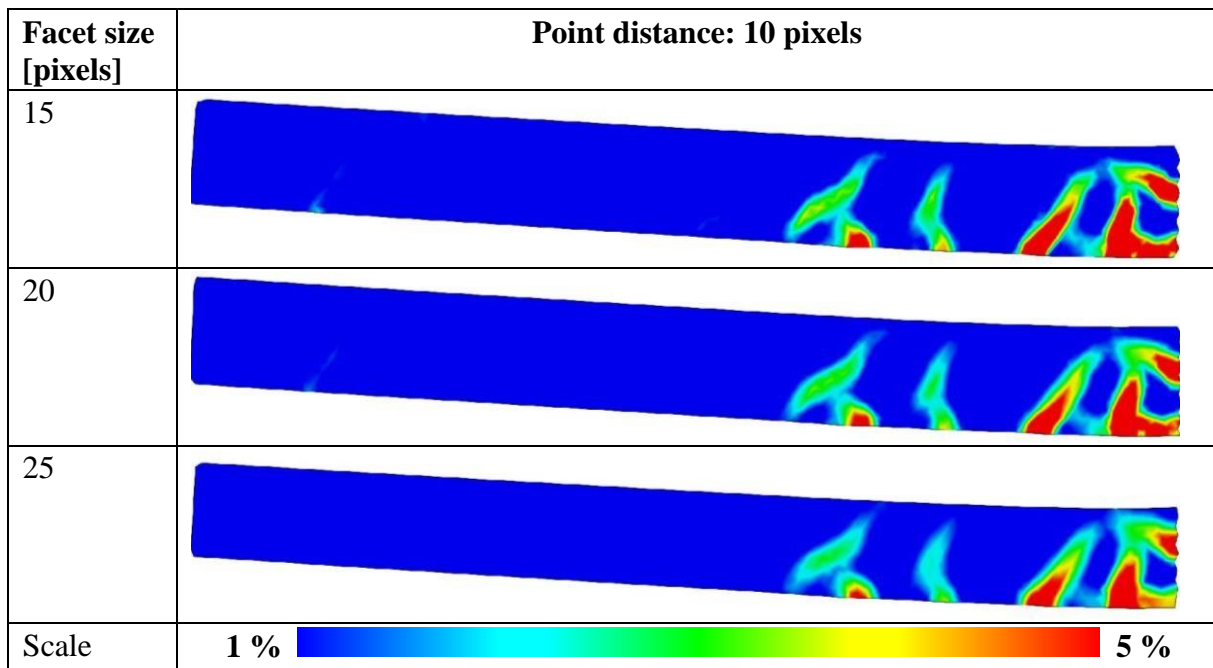
Table C.3   Strain field with point distance 15 pixels and different facet sizes.

Facet size [pixels]	Point distance: 15 pixels
20	
25	
Scale	1 % ▬▬▬▬▬▬▬▬▬▬▬ 5 %
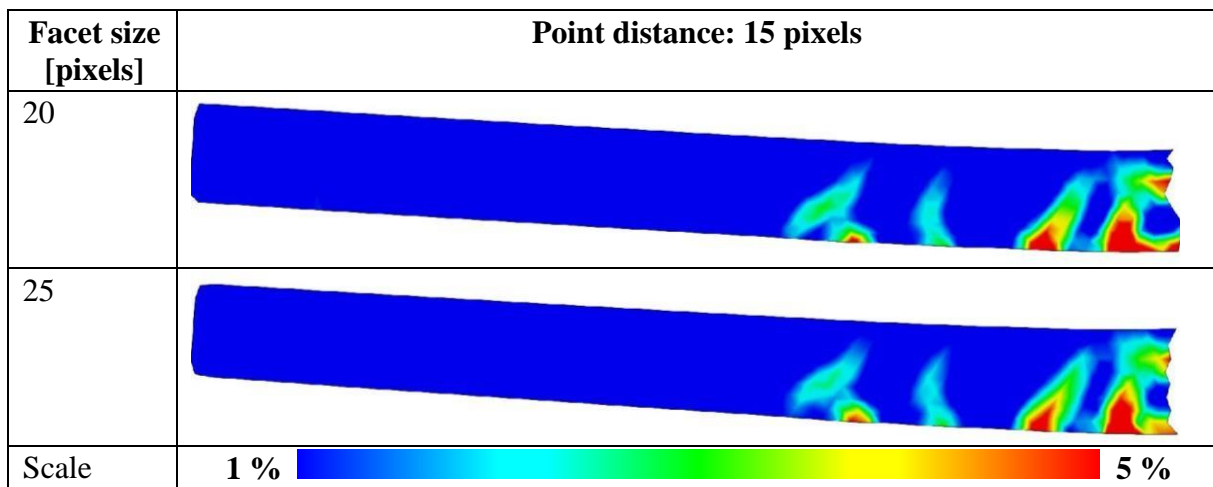
Table C.4   Strain field with point distance 20 pixels and facet size 25 pixels.

Facet size [pixels]	Point distance: 20 pixels
25	
Scale	1 % ▬▬▬▬▬▬▬▬▬▬▬ 5 %
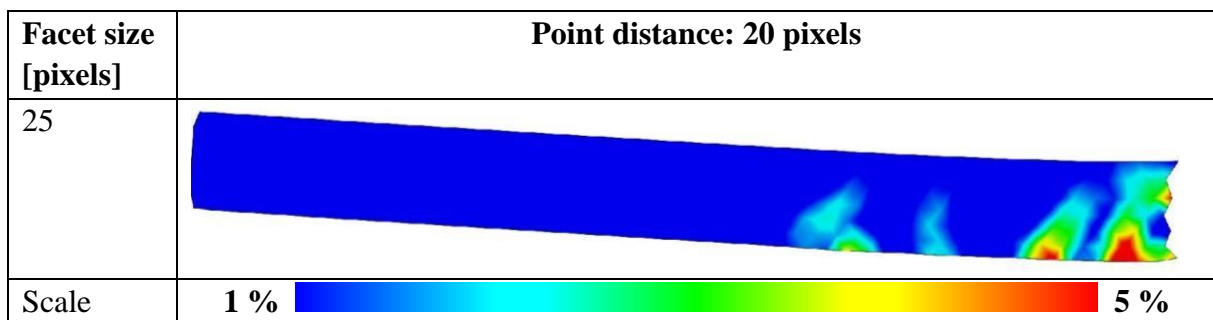
D Appendix – Velocity of Drop Weight

Velocities of drop weight during impact for all cases drop heights and beam type are presented in Figure D.1 to Figure D.3.
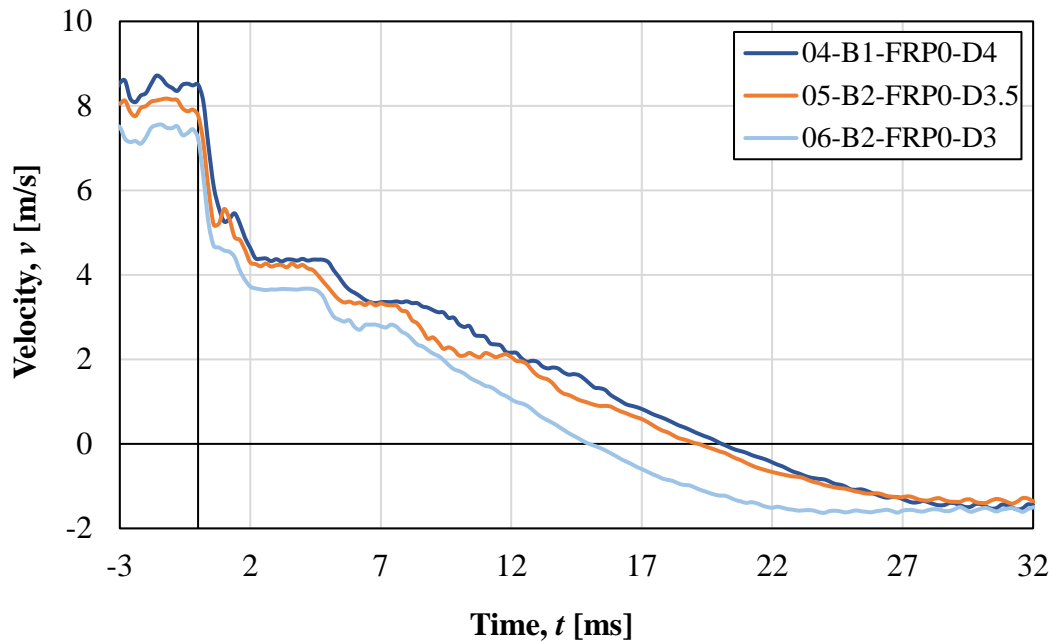
Figure D.1   Velocity of drop weight for unstrengthened beams subjected to 4 m, 3.5 m and 3 m drop weight impact.
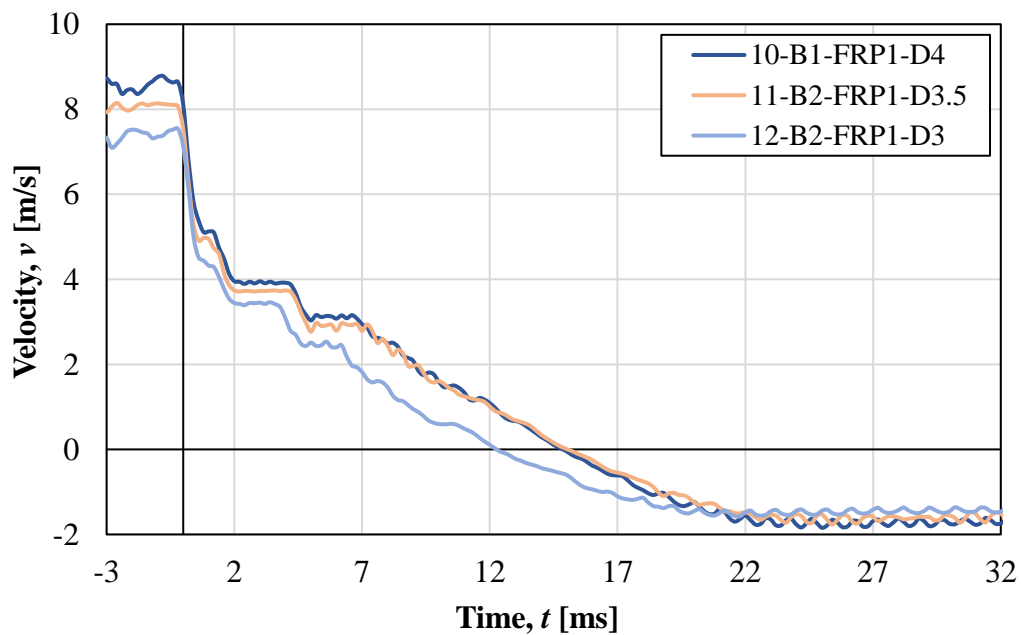
Figure D.2   Velocity of drop weight for 1 layer FRP strengthened beams subjected to 4 m, 3.5 m and 3 m drop weight impact.
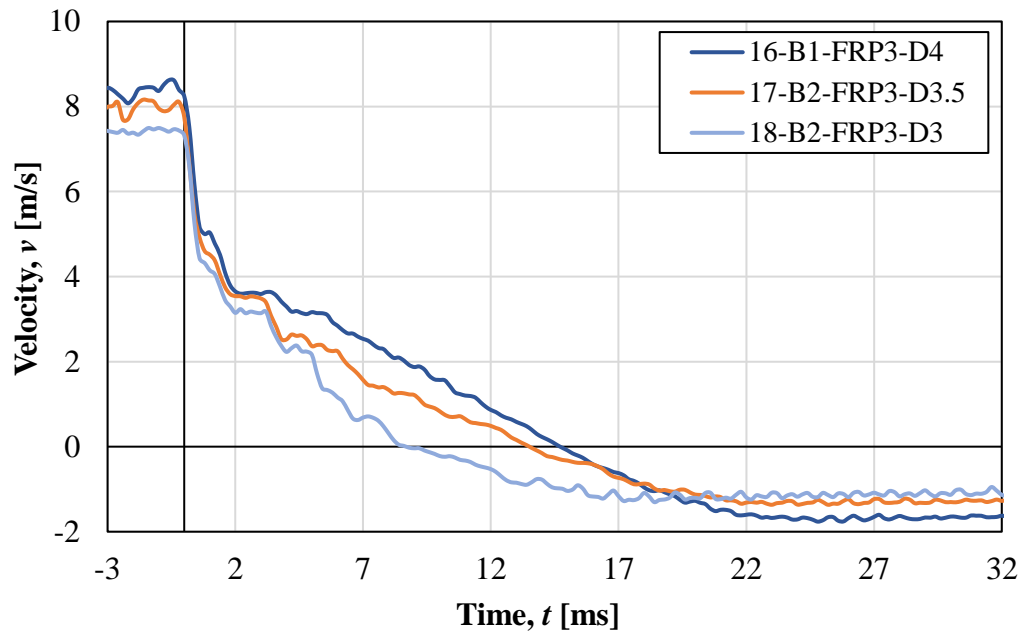
Figure D.3   Velocity of drop weight for 3 layers FRP strengthened beams subjected to 4 m, 3.5 m and 3 m drop weight impact.

E   Appendix – Deformed Shape for 3.5 m Drop Height

Deformed shape for the initial 2.0 ms for beams subjected to 3.5 m drop weight impact are here presented in deflection and relative deflection over half of the beam. The estimated times for 0.2 ms after impact from camera 1 are presented in Table E.1.

Table E.1   Estimated times from camera 1 for 0.2 ms after impact from camera 2, for beams subjected to drop weight impact of 3.5 m drop height.

Beam	Time [ms]
05-B2-FRP0-D3.5	0.165
11-B2-FRP1-D3.5	0.207
17-B2-FRP3-D3.5	0.165

Deflection over the beam for the initial 2.0 ms after impact are presented in Figure E.1 to Figure E.3 for beams subjected to 3.5 m drop height impact.
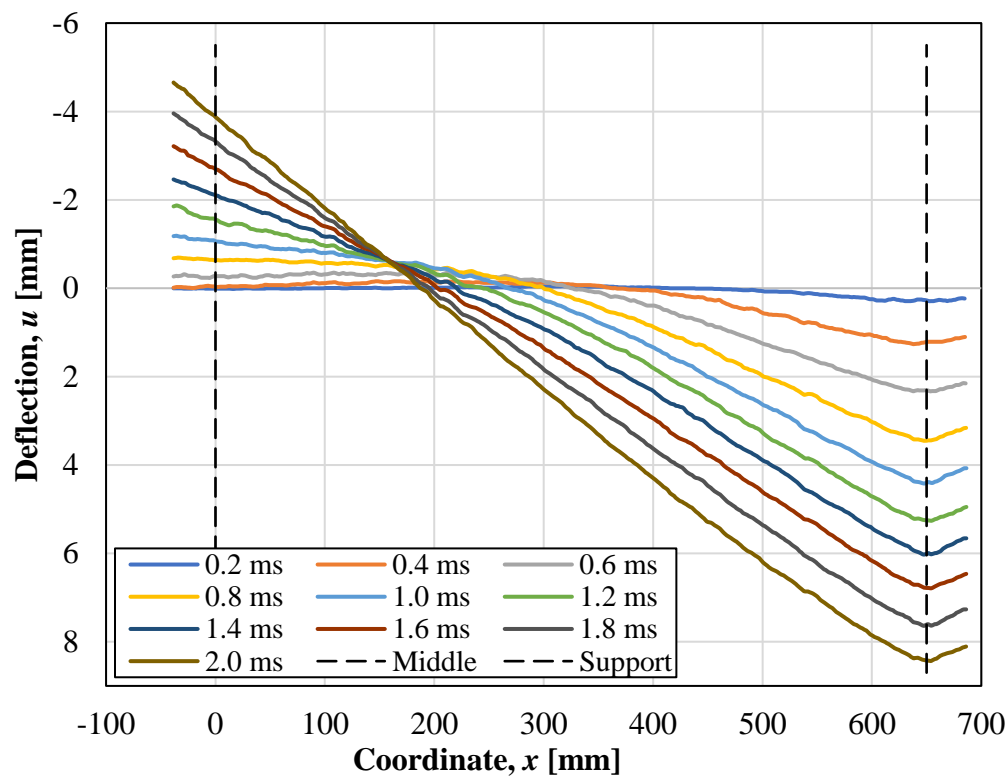
Figure E.1   Deformed shape for the initial 2 ms of the drop weight impact illustrating the behaviour of deflection for beam 05-B2-FRP0-D3.5.
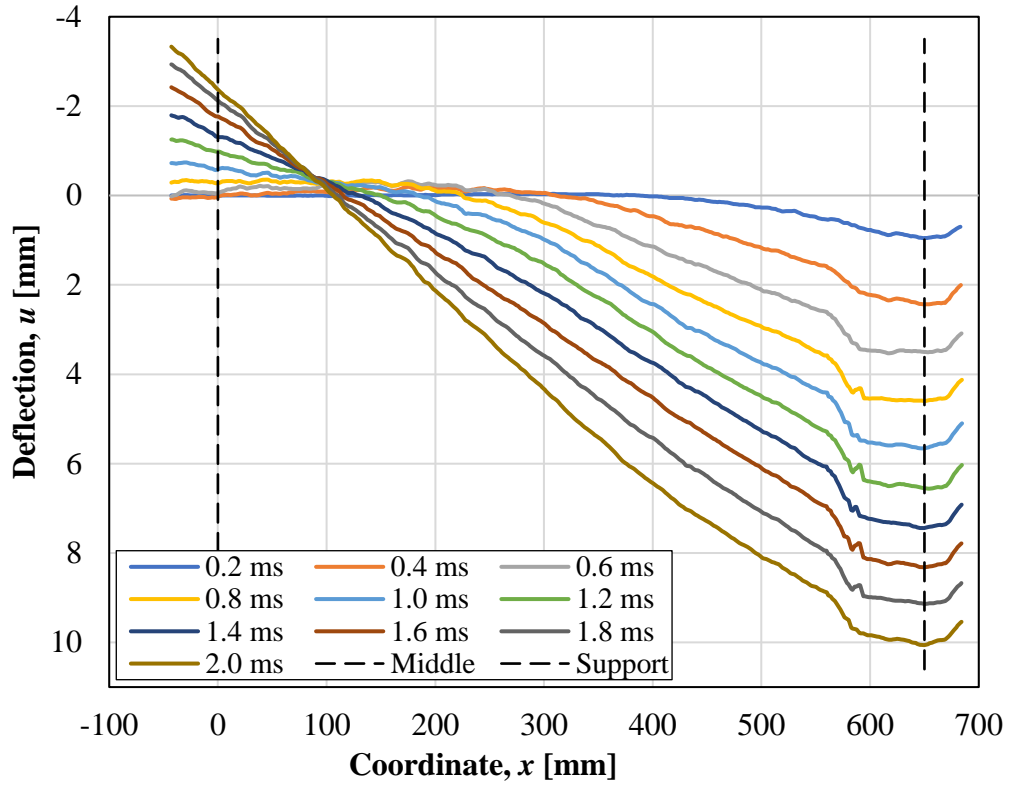
Figure E.2   Deformed shape for the initial 2 ms of the drop weight impact illustrating the behaviour of deflection for beam 11-B2-FRP1-D3.5.
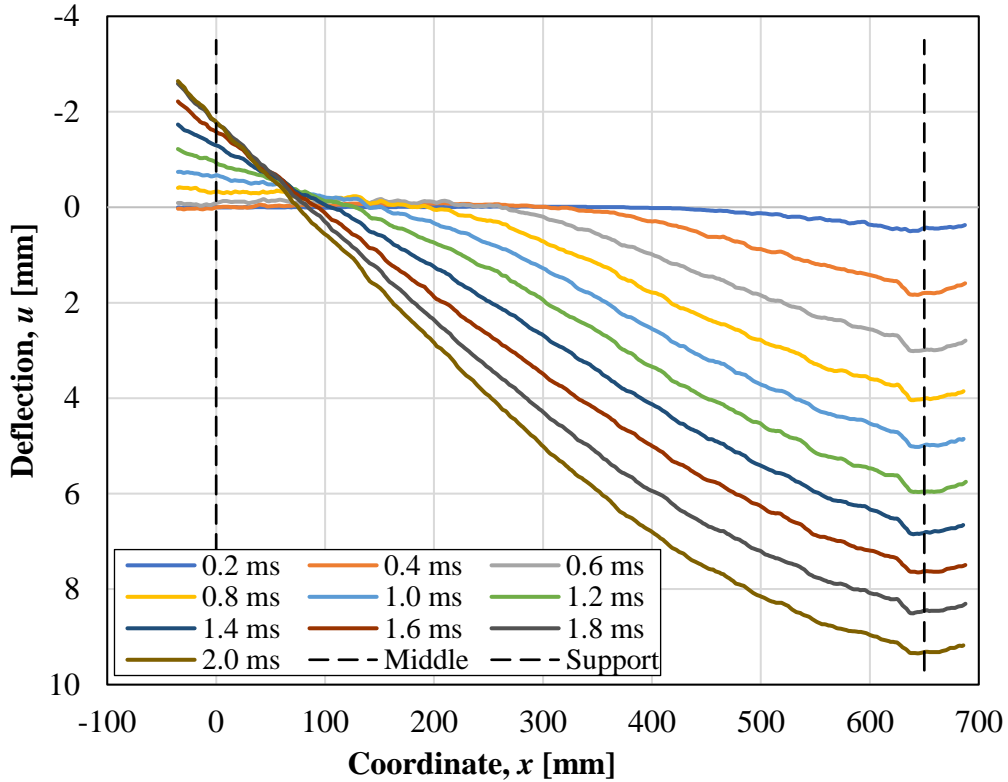
Figure E.3   Deformed shape for the initial 2 ms of the drop weight impact illustrating the behaviour of deflection for beam 17-B2-FRP3-D3.5.

Relative deflection over the beam for the initial 2.0 ms after impact are presented in Figure E.4 to Figure E.6 for beams subjected to 3.5 m drop height.
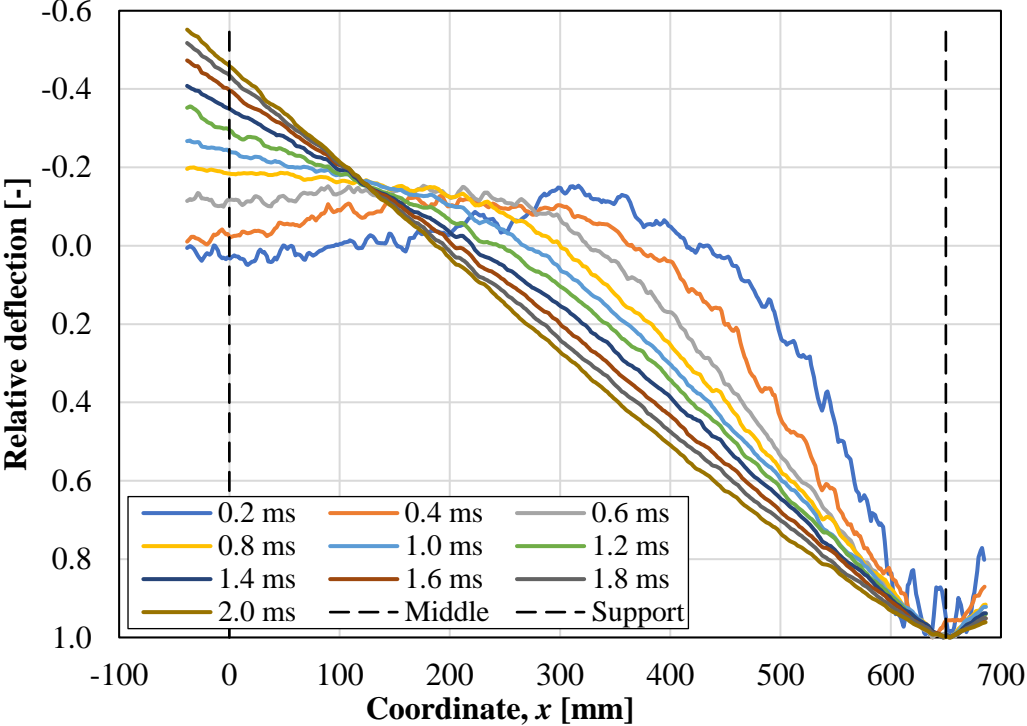
Figure E.4   *Relative deformed shape for the initial 2 ms of the drop weight impact illustrating the behaviour of deflection for beam 05-B2-FRP0-D3.5.*
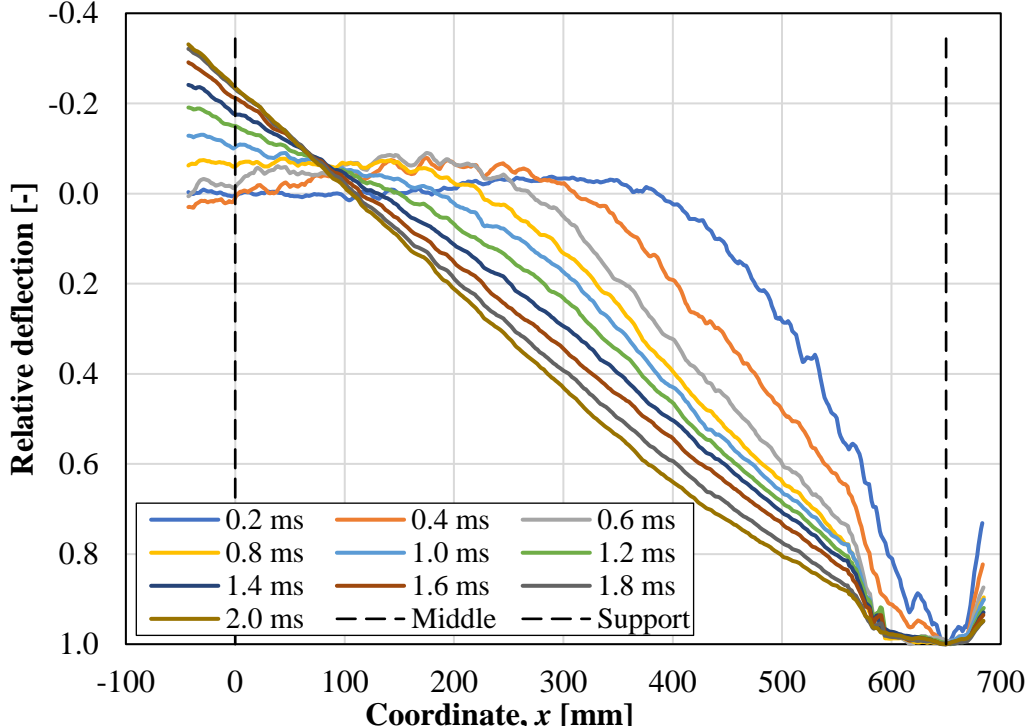
Figure E.5   *Relative deformed shape for the initial 2 ms of the drop weight impact illustrating the behaviour of deflection for beam 11-B2-FRP1-D3.5.*
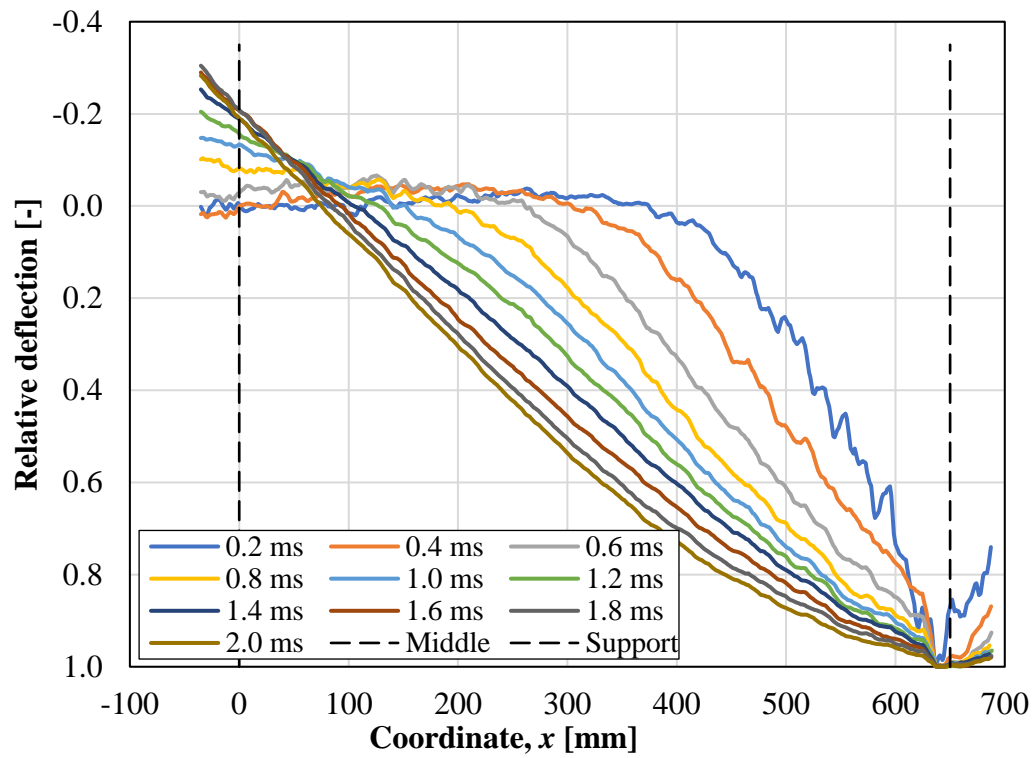
Figure E.6   Relative deformed shape for the initial 2 ms of the drop weight impact illustrating the behaviour of deflection for beam 17-B2-FRP3-D3.5.

F Appendix – Deformed Shape for 3 m Drop Height

Deformed shape for the initial 2.0 ms for beams subjected to 3 m drop weight impact are here presented in deflection and relative deflection over half of the beam. The estimated time for 0.2 ms after impact from camera 1 are presented in Table F.1.

Table F.1   Estimated times from camera 1 for 0.2 ms after impact, for beams subjected to drop weight impact of 3 m drop height.

Beam	Time [ms]
06-B2-FRP0-D3	0.150
12-B2-FRP1-D3	0.165
18-B2-FRP3-D3	0.287

Deflection over the beam for the initial 2.0 ms after impact are presented in Figure F.1 to Figure F.3 for beams subjected to 3 m drop height.
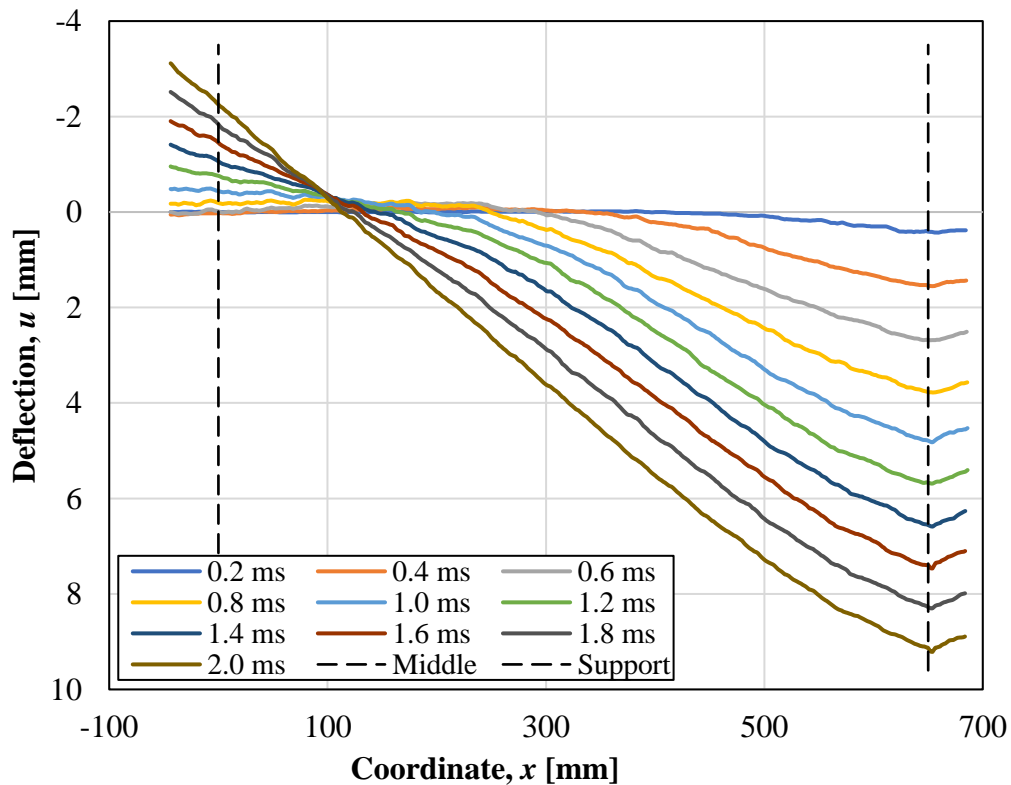
Figure F.1   Deformed shape for the initial 2 ms of the drop weight impact illustrating the behaviour of deflection for beam 06-B2-FRP0-D3.
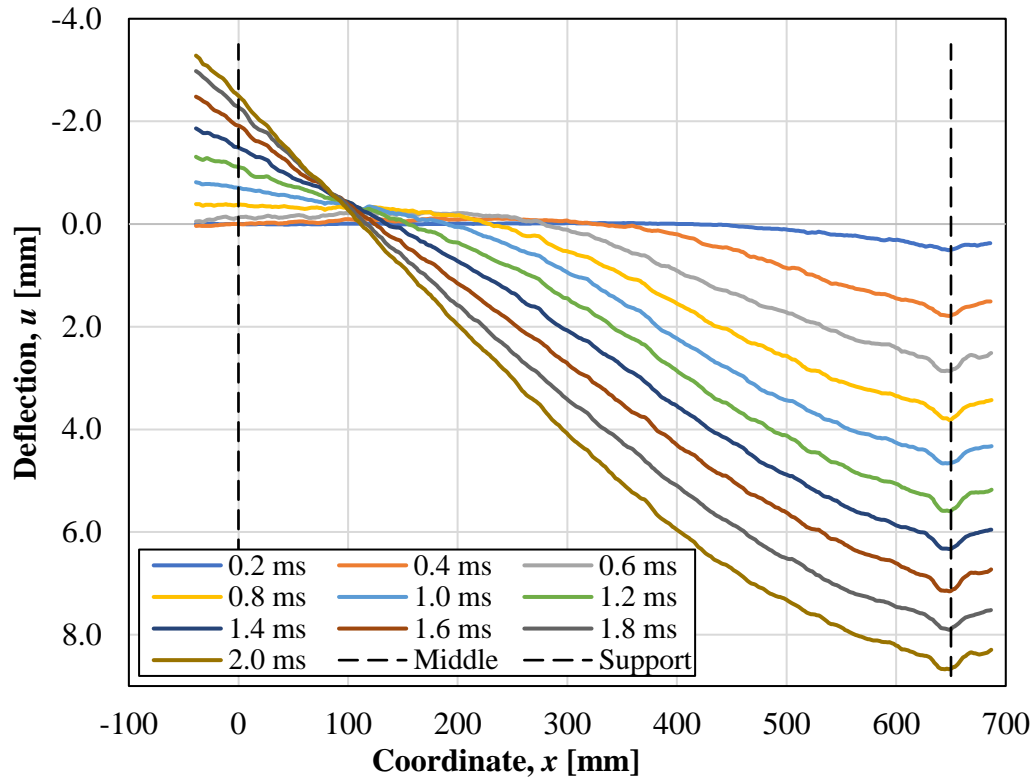
Figure F.2   Deformed shape for the initial 2 ms of the drop weight impact illustrating the behaviour of deflection for beam 12-B2-FRP1-D3.
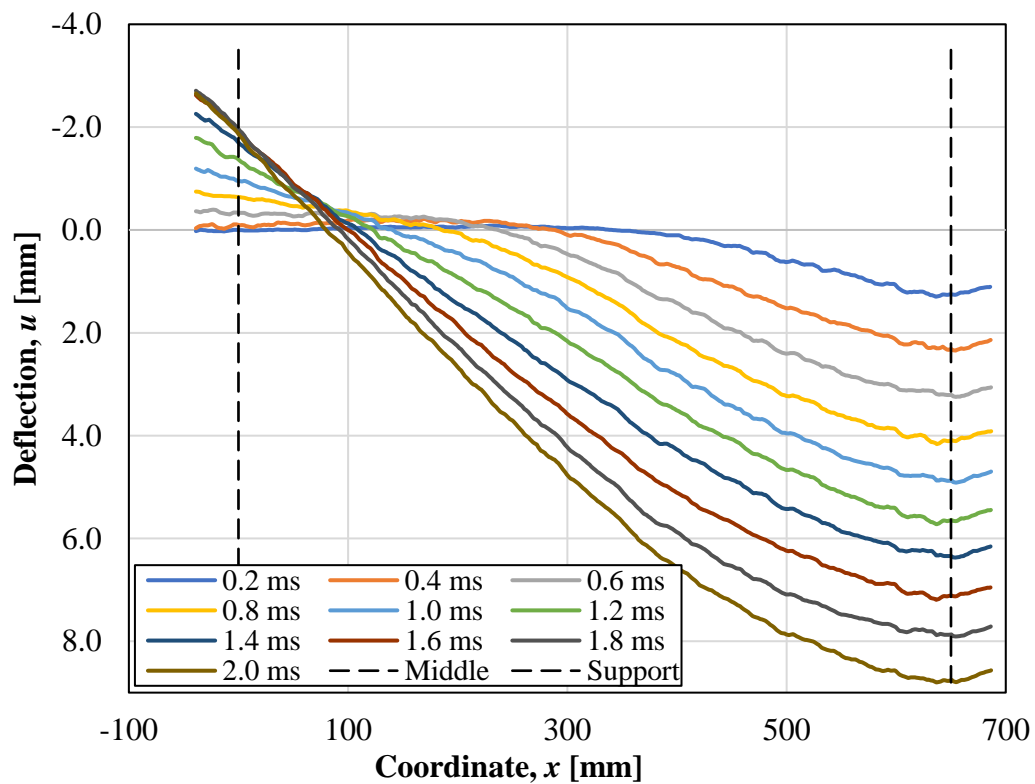
Figure F.3   Deformed shape for the initial 2 ms of the drop weight impact illustrating the behaviour of deflection for beam 18-B2-FRP3-D3.

Relative deflection over the beam for the initial 2.0 ms after impact are presented in Figure F.4 to Figure F.6 for beams subjected to 3 m drop height.
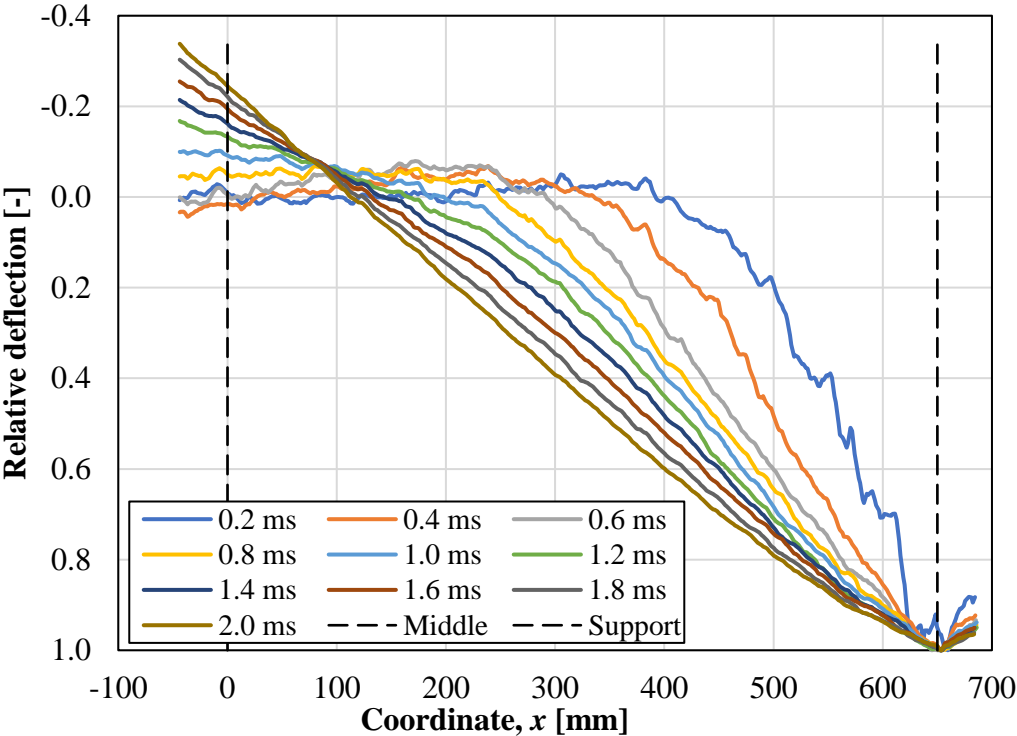
Figure F.4   *Relative deformed shape for the initial 2 ms of the drop weight impact illustrating the behaviour of deflection for beam 06-B2-FRP0-D3.*
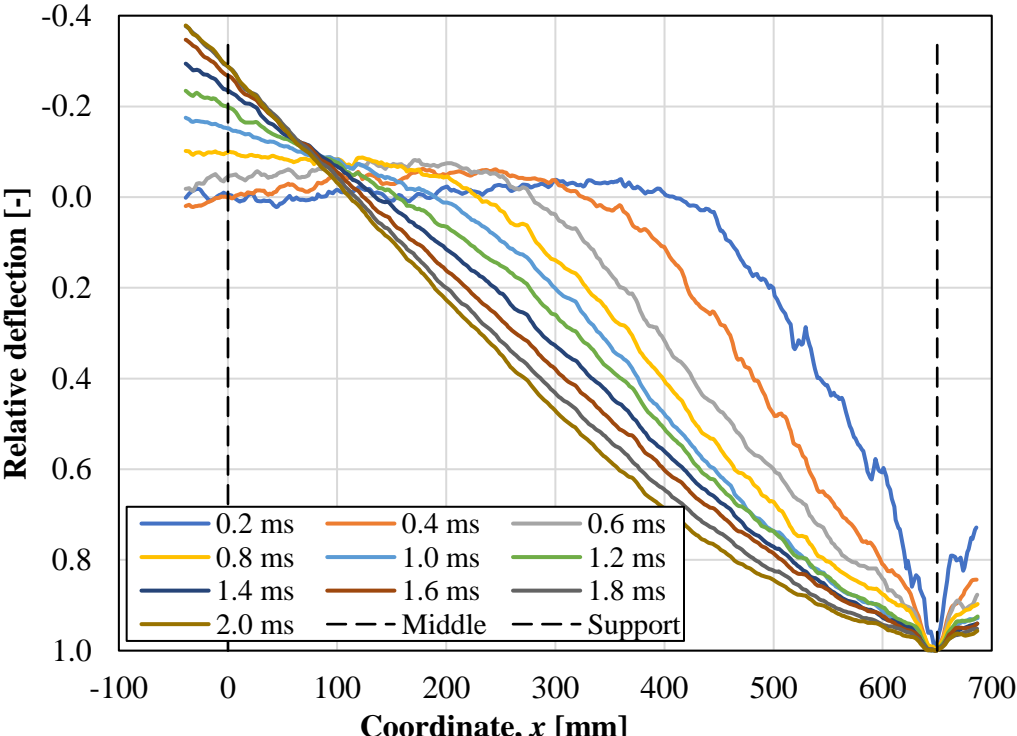
Figure F.5   *Relative deformed shape for the initial 2 ms of the drop weight impact illustrating the behaviour of deflection for beam 12-B2-FRP1-D3.*
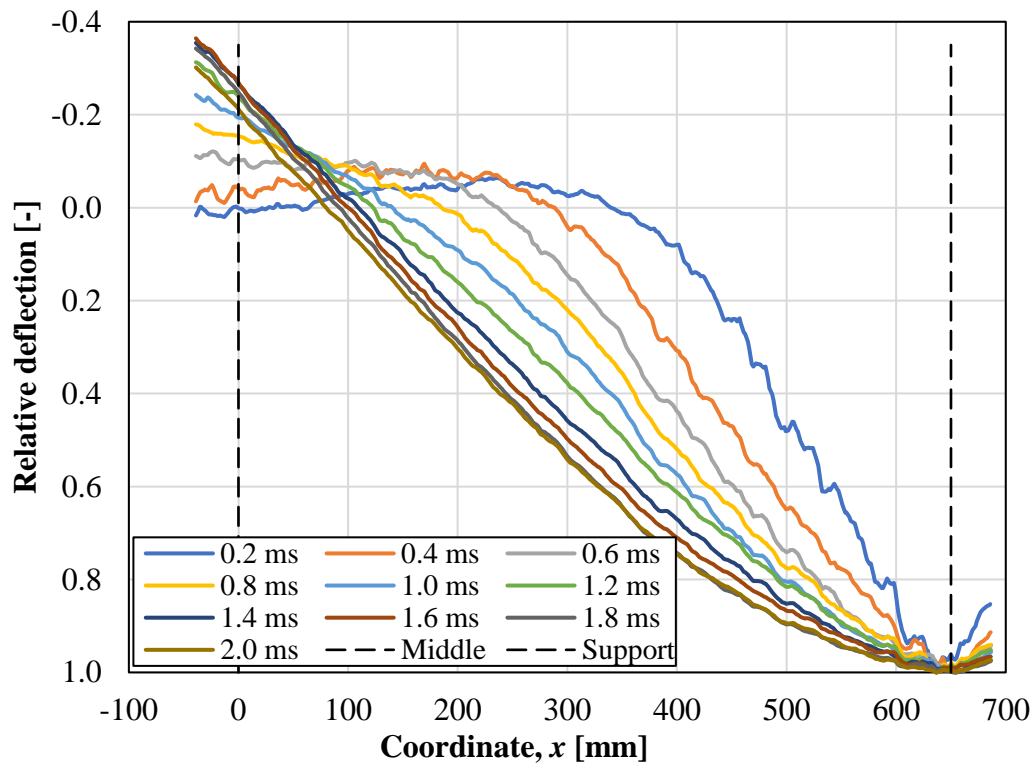
Figure F.6 *Relative deformed shape for the initial 2 ms of the drop weight impact illustrating the behaviour of deflection for beam 18-B2-FRP3-D3.*

G Appendix – Determination of Plastic Deformation from Impact Loading

To determine the plastic deformation resulted from impact loading, the impacted beam was placed in the same position in approximately the same position as it was placed on the support before impact took place, see Figure G.1 and Figure G.2. Then, footage was taken by DIC in order to determine the midpoint plastic deformation of the beam. It is seen that the deformation at the support was not equal to zero on the image of impacted beam from which the plastic deformation was calculated. In order to correct this the midpoint plastic deformation was calculated from midpoint deformation, u_{mid}, and the support deflection, u_{sup}, as

$$u_{pl} = u_{mid} - u_{sup} \qquad\qquad\qquad (G.1)$$

Figure G.1   Image of beam 10-B1-FRP1-D4 before impact, used as reference image.
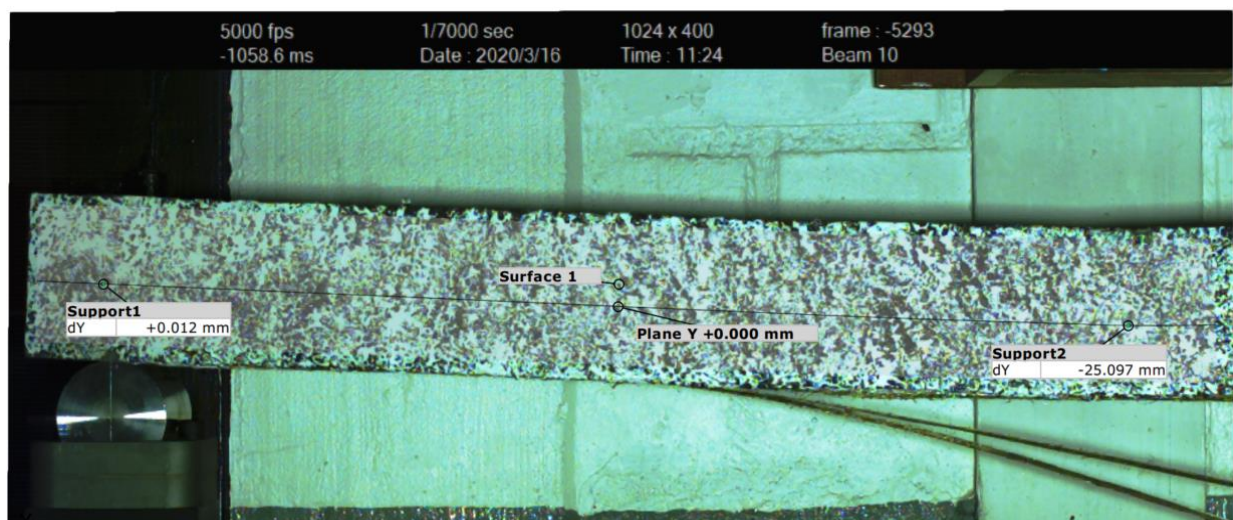
Figure G.2   Image of beam 10-B1-FRP1-D4 after impact, used as reference image.

H   Appendix – Propagation Velocity of Initial Deflection

The propagation velocity of initial deflection for beams subjected to 3.5 m and 3 m drop height are presented in Table H.1 and Table H.2. Figure H.1 and Figure H.2 illustrates the relation between average propagation velocity of initial deflection and span to depth ratio for beams subjected to 3.5 m and 3 m drop weight impact.

Table H.1   *Velocity of initial deflection for the deformed shape of beams subjected to a drop weight impact of 3.5 m.*

Beam	05-B2-FRP0-D3.5	11-B2-FRP1-D3.5	17-B2-FRP3-D3.5
Time [ms]	Propagation velocity of initial deformation [m/s]		
0.4	364	370	340
0.6	190	215	222
0.8	129	222	334
1.0	167	204	217
1.2	111	167	117
1.4	124	99	111
1.6	92	74	68
1.8	38	31	43
2.0	37	19	37

Table H.2   *Velocity of initial deflection for the deformed shape of beams subjected to a drop weight impact of 3 m.*

Beam	06-B2-FRP0-D3	12-B2-FRP1-D3	18-B2-FRP3-D3
Time [ms]	Propagation velocity of initial deformation [m/s]		
0.4	352	426	271
0.6	222	234	259
0.8	222	247	260
1.0	254	198	222
1.2	154	173	80
1.4	111	105	74
1.6	68	55	50
1.8	37	25	37
2.0	56	31	62
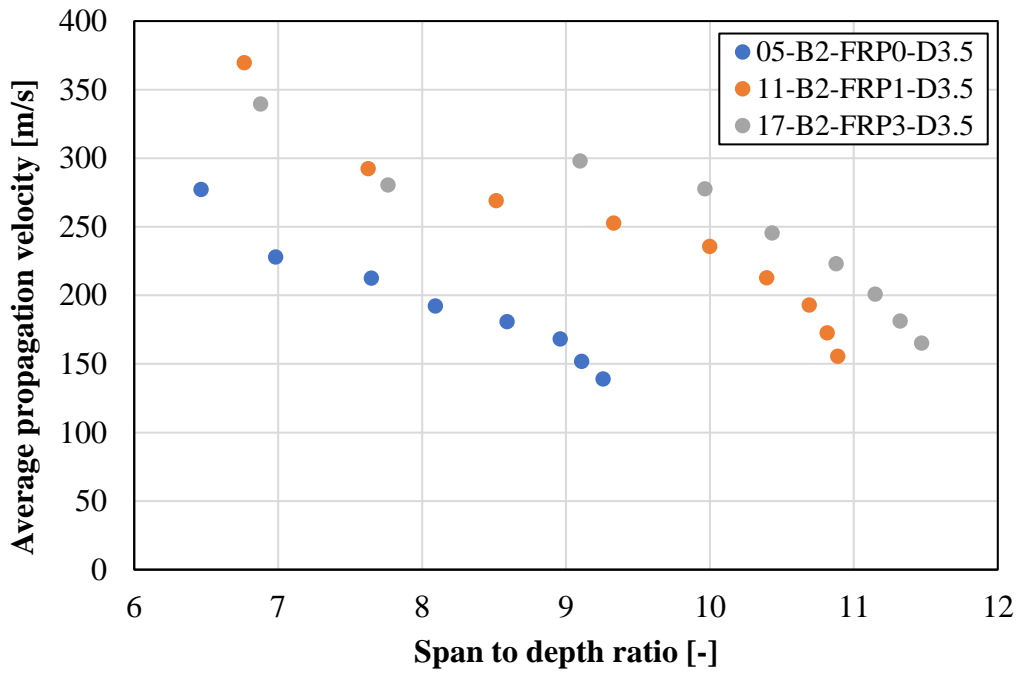
Figure H.1   *Average propagation velocity for the initial 2 ms of the drop weight impact, starting with values for 0.4 ms and continues with time steps of 0.2 ms for the beams subjected to 3.5 m drop height impact.*
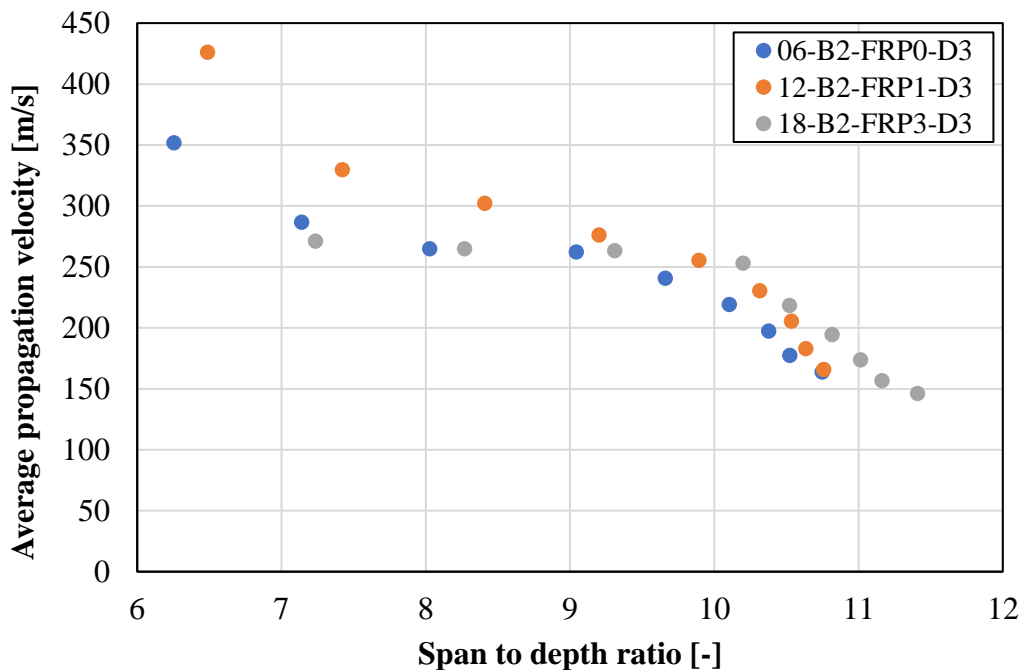
Figure H.2   *Average propagation velocity for the initial 2 ms of the drop weight impact, starting with values for 0.4 ms and continues with time steps of 0.2 ms for the beams subjected to 3 m drop height impact.*

I Appendix – Calculation of Stiffness

How the different stiffnesses, k_I, k_{cy} and k_{II}, are presented in Section 9.3 are illustrated in Figure I.1 and Figure I.2. The stiffness, k_i, is calculated from change in force and change in deformation from load-deformation curves of static tests as

$$k_i = \frac{\Delta F_i}{\Delta u_i} \tag{I.1}$$
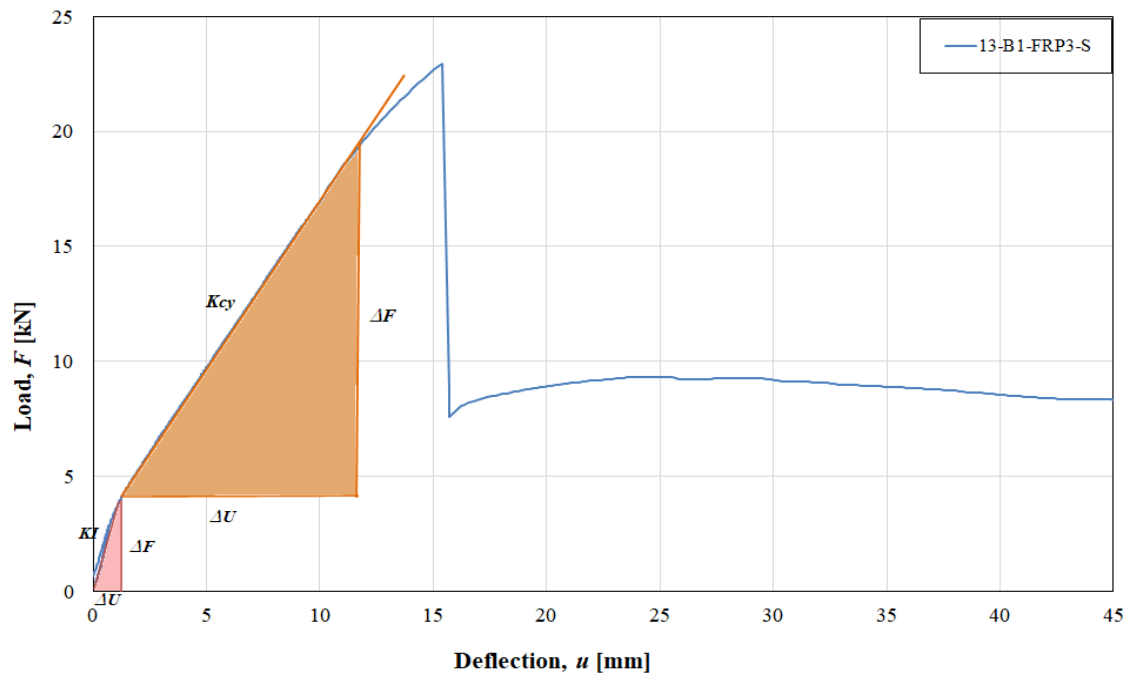
Figure I.1   Illustration of derivation of k_I and k_{cy} from test results.
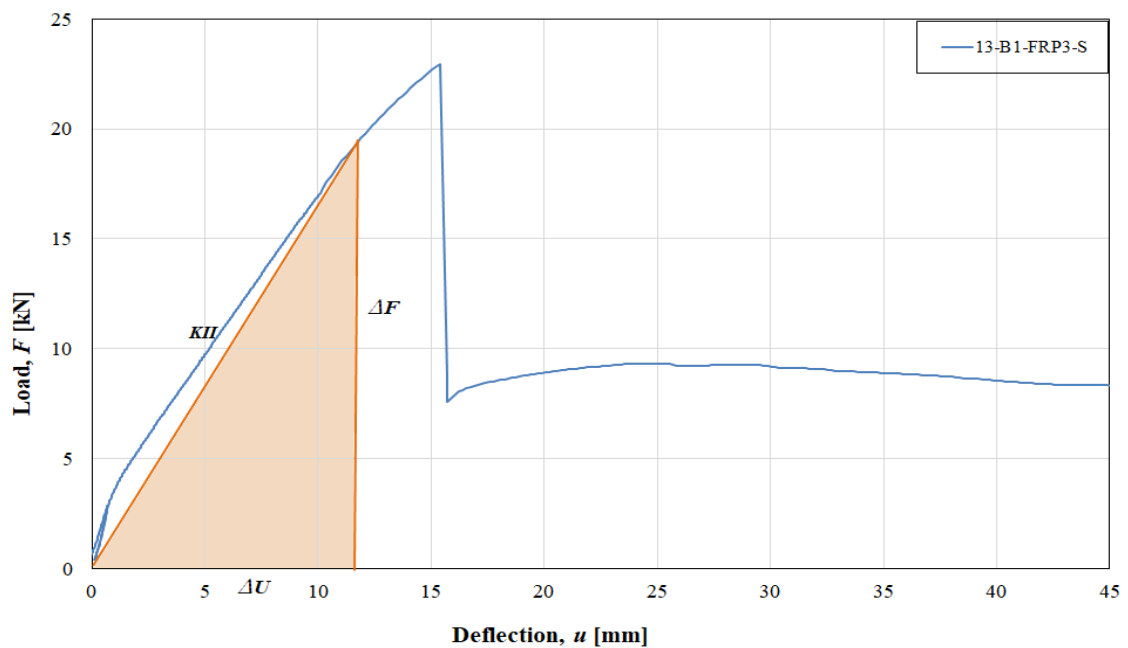
Figure I.2   Illustration of derivation of k_{II} from test results.

J   Appendix – Calculation of Internal Work

The internal work is calculated for different load levels. For FRP strengthened beams, the 100 % load level is taken as the same maximum force encountered in unstrengthen beams i.e., F_{Rmax}. Thus, different load levels are taken as a percentage of F_{Rmax}. Secant state II stiffness is also assumed for reference beam. For strengthened beams the secant stiffness in state II is assumed to collide with the dropping point of load deformation plot after debonding, taking the internal work prior to debonding as elastic internal work. The internal work is calculated as the area under the load deformation curve. Plastic internal work at different load levels for unstrengthened beams and FRP strengthened beams are illustrated in Figure J.1 to Figure J.3.
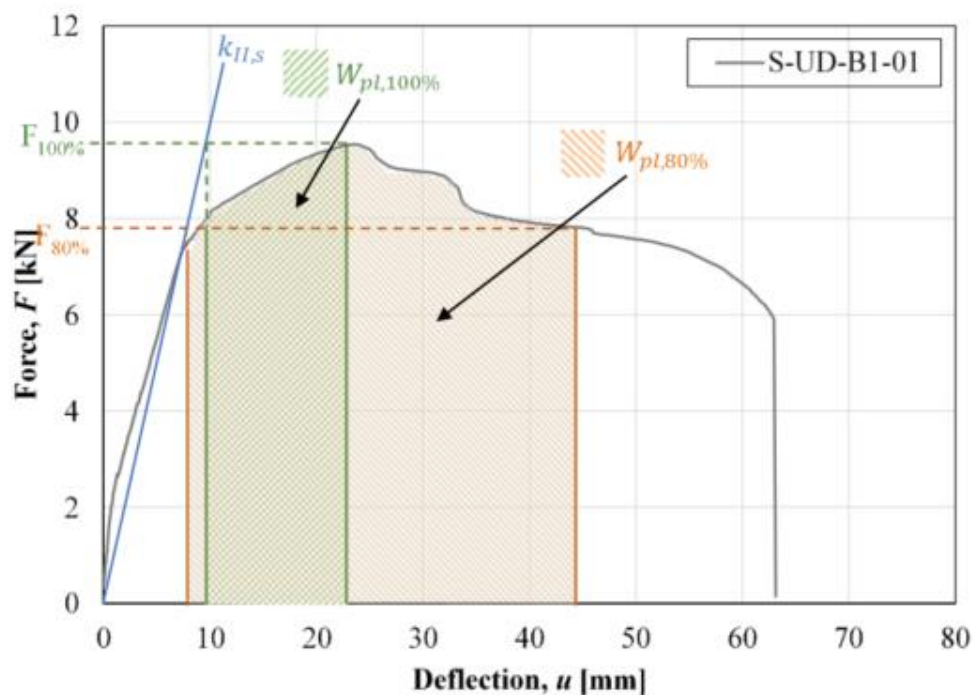
Figure J.1   Illustration of internal work for FRP strengthened beams from test results for unstrengthened beams, from Andersson and Petersson (2019).
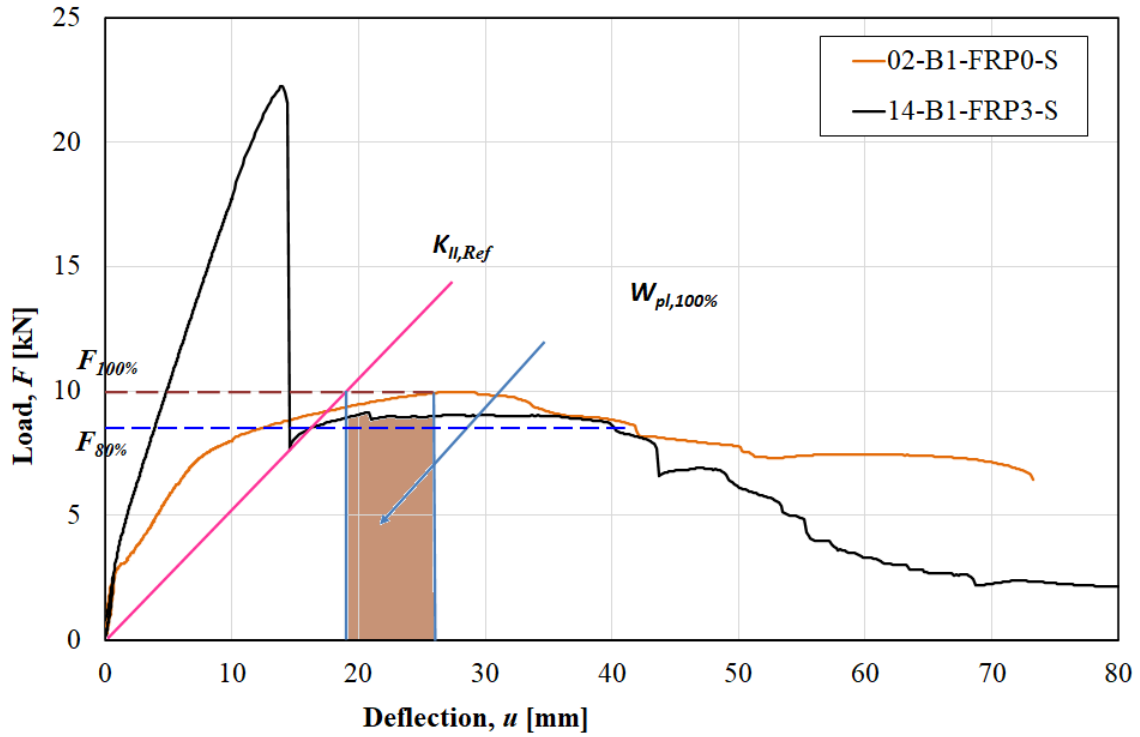
Figure J.2   Illustration of internal work, $W_{pl,100\%}$ for FRP strengthened beams from test results.
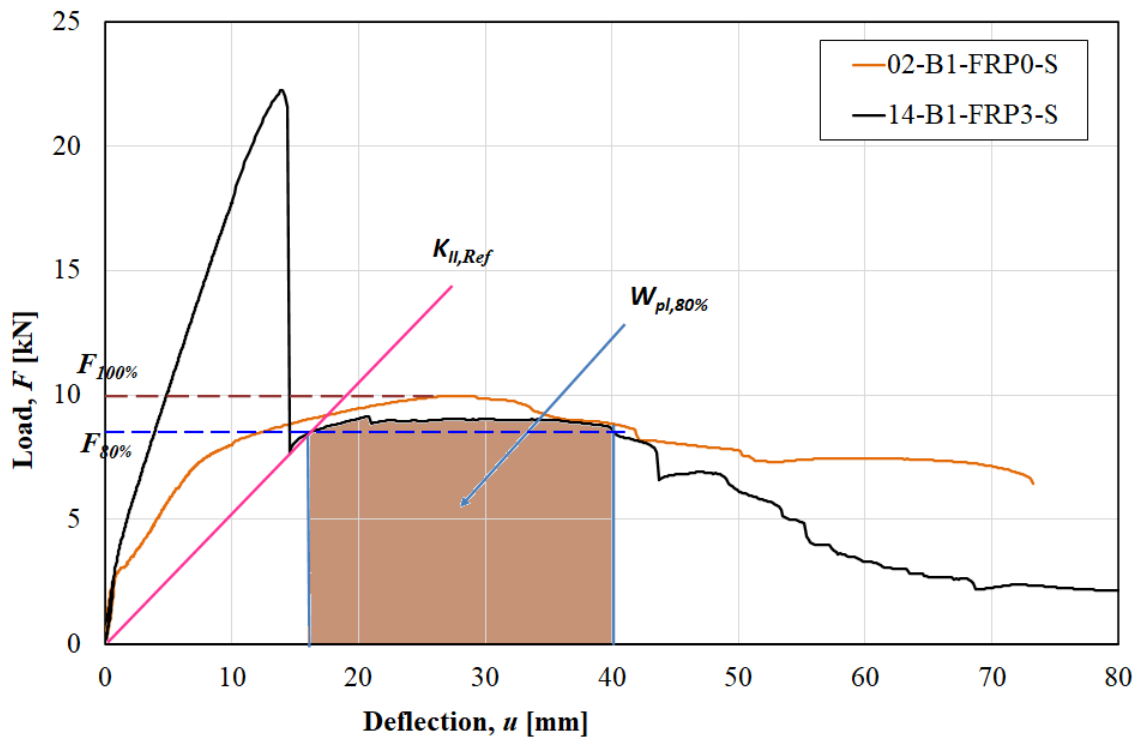
Figure J.3   Illustration of internal work, $W_{pl,80\%}$, for FRP strengthened beams from test results.

K Appendix – Approximation of Internal Work

To see how the impact loading influenced the internal work, approximate calculation is done and presented in section 9.3.2.3. A section of internal work, W_{imp}, from the only statically loaded beams is calculated to compensate for the loss due to drop weight impact. Then W_{imp} is added with the plastic internal work of this statically loaded impacted beam to get $W_{imp+stat}$, see Figure K.1 to Figure K.3.
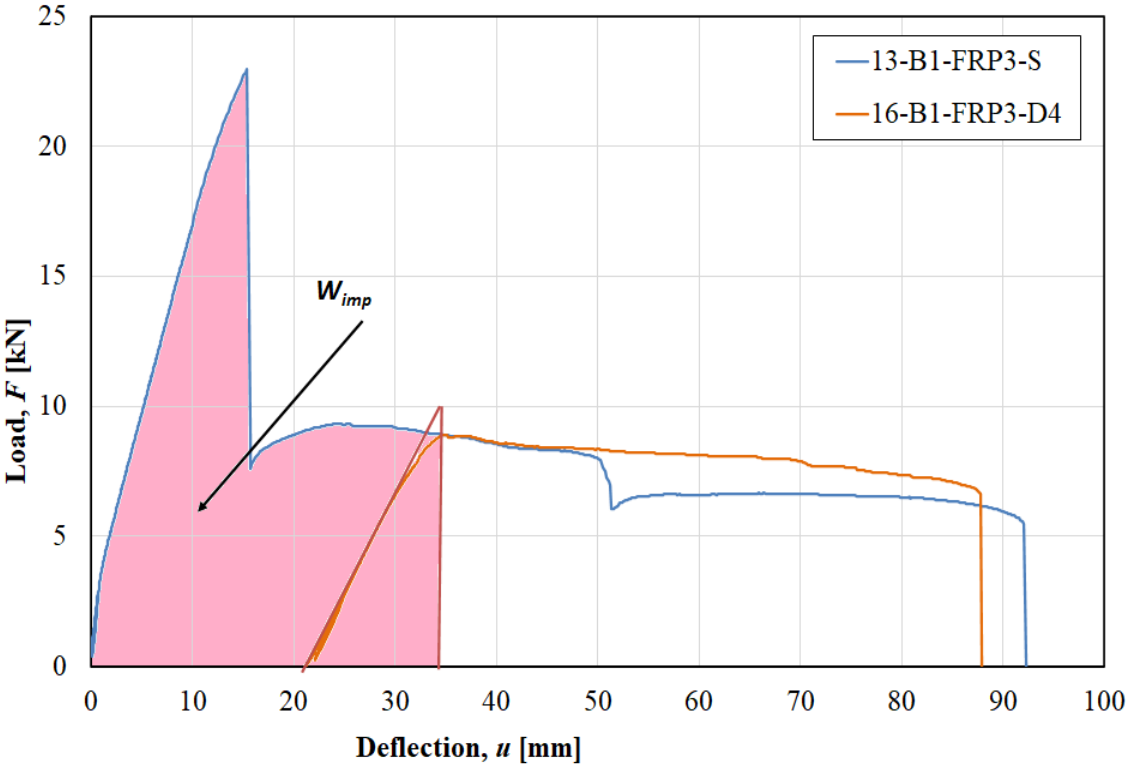
Figure K.1   Illustration of internal work, W_{imp}, for FRP strengthened beams from test results.
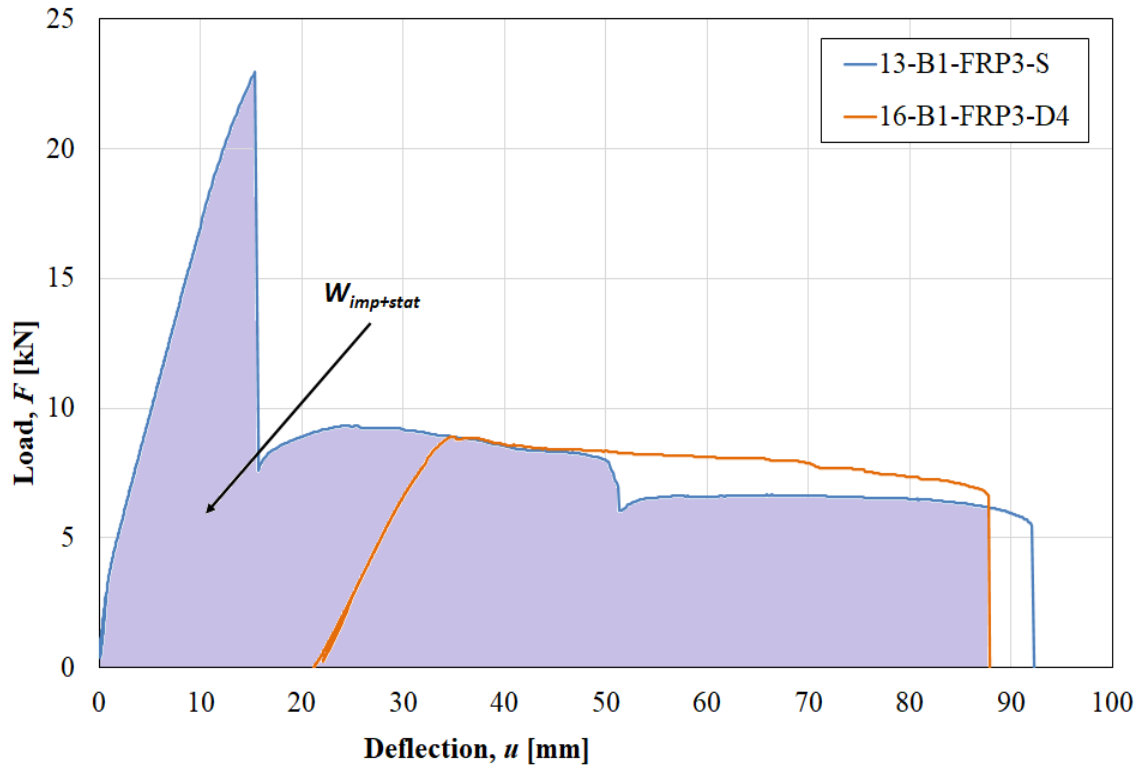
Figure K.2   Illustration of internal work, W_{imp}, for FRP strengthened beams from test results.
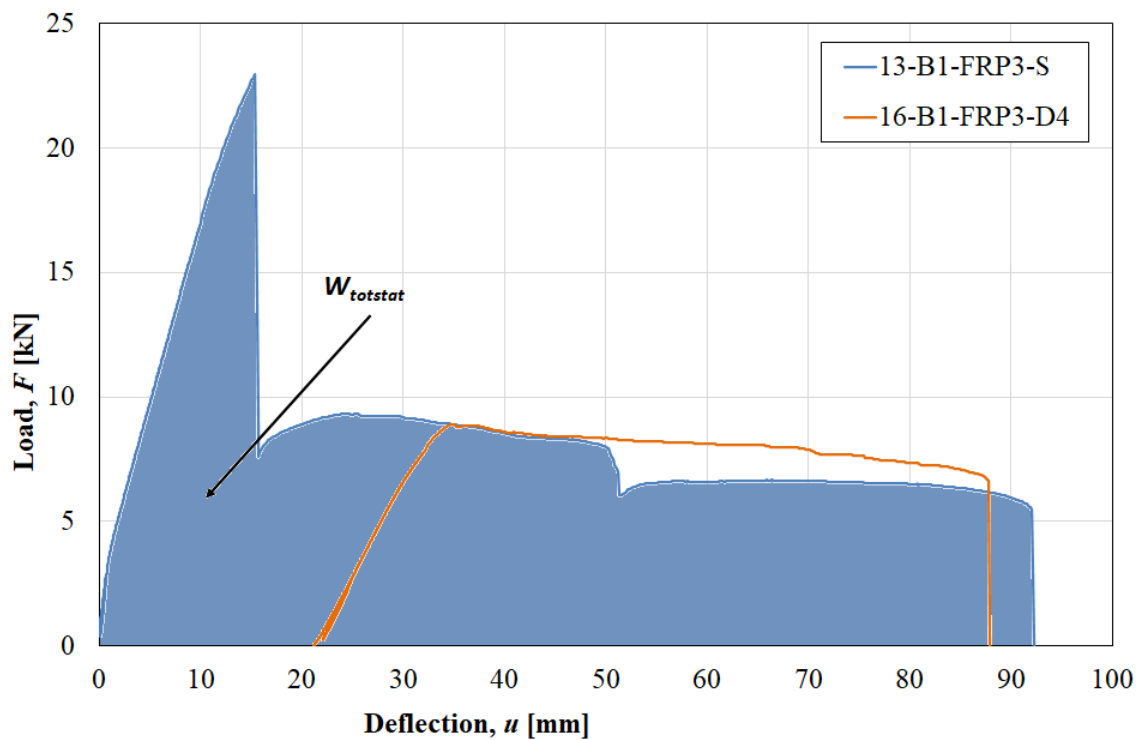
Figure K.3   Illustration of internal work, $W_{totstat}$ for FRP strengthened beams from test results.

L   Appendix – Convergence Study for 2DOF Model

To find the internal resistance of the drop weight, R_1, and the stiffness of the spring between the drop weight and the beam, k_1, for the 2DOF model a convergence study were made. The most relevant values for R_1 were plotted and the corresponding k_1 was calculated according to hertz contact theory, see Appendix M. These results were then compared with the results from the experimental tests. The values chosen for R_1 were based on the convergence study conducted by Andersson and Pettersson (2019). The convergence study is illustrated in Figure L.1, input data for R_1 and k_1 are found in Table L.1 and other input data for the convergence study are tabulated in Table L.2.

Table L.1   Input data for R_1 and k_1 that were used in the convergence study.

R_1 [kN]	40	50	60	70	80
k_1 [MN/m]	239	258	274	289	301

Table L.2   Input data that were used in the convergence study.

Drop height [m]	v_0 [m/s]	$R_{2,measured}$ [kN]	k_2 [MN/m]	I_{II} [m⁴]
4	8.49	8.80	1.07	$1.42 \cdot 10^{-6}$
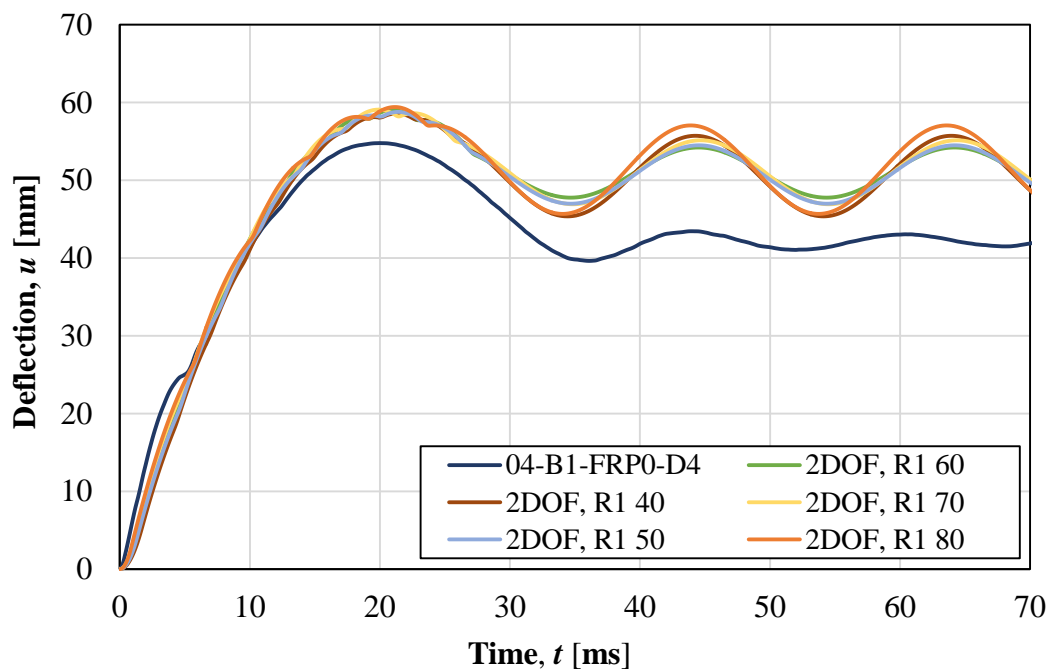
Figure L.1   Convergence study to find internal resistance of the drop weight, R_1, and the stiffness of the spring between the drop weight and the beam, k_1.

M Appendix – Hertz Contact Theory for 2DOF Model

The stiffness of the spring between the drop weight and the beam, k_1, for the 2DOF model was found through Hertz contact theory. In combination with a convergence study, see Appendix L, the internal resistance of the drop weight, R_1, was estimated to 50 kN. Impact load, F_1, was calculated using Equation (M.2) by using a constant k_1 from Equation (M.2). With R_1 put in the impact load - local deformation curve, the secant could be found which is stiffness k_1, see Figure M.1.

$$k_1 = \frac{4 \cdot \sqrt{r_1}}{3} \left[\frac{1 - v_1^2}{E_1} + \frac{1 - v_2^2}{E_2} \right]^{-1}$$

(M.1)

$$F_1 = k_1 \cdot \delta^{3/2}$$

(M.2)
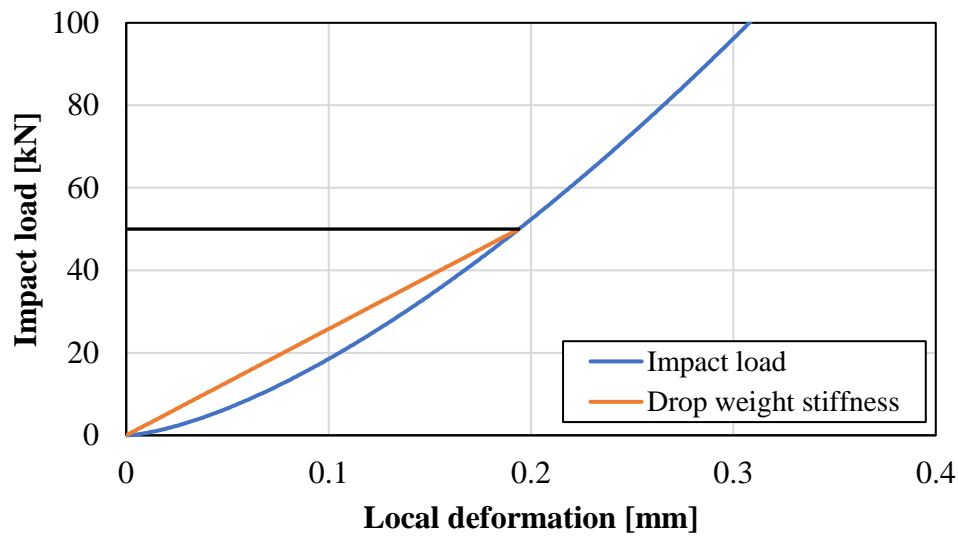
Figure M.1   Impact load-local deformation curve illustrating the stiffness of the spring between the drop weight and the beam, k_1.

N   Appendix – Matlab Script for 2DOF Model

```matlab
%%%%%%%%%%%%%%%%%%%%%%%%%%%%%%%%%%%%%%%%%%%%%%%%%%%%%%%%%%%%%%%%%%%%%%%
%%%%%%%%%%%%                                               %%%%%%%%%%%%
%%%%%%%%%%%% Simplified 2DOF system                        %%%%%%%%%%%%
%%%%%%%%%%%%                                               %%%%%%%%%%%%
%%%%%%%%%%%% Yeabkal Zeleke Nigani                         %%%%%%%%%%%%
%%%%%%%%%%%% Gabriella Nordström                           %%%%%%%%%%%%
%%%%%%%%%%%%                                               %%%%%%%%%%%%
%%%%%%%%%%%% Modified from the version made by             %%%%%%%%%%%%
%%%%%%%%%%%% Fabio Lozano Mendoza and Josef Makdesi Aphram %%%%%%%%%%%%
%%%%%%%%%%%%                                               %%%%%%%%%%%%
%%%%%%%%%%%% Chalmers University of Technology             %%%%%%%%%%%%
%%%%%%%%%%%%                                               %%%%%%%%%%%%
%%%%%%%%%%%% 22/5-20                                       %%%%%%%%%%%%
%%%%%%%%%%%%                                               %%%%%%%%%%%%
%%%%%%%%%%%%                                               %%%%%%%%%%%%
%%%%%%%%%%%%%%%%%%%%%%%%%%%%%%%%%%%%%%%%%%%%%%%%%%%%%%%%%%%%%%%%%%%%%%%%%
clear all
close all
clc

conditions=1;              %Indata for different impact conditions
                           % 1 - 4 m drop height
                           % 2 - 3.5 m drop height
                           % 3 - 3 m drop height


resistance=1;              %Indata for resistance
                           % 1 - calculated resistance, no FRP
                           % 2 - measured resistance, no FRP


%%%%%%%%%%%%%%%%%%%%%%%%%%%%%%%%%%%%%%%%%%%%%%%%%%%%%%%%%%%%%%%%%%%%%%%

if conditions==1
    height=3.97;           %Drop height [m]
    v_d=8.49;              %Velocity of drop weight [m/s]
elseif conditions==2
    height=3.44;           %Drop height [m]
    v_d=8.03;              %Velocity of drop weight [m/s]
elseif conditions==3
    height=2.94;           %Drop height [m]
    v_d=7.42;              %Velocity of drop weight [m/s]
end

if resistance==1
    R_u=8.10e3;            %Calculated resistance [N]
elseif resistance==2
    R_u=8.80e3;            %Measured resistance [N]
end
```

```matlab
%MATERIAL PROPERTIES
%Concrete
r_c=2432;                   %Mass density [kg/m3]
E_c=34.7e9;                 %Modulus of elasticity [Pa]


%Reinforcement
r_s=7800;                   %Mass density (common value for rebars) [kg/m3]
E_s=196e9;                  %Modulus of elasticity [Pa]




%GEOMETRY
%Drop weight
r_d=0.04;                   %Radius of drop weight [m]
A_1=pi*0.04^2;              %Area of drop weight [m2]
L_d=0.505;                  %Height of drop weight [m]

%Beam
h_b=0.1;                    %Height of beam [m]
w_b=0.1;                    %Width of beam [m]
A_2=h_b*w_b;                %Area of beam [m2]
L_b=1.3;                    %Length of span of beam [m]




%TRANSFORMATION FACTORS
%Transformation factors for the drop weight
k_d_m=1;                    %Plastic mass transformation factor [-]
k_d_F=1;                    %Plastic load transformation factor [-]
k_d_K=1;                    %Plastic stiffness transformation factor [-]


%Transformation factors for the beam
k_b_m_el=0.486;            %Elastic mass transformation factor [-]
k_b_m_pl=0.333;            %Plastic mass transformation factor [-]

k_b_F_el=1;               %Elastic load transformation factor [-]
k_b_F_pl=1;               %Plastic load transformation factor [-]

k_b_K_el=1;               %Elastic stiffness transformation factor [-]
k_b_K_pl=1;               %Plastic stiffness transformation factor [-]




%MASS PROPERTIES
m_1=20;                     %Mass of drop weight [kg]
m_2=r_c*A_2*L_b;            %Mass of beam [kg]

%Mass matrix
M=[m_1*k_d_m 0; 0 m_2*k_b_m_pl];
```

```matlab
%STIFFNESS PROPERTIES
I_b_ii=1.416e-6;           %Second moment of inertia of beam, state II [m4]
                           %calculated in mathcad


% K_el_1=A_1*E_s/L_d;      %Elastic stiffness of drop weight 1.9509e+09 [N/m]
K_el_1=2.58e+8;            %Elastic stiffness of drop weight [N/m]


K_el_2=48*E_c*I_b_ii/L_b^3;%Elastic stiffness of the beam  1.0735e+06 [N/m]


%Initial stiffness matrix
K_el=[K_el_1 -K_el_1
    -K_el_1 K_el_1+K_el_2];



%MATERIAL RESPONSE
%Drop weight
R_1=50e+3;                 %Plastic resistance [N]


u_el_1=R_1/K_el_1;         %Limit of elastic deformation [m]
u_rd_1=50;                 %Limit of plastic deformation [m]


%Beam
R_2_sw=r_c*9.81*A_2*L_b/2;   %Reduction of plastic resistance due to
                             %self-weight [N]
R_2=R_u-R_2_sw;            %Plastic resistance [N]


u_el_2=R_2/K_el_2;         %Limit of elastic deformation [m]
u_rd_2=50;                 %Limit of plastic deformation [m]



%DETERMINATION OF EIGENFREQUENCIES


[L,X]=eig(K_el, M);        %L is a matrix containing the eigenvectors
                           %X is a matrix containing the eigenvalues


%Maximum eigenfrequency
w_max=sqrt(max(max(X)));



%CRITICAL TIME-STEP


h_crit=2/w_max;            %Maximum admissible value [s]
h=0.1e-4;                  %Chosen time step [s]


t_end=80e-3;              %End of sequence [s]
t=linspace(0,t_end,t_end/h);  %Time vector


if h>=h_crit
    disp('ERROR, chosen time step too large')
end
```

```matlab
%INITIAL CONDITIONS
%Empty matrices
dofs=2;                      %Number of degree of freedom
u=zeros(dofs, length(t));    %Empty matriX storing displacement vectors
v=zeros(dofs, length(t)-1);  %Velocity vectors
a=zeros(dofs, length(t)-1);  %Acceleration vecors

%Assigning initial values
u(:,1)=[0;0];                %Initial displacement


% v_d=sqrt(2*9.81*height);   %Initial velocity of drop weight [m/s]
v(:,1)=[v_d; 0];             %Velocities at time t=0

a_0=inv(M)*(-K_el*u(:,1));   %Initial acceleration vector
a(:,1)=a_0;                  %Initial acceleration as calculated before

u_b0=u(:,1)-h*v(:,1)+h^2/2*a(:,1); %Displacement at time step n-1

%Initial plastic deformation
u_pl_1=0;                    %Plastic deformation of rod
u_pl_2_pos=0;                %Plastic deformation of beam in compression
u_pl_2_neg=0;                %Plastic deformation of beam in tension



%CENTRAL DIFFERENTIAL METHOD
for i=2:length(t)
    du=u(1,i-1)-u(2,i-1);     %Relative displacement between beam and
                              %drop weight [m]
    u2=u(2,i-1);              %Downward displacement for beam [m]


    %Determining resistance and stiffness of fictitious spring between
    %drop weight and beam

    %if du=0, set stiffness equal to elastic stiffness
    if du==0
        K_1=K_el_1;
        %If spring is in tension set stiffness to 0
    elseif du < u_pl_1
        K_1=0;
        %If spring is in elastic range
    elseif du > u_pl_1 && du <= u_pl_1+u_el_1
        R=K_el_1*(du-u_pl_1);
        K_1=R/du;
        %If spring is in plastic range
    elseif du > u_pl_1+u_el_1
        K_1=R_1/du;
        u_pl_1=du-u_el_1;
    end
```

```matlab
    %Determining resistance and stiffness of beam spring
    %If u2=0, set stiffness equal to elastic stiffness
    if u2==0
        K_2=K_el_2;
        %If spring is in elastic tension/compression
    elseif u2 > u_pl_2_pos-u_el_2 && u2 <= u_pl_2_pos+u_el_2
        R=K_el_2*(u2-u_pl_2_pos);
        K_2=R/u2;
        %If spring is in plastic compression
    elseif u2 > u_pl_2_pos+u_el_2
        K_2=R_2/u2;
        u_pl_2_pos=u2-u_el_2;
        %If spring is in plastic tension
    elseif u2 <= u_pl_2_pos-u_el_2
        K_2=-R_2/u2;
        u_pl_2_neg=abs(u2+u_el_2-u_pl_2_pos);
        u_pl_2_pos=u_pl_2_pos-u_pl_2_neg;
    end

    %Storing values of resistance for all time steps
    RES(1,i-1)=K_1*du;
    RES(2,i-1)=K_2*u2;

    %Computing stiffness matrix
    K=[(K_1) (-K_1); (-K_1) (K_1)+(K_2)];

    %Calculation of displacement, velocity and acceleration
    if i==2
        u(:,i)=inv(M/h^2)*(-(K-2*M/h^2)*u(:,i-1)-(M/h^2)*u_b0);
    else
        u(:,i)=inv(M/h^2)*(-(K-2*M/h^2)*u(:,i-1)-(M/h^2)*u(:,i-2));
        v(:,i-1)=(u(:,i)-u(:,i-2))/(2*h);
        a(:,i-1)=(u(:,i)-2*u(:,i-1)+u(:,i-2))/h^2;
    end
end
end

%CALCULATION OF ENERGY
%External work of beam
DeltaWe(1)=0;
We(1)=0;
for i=2:(length(t)-1)
    DeltaWe(i)=0.5*(RES(1,i-1)+RES(1,i))*(u(2,i)-u(2,i-1));
    We(i)=We(i-1)+DeltaWe(i);
end

%Internal work of beam
DeltaWi(1)=0;
Wi(1)=0;
for i=2:(length(t)-1)
    DeltaWi(i)=0.5*(RES(2,i-1)+RES(2,i))*(u(2,i)-u(2,i-1));
    Wi(i)=Wi(i-1)+DeltaWi(i);
end
%Kinetic energy
Wk(1)=0;
```

```
for i=2:(length(t)-1)
    Wk(i)=m_2*k_b_m_pl*0.5*v(2,i-1)^2;
end

%Total energy
Wt(1)=0;
for i=2:(length(t)-1)
    Wt(i)=Wi(i)+Wk(i);
end


%CREATING PLOTS
%Displacement-time
figure(1)
plot(t*1000,u(1,:)*1000,'LineWidth',3)
set(gca,'fontsize',16)
title('Displacement of mass 1','FontSize',30)
xlabel('Time [ms]');
ylabel('Displacement [mm]');

% figure(2)
plot(t*1000,u(2,:)*1000,'LineWidth',3)
grid on
set(gca,'fontsize',16)
title('Displacement of mass 2','FontSize',30)
xlabel('Time [ms]');
ylabel('Displacement [mm]');
hold on

%Resistance-displacement
figure(3)
plot(u(2,1:length(u)-1)*1000,RES(2,:)/1000,'LineWidth',3)
set(gca,'fontsize',16)
title('Internal resistance vs displacement - body 2','FontSize',30)
xlabel('Displacement [mm]');
ylabel('Resistance [kN]');

figure(4)
plot(u(1,1:1500)*1000-u(2,1:1500)*1000,RES(1,1:1500)/1000,'LineWidth',3)
set(gca,'fontsize',16)
title('Internal resistance vs displacement - body 1','FontSize',30)
xlabel('Displacement [mm]');
ylabel('Resistance [kN]');

%Resistance-time
figure(5)
plot(t(1:length(t)-1)*1000,RES(2,:)/1000,'LineWidth',3)
set(gca,'fontsize',16)
title('Internal resistance vs time - body 2','FontSize',30)
xlabel('Time [ms]');
ylabel('Resistance [kN]');

figure(6)
plot(t(1:1500)*1000,RES(1,1:1500)/1000,'LineWidth',3)
```

```matlab
set(gca,'fontsize',16)
title('Internal resistance vs time - body 1','FontSize',30)
xlabel('Time [ms]');
ylabel('Resistance [kN]');

% Velocity-time
figure(7)
plot(t(1:(length(t)-1))*1000,v(1,:),'LineWidth',3)
set(gca,'fontsize',16)
title('Velocity of body 1','FontSize',30)
xlabel('Time [ms]');
ylabel('Velocity [m/s]');
hold on

figure(8)
plot(t(1:(length(t)-1))*1000,v(2,:),'LineWidth',3)
set(gca,'fontsize',16)
title('Velocity of body 2','FontSize',30)
xlabel('Time [ms]');
ylabel('Velocity [m/s]');
hold on

%Work-time
figure(9)
plot(t(1:(length(t)-1))*1000,We(:),'LineWidth',3)
hold on
plot(t(1:(length(t)-1))*1000,Wi(:),'LineWidth',3)
hold on
plot(t(1:(length(t)-1))*1000,Wk(:),'LineWidth',3)
hold on
plot(t(1:(length(t)-1))*1000,Wt(:),'LineWidth',3)
set(gca,'fontsize',16)
title('External work of body 2','FontSize',30)
xlabel('Time [ms]');
ylabel('work [J]');

height;
v_init=v(1,2);
maxdisp=max(max(u(2,:)));
u_pl=maxdisp-u_el_2;
[height v_init maxdisp u_pl]




%1 - Drop weight
%2 - Beam





%CREATE TXT-FILE WITH DATA
% Create a table with the data for beam deflection-time curve
```

```matlab
a=t*1000;
b=u(2,:)*1000;
A = a.';
B = b.';
AB = table(A, B, 'VariableNames', { 'A', 'B'} );
% Write data to text file
writetable(AB, 'MyFileforce.txt');


% Create a table with the data for drop weight velocity-time curve
c=t(1:(length(t)-1))*1000;
d=v(1,:);
C = c.';
D = d.';
CD = table(C, D, 'VariableNames', { 'C', 'D'} );
% Write data to text file
writetable(CD, 'MyFilevelocity.txt')
```

Published with MATLAB® R2017b

O   Appendix - Mathcad Calculation

1 Load capacity of reference beam

1.1   Input data

1.1.1 Geometry

$h := 0.1 \ m$

Beam height

$b := 0.1 \ m$

Beam width

$L := 1.3 \ m$

Effective span length

$\Phi := 6 \ mm$

Nominal bar diameter

$A_{bar} := \pi \cdot \dfrac{\Phi^2}{4} = 28.274 \ mm^2$

Area of reinforcement

$n' := 2$

Number of top rebars

$n := 2$

Number of bottom rebars

$A_s' := n' \cdot A_{bar} = 56.549 \ mm^2$

Area of top reinfcement

$A_s := n \cdot A_{bar} = 56.549 \ mm^2$

Area of bottom reinforcement

$c := 0.02 \ m - \dfrac{\Phi}{2} = 17 \ mm$

Concrete cover

$d := h - \left(\dfrac{\Phi}{2} + c \right) = 80 \ mm$

Distance from the top edge to bottom reinforcement

$d' := \left(\dfrac{\Phi}{2} + c \right) = 20 \ mm$

Distance from the top edge to top reinforcement

1.1.2 Material properties

1.1.2.1 Concrete

$f_{cm} := 45.54 \ MPa$
Mean compressive strength

$f_{ck} := f_{cm} - 8 \ MPa = 37.54 \ MPa$
Characterstics compressive strength

$f_{ctm.sp} := 0.9 \cdot 6.56 \ MPa = 5.904 \ MPa$
Mean tensile strength from splitting test

$f_{ctm.ck} := 0.3 \cdot 37.54^{\frac{2}{3}} \ MPa = 3.363 \ MPa$
Mean tensile strength

$k := 1.6 - \dfrac{100}{1000} = 1.5$
Factor for flexural tensile strength

$f_{ct.fl} := k \cdot f_{ctm.ck} = 5.045 \ MPa$
Flexural tensile strength

$E_{cm} := 34.7 \ GPa$
Mean modulus of elasticity

$\gamma_c := 1.0$
Partial safety factor

$f_{cd} := \dfrac{f_{cm}}{\gamma_c} = 45.54 \ MPa$
Design compresssive strength of concrete

$\varepsilon_{cu} := 0.0035$
Ultimate concrete strain

1.1.2.2 Reinforcing steel

$f_{ym} := 543 \ MPa$
Mean yield strength

$f_t := 660 \ MPa$
Ultimate tensile strength

$E_{sm} := 196 \ GPa$
Mean modulus of elasticity

$\gamma_s := 1$
Partial factor

$f_{yd} := \dfrac{f_{ym}}{\gamma_s} = 543 \ MPa$
Design tensile strength for reinforcing steel

1.2 Stress-strain relationship

1.2.1 Stress-strain relationship for concrete

$\varepsilon_{c2} := 2 \cdot 10^{-3}$
Concrete strain at maximum strength

$$\varepsilon_{cu2} := 3.5 \cdot 10^{-3}$$

Ultimate concrete strain

$$n := 2$$

Exponent

$$\sigma_c\left(\varepsilon_c\right) := \begin{Vmatrix} \text{if } 0 \leq \varepsilon_c \leq \varepsilon_{c2} \\ \quad \left\| \left(1-\left(1-\dfrac{\varepsilon_c}{\varepsilon_{c2}}\right)^n\right) \cdot f_{cm} \right\| \\ \text{if } \varepsilon_{c2} \leq \varepsilon_c \leq \varepsilon_{cu2} \\ \quad \left\| f_{cm} \right. \end{Vmatrix}$$

$$\varepsilon_c := 0, 0.0001 .. \varepsilon_{cu2}$$

A vector of strain

Stress-strain relationship

$$\sigma_c\left(\varepsilon_c\right) \left(\dfrac{kg}{m \cdot s^2}\right)$$

$$\varepsilon_c$$
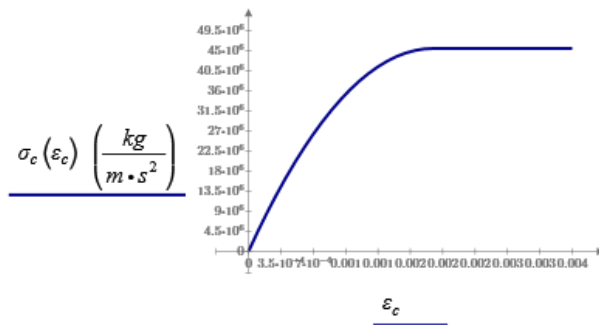
Area under the curve for a given value of strain

Determination of block factors

$$Area\left(\varepsilon_c\right) := \int_0^{\varepsilon_c} \sigma_c\left(\varepsilon_c\right) \, d\varepsilon_c$$

Area under the curve multiplied by the distance from the origin to the centre of gravity

$$A\_\varepsilon\left(\varepsilon_c\right) := \int_0^{\varepsilon_c} \sigma_c\left(\varepsilon_c\right) \cdot \varepsilon_c \, d\varepsilon_c$$

$$\alpha_{Rs}\left(\varepsilon_c\right) := \dfrac{Area\left(\varepsilon_c\right)}{f_{cm} \cdot \varepsilon_c}$$

$$\beta_{Rs}\left(\varepsilon_c\right) := \dfrac{\varepsilon_c - \dfrac{A\_\varepsilon\left(\varepsilon_c\right)}{Area\left(\varepsilon_c\right)}}{\varepsilon_c}$$

Concrete stress blocks at ultimate concrete strain as

$$\alpha_R := 0.81$$

$$\beta_R := 0.416$$

1.2.2 Stress-strain relationship for reinforcement steel

$$\varepsilon_{su} := 0.087$$ Ultimate steel strain

$$\varepsilon_{sy} := \frac{f_{ym}}{E_{sm}} = 0.003$$ Steel strain at maximum strength

$$p_1(\varepsilon_s) := \frac{\varepsilon_s - \varepsilon_{sy}}{\varepsilon_{su} - \varepsilon_{sy}}$$

$$\varepsilon_s := 0, 0.001 .. \varepsilon_{su}$$ A vector of different strain

$$\sigma_s(\varepsilon_s) := \left\| \begin{array}{l} \text{if } \varepsilon_s \le \varepsilon_{sy} \\ \quad \left\| E_{sm} \cdot \varepsilon_s \right. \\ \text{if } \varepsilon_s > \varepsilon_{sy} \\ \quad \left\| f_{ym} + p_1(\varepsilon_s) \cdot (f_t - f_{ym}) \right. \end{array} \right\|$$

$\sigma_s(\varepsilon_s)$ (MPa)
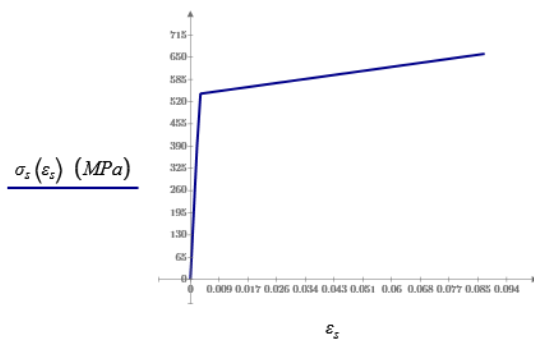
1.3 Load capacity in ultimate limit state

1.3.1 Analysis without top reinforcement

Assume yielding

$$\varepsilon_{s.1} > \varepsilon_{s.y} \qquad \varepsilon_{s.1} = \frac{d - X_1}{X_1} \cdot \varepsilon_{cu}$$

Assume neutral axis

$$X_{u.1} := 20 \ mm$$

$$X_{u.1} := \mathbf{root}\left(\left(\alpha_R \cdot f_{cd} \cdot b \cdot X_{u.1}\right) - \sigma_s\left(\frac{d - X_{u.1}}{X_{u.1}} \cdot \varepsilon_{cu}\right) \cdot A_s, X_{u.1}\right)$$

$$X_{u.1} = 8.863 \ mm$$

Check strain

$$\varepsilon_{s.1} := \frac{d - X_{u.1}}{X_{u.1}} \cdot \varepsilon_{cu} = 0.028 \qquad\qquad \varepsilon_{s.y} := \varepsilon_{sy} \qquad\qquad \varepsilon_{s.1} > \varepsilon_{s.y} = 1$$

Moment capacity

$$M_{u.1} := \alpha_R \cdot f_{cd} \cdot b \cdot X_{u.1} \cdot \left(d - \beta_R \cdot X_{u.1}\right)$$

$$M_{u.1} = 2.495 \ kN \cdot m$$

$$F_{u.1} := \frac{4 \cdot M_{u.1}}{L} = 7.677 \ kN$$

Calculation of stress in steel bars:

$$\sigma_{s.1} := \sigma_s\left(\varepsilon_{s.1}\right) \qquad\qquad \sigma_{s.1} = 578.171 \ MPa$$

Calculation of curvature at failure

$$\varepsilon_{s.1} = 0.028 \qquad\qquad \Phi u1 := \frac{\varepsilon_{s.1}}{d - X_{u.1}} = 0.395 \ \frac{1}{m}$$

1.3.2 Moment and load capacity including top reinforcement

Assuming the neutral axis is located above the top reinforcement (tension in top and bottom)

$$\varepsilon_{s.2} = \frac{d - X_{c.2}}{X_{c.2}} \cdot \varepsilon_{cu}$$ 　　　　Strain in bottom reinforrcement

$$\varepsilon'_{s.2} = \frac{d' - X_{c.2}}{X_{c.2}} \cdot \varepsilon_{cu}$$ 　　　　Strain in top reinforcement

Assume neutral axis

$$X_{c.2} := 20 \ mm$$

$$X_{c.2} := \mathbf{root}\left(\left(\alpha_R \cdot f_{cd} \cdot b \cdot X_{c.2}\right) - \sigma_s\left(\frac{d' - X_{c.2}}{X_{c.2}} \cdot \varepsilon_{cu}\right) \cdot A_s' - \sigma_s\left(\frac{d - X_{c.2}}{X_{c.2}} \cdot \varepsilon_{cu}\right) \cdot A_s, X_{c.2}\right)$$

$$X_{c.2} = 13.59 \ mm$$

The assumption is correct the neutral axis is located above the top reinforcement

$$\varepsilon_{sy} = 0.003$$

Check strain in rebars

$$\varepsilon_{s.2} := \frac{d - X_{c.2}}{X_{c.2}} \cdot \varepsilon_{cu}$$ 　　　　　$$\varepsilon_{s.2} = 0.017$$ 　　　　$$\varepsilon_{s.2} > \varepsilon_{sy} = 1$$

$$\varepsilon'_{s.2} := \frac{d' - X_{c.2}}{X_{c.2}} \cdot \varepsilon_{cu}$$ 　　　　　$$\varepsilon'_{s.2} = 0.002$$ 　　　　$$\varepsilon'_{s.2} > \varepsilon_{sy} = 0$$

Moment capacity

$$M_{u.2} := \alpha_R \cdot f_{cd} \cdot b \cdot X_{c.2} \cdot \left(d - \beta_R \cdot X_{c.2}\right) - \sigma_s\left(\frac{d' - X_{c.2}}{X_{c.2}} \cdot \varepsilon_{cu}\right) \cdot A_s' \cdot (d - d')$$

$$M_{u.2} = 2.629 \ kN \cdot m$$

$$F_{u.2} := \frac{4 \cdot M_{u.2}}{L} = 8.09 \ kN$$

Calculation of stress in the steel bars

$$\sigma'_{s.2} := \sigma_s \left(\varepsilon'_{s.2} \right) \qquad\qquad \sigma'_{s.2} = 323.575 \ MPa$$

$$\sigma_{s.2} := \sigma_s \left(\varepsilon_{s.2} \right) \qquad\qquad \sigma_{s.2} = 562.91 \ MPa$$

Calculation of curvature at failure

$$\varepsilon_{s.2} = 0.017 \qquad\qquad\qquad \Phi u1 := \frac{\varepsilon_{s.2}}{d - X_{c.2}} = 0.258 \ \frac{1}{m}$$

1.3.3 Theoretical load vs deformation relationship

Determination of cracking moment and cracking curvature

Modular ratio

$$\alpha_s := \frac{E_{sm}}{E_{cm}} = 5.648 \qquad\qquad n = 2$$

$$I_I := b \cdot \frac{h^3}{12} + \left(\alpha_s - 1 \right) \cdot 2 \cdot n \cdot A_{bar} \cdot \left(d - \frac{h}{2} \right)^2$$

Moment of inertia in state I

$$I_I = \left(8.806 \cdot 10^6 \right) \ mm^4$$

$$M_{cr} := f_{ct.fl} \cdot \frac{I_I}{0.5 \cdot h} = 0.889 \ \left(kN \cdot m \right)$$

Cracking moment

Cracking force

$$F_{cr} := 4 \cdot \frac{M_{cr}}{L} = 2.734 \ kN$$

1.3.3.1 Determination of moment of inertia for state II

Calculation of position of neutral axis

First moment of area considered to be around the neutral axis

$$b \cdot \frac{X_{II}^2}{2} + \left(\alpha_s - 1 \right) \cdot A_s' \cdot \left(X_{II} - d' \right) = \alpha_s \cdot A_s \cdot \left(d - X_{II} \right)$$

first guess

$$X_{II} := 50 \ mm$$

$$X_{II} := \mathbf{root}\left(\left(b \cdot 0.5 \cdot X_{II}{}^2\right) - \left(\alpha_s\right) \cdot A_s' \cdot \left(d' - X_{II}\right) - \alpha_s \cdot A_s \cdot \left(d - X_{II}\right), X_{II}\right)$$

$$X_{II} = 19.682 \; mm$$

Moment of inertia in state II

$$I_{II} := b \cdot \frac{X_{II}{}^3}{3} + \left(\alpha_s\right) \cdot A_s' \cdot \left(d' - X_{II}\right)^2 + \alpha_s \cdot A_s \cdot \left(d - X_{II}\right)^2$$

$$I_{II} = \left(1.416 \cdot 10^{-6}\right) \; m^4$$

Load-deformation plot

$$K_I := \frac{48 \cdot E_{cm} \cdot I_I}{L^3} = 6.676 \; \frac{kN}{mm} \qquad \qquad \text{Stiffness in state I}$$

$$K_{II} := \frac{48 \cdot E_{cm} \cdot I_{II}}{L^3} = 1.074 \; \frac{kN}{mm} \qquad \qquad \text{Stiffness in state II}$$

3.3.2 Deformation for state I and state II

$$F_{cr} = 2.734 \; kN \qquad \qquad \qquad \qquad \text{Cracking load}$$

$$U_{cr} := \frac{F_{cr}}{K_I} = 0.41 \; mm \qquad \qquad \qquad \text{Cracking deflection}$$

$$F_{u.2} = 8.09 \; kN \qquad \qquad \qquad \qquad \text{Peak load}$$

$$U_{u.2} := \frac{F_{u.2}}{K_{II}} = 7.534 \; mm \qquad \qquad \qquad \text{Deflection at peak load}$$

$$K_{cy} := \frac{F_{u.2} - F_{cr}}{U_{u.2} - U_{cr}} = 0.752 \; \frac{kN}{mm}$$

$$u := 0 \; mm, 0.1 \; mm .. 20 \; mm$$

$$F_I(u) := \begin{Vmatrix} \text{if } u \le U_{cr} \\ \quad \begin{Vmatrix} K_I \cdot u \end{Vmatrix} \\ \text{if } u > U_{cr} \\ \quad \begin{Vmatrix} F_{cr} + (u - U_{cr}) \cdot K_{cy} \end{Vmatrix} \\ \text{if } u > U_{u.2} \\ \quad \begin{Vmatrix} F_{u.2} \end{Vmatrix} \end{Vmatrix}$$

$$Load.(u) := F_I(u)$$

Deformation considering only state II

$$F_{u.2} = 8.09 \ kN \qquad\qquad\qquad\qquad \text{Peak load}$$

$$U_{u.2} := \frac{F_{u.2}}{K_{II}} = 7.534 \ mm \qquad\qquad \text{Deflection at peak load}$$

$$F_{II}(u) := \begin{Vmatrix} \text{if } u \le U_{u.2} \\ \quad \begin{Vmatrix} K_{II} \cdot u \end{Vmatrix} \\ \text{if } u > U_{u.2} \\ \quad \begin{Vmatrix} F_{u.2} \end{Vmatrix} \end{Vmatrix}$$

$$Load(u) := F_{II}(u)$$

$\underline{Load(u) \ (kN)}$

$\underline{Load.(u) \ (kN)}$

$\underline{u \ (mm)}$
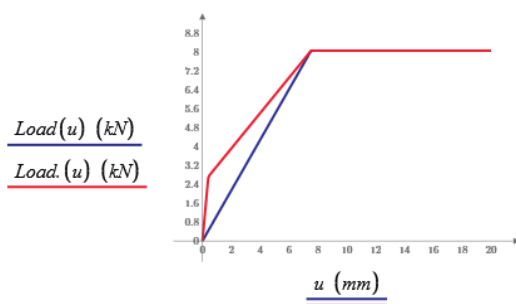
1.4 Prediction of plastic rotation capacity for unstrengthened beam

4.1 Geometry

$h := 0.1 \; m$ Beam height

$b := 0.1 \; m$ Beam width

$L = 1.3 \; m$ Effective span length

$Lo := \dfrac{L}{2} = 0.65 \; m$ Distance from the critical section to the support

$d = 0.08 \; m$ Effective height

1.4.2 Rotation capacity according to Eurocode

$X_u := X_{u.1} = 8.863 \; mm$ Neutral axis disregarding top reinforcemnt

$\dfrac{X_u}{d} = 0.111$

$\theta_{pl} \; [10^{-3} \; rad]$
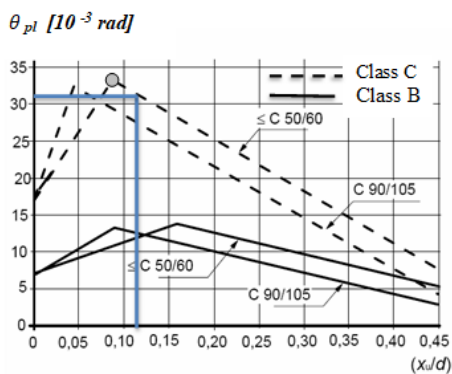
$\Theta_{ECR.ch} := 0.031$ Rotation capacity from the chart

$\lambda := \dfrac{Lo}{d} = 8.125$

$$K_\lambda := \sqrt{\frac{\lambda}{3}} = 1.646$$

$$\Theta_{tot.EC} := K_\lambda \cdot \Theta_{ECR.ch} = 0.051$$

Final value of rotation capacity according to

$$\Theta_{pl.EC} := \frac{\Theta_{tot.EC}}{2} = 0.026$$

$$U_{pl.EC} := \Theta_{pl.EC} \cdot \frac{L}{2} = 16.58 \ mm$$

1.4.3 Rotation capacity according to Bk 25

Emprical expression

$$l_{pl.Bk25} := 0.5 \cdot d + 0.15 \cdot L = 0.235 \ m$$ 　　　　　　　Plastic hinge length

$$A_s = 56.549 \ mm^2$$

　　　　　　　　　　　　　　　　　　　　　　Area of tensile reinforcement

$$\omega_s := \frac{A_s \cdot f_{ym}}{b \cdot d \cdot f_{cm}} = 0.084$$

$$A_c := 0 \ m^2$$ 　　　　　　　　　　　　　　　　Area of compression reinforcemnt

$$\omega'_s := \frac{A_c \cdot f_{ym}}{b \cdot d \cdot f_{cm}} = 0$$ 　　　　　　　　Top reinforcement under tension

Dominant failure mode

$$\omega_{s.cri} := \frac{0.8 \cdot \varepsilon_{cu2}}{\varepsilon_{cu2} + \varepsilon_{su}} = 0.031$$

　　　　　　　　　　　　　　　　　　　　　　Dominant failure mode is
　　　　　　　　　　　　　　　　　　　　　　concrete crushing

$$\omega_s > \omega_{s.cri} = 1$$

$$\Theta_{pl.bK25} := \frac{0.4 \cdot \varepsilon_{cu}}{\omega_s} \cdot \left(1 + 0.3 \cdot \frac{L}{d}\right) = 0.098$$

$$U_{pl.Bk25} := \frac{\Theta_{pl.bK25} \cdot L}{2} = 63.432 \ mm$$

2 Load capacity of reinforced concrete beam with FRP strengthening

2.1 Input data

2.1.1 Geometry

$h := 0.1 \ m$ Beam height

$b := 0.1 \ m$ Beam width

$L := 1.3 \ m$ Effective span length

$\Phi := 6 \ mm$ Nominal bar diameter

$A_{bar} := \pi \cdot \dfrac{\Phi^2}{4} = 28.274 \ mm^2$ Area of reinforcement

$n' := 2$ Number od top rebars

$n := 2$ Number od bottom rebars

$A_s' := n' \cdot A_{bar} = 56.549 \ mm^2$ Area of top reinfcement

$A_s := n \cdot A_{bar} = 56.549 \ mm^2$ Area of bottom reinforcement

$c := 0.02 \ m - \dfrac{\Phi}{2} = 17 \ mm$ Concrete cover

$d := h - \left(\dfrac{\Phi}{2} + c \right) = 80 \ mm$ Distance from the top edge to bottom reinforcement

$d' := \left(\dfrac{\Phi}{2} + c \right) = 20 \ mm$ Distance from the top edge to top reinforcement

$d_b := 20 \ mm$ Distance from the bottom edge to bottom reinforcement

2.1.1.1 Concrete material properties

$$f_{cm} := 45.54 \ MPa$$ 　　　　　　　　　　　Mean compressive strength

$$f_{ck} := f_{cm} - 8 \ MPa = 37.54 \ MPa$$ 　　　　Characterstics compressive strength

$$f_{ctm.sp} := 0.9 \cdot 6.56 \ MPa = 5.904 \ MPa$$ 　　Mean tensile strength from splitting test

$$f_{ctm.ck} := 0.3 \cdot 37.54^{\frac{2}{3}} \ MPa = 3.363 \ MPa$$ 　　Mean tensile strength

$$k := 1.6 - \frac{100}{1000} = 1.5$$ 　　　　　　　　factor for flexural tensile strength

$$f_{ct.fl} := k \cdot f_{ctm.ck} = 5.045 \ MPa$$ 　　　　flexural tensile strength

$$E_{cm} := 22 \cdot \left(\frac{45.54}{10}\right)^{0.3} = 34.669$$ 　　　Mean modulus of elasticity

$$E_{cm} := 34.7 \ GPa$$

$$\gamma_c := 1.0$$ 　　　　　　　　　　　　　　Partial factor

$$f_{cd} := \frac{f_{cm}}{\gamma_c} = 45.54 \ MPa$$ 　　　　　Design compresssive strength of concrete

$$\varepsilon_{cu} := 0.0035$$ 　　　　　　　　　　　Ultimate concrete strain

2.1.1.2 Reinforcing steel

$$f_{ym} := 543 \ MPa$$ 　　　　　　　　　　　Mean yield strength

$$f_t := 660 \ MPa$$ 　　　　　　　　　　　　Ultimate tensile strength

$$\gamma_s := 1$$ 　　　　　　　　　　　　　　　Partial factor

$$f_{yd} := \frac{f_{ym}}{\gamma_s} = 543 \ MPa$$ 　　　　　Design tensile strength for reinforcing steel

$$E_{sm} := 196 \ GPa$$ 　　　　　　　　　　Mean modulus of elasticity

$$\varepsilon_{sy} := \frac{f_{ym}}{E_{sm}} = 0.003$$ 　　　　　　　Steel strain

$$\alpha_s := \frac{E_{sm}}{E_{cm}} = 5.648$$

Mean modulus of elasticity

$$\varepsilon_{su} := 0.087$$

Ultimate strain

2.1.1.3 FRP geometry and material parameters

$$L_{fe} := 1.2 \ m$$

Length of FRP

$$t_{FRP} := 0.2 \ mm = 0.2 \ mm$$

Design thickness of FRP

$$t_{ADH} := 0.1 \ mm$$

Thickness of resin

$$t_{fe} := 1 \cdot t_{FRP} + 1 \cdot t_{ADH} = 0.3 \ mm$$

Thickness of FRP and adhesive

$$\beta := 0.9$$

$$b_{fe} := 100 \ mm = 100 \ mm$$

Width of FRP

$$d_{fe} := 100.3 \ mm$$

Distance to the layer of FRP

$$A_{fe} := 0.9 \cdot t_{fe} \cdot b_{fe} = 27 \ mm^2$$

Area of FRP

$$E_{FRP} := 120 \ GPa$$

Modulus of elasticity of FRP from the specification provided by the supplier

$$E_{ADH} := 6.5 \ GPa$$

$$A_{FRP} := 0.9 \cdot b_{fe} \cdot t_{FRP} = 18 \ mm^2$$

Area of total strengthening

$$A_{ADH} := A_{fe} - A_{FRP} = 9 \ mm^2$$

Area of total strengthening

$$E_{fe} := \frac{E_{FRP} \cdot A_{FRP} + E_{ADH} \cdot A_{FRP}}{A_{fe}} = 84.333 \ GPa$$

Mean modulus of elasticity of FRP

$$f_f := 2.900 \ GPa$$

Tensile strength of FRP

$$\gamma_f := 1$$

Partial factor

$$f_{fe} := \frac{f_f}{\gamma_f} = 2.9 \ GPa$$

Design tensile strength of FRP

$$\alpha_{fe} := \frac{E_{fe}}{E_{cm}} = 2.43$$

Modular ratio

$$\varepsilon_{fe} := \frac{f_{fe}}{E_{fe}} = 0.034$$ FRP strain

2.2 Stress-strain relationship

$$\varepsilon_{c2} := 2 \cdot 10^{-3}$$ Concrete strain at maximum strength

$$\varepsilon_{cu2} := 3.5 \cdot 10^{-3}$$ Ultimate concrete strain

Stress block factors

$$\alpha_R := 0.8$$

$$\beta_R := 0.4$$

2.3 Calculation load capacity in ULS

2.3.1 Calculation of cracking force including FRP

First moment of inertia

$$I_I := \frac{b \cdot h^3}{12} + 2 \cdot (\alpha_s - 1) \cdot A_s \cdot \left(\frac{h}{2} - d'\right)^2 + \alpha_{fe} \cdot A_{fe} \cdot \left(\frac{h}{2} + \frac{t_{fe}}{2}\right)^2 = (8.972 \cdot 10^6) \; mm^4$$

$$M_{crfe} := f_{ct,fl} \cdot \frac{I_I}{0.5 \cdot h} = 0.905 \; kN \cdot m$$

$$F_{cr,fe} := 4 \cdot \frac{M_{crfe}}{L} = 2.785 \; kN$$

2.3.2 Calculation of yielding load with FRP strengthening

Neutral axis in cracked state

Assume the neutral axis located below the top reinforcement (top reinforcement under compression)

$$X_{fec} := 25 \; mm$$

$$\left(b \cdot \frac{X_{fec}^{2}}{2}\right) + (\alpha_s - 1) \cdot A_s' \cdot (X_{fec} - d') = \alpha_s \cdot A_s \cdot (d - X_{fec}) + \alpha_{fe} \cdot A_{fe} \cdot (d_{fe} - X_{fec})$$

$$X_{fec} := \mathbf{root}\left(\left(\left(b \cdot \frac{X_{fec}^{2}}{2} + (\alpha_{s}-1) \cdot A_{s}' \cdot (X_{fec}-d') - \alpha_{s} \cdot A_{s} \cdot (d-X_{fec}) - \alpha_{fs} \cdot A_{fs} \cdot (d_{fs}-X_{fec})\right), X_{fec}\right)\right.$$

$$X_{fec} = 21.625 \ mm$$

Strain at yielding of bottom reinforcement

$$\varepsilon_{cu2} := 0.0035$$

$$\varepsilon'_{sy} := \frac{X_{fec}-d'}{d-X_{fec}} \cdot \varepsilon_{sy} = 7.71 \cdot 10^{-5} \qquad \text{Strain at top reinforcement}$$

$$\varepsilon'_{cuy} := \frac{X_{fec}}{d-X_{fec}} \cdot \varepsilon_{sy} = 0.001 \qquad \text{Concrete strain at top edge}$$

$$\varepsilon_{fy} := \frac{d_{fs}-X_{fec}}{d-X_{fec}} \cdot \varepsilon_{sy} = 0.004 \qquad \text{FRP strain}$$

$$M_{y.k.sy} := b \cdot X_{fec} \cdot \varepsilon'_{cuy} \cdot E_{cm} \cdot \left(X_{fec} - \frac{X_{fec}}{3}\right) + \varepsilon'_{sy} \cdot E_{sm} \cdot A_{s}' \cdot (X_{fec}-d') + f_{yd} \cdot A_{s} \cdot (d-X_{fec}) + \varepsilon_{fy} \cdot E_{fs} \cdot A_{fs} \cdot (d_{fs}-X_{fec})$$

$$M_{y.k.sy} = 3.573 \ m \cdot kN$$

$$F_{yield} := \frac{4 \cdot M_{y.k.sy}}{L} = 10.994 \ kN$$

2.3.2 Ultimate load

Assumptions

1. Steel started yielding before concrete crushing

2. Failure due to Concrete crushing at ultimate concrete strain, $\varepsilon_{cu2} = 0.035$

3. Early debonding did not occcur

$$\alpha_{R} := 0.8 \qquad\qquad \beta_{R} := 0.4$$

$$n := 1$$

$$\varepsilon_{fdic} := 0.41 \cdot \sqrt{\frac{f_{cd}}{n \cdot E_{fe} \cdot \frac{t_{fe}}{mm}}} = 0.017 \qquad \text{Strain limit in the FRP}$$

$$\varepsilon_{fe} = 0.034$$

$$\varepsilon_{fdic} < \varepsilon_{fe} = 1$$

$$\varepsilon_{cu2} := 3.5 \cdot 10^{-3}$$

Initial guess for neutral axis at ultimate state

$$x_{uf} := 30 \ mm$$

$$x_{uf} := \mathbf{root}\left(\left(\alpha_R \cdot f_{cd} \cdot b \cdot x_{uf} + A_s \cdot E_{sm} \cdot \frac{\varepsilon_{cu2}}{x_{uf}} \cdot \left(x_{uf} - d'\right) - A_s \cdot f_{yd} - A_{fe} \cdot E_{fe} \cdot \frac{\varepsilon_{fdic}}{x_{uf}} \cdot \left(d_{fe} - x_{uf}\right)\right), x_{uf}\right)$$

$$x_{uf} = 30.145 \ mm$$

Check strain

Strain at bottom reinforcement

$$\varepsilon_{syf} := \frac{\varepsilon_{cu2}}{x_{uf}} \cdot \left(d - x_{uf}\right) = 0.006 \qquad\qquad \varepsilon_{syf} > \varepsilon_{sy} = 1$$

Strain at top reinforcement

$$\varepsilon'_{syf} := \frac{\varepsilon_{cu2}}{x_{uf}} \cdot \left(x_{uf} - d'\right) = 0.001 \qquad\qquad \varepsilon'_{syf} > \varepsilon_{sy} = 0$$

Strain at FRP

$$\varepsilon_{Fyu} := \frac{\varepsilon_{cu2}}{x_{uf}} \cdot \left(d_{fe} - x_{uf}\right) = 0.008 \qquad\qquad \varepsilon_{Fyu} < \varepsilon_{fe} = 1 \qquad \text{Debonding due to FRP rupture did not occur}$$

$$\varepsilon_{Fyu} := 0.009 \qquad\qquad \varepsilon_{Fyu} < \varepsilon_{fdic} = 1 \qquad \text{FRP strain is the limit}$$

Guess for neutral axis at ultimate state

$$x_{uf} := 30 \ mm$$

$$x_{uf} := \mathbf{root}\left(\left(\alpha_R \cdot f_{cd} \cdot b \cdot x_{uf} + A_s \cdot E_{sm} \cdot \varepsilon_{sy} - A_s \cdot f_{yd} - A_{fe} \cdot E_{fe} \cdot \frac{\varepsilon_{Fyu}}{x_{uf}} \cdot \left(d_{fe} - x_{uf}\right)\right), x_{uf}\right)$$

$$x_{uf} = 21.106 \ mm$$

Check strain

Strain at bottom reinforcement

$$\varepsilon_{syf} := \frac{\varepsilon_{cu2}}{x_{uf}} \cdot (d - x_{uf}) = 0.01 \qquad\qquad \varepsilon_{syf} > \varepsilon_{sy} = 1$$

Strain at top reinforcement

$$\varepsilon'_{syf} := \frac{\varepsilon_{cu2}}{x_{uf}} \cdot (x_{uf} - d') = 1.834 \cdot 10^{-4} \qquad\qquad \varepsilon'_{syf} > \varepsilon_{sy} = 0$$

Strain at FRP

$$\varepsilon_{Fyu} := \frac{\varepsilon_{cu2}}{x_{uf}} \cdot (d_{fe} - x_{uf}) = 0.013 \qquad\qquad \varepsilon_{Fyu} < \varepsilon_{fe} = 1 \qquad \text{Debonding due to FRP rupture did not occur}$$

$$\varepsilon_{Fyu} < \varepsilon_{fdic} = 1 \qquad \text{FRP strain is the limit}$$

Ultimate moment

$$M_{uf2} := \alpha_R \cdot f_{cd} \cdot b \cdot x_{uf} \cdot (x_{uf} - \beta_R \cdot x_{uf}) + A_s' \cdot E_{sm} \cdot \varepsilon'_{syf} \cdot (x_{uf} - d') + f_{yd} \cdot A_s \cdot (d - x_{uf}) + \varepsilon_{Fyu} \cdot E_{fe} \cdot A_{fe} \cdot (d_{fe} - x_{uf})$$

$$M_{uf2} = 5.153 \ kN \cdot m$$

$$F_{uf} := \frac{M_{uf2} \cdot 4}{L} = 15.854 \ kN$$

2.4 Load-deformation plot

Calculation of neutral axis in state II

Initial guess

$$X_{II} := 30 \ mm$$

$$X_{II} := \mathbf{root}\left((b \cdot 0.5 \cdot X_{II}^2) - (\alpha_s - 1) \cdot A_s' \cdot (d' - X_{II}) - \alpha_s \cdot A_s \cdot (d - X_{II}) - \alpha_{fe} \cdot A_{fe} \cdot (d_{fe} - X_{II}), X_{II}\right)$$

$$X_{II} = 21.625 \ mm$$

Moment of inertia in state II

$$I_{II} := b \cdot \frac{X_{II}^3}{3} + (\alpha_s - 1) \cdot A_s' \cdot (d' - X_{II})^2 + \alpha_s \cdot A_s \cdot (d - X_{II})^2 + \alpha_{fe} \cdot A_{fe} \cdot (d_{fe} - X_{II})^2$$

$$I_{II} = (1.832 \cdot 10^6) \ mm^4$$

Deformation considering only state II

$$F_{uf} = 15.854 \ kN \hspace{4cm} \text{Peak load}$$

$$K_{IIfe} := \frac{48 \cdot E_{cm} \cdot I_{II}}{L^3} = 1.389 \ \frac{kN}{mm} \hspace{2cm} \text{Stiffness in state II}$$

$$U_{u.2} := \frac{F_{uf}}{K_{IIfe}} = 11.412 \ mm \hspace{2cm} \text{Deflection at peak load}$$

$$F_{IIf}(u) := \left\| \begin{array}{l} \text{if } u \le U_{u.2} \\ \quad \left\| K_{IIfe} \cdot u \right. \\ \text{if } u > U_{u.2} \\ \quad \left\| F_{uf} \right. \end{array} \right.$$

$$Load.(u) := F_{IIf}(u)$$

Load-deformation for state I and state II

$$F_{cr,fe} = 2.785 \ kN \hspace{4cm} \text{Cracking load}$$

$$K_{Ife} := \frac{48 \cdot E_{cm} \cdot I_I}{L^3} = 6.802 \ \frac{kN}{mm} \hspace{2cm} \text{Stiffness in state I}$$

$$K_{IIfe} := \frac{48 \cdot E_{cm} \cdot I_{II}}{L^3} = 1.389 \ \frac{kN}{mm} \hspace{2cm} \text{Stiffness in state II}$$

$$U_{cr} := \frac{F_{cr,fe}}{K_{Ife}} = 0.41 \ mm \hspace{2cm} \text{Cracking deflection}$$

$$F_{uf} = 15.854 \ kN \hspace{4cm} \text{Peak load}$$

$$U_{u.2} := \frac{F_{uf}}{K_{IIfe}} = 11.412 \ mm \hspace{2cm} \text{Deflection at peak load}$$

$$K_{cyf} := \frac{F_{uf} - F_{cr,fe}}{U_{u.2} - U_{cr}} = 1.188 \ \frac{kN}{mm}$$

$$u := 0 \ mm, 0.1 \ mm .. 20 \ mm$$

$$F_{IIf}(u) := \begin{Vmatrix} \text{if } u \le U_{cr} \\ \quad \begin{Vmatrix} K_{Ife} \cdot u \end{Vmatrix} \\ \text{if } u > U_{cr} \\ \quad \begin{Vmatrix} F_{cr,fe} + (u - U_{cr}) \cdot K_{cyf} \end{Vmatrix} \\ \text{if } u > U_{u.2} \\ \quad \begin{Vmatrix} F_{uf} \end{Vmatrix} \end{Vmatrix}$$

$$Load(u) := F_{IIf}(u)$$

$\underline{Load.(u)\ (kN)}$

$\underline{Load(u)\ (kN)}$

$\underline{u\ (mm)}$
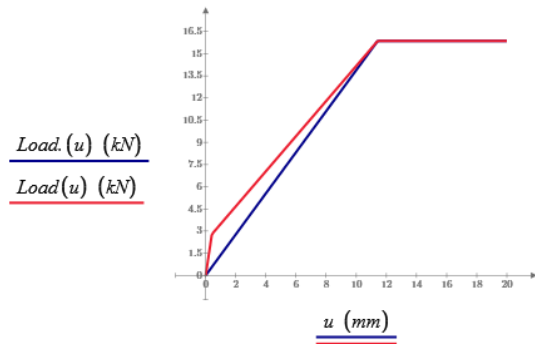
3 Load capacity of reinforced concrete beam with 3 layer FRP strengthening

3.1 Input data

3.1.1 Geometry

$h := 0.1 \; m$

Beam height

$b := 0.1 \; m$

Beam width

$L := 1.3 \; m$

Effective span length

$\Phi := 6 \; mm$

Nominal bar diameter

$A_{bar} := \pi \cdot \dfrac{\Phi^2}{4} = 28.274 \; mm^2$

Area of reinforcement

$n' := 2$

Number of top rebars

$n := 2$

Number of bottom rebars

$A_s' := n' \cdot A_{bar} = 56.549 \; mm^2$

Area of top reinforcement

$A_s := n \cdot A_{bar} = 56.549 \; mm^2$

Area of bottom reinforcement

$c := 0.02 \; m - \dfrac{\Phi}{2} = 17 \; mm$

Concrete cover

$d := h - \left(\dfrac{\Phi}{2} + c \right) = 80 \; mm$

Distance from the top edge to bottom reinforcement

$d' := \left(\dfrac{\Phi}{2} + c \right) = 20 \; mm$

Distance from the top edge to top reinforcement

$d_b := 20 \; mm$

Distance from the bottom edge to bottom reinforcement

3.1.2 Concrete material properties

$f_{cm} := 45.54 \; MPa$

Mean compressive strength

$f_{ck} := f_{cm} - 8 \; MPa = 37.54 \; MPa$

Characterstics compressive strength

$f_{ctm.sp} := 0.9 \cdot 6.56 \; MPa = 5.904 \; MPa$

Mean tensile strength from splitting test

$f_{ctm.ck} := 0.3 \cdot 37.54^{\frac{2}{3}} \; MPa = 3.363 \; MPa$

Mean tensile strength

$$k := 1.6 - \frac{100}{1000} = 1.5$$ Factor for flexural tensile strength

$$f_{ct,fl} := k \cdot f_{ctm.ck} = 5.045 \ MPa$$ Flexural tensile strength

$$E_{cm} := 22 \cdot \left(\frac{45.54}{10}\right)^{0.3} = 34.669$$

$$E_{cm} := 34.7 \ GPa$$ Mean modulus of elasticity

$$\gamma_c := 1.0$$ Partial factor

$$f_{cd} := \frac{f_{cm}}{\gamma_c} = 45.54 \ MPa$$ Design compresssive strength of concrete

$$\varepsilon_{cu} := 0.0035$$ Ultimate concrete strain

3.1.3 Reinforcing steel

$$f_{ym} := 543 \ MPa$$ Mean yield strength

$$f_t := 660 \ MPa$$ Ultimate tensile strength

$$\gamma_s := 1$$ Partial factor

$$f_{yd} := \frac{f_{ym}}{\gamma_s} = 543 \ MPa$$ Design tensile strength for reinforcing steel

$$E_{sm} := 196 \ GPa$$

$$\varepsilon_{sy} := \frac{f_{ym}}{E_{sm}} = 0.003$$ Mean modulus of elasticity of steel

$$\alpha_s := \frac{E_{sm}}{E_{cm}} = 5.648$$ Mean modulus of elasticity

$$\varepsilon_{su} := 0.087$$ Ultimate steel strain

3.1.4 FRP geometry and material parameters

$$L_{fe} := 1.2 \ m$$ Length of FRP

$$t_{FRP} := 3 \cdot 0.2 \ mm = 0.6 \ mm$$ Design thickness of FRP

$$t_{ADH} := 3 \cdot 0.1 \ mm$$ Thickness of resin

$$t_{fe} := 1 \cdot t_{FRP} + 1 \cdot t_{ADH} = 0.9 \ mm$$ Total thickness of strengthening

$\beta := 0.9$

$b_{fe} := 100 \ mm = 100 \ mm$ Width of FRP

$d_{fe} := 100.45 \ mm$ Distance to the layer of FRP

$A_{fe} := 0.9 \cdot t_{fe} \cdot b_{fe} = 81 \ mm^2$ Total area of strengthening

$E_{FRP} := 120 \ GPa$ Modulus of elasticity of FRP

$E_{ADH} := 6.5 \ GPa$ Modulus of elasticity of resin

$A_{FRP} := 0.9 \cdot b_{fe} \cdot t_{FRP} = 54 \ mm^2$ Area of FRP

$A_{ADH} := A_{fe} - A_{FRP} = 27 \ mm^2$ Area of resin

$E_{fe} := \dfrac{E_{FRP} \cdot A_{FRP} + E_{ADH} \cdot A_{FRP}}{A_{fe}} = 84.333 \ GPa$ Modulus of elasticity of strengthening

$f_f := 2.900 \ GPa$ Tensile strength of FRP

$\gamma_f := 1$ Partial factor

$f_{fe} := \dfrac{f_f}{\gamma_f} = 2.9 \ GPa$ Design tensile strength of FRP

$\alpha_{fe} := \dfrac{E_{fe}}{E_{cm}} = 2.43$ Modular ratio

$\varepsilon_{fe} := \dfrac{f_{fe}}{E_{fe}} = 0.034$ Ultimate FRP strain

Stress-strain relationship

$\varepsilon_{c2} := 2 \cdot 10^{-3}$ Concrete strain at maximum strength

$\varepsilon_{cu2} := 3.5 \cdot 10^{-3}$ Ultimate concrete strain

Stress block factors

$\alpha_R := 0.8$

$\beta_R := 0.4$

3.2 Calculation of load capacity

3.2.1 Calculation of cracking force including FRP

First moment of inertia

$$I_I := \frac{b \cdot h^3}{12} + 2 \cdot (\alpha_s - 1) \cdot A_s \cdot \left(\frac{h}{2} - d'\right)^2 + \alpha_{fe} \cdot A_{fe} \cdot \left(\frac{h}{2} + \frac{t_{fe}}{2}\right)^2 = \left(9.308 \cdot 10^6\right) \ mm^4$$

$$M_{crfe} := f_{ct,fl} \cdot \frac{I_I}{0.5 \cdot h} = 0.939 \ kN \cdot m$$

$$F_{cr,fe} := 4 \cdot \frac{M_{crfe}}{L} = 2.89 \ kN$$

3.2.2 Yielding load with FRP strengthening

Neutral axis in cracked state

Assume the neutral axis located below the top reinforcement (top reinforcement under compression)

$$X_{fec} := 25 \ mm$$

$$\left(b \cdot \frac{X_{fec}^2}{2}\right) + (\alpha_s - 1) \cdot A_s' \cdot (X_{fec} - d') = \alpha_s \cdot A_s \cdot (d - X_{fec}) + \alpha_{fe} \cdot A_{fe} \cdot (d_{fe} - X_{fec})$$

$$X_{fec} := \mathbf{root}\left(\left(b \cdot \frac{X_{fec}^2}{2} + (\alpha_s - 1) \cdot A_s' \cdot (X_{fec} - d') - \alpha_s \cdot A_s \cdot (d - X_{fec}) - \alpha_{fe} \cdot A_{fe} \cdot (d_{fe} - X_{fec})\right), X_{fec}\right)$$

$$X_{fec} = 24.956 \ mm$$

Strain at yielding of bottom reinforcement

$$\varepsilon_{cu2} := 0.0035$$

$$\varepsilon'_{sy} := \frac{X_{fec} - d'}{d - X_{fec}} \cdot \varepsilon_{sy} = 2.494 \cdot 10^{-4} \qquad\qquad \text{Strain at top reinforcement}$$

$$\varepsilon'_{cuy} := \frac{X_{fec}}{d - X_{fec}} \cdot \varepsilon_{sy} = 0.001 \qquad\qquad \text{Concrete strain at top edge}$$

$$\varepsilon_{fy} := \frac{d_{fe} - X_{fec}}{d - X_{fec}} \cdot \varepsilon_{sy} = 0.004 \qquad\qquad \text{FRP strain}$$

$$M_{y.k.sy} := b \cdot X_{fec} \cdot \varepsilon'_{cuy} \cdot E_{cm} \cdot \left(X_{fec} - \frac{X_{fec}}{3} \right) + \varepsilon'_{sy} \cdot E_{sm} \cdot A_s' \cdot \left(X_{fec} - d' \right) + f_{yd} \cdot A_s \cdot \left(d - X_{fec} \right) + \varepsilon_{fy} \cdot E_{fe} \cdot A_{fe} \cdot \left(d_{fe} - X_{fec} \right)$$

$$M_{y.k.sy} = 5.473 \ m \cdot kN$$

$$F_{yield} := \frac{4 \cdot M_{y.k.sy}}{L} = 16.84 \ kN$$

3.2.3 Ultimate load

Assumptions

1. Steel started yielding before concrete crushing

2. Failure due to concrete crushing at ultimate concrete strain, $\varepsilon_{cu2} = 0.035$

3. Debonding did not occccur

$$\alpha_R := 0.8 \qquad\qquad \beta_R := 0.4$$

$$n := 3$$

$$\varepsilon_{fdic} := 0.41 \cdot \sqrt{\frac{f_{cd}}{n \cdot E_{fe} \cdot \dfrac{t_{fe}}{mm}}} = 0.006 \qquad\qquad\qquad \text{Strain limit in FRP}$$

$$\varepsilon_{fe} = 0.034$$

$$\varepsilon_{fdic} < \varepsilon_{fe} = 1$$

$$\varepsilon_{cu2} := 3.5 \cdot 10^{-3}$$

Initial guess for neutral axis at ultimate state

$$x_{uf} := 30 \ mm$$

$$x_{uf} := \mathbf{root}\left(\left(\left(\alpha_R \cdot f_{cd} \cdot b \cdot x_{uf} + A_s \cdot E_{sm} \cdot \frac{\varepsilon_{cu2}}{x_{uf}} \cdot \left(x_{uf} - d' \right) - A_s \cdot f_{yd} - A_{fe} \cdot E_{fe} \cdot \frac{\varepsilon_{fdic}}{x_{uf}} \cdot \left(d_{fe} - x_{uf} \right) \right) \right), x_{uf} \right)$$

$$x_{uf} = 30.168 \ mm$$

Check strain

Strain at bottom reinforcement

$$\varepsilon_{syf} := \frac{\varepsilon_{cu2}}{x_{uf}} \cdot \left(d - x_{uf} \right) = 0.006 \qquad\qquad \varepsilon_{syf} > \varepsilon_{sy} = 1$$

Strain at top reinforcement

$$\varepsilon'_{syf} := \frac{\varepsilon_{cu2}}{x_{uf}} \cdot (x_{uf} - d') = 0.001 \qquad \varepsilon'_{syf} > \varepsilon_{sy} = 0$$

Strain at FRP

$$\varepsilon_{Fyu} := \frac{\varepsilon_{cu2}}{x_{uf}} \cdot (d_{fe} - x_{uf}) = 0.008 \qquad \varepsilon_{Fyu} < \varepsilon_{fe} = 1 \qquad \text{Debonding due to FRP}$$
rupture did not occur

$$\varepsilon_{Fyu} := 0.004 \qquad \varepsilon_{Fyu} < \varepsilon_{fdic} = 1 \qquad \text{FRP strain is the limit}$$

Guess for neutral axis at ultimate state

$$x_{uf} := 30 \ mm$$

$$x_{uf} := \mathbf{root}\left(\left(\alpha_R \cdot f_{cd} \cdot b \cdot x_{uf} + A_s \cdot E_{sm} \cdot \varepsilon_{sy} - A_s \cdot f_{yd} - A_{fe} \cdot E_{fe} \cdot \frac{\varepsilon_{Fyu}}{x_{uf}} \cdot (d_{fe} - x_{uf})\right), x_{uf}\right)$$

$$x_{uf} = 23.953 \ mm$$

Check strain

Strain at bottom reinforcement

$$\varepsilon_{syf} := \frac{\varepsilon_{cu2}}{x_{uf}} \cdot (d - x_{uf}) = 0.008 \qquad \varepsilon_{syf} > \varepsilon_{sy} = 1$$

Strain at top reinforcement

$$\varepsilon'_{syf} := \frac{\varepsilon_{cu2}}{x_{uf}} \cdot (x_{uf} - d') = 5.776 \cdot 10^{-4} \qquad \varepsilon'_{syf} > \varepsilon_{sy} = 0$$

Strain at FRP

$$\varepsilon_{Fyu} := \frac{\varepsilon_{cu2}}{x_{uf}} \cdot (d_{fe} - x_{uf}) = 0.011$$

$$\varepsilon_{Fyu} < \varepsilon_{fe} = 1 \qquad \text{Debonding due to FRP}$$
rupture did not occur

$$\varepsilon_{Fyu} < \varepsilon_{fdic} = 0 \qquad \text{FRP strain is the limit}$$

Ultimate moment for FRP strain considering concrete crushing

$$M_{uf2} := \alpha_R \cdot f_{cd} \cdot b \cdot x_{uf} \cdot (x_{uf} - \beta_R \cdot x_{uf}) + A_s' \cdot E_{sm} \cdot \varepsilon'_{syf} \cdot (x_{uf} - d') + f_{yd} \cdot A_s \cdot (d - x_{uf}) + \varepsilon_{Fyu} \cdot E_{fe} \cdot A_{fe} \cdot (d_{fe} - x_{uf})$$

$$M_{uf2} = 8.841 \ kN \cdot m$$

$$F_{uf} := \frac{M_{uf2} \cdot 4}{L} = 27.205 \ kN$$

3.2.4 Load deformation plot

Calculation of neutral axis in state II

Initial guess

$X_{II} := 30 \; mm$

$X_{II} := \mathbf{root}\left(\left(b \cdot 0.5 \cdot {X_{II}}^2\right) - \left(\alpha_s - 1\right) \cdot A_s' \cdot \left(d' - X_{II}\right) - \alpha_s \cdot A_s \cdot \left(d - X_{II}\right) - \alpha_{fe} \cdot A_{fe} \cdot \left(d_{fe} - X_{II}\right), X_{II}\right)$

$X_{II} = 24.956 \; mm$

Moment of inertia in state II

$I_{II} := b \cdot \dfrac{{X_{II}}^3}{3} + \left(\alpha_s - 1\right) \cdot A_s' \cdot \left(d' - X_{II}\right)^2 + \alpha_s \cdot A_s \cdot \left(d - X_{II}\right)^2 + \alpha_{fe} \cdot A_{fe} \cdot \left(d_{fe} - X_{II}\right)^2$

$I_{II} = \left(2.614 \cdot 10^6\right) \; mm^4$

Deformation considering only state II

$F_{uf} = 27.205 \; kN$ Peak load

$K_{IIfe} := \dfrac{48 \cdot E_{cm} \cdot I_{II}}{L^3} = 1.982 \; \dfrac{kN}{mm}$ Stiffness in state II

$U_{u.2} := \dfrac{F_{uf}}{K_{IIfe}} = 13.726 \; mm$ Deflection at peak load

$F_{IIf}(u) := \begin{Vmatrix} \text{if } u \le U_{u.2} \\ \quad \begin{Vmatrix} K_{IIfe} \cdot u \end{Vmatrix} \\ \text{if } u > U_{u.2} \\ \quad \begin{Vmatrix} F_{uf} \end{Vmatrix} \end{Vmatrix}$

$Load.(u) := F_{IIf}(u)$

Load-deformation for state I and state II

$F_{cr.fe} = 2.89 \; kN$ Cracking load

$K_{Ife} := \dfrac{48 \cdot E_{cm} \cdot I_I}{L^3} = 7.056 \; \dfrac{kN}{mm}$ Stiffness in state I

$K_{IIfe} := \dfrac{48 \cdot E_{cm} \cdot I_{II}}{L^3} = 1.982 \; \dfrac{kN}{mm}$ Stiffness in state II

$$U_{cr} := \frac{F_{cr,fe}}{K_{Ife}} = 0.41 \ mm$$

Cracking deflection

$$F_{uf} = 27.205 \ kN$$

Peak load

$$U_{u.2} := \frac{F_{uf}}{K_{IIfe}} = 13.726 \ mm$$

Deflection at peak load

$$K_{cxf} := \frac{F_{uf} - F_{cr,fe}}{U_{u.2} - U_{cr}} = 1.826 \ \frac{kN}{mm}$$

$$u := 0 \ mm, 0.1 \ mm .. 20 \ mm$$

$$F_{IIf}(u) := \left\| \begin{array}{l} \text{if } u \leq U_{cr} \\ \quad \left\| K_{Ife} \cdot u \right. \\ \text{if } u > U_{cr} \\ \quad \left\| F_{cr,fe} + (u - U_{cr}) \cdot K_{cxf} \right. \\ \text{if } u > U_{u.2} \\ \quad \left\| F_{uf} \right. \end{array} \right.$$

$$Load(u) := F_{IIf}(u)$$

$$\underline{\underline{Load.(u) \ (kN)}}$$
$$\underline{\underline{Load(u) \ (kN)}}$$

$$\underline{\underline{u \ (mm)}}$$